Reservoir Modeling of CO₂ Injection in Arbuckle Saline Aquifer at Wellington Field, Sumner County, Kansas

Principal Author: Yevhen Holubnyak
Contributors: Willard Watney, Tiraz Birdie, Jason Rush, and Mina Fazelalavi
Kansas Geological Survey and Tbirdie Consulting

Disclaimer

1. Introduction

This section presents details of the Arbuckle reservoir simulation model that was constructed to project the results of the Wellington Field short-term Arbuckle CO_2 pilot injection project and delineate the EPA Area of Review (AoR). Work was performed under DEFE0006821 to fulfill Task 18—Reside Site Characterization Models and Simulations for Carbon Storage. As required under §146.84(c) of EPA Class VI Well rule, the AoR must be delineated using a computational model that can accurately predict the projected lateral and vertical migration of the CO_2 plume and formation fluids in the subsurface from the commencement of injection activities until the plume movement ceases and until pressure differentials sufficient to cause the movement of injected fluids or formation fluids into a underground source of drinking water USDW are no longer present. The model must:

i. Be based on detailed geologic data collected to characterize the injection zone(s), confining zone(s), and any additional zones; and anticipated operating data, including injection pressures, rates, and total volumes over the proposed life of the geologic sequestration project;

ii. Take into account any geologic heterogeneities, other discontinuities, data quality, and their possible impact on model predictions; and

iii. Consider potential migration through faults, fractures, and artificial penetrations.

This section presents the reservoir simulations conducted to fulfill §146.84 requirements stated above. The simulations were conducted assuming a maximum injection of 40,000 metric tons of CO_2 over a period of nine months. Based on market conditions, KGS/Berexco now plans to inject a total of only 26,000 tons at the rate of 150 tons/day for a total period of approximately 175 days. The simulation results, therefore, represent impacts of the maximum quantity of CO_2 that was originally planned for the Wellington project. The modeling results indicate that the induced pore pressures in the Arbuckle aquifer away from the injection well are of insufficient magnitude to cause the Arbuckle brines to migrate up into the USDW even if there were any artificial or natural penetration in the Arbuckle Group or the overlying confining units.

The simulation results also indicate that the free-phase CO_2 plume is contained within the total CO_2 plume (i.e., in the free plus dissolved phases) and that it extends to a maximum lateral distance of 2,150 ft from the injection well. The EPA Area of Review (AoR) is defined by

the 1% saturation isoline of the stabilized free-phase plume.

2. Conceptual Model and Arbuckle Hydrogeologic State Information

2.1 Modeled Formation

The simulation model spans the entire thickness of the Arbuckle aquifer. The CO_2 is to be injected in the lower portion of the Arbuckle in the interval 4,910–5,050 feet, which has relatively high permeability based on the core data collected at the site. Preliminary simulations indicated that the bulk of the CO_2 will remain confined in the lower portions of the Arbuckle because of the low permeability intervals in the baffle zones and also shown in analysis of geologic logs at wells KGS 1-28 and KGS 1-32. Therefore, no-flow boundary conditions were specified along the top of the Arbuckle. The specification of a no-flow boundary at the top is also in agreement with hydrogeologic analyses presented, which indicate that the upper confining zone—comprising the Simpson Group, the Chattanooga Shale, and the Pierson formation—has very low permeability, which should impede any vertical movement of groundwater from the Arbuckle Group. Evidence for sealing integrity of the confining zone and absence of transmissive faults include the following:

1) under-pressured Mississippian group of formations relative to pressure gradient in the Arbuckle,

2) elevated chlorides in Mississippian group of formations relative to brine recovered at the top of the Arbuckle,

3) geochemical evidence for stratification of Arbuckle aquifer system and presence of a competent upper confining zone.

Additionally, entry pressure analyses indicate that an increase in pore pressure of more than 956 psi within the confining zone at the injection well site is required for the CO_2-brine to penetrate through the confining zone. As discussed in the model simulation results section below, the maximum increase in pore pressure at the top of the Arbuckle is less than 1.5 psi under the worst-case scenario (which corresponds to a low permeability–low porosity alternative model case as discussed in Section 5.10). This small pressure rise at the top of the Arbuckle is due to CO_2 injection below the lower vertical-permeability baffle zones present in the middle of the Arbuckle Group, which confines the CO_2 in the injection interval in the lower portions of the Arbuckle Group. The confining zone is also documented to be locally free of transmissive

fractures based on fracture analysis conducted at KGS 1-28 (injection well). There are no known transmissive faults in the area. It should be noted that an Operation Plan For Safe and Efficient Injection has been submitted to the EPA, which has a provision for immediate cessation of injection should an anomalous pressure drop be detected owing to development or opening of fractures.

Based on the above evidence, it is technically appropriate to restrict the simulation region within the Arbuckle Group for purposes of numerical efficiency, without compromising predictions of the effects of injection on the plume or pressure fronts. Because of the presence of the Precambrian granitic basement under the Arbuckle Group, which is expected to provide hydraulic confinement, the bottom of the model domain was also specified as a no-flow boundary. Active, real-time pressure and temperature monitoring of the injection zone at the injection and monitoring wells will likely be able to detect any significant movement of CO_2 out of the injection zone along fractures. Also, the 18-seismometer array provided by Incorporated Research Institutions for Seismology (IRIS) will detect small seismicity and their hypocenters within several hundred feet resolution to provide additional means to monitor the unlikely movement of CO_2 above or below the Arbuckle injection zone.
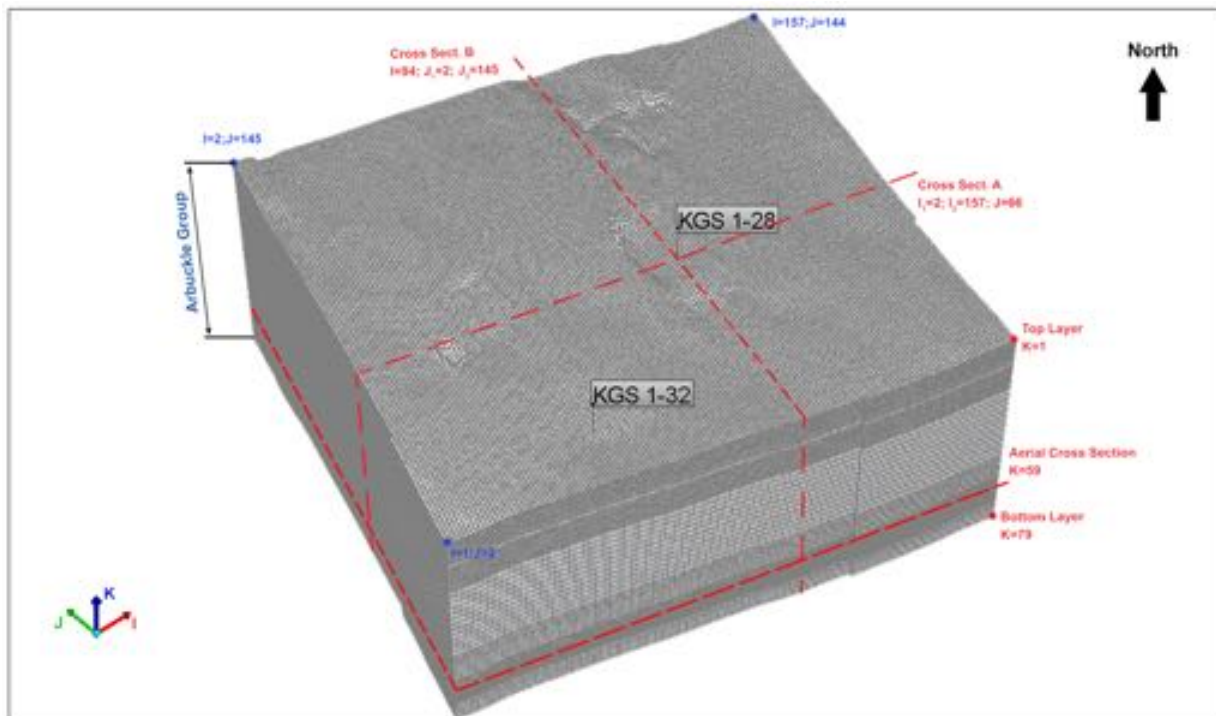

Figure 1a. Model mesh in 3-D showing location of Arbuckle injection (KGS 1-28) and monitoring (KGS 1-32) wells along with the east-west and north-south cross sections.
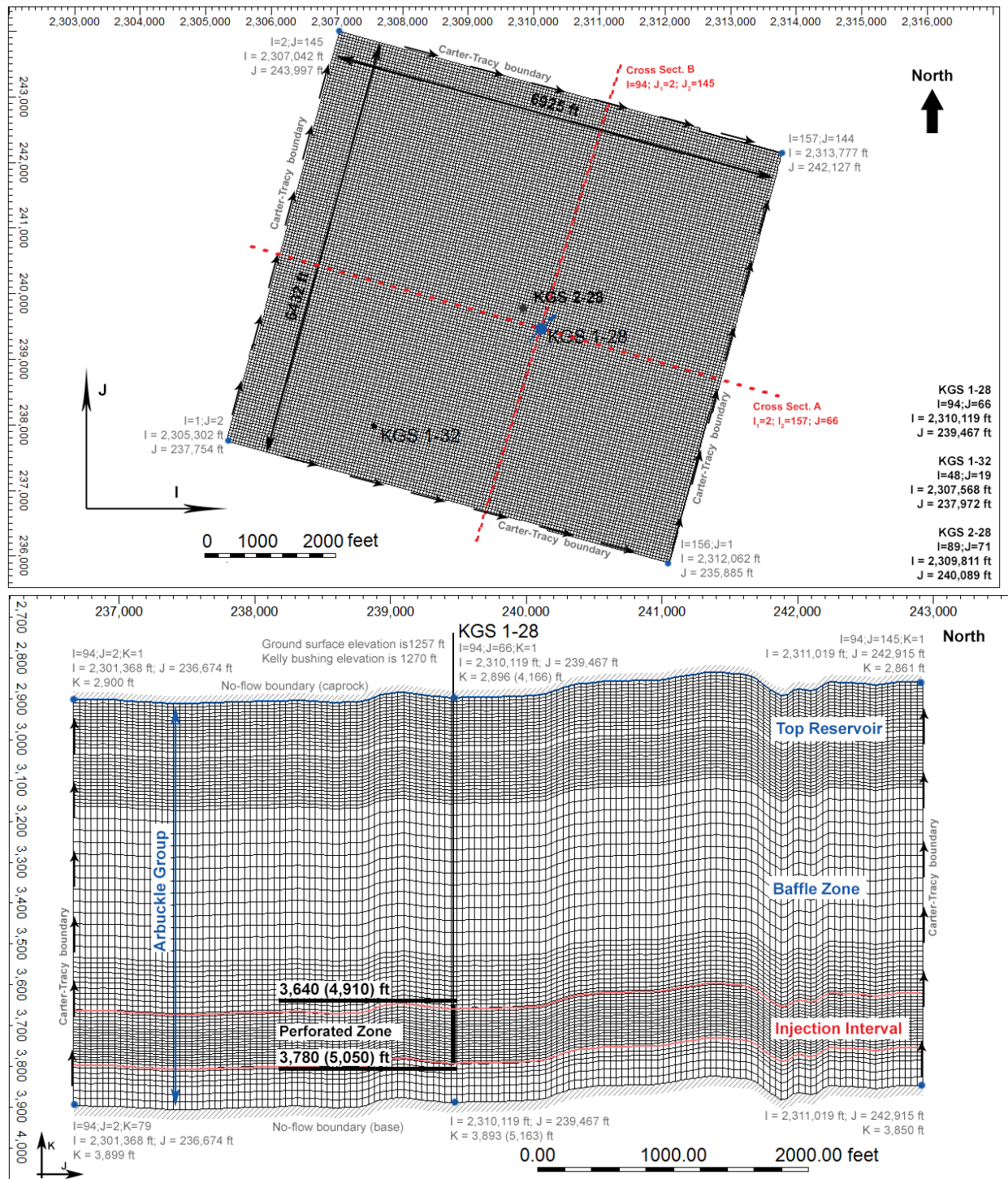
Figure 1b. North-south cross section of model grid along column 94 showing boundary conditions.
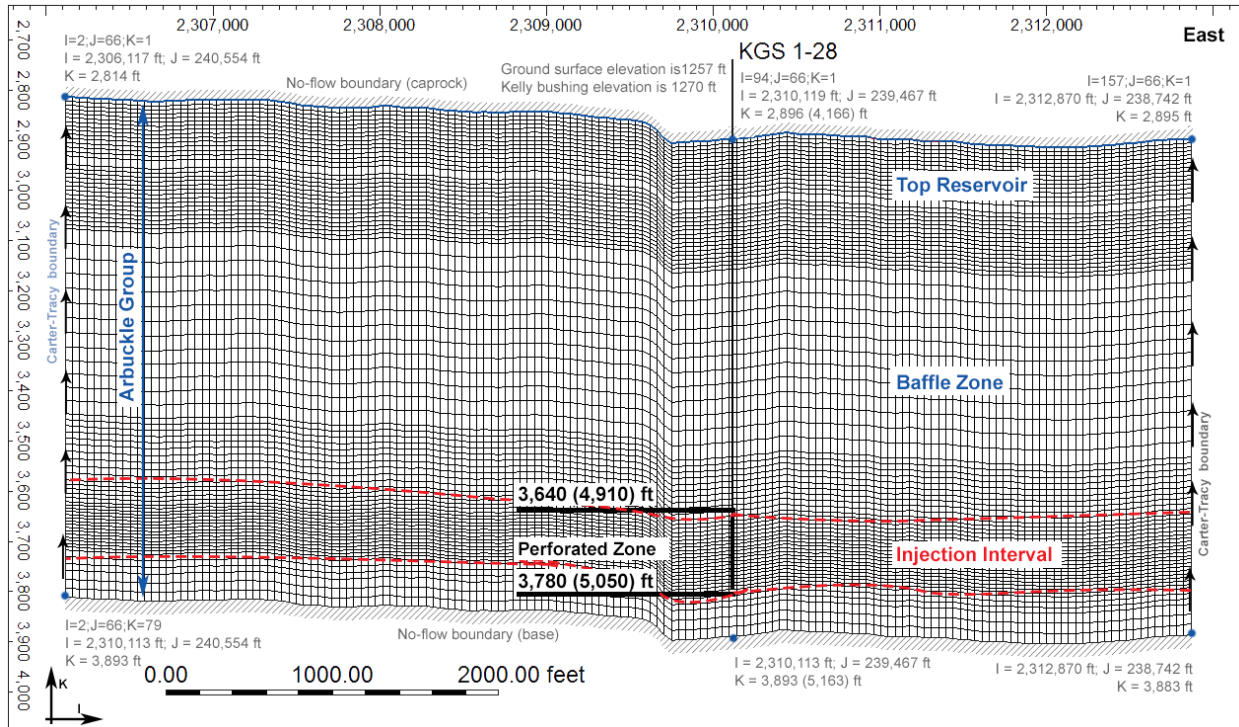
Figure 1c. East-west cross section of model grid along row 66 showing boundary conditions.

2.2   Modeled Processes

Physical processes modeled in the reservoir simulations included isothermal multi-phase flow and transport of brine and CO_2. Isothermal conditions were modeled because the total variation in subsurface temperature in the Arbuckle Group from the top to the base is only slightly more than 10°F (which should not significantly affect the various storage modes away from the injection well) and because it is assumed that the temperature of the injected CO_2 will equilibrate to formation temperatures close to the well. Also, non-isothermal sensitivity simulations were conducted for the EPA in which it was demonstrated that including temperature as a variable impacts the plume extent and the pressure distribution only minimally. Uniform salinity concentration was assumed as the effects of water salinity on the simulated AoR were found to be negligible (less than 0.5%).

Subsurface storage of CO_2 occurs via the following four main mechanisms:

- structural trapping,

- aqueous dissolution,

- hydraulic trapping, and

- mineralization.

The first three mechanisms were simulated in the Wellington model. Mineralization was not simulated as geochemical modeling indicated that due to the short-term and small- scale nature of the pilot project, mineral precipitation is not expected to cause any problems with clogging of pore space that may reduce permeability and negatively impact injectivity. Therefore, any mineral storage that may occur will only result in faster stabilization of the CO_2 plume and make projections presented in this model somewhat more conservative with respect to the extent of plume migration and CO_2 concentrations.

2.3   Geologic Structure

There are no transmissive faults in the Arbuckle Group that breach the overlying confining zone in proximity to the AoR derived from the model results. The closest large mapped fault on top of the Arbuckle and the Mississippian is approximately 12.5 mi southeast of Wellington. The seismic data at the Wellington site also points to the absence of large faults in the immediate vicinity of Wellington Field.

2.4   Arbuckle Hydrogeologic State Information

The ambient pore pressure, temperature, and salinity vary nearly linearly with depth in the Arbuckle Group. By linear extrapolation, the relationship between depth and these three parameters can be expressed by the following equations:

$$\text{Temperature (°F)} = (0.011 * \text{Depth} + 73.25) \quad \text{Pressure (psi)} = (0.487 * \text{Depth} - 324.8)$$

$$\text{Chloride (mg/l)} = (100.9 * \text{Depth} - 394.786)$$

Where, depth is in feet below kelly bushing (KB)

Using the above relationships, the temperature, pressure, and salinity at the top and bottom of the Arbuckle Group at the injection well site (KGS 1-28) are presented in table 1.

Table 1. Temperature, pressure, and salinity at the top and bottom of the Arbuckle Group at the injection well site (KGS 1-28).

	Top of Arbuckle (4,168 ft)	Bottom of Arbuckle (5,160 ft)
Temperature (°F)	115	130
Pressure (psi)	1,705	2,188
Chloride (mg/l)	25,765	125,858

2.5   Arbuckle Groundwater Velocity

On a regional basis, groundwater flows from east to west in the Arbuckle, as shown in the potentiometric surface map. Groundwater velocity, however, is estimated to be very slow. The head in Sumner County drops approximately 100 ft over 20 mi, resulting in a head gradient of approximately $1.0e^{-03}$ ft/ft. Assuming an average large-scale Arbuckle porosity of approximately 6% and a median permeability of 10 mD based on the statistical distribution of this parameter, the pore velocity in the Arbuckle is approximately 0.2 ft/year, which is fairly small and can be neglected in specification of ambient boundary conditions for the purpose of this modeling study.

2.6   Model Operational Constraints

The bottomhole injection pressure in the Arbuckle should not exceed 90% of the estimated fracture gradient of 0.75 psi/ft (measured from land surface). Therefore, the maximum induced pressure at the top and bottom of the Arbuckle Group should be less than 2,813 and 3,483 psi, respectively, as specified in table 2. At the top of the perforations (4,910 ft), pressure will not exceed 2,563 psi.

Table 2. Maximum allowable pressure at the top and bottom of the Arbuckle Group based on 90% fracture gradient of 0.675 psi/ft.

Depth (feet, bls)	Maximum Pore Pressure (psi)
4,166 (Top of Arbuckle)	2,813
4,910 (Top of Perforation)	3,314
5,050 (Bottom of Perforation)	3,408
5,163 (Bottom of Arbuckle)	3,483

3.   Geostatistical Reservoir Characterization of Arbuckle Group

Statistical reservoir geomodeling software packages have been used in the oil and gas industry for decades. The motivation for developing reservoir models was to provide a tool for better reconciliation and use of available hard and soft data (fig. 2). Benefits of such numerical models include 1) transfer of data between disciplines, 2) a tool to focus attention on critical unknowns, and 3) a 3-D visualization tool to present spatial variations to optimize reservoir development. Other reasons for creating high-resolution geologic models include the following:

- volumetric estimates;

- multiple realizations that allow unbiased evaluation of uncertainties before finalizing a drilling program;

- lateral and top seal analyses;

- integration (i.e., by gridding) of 3-D seismic surveys and their derived attributes assessments of 3-D connectivity;

- flow-simulation-based production forecasting using different well designs;

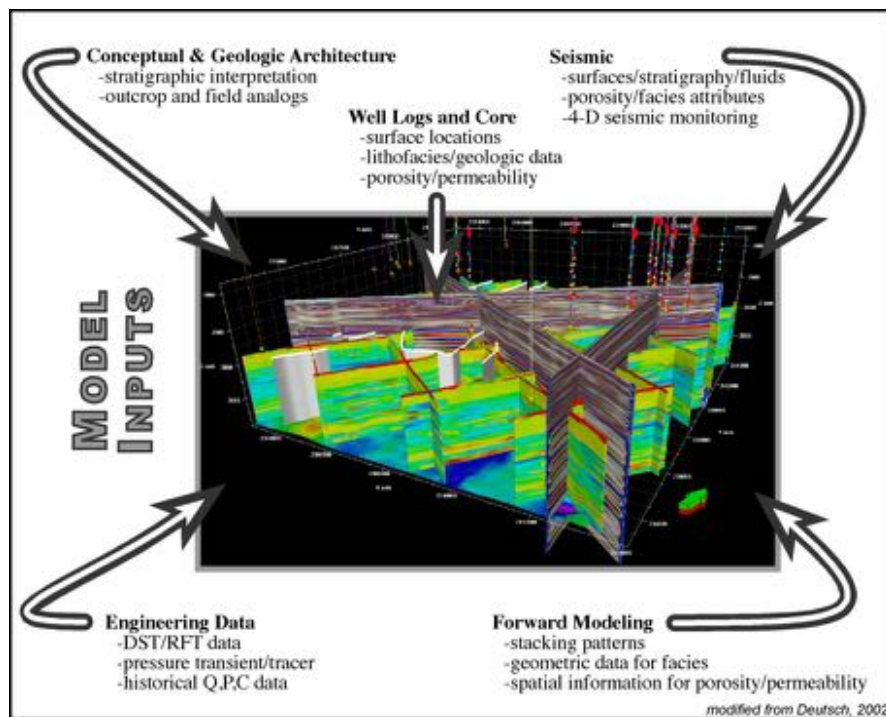- optimizing long-term development strategies to maximize return on investment.

Figure 2. A static, geocellular reservoir model showing the categories of data that can be incorporated (source: modified from Deutsch, 2002).

Although geocellular modeling software has largely flourished in the energy industry, its utility can be important for reservoir characterization in CO_2 research and geologic storage projects, such as the Wellington Field. The objective in the Wellington project is to integrate various data sets of different scales into a cohesive model of key petrophysical properties, especially porosity and permeability. The general steps for applying this technology are to model the large-scale features followed by modeling progressively smaller, more uncertain, features. The first step applied at the Wellington Field was to establish a conceptual depositional model

and its characteristic stratigraphic layering. The stratigraphic architecture provided a first-order constraint on the spatial continuity of facies, porosity, permeability, saturations, and other attributes within each layer. Next, facies (i.e., rock fabrics) were modeled for each stratigraphic layer using cell-based or object-based techniques. Porosity was modeled by facies and conditioned to "soft" trend data, such as seismic inversion attribute volumes. Likewise, permeability was modeled by facies and collocated, co-kriged to the porosity model.

4. Conceptual Geological Model

Lower Arbuckle core from Wellington reveals sub-meter-scale, shallowing-upward peritidal cycles. The two common motifs are cycles passing from basal dolo-mudstones/wackestones into algal dololaminites or matrix-poor monomict breccias. Bioclasts are conspicuously absent. Breccias are clast-supported, monomictic, and angular, and their matrix dominantly consists of cement. They are best classified as crackle to mosaic breccias (Loucks, 1999) because there is little evidence of transportation. Lithofacies and stacking patterns (i.e., sub-meter scale, peritidal cycles) are consistent with an intertidal to supratidal setting. Breccia morphologies, scale (<0.1 m), mineralogy (e.g., dolomite, anhydrite, length-slow chalcedony), depositional setting, greenhouse climate, and paleo-latitude (~15º S) support mechanical breakdown processes associated with evaporite dissolution. The Arbuckle-Simpson contact (~800 ft above the proposed injection interval) records the super-sequence scale, Sauk-Tippecanoe unconformity, which records subaerial-related karst landforms across the Early Phanerozoic supercontinent Laurentia.

4.1 Facies Modeling

The primary depositional lithofacies were documented during core description at KGS 1-32. A key issue was reconciling large variations between permeability measurements derived from wireline logs (i.e., nuclear resonance tool), whole core, and step-rate tests. Poor core recovery from the injection zone resulted from persistent jamming, which is commonly experienced in fractured or vuggy rocks. Image logs acquired over this interval record some intervals with large pores (cm scale) that are likely solution-enlarged vugs (touching-vugs of Lucia, 1999; fig. 4). Touching-vug fabrics commonly form a reservoir-scale, interconnected pore

system characterized by Darcy-scale permeability. It is hypothesized that a touching-vug pore system preferentially developed within fracture-dominated crackle and mosaic breccias—formed in response to evaporite removal—which functioned as a strataform conduit for undersaturated meteoric fluids (fig. 5). As such, this high-permeability, interwell-scale, touching-vug pore system is largely strataform and, therefore, predictable.

Figure 3. Example of the carbonate facies and porosity in the injection zone in the lower Arbuckle (part of the Gasconade Dolomite Formation). Upper half is light olive-gray, medium-grained dolomitic packstone with crackle breccia. Scattered subvertical fractures and limited cross stratification. Lower half of interval shown has occasional large vugs that crosscut the core consisting of a light olive-gray dolopackstone that is medium grained. Variable-sized vugs range from cm-size irregular to subhorizontal.

4.2 Petrophysical Properties Modeling

The approach taken for modeling a particular reservoir can vary greatly based on available information and often involves a complicated orchestration of well logs, core analysis, seismic surveys, literature, depositional analogs, and statistics. Because well log data were available in only two wells (KGS 1-28 and KGS 1-32) that penetrate the Arbuckle reservoir at the Wellington site, the geologic model also relied on seismic data, step-rate test, and drill-stem test information. Schlumberger's Petrel™ geologic modeling software package was used to produce the current geologic model of the Arbuckle saline aquifer for the pilot project area. This geomodel extends 1.3 mi by 1.2 mi laterally and is approximately 1,000 ft in thickness, spanning the entire

Arbuckle Group as well as a portion of the sealing units (Simpson/Chattanooga shale).

4.3 Porosity Modeling

In contrast to well data, seismic data are extensive over the reservoir and are, therefore, of great value for constraining facies and porosity trends within the geomodel. Petrel's volume attribute processing (i.e., genetic inversion) was used to derive a porosity attribute from the prestack depth migration (PSDM) volume to generate the porosity model (fig. 6). The seismic volume was created by re-sampling (using the original exact amplitude values) the PSDM 50 ft above the Arbuckle and 500 ft below the Arbuckle (i.e., approximate basement). The cropped PSDM volume and conditioned porosity logs were used as learning inputs during neural network processing.

A correlation threshold of 0.85 was selected and 10,000 iterations were run to provide the best correlation. The resulting porosity attribute was then re-sampled, or upscaled (by averaging), into the corresponding 3-D property grid cell.

The porosity model was constructed using sequential Guassian simulation (SGS). The porosity logs were upscaled using arithmetic averaging. The raw upscaled porosity histogram was used during SGS. The final porosity model was then smoothed. The following parameters were used as inputs:

I.   Variogram

   a.   Type: spherical

   b.   Nugget: 0.001

   c.   Anisotropy range and orientation

      i.   Lateral range (isotropic): 5,000 ft

      ii. Vertical range: 10 ft

II. Distribution: actual histogram range (0.06–0.11) from upscaled logs

III. Co-Kriging

   a.   Secondary 3-D variable: inverted porosity attribute grid
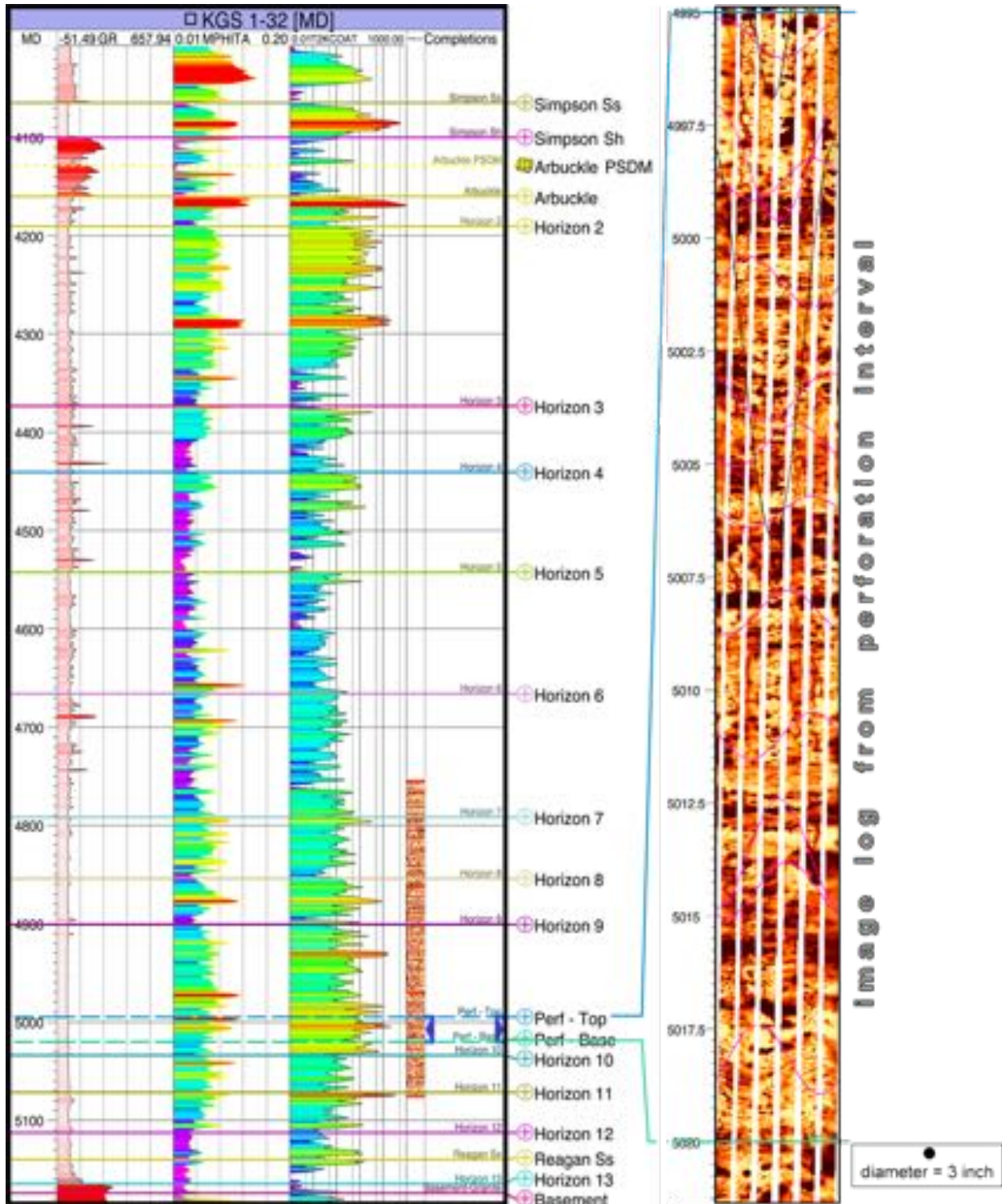
   b.   Correlation coefficient: 0.75

Figure 4. Geophysical logs within the Arbuckle Group at KGS 1-32. (Notes: MPHITA represents Haliburton porosity. Horizon markers represent porosity package. Image log on right presented to provide example of vugs; 3-in diameter symbol represents size of vug).
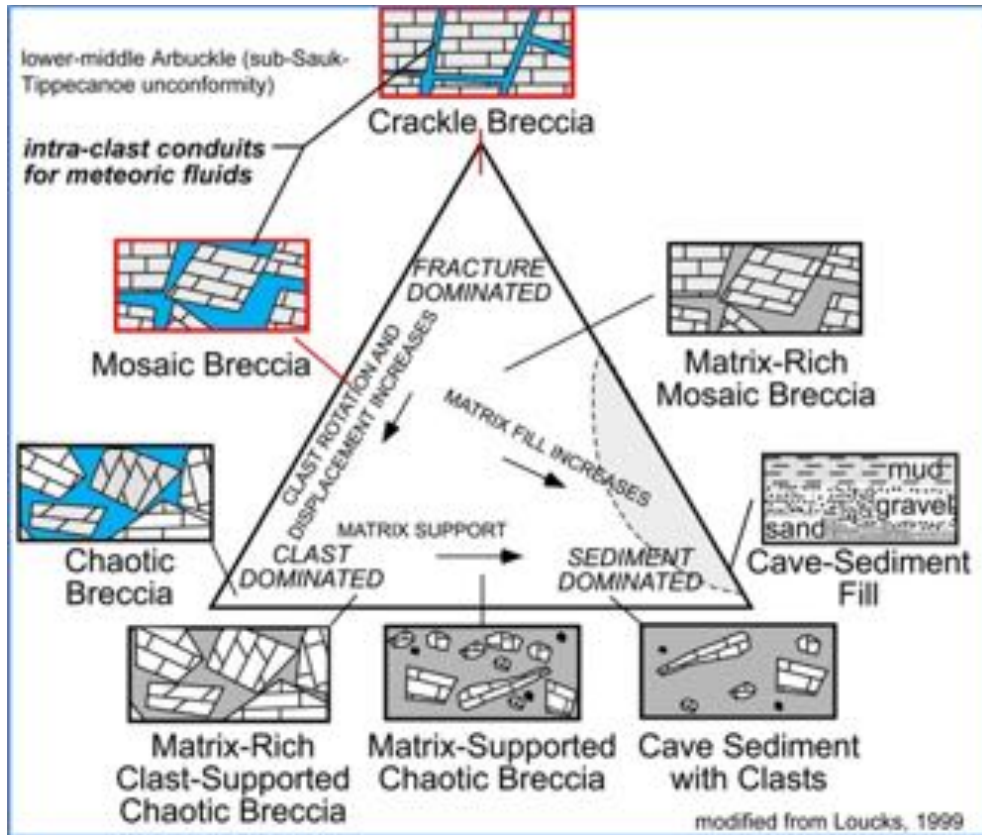
Figure 5. Classification of breccias and clastic deposits in cave systems exhibiting relationship between chaotic breccias, crackle breccias, and cave-sediment fill (source: Loucks, 1999).
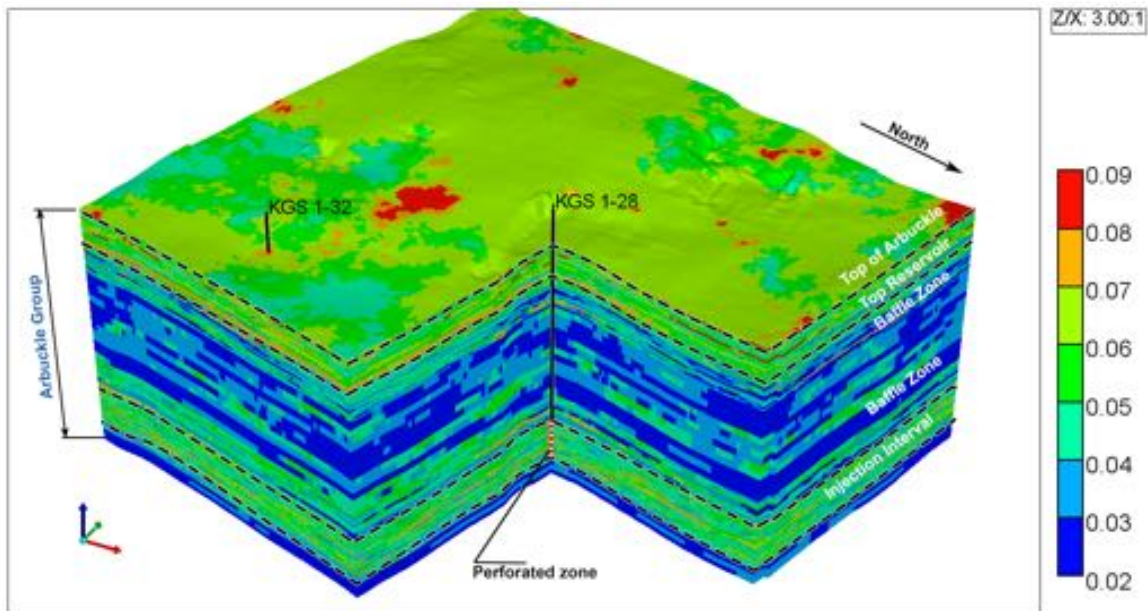

Figure 6. Upscaled porosity distribution in the Arbuckle Group based on the Petrel geomodel.

4.4 Permeability Modeling

The upscaled permeability logs shown in fig. 4 were created using the following controls: geometric averaging method; logs treated as points; and method set to simple. The permeability model was constructed using SGS. Isotropic semi-variogram ranges were set to 3,000 ft horizontally and 10 ft vertically. The permeability was collocated and co-Kriged to the porosity model using the calculated correlation coefficient (~0.70). The resulting SGS-based horizontal and vertical permeability distributions are presented in fig. 7a–f, which shows the relatively high permeability zone selected for completion within the injection interval. Table 3 presents the minimum, maximum, and average permeabilities within the Arbuckle Group in the geomodel.

Table 3. Hydrogeologic property statistics in hydrogeologic characterization and simulation models.

	Reservoir Characterization Geomodel			Reservoir Simulation Numerical Model		
Property	min	max	avg	min	max	avg
Porosity (%)	3.2	12.9	6.8	3.2	12.9	6.7
Horizontal Permeability (mD)	0.05	23,765	134.2	0.05	23,765	130.7
Vertical Permeability (mD)	.005	1,567	387	0.005	1,567	385

5. Arbuckle Reservoir Flow and Transport Model

Extensive computer simulations were conducted to estimate the potential impacts of CO_2 injection in the Arbuckle injection zone. The key objectives were to determine the resulting rise in pore pressure and the extent of CO_2 plume migration. The underlying motivation was to determine whether the injected CO_2 could affect the USDW or potentially escape into the atmosphere through existing wells or hypothetical faults/fractures that might be affected by the injected fluid.

As in all reservoirs, there are data gaps that prevent an absolute or unique characterization of the geology and petrophysical properties. This results in conceptual, parametric, and boundary condition uncertainties. To address these uncertainties, comprehensive simulations were conducted to perform a sensitivity analysis using alternative parameter sets. A key objective was to derive model parameter sets that would result in the

most negative impacts (the worst-case scenario; i.e., maximum formation pressures and largest extent of plume migration). However, simulations involving alternative parameter and boundary conditions that resulted in more favorable outcomes were also conducted to bracket the range of possible induced system states and outcomes.
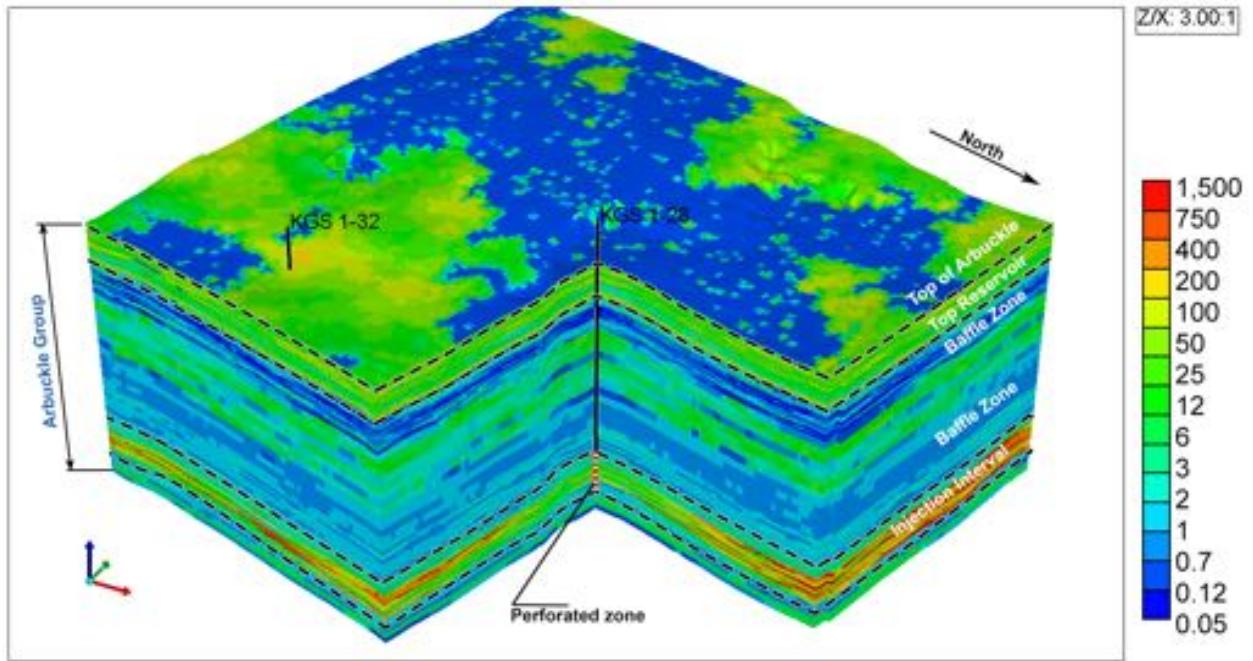

Figure 7a. Upscaled horizontal permeability (mD) distributions in the Arbuckle Group derived from Petrel geo-model.
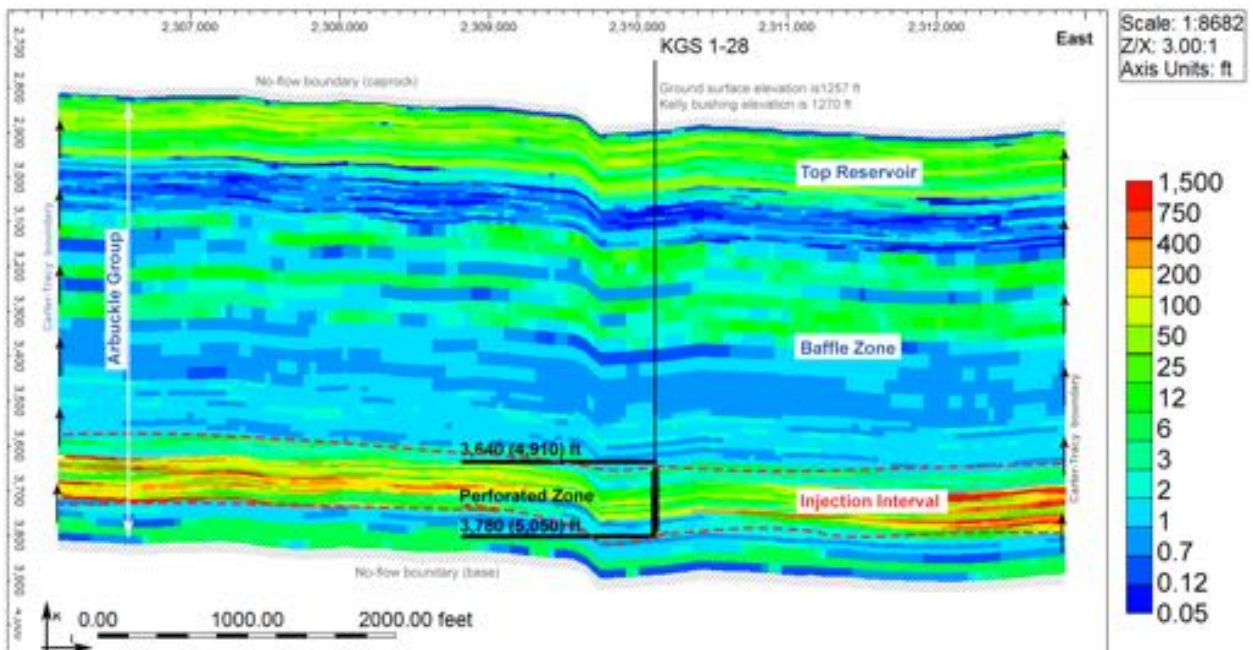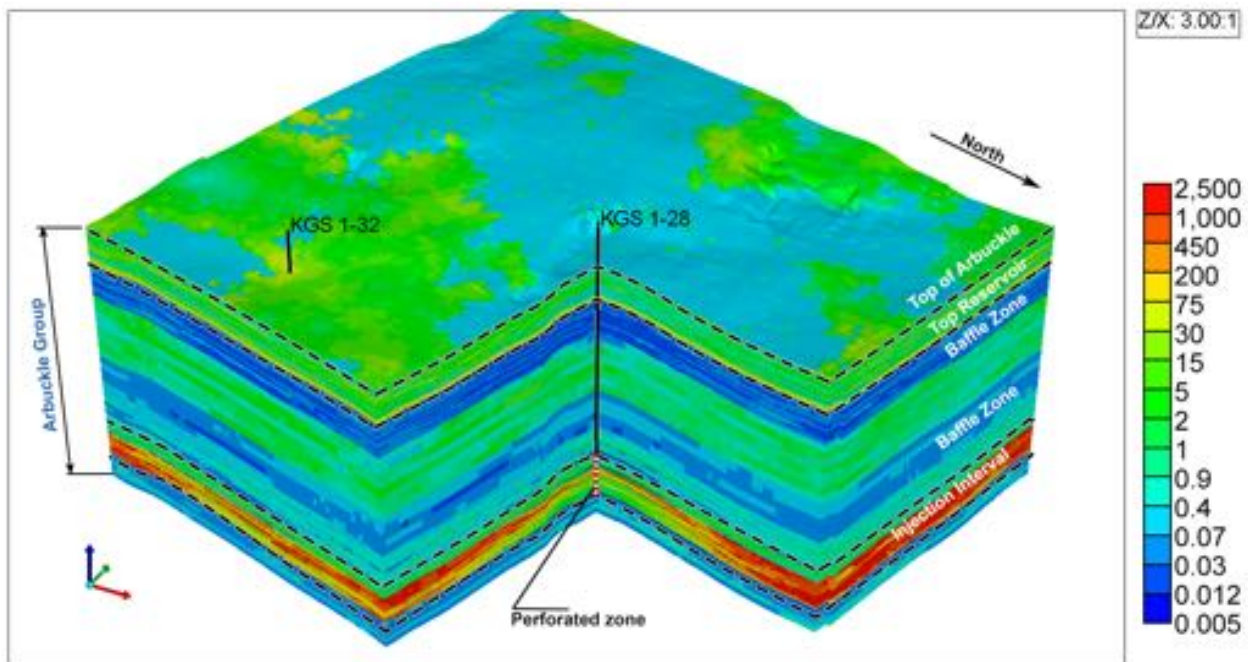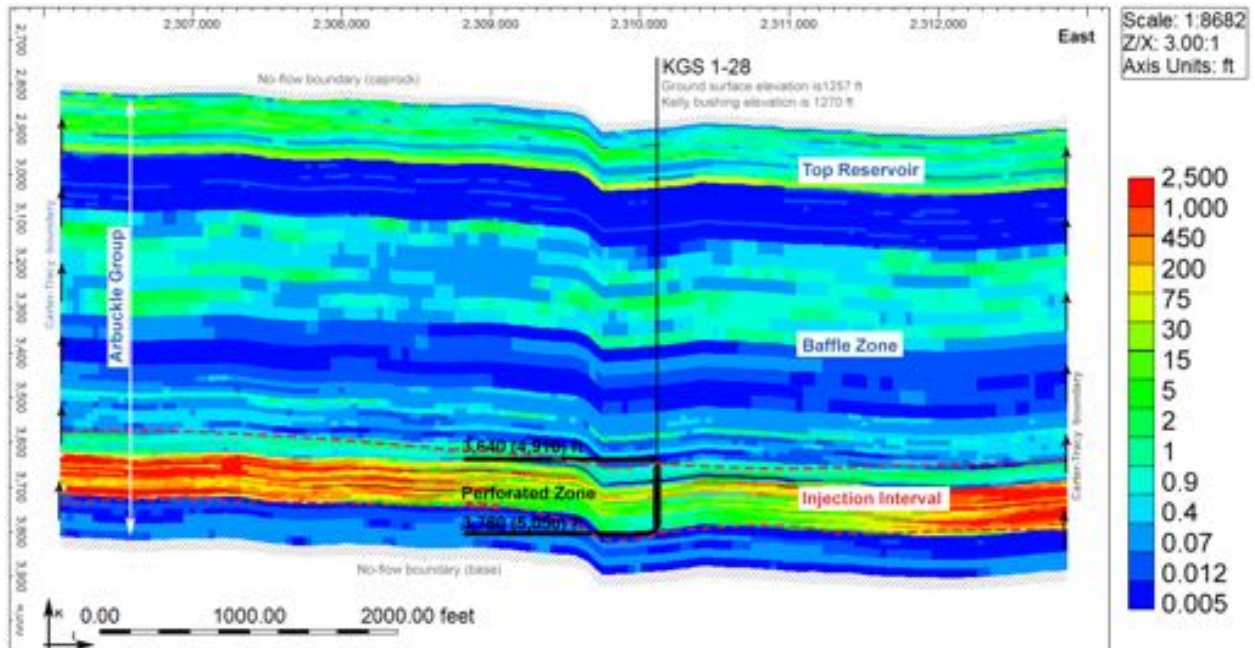
Figure 7b. Horizontal permeability (mD) distribution within an east-west cross section through the injection well (KGS 1-28), vertical cross-section A. Location of cross section shown in fig. 1a.
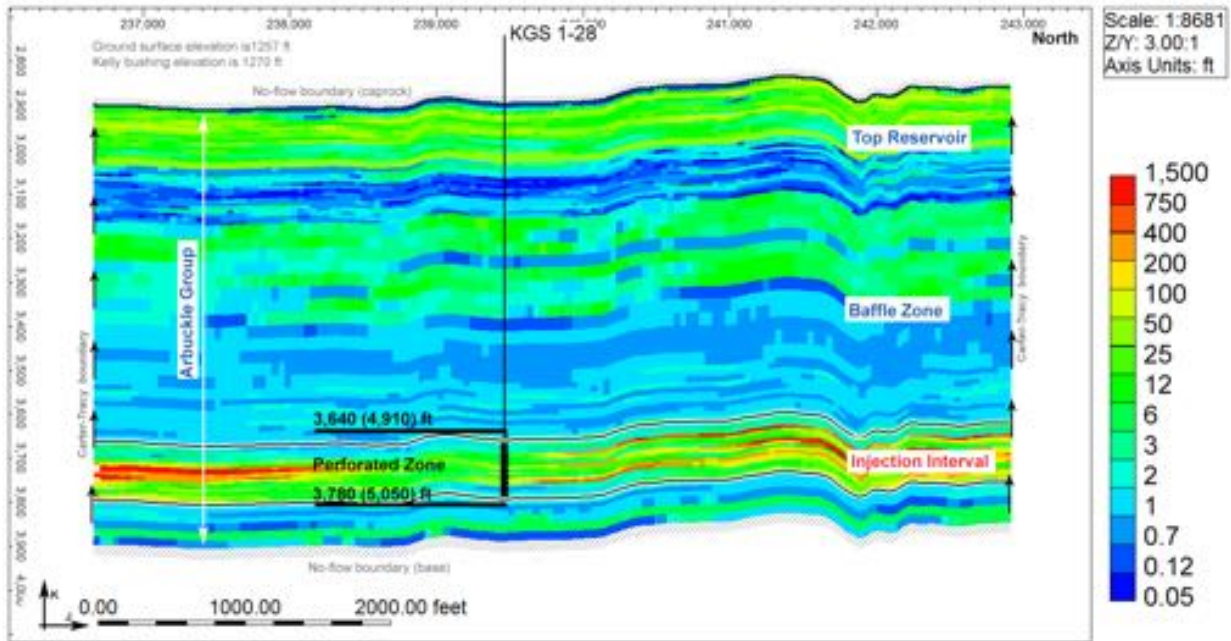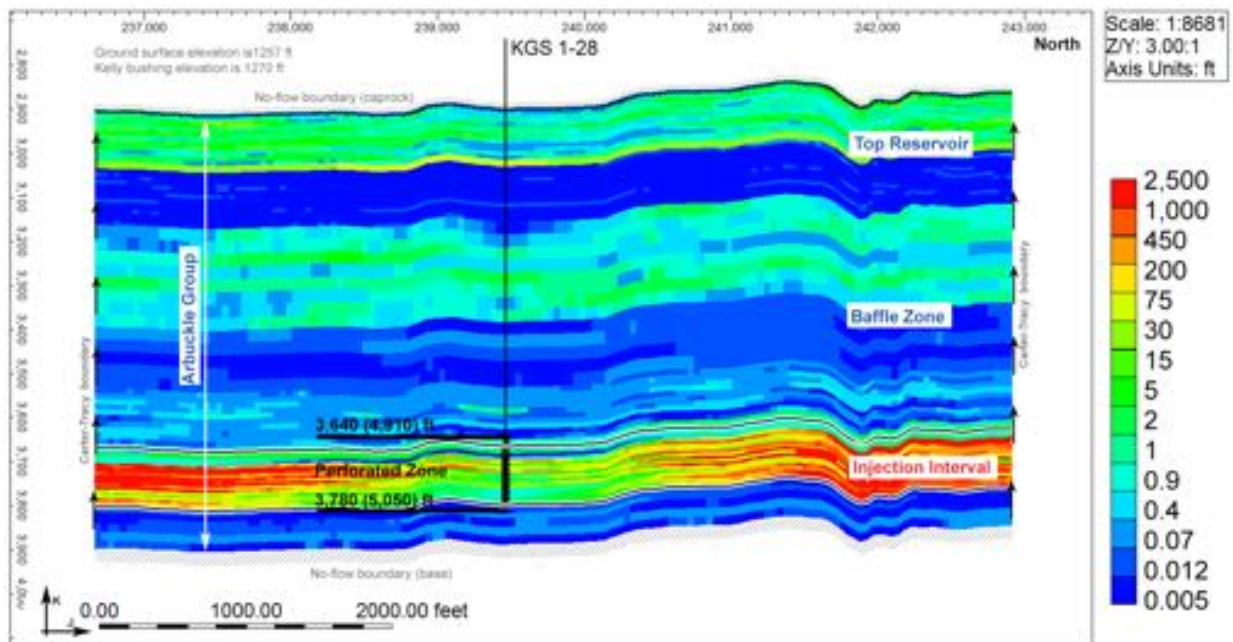

Figure 7c. Horizontal permeability (mD) distribution within a north-south cross section through the injection well (KGS 1-28), vertical cross-section B. Location of cross section shown in fig. 1a.

Figure 7d. Upscaled vertical permeability (mD) distributions in the Arbuckle Group derived from Petrel geomodel.

Figure 7e. Vertical permeability (mD) distribution within an east-west cross section through the injection well (KGS 1-28), vertical cross-section A. Location of cross section shown in fig. 1a.

Figure 7f. Vertical permeability (mD) distribution within a north-south cross section through the injection well (KGS 1-28), vertical cross-section B. Location of cross section shown in fig. 1a.

5.2   Simulation Software Description

The reservoir simulations were conducted using the Computer Modeling Group (CMG) GEM simulator. GEM is a full equation of state compositional reservoir simulator with advanced features for modeling the flow of three-phase, multi-component fluids and has been used to conduct numerous CO_2 studies (Chang et al., 2009; Bui et al., 2010). It is considered by DOE to be an industry standard for oil/gas and CO_2 geologic storage applications. GEM is an essential engineering tool for modeling complex reservoirs with complicated phase behavior interactions that have the potential to impact CO_2 injection and transport. The code can account for the thermodynamic interactions between three phases: liquid, gas, and solid (for salt precipitates). Mutual solubilities and physical properties can be dynamic variables depending on the phase composition/system state and are subject to well-established constitutive relationships that are a function of the system state (pressures, saturation, concentrations, temperatures, etc.). In particular, the following assumptions govern the phase interactions:

- Gas solubility obeys Henry's Law (Li and Nghiem, 1986)

- The fluid phase is calculated using Schmit-Wenzel or Peng-Robinson (SW-PR) equations of state (Søreide and Whitson, 1992)

- Changes in aqueous phase density with CO_2 solubility, mineral precipitations, etc., are accounted for with the standard or Rowe and Chou correlations.

- Aqueous phase viscosity is calculated based on Kestin, Khalifa, and Correia (1981).

5.3   Model Mesh and Boundary Conditions

The Petrel-based geomodel mesh discussed above consists of a 706 x 654 horizontal grid and 79 vertical layers for a total of 36,476,196 cells. The model domain spans from the base of the Arbuckle Group to the top of the Pierson Group. To reduce reservoir simulation time, this model was upscaled to a 157 x 145 horizontal mesh with 79 layers for a total of 1,798,435 cells to represent the same rock volume as the Petrel model for use in the CMG simulator. The thickness of the layers varies from 5 to 20 ft based on the geomodel, with an average of 13 feet.

Based on preliminary simulations, it was determined that due to the small scale of injection and the presence of a competent confining zone, the plume would be contained within the Arbuckle system for all alternative realizations of reservoir parameters. Therefore, the reservoir model domain was restricted to the Arbuckle aquifer with no-flow boundaries specified along the top (Simpson Group) and bottom (Precambrian basement) of the Arbuckle group. As discussed in Section 5.2.1, the specification of no-flow boundaries along the top and bottom of the Arbuckle Group is justified because of the low permeabilities in the overlying and underlying confining zones as discussed in Section 4.7.3. The permeability in the Pierson formation was estimated to be as low as 1.6 nanoDarcy (nD; 1.0^{-9} Darcy).

The simulation model, centered approximately on the injection well (KGS 1-28), extends approximately 1.2 mi in the east-west and 1.3 mi in the north-south orientations. Vertically, the model extends approximately 1,000 ft from the top of the Precambrian basement to the bottom of the Simpson Group. As discussed above, the model domain was discretized laterally by 157 x 145 cells in the east-west and north-south directions and vertically in 79 layers. The lateral boundary conditions were set as an infinite-acting Carter-Tracy aquifer (Dake, 1978; Carter and Tracy, 1960) with leakage. This is appropriate since the Arbuckle is an open hydrologic system extending over most of Kansas. Sensitivity simulations indicated that the increases in pore pressures and the plume extent were not meaningfully different by using a closed boundary instead of a Carter-Tracy boundary.

5.4 Hydrogeologic Properties

Geologic and hydrologic data pertaining to the Arbuckle Group are detailed in Sections 3 and 4 of the permit application. Site-specific hydrogeologic properties were used to construct a geomodel at the Wellington site. The porosity and permeability of the geomodel were upscaled to the coarser grid using a weighted averaging approach so that the total pore space volume in the Petrel geomodel was maintained in the upscaled reservoir simulation model. As shown in figs. 8a–b and 9, the qualitative representation (i.e., the shape) of the permeability and porosity distribution remained similar in both the geo and reservoir models. The upscaled reservoir grid was imported from Petrel into CMG Builder, where the model was prepared for dynamic simulations assuming an equivalent porous medium model with flow limited to only the rock matrix. The minimum, maximum, and average porosity and

permeabilities in the reservoir model are documented in table 3 alongside the statistics for the geomodel.

5.5 Rock Type Assignment

Nine rock types and corresponding tables with capillary pressure hysteresis were developed based on reservoir quality index (RQI) ranges, where RQI is calculated for each grid cell using the formula:

$$RQI = 0.0314 \sqrt{Perm/Porosity}$$

Using RQI ranges, rock types are assigned using CMG Builder's Formula Manager. The resulting maps of rock type distribution in the model are shown in fig. 10a–c. The division of the nine rock-types (RT) was based on dividing the irreducible water saturation into nine ranges to find their equivalent RQI as shown in table 4. Relative permeability and capillary pressure curves were calculated for each of the nine RQI values.

Table 4.RQI and Relative Permeability Types assignments (RT)

	RQI		
RT	RQI from	RQI To	Ave RQI
1	40	10	25
2	10	2.5	6.25
3	2.5	1	1.75
4	1	0.5	0.75
5	0.5	0.4	0.45
6	0.4	0.3	0.35
7	0.3	0.2	0.25
8	0.2	0.1	0.15
9	0.1	0.01	0.055
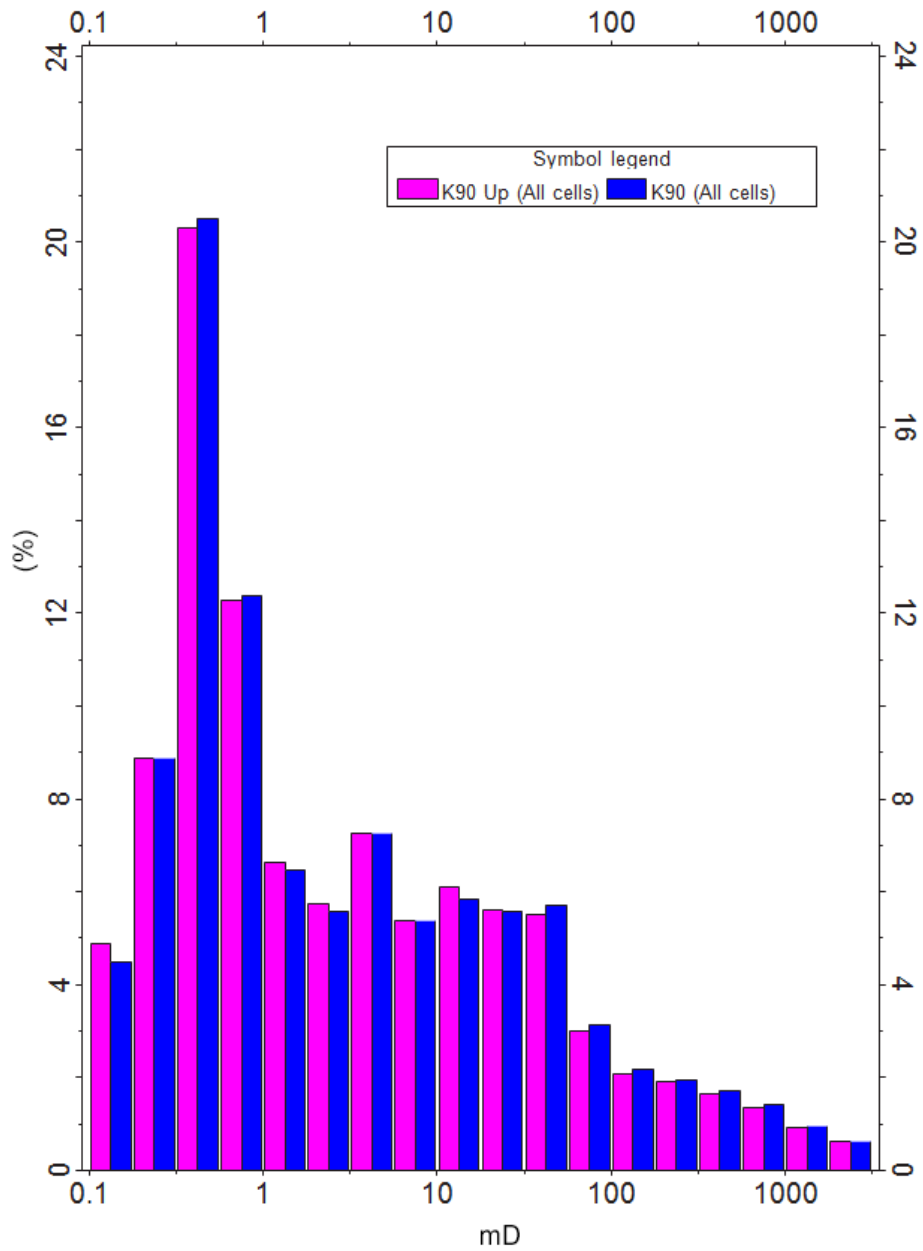
Figure 8a. Horizontal permeability distribution histogram comparison for original (blue) and upscaled (pink) model properties. (Note: x-axis represents permeability in milliDarcy, mD.)
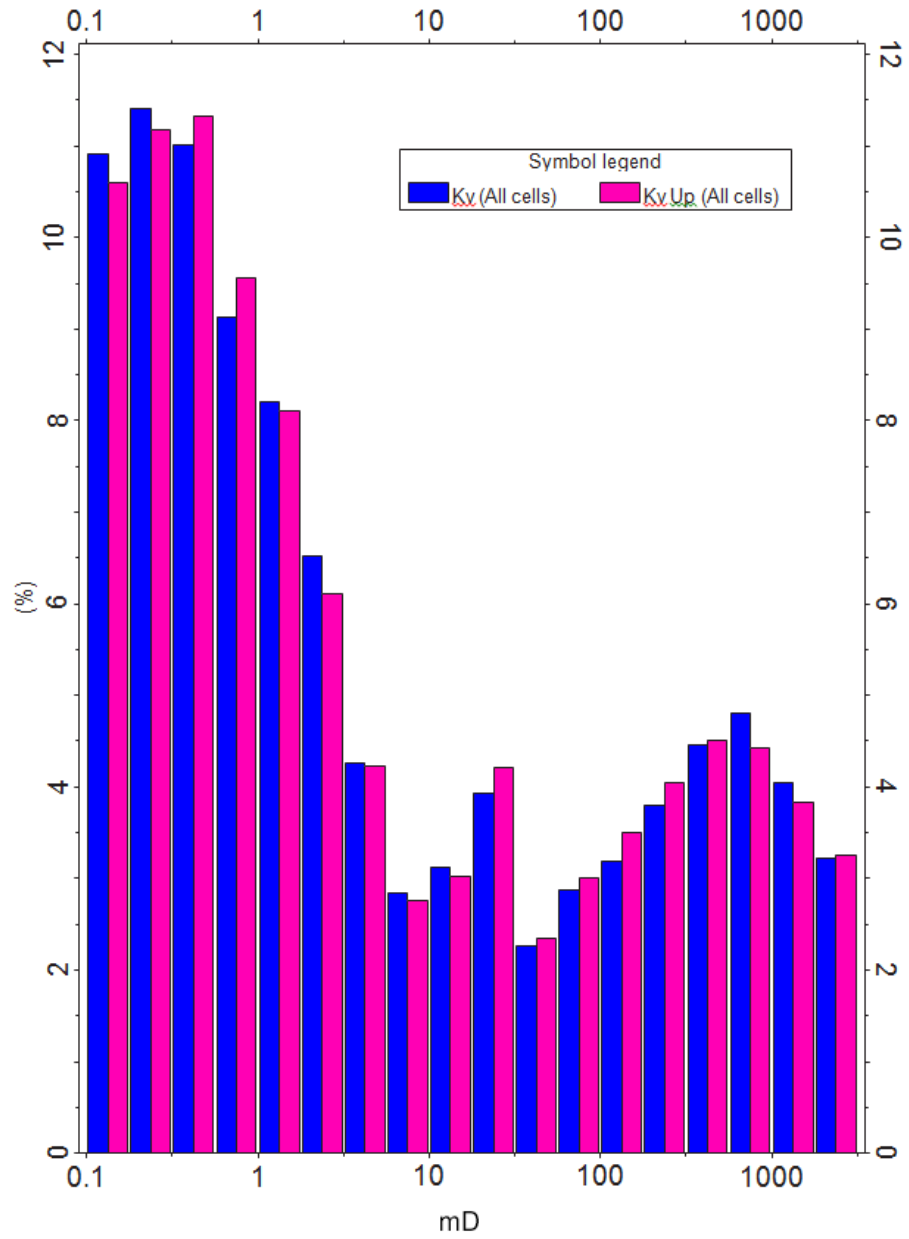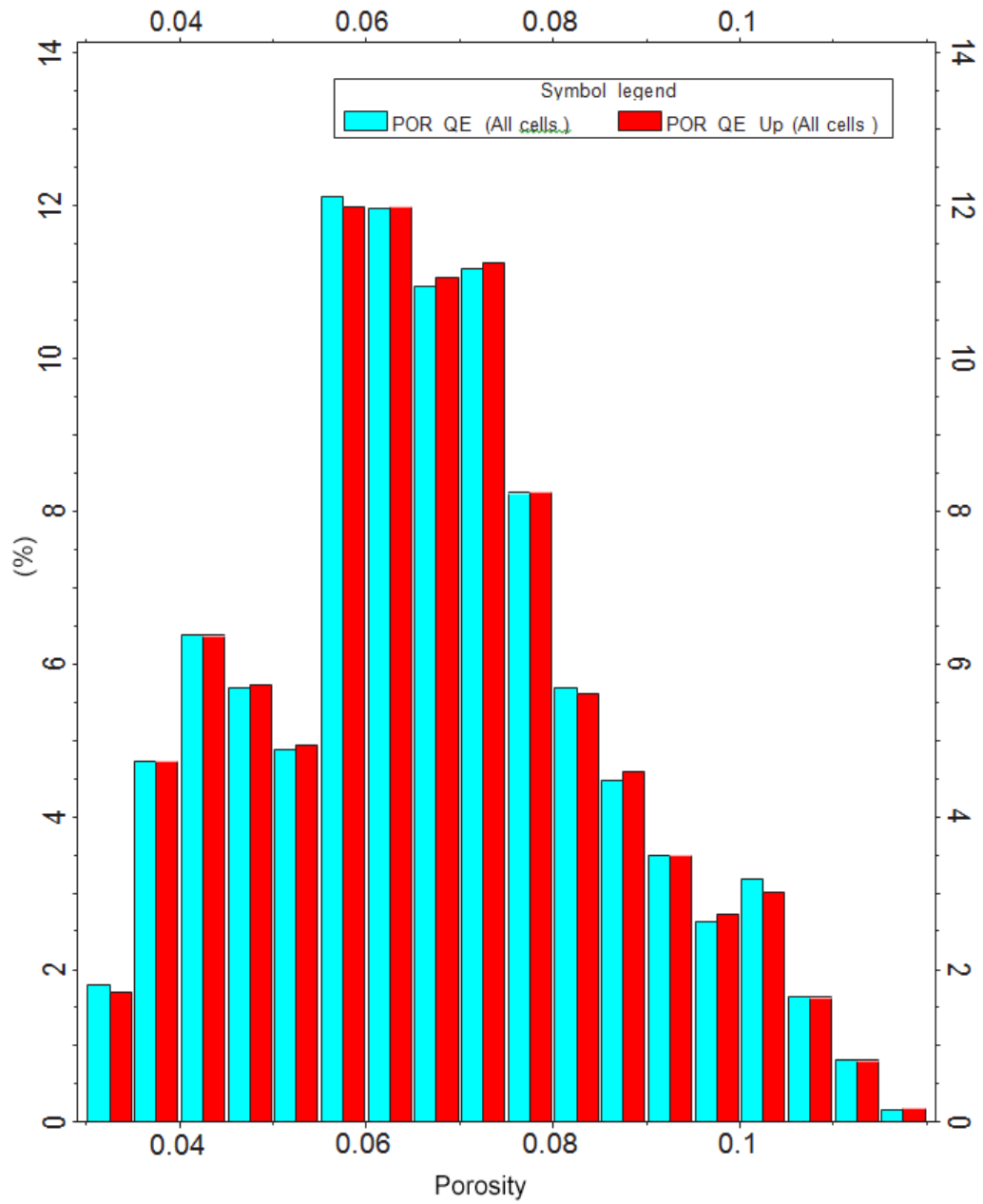
Figure 8b. Vertical permeability distribution histogram comparison for original (blue) and upscaled (pink) model properties. (Note: x-axis represents permeability in milliDarcy, mD.)

Figure 9. Porosity distribution histogram comparison for original and upscaled model properties. (Note: x-axis represents porosity.)
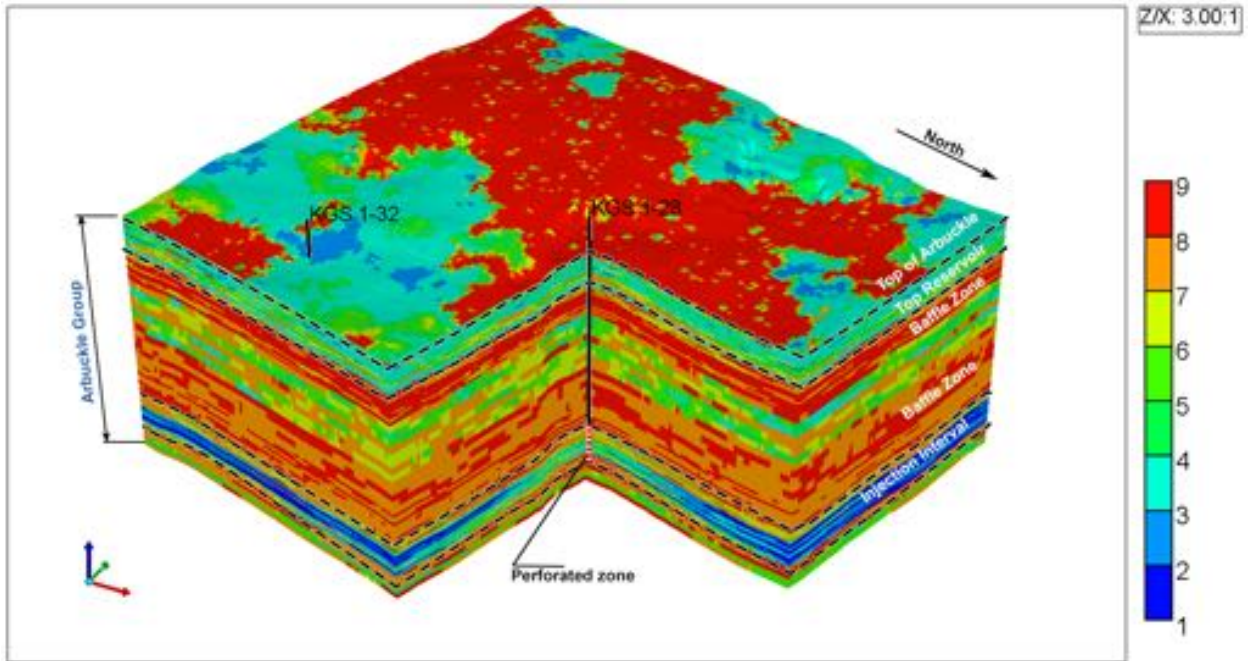
Figure 10a. Rock type distribution model.
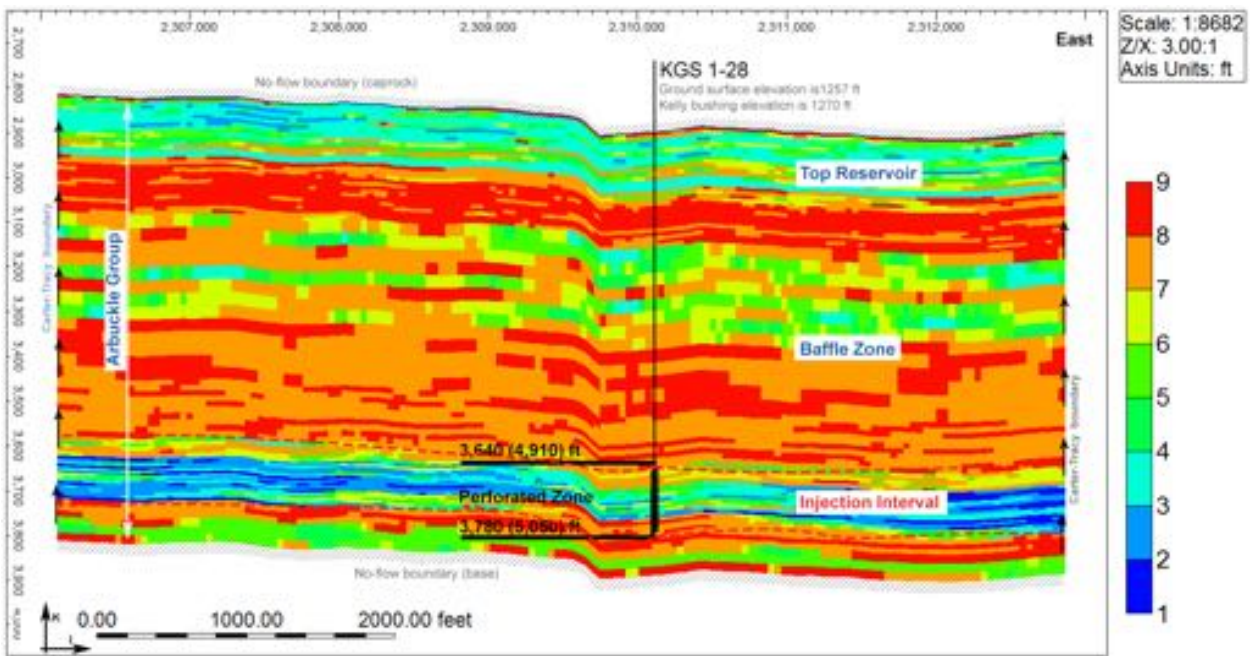
Figure 10b. Rock type distribution model, distribution within an east-west cross section through the injection well (KGS 1-28), vertical cross-section A.
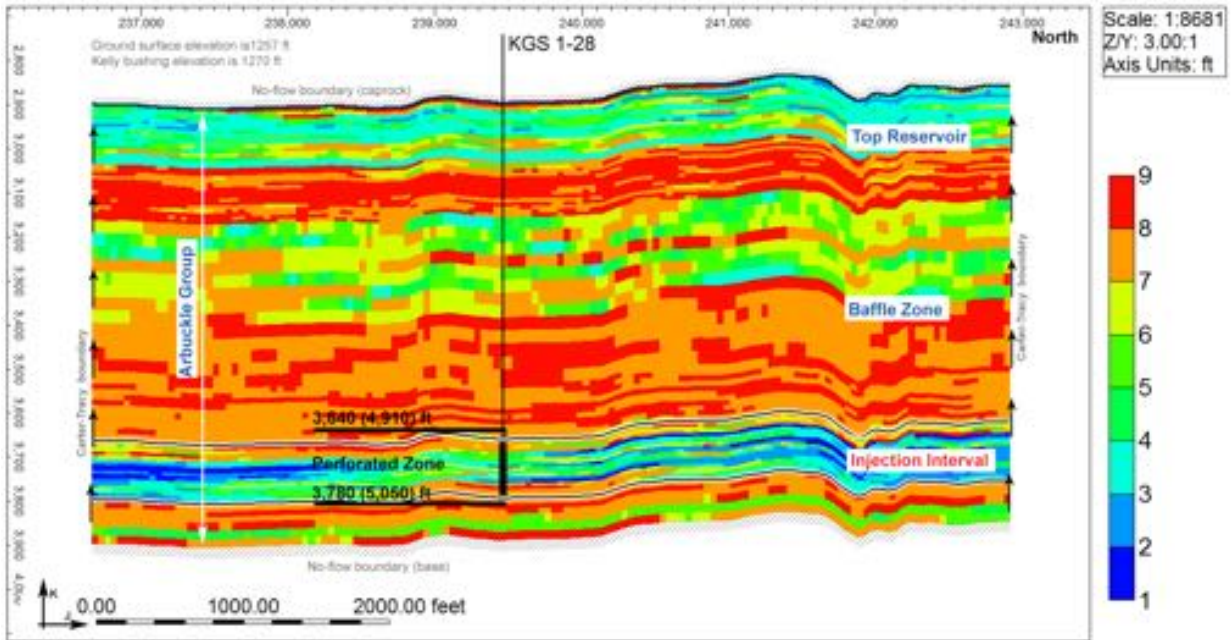
Figure 10c. Rock type distribution within a north-south cross section through the injection well (KGS 1-28), vertical cross-section B.

5.6   Relative Permeability

Nine sets of relative permeability curves for both drainage and imbibition were calculated for the nine rock types. These sets of relative permeability curves were calculated based on a recently patented formula (SMH reference No: 1002061-0002) that relates the end points to RQI, thereby resulting in a realistic relative permeability data set. The validation of the method is presented below under Validation of the Capillary Pressure and Relative Permeability Methods. Literature experimental studies, including Krevor and Benson (2012, 2015), indicate that the maximum experimental CO_2 saturation (SCO_{2max}) and maximum CO_2 relative permeability ($KrCO_{2max}$) in higher permeability samples typically do not reach their actual values and are lower than expected. The authors note that the cause of low experimental end points are the unattainable high capillary pressure in the high permeability core samples. Calculations based on the new patented method addresses and resolves this issue. The highest maximum CO_2 relative permeability ($KrCO_{2\ max}$) for drainage curves from literature (Bennion and Bachu, 2007) is 0.54, which is lower than expected; however, the highest maximum CO_2 relative permeability using the new method is 0.71, which is a more realistic value. As noted above, measured relative permeabilities from literature do not represent the end points of relative permeability curves and they need to be adjusted. Using this new method, SCO_{2max} and

KrCO$_{2max}$ are scaled up to reasonable values.

Highest and lowest Corey CO$_2$ exponent values from Bennion and Bachu (2010) were selected and they were assigned to the nine RQI values in a descending order from high to low. The full range of RQI assignments and relative permeability tables can be found in Appendix B. An example of capillary pressure and relative permeability for both drainage and imbibition is presented in table 5. Corey Water exponents for different permeabilities from literature did not show much variability. Therefore, average values were used for both drainage and imbibition curves. Figure 11a presents relative permeability curves for an RQI value of 0.35 for illustrative purposes. Figure 11b presents the same set of curves for the full range of RQI values. Residual CO$_2$ saturation (SCO$_2$r) for calculating imbibition curves was needed. SCO$_2$r was calculated based on a correlation between residual CO$_2$ saturation (SCO$_2$r) and initial CO$_2$ saturation (SCO$_2$i) (Burnside and Naylor, 2014).
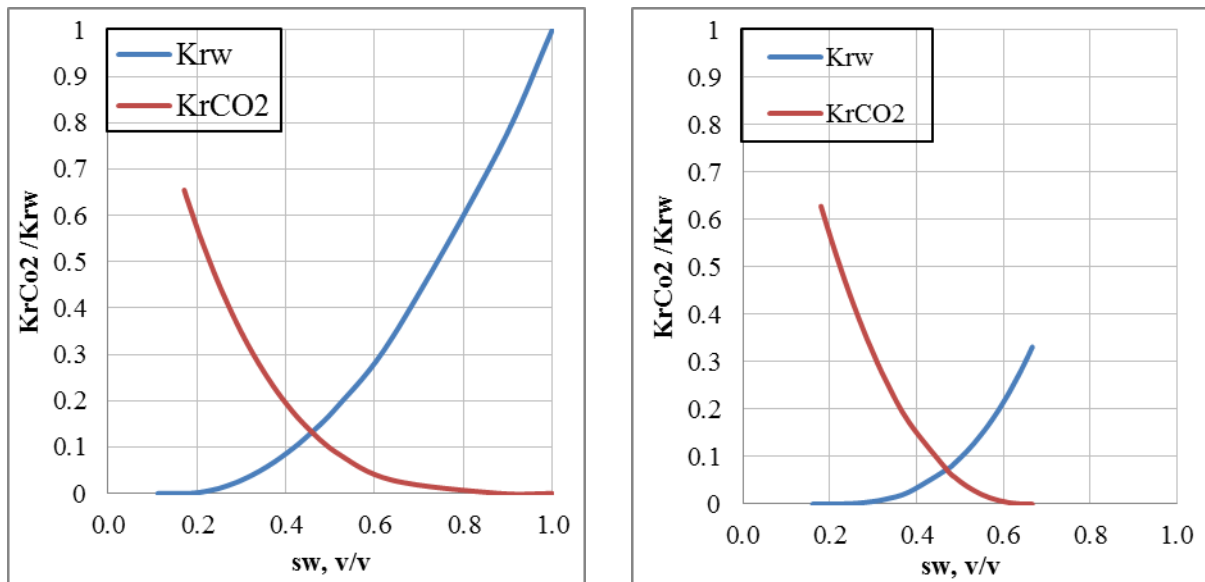
Figure 11a. Calculated relative permeability for drainage (left) and imbibition (right) for RQI=0.35.
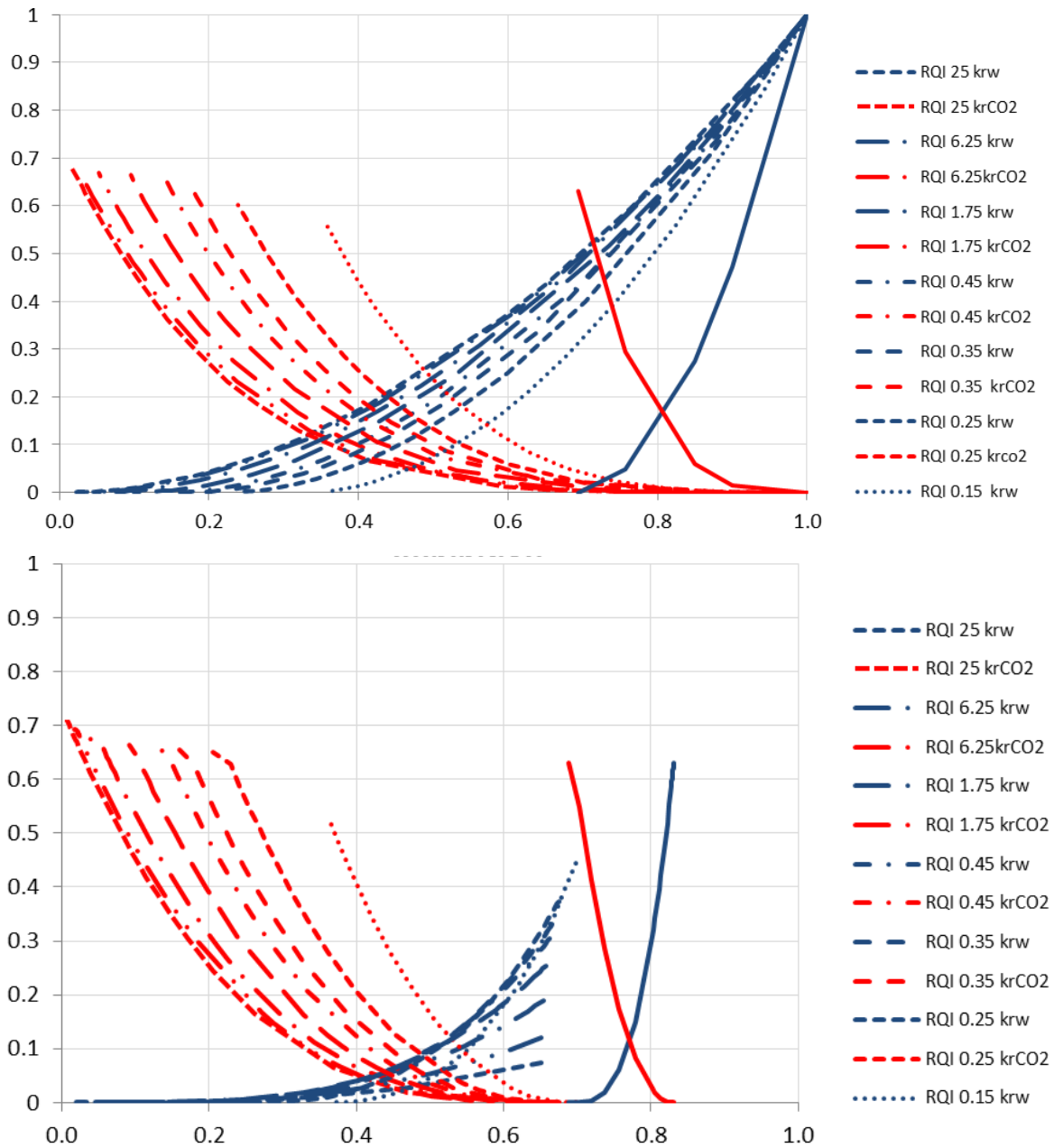
Figure 11b. Calculated relative permeability for drainage (top) and imbibition (bottom) for full set of RQI.

Table 5. Example of capillary pressure and relative permeability drainage and imbibition tables for rock type 6 (RQI=0.35).

Drainage Curves

RQI range from 0.3-0.4-AveRQI=0.35			
Pc	Sw	sCO_2	Krw	$krCO_2$
1	1.000	0.000	1.000	0.000
2	0.877	0.123	0.735	0.001
3	0.641	0.359	0.338	0.029
4	0.518	0.482	0.190	0.086
5	0.443	0.557	0.119	0.148
6	0.392	0.608	0.080	0.205
7	0.354	0.646	0.056	0.257
8	0.326	0.674	0.041	0.302
9	0.304	0.696	0.030	0.341
10	0.286	0.714	0.023	0.375
12	0.258	0.742	0.013	0.432
14	0.238	0.762	0.008	0.478
18	0.211	0.789	0.003	0.545
20	0.201	0.799	0.002	0.571
25	0.183	0.817	0.000	0.620
30	0.171	0.829	0.000	0.655
40	0.156	0.844	0.000	0.655
50	0.146	0.854	0.000	0.655
60	0.140	0.860	0.000	0.655
70	0.135	0.865	0.000	0.655
80	0.131	0.869	0.000	0.655
90	0.129	0.871	0.000	0.655
100	0.126	0.874	0.000	0.655
150	0.119	0.881	0.000	0.655
200	0.116	0.884	0.000	0.655
300	0.112	0.888	0.000	0.655

Imbibition Curves

RQI range from 0.3-0.4-AveRQI=0.35			
Pc	Sw	sCO_2	Krw	$krCO_2$
0	0.666	0.334	0.331	0.000
0.00	0.665	0.335	0.328	0.000
0.01	0.663	0.337	0.325	0.000
0.02	0.660	0.340	0.319	0.000
0.03	0.657	0.343	0.313	0.000
0.04	0.654	0.346	0.308	0.000
0.05	0.652	0.348	0.302	0.000
0.06	0.649	0.351	0.297	0.000
0.07	0.646	0.354	0.292	0.000
0.08	0.643	0.357	0.287	0.000
0.09	0.640	0.360	0.282	0.001
0.1	0.638	0.362	0.277	0.001
0.2	0.612	0.388	0.234	0.003
0.3	0.589	0.411	0.200	0.008
0.4	0.569	0.431	0.171	0.013
0.5	0.550	0.450	0.148	0.020
0.6	0.532	0.468	0.128	0.029
0.7	0.516	0.484	0.112	0.038
0.8	0.501	0.499	0.098	0.047
0.9	0.487	0.513	0.086	0.057
1	0.474	0.526	0.076	0.067
2	0.383	0.617	0.026	0.172
3	0.329	0.671	0.011	0.261
4	0.293	0.707	0.005	0.333
5	0.267	0.733	0.002	0.390
6	0.248	0.752	0.001	0.437
7	0.233	0.767	0.001	0.476
8	0.221	0.779	0.000	0.508
9	0.211	0.789	0.000	0.536
10	0.203	0.797	0.000	0.559
12	0.189	0.811	0.000	0.598
14	0.180	0.820	0.000	0.629
20	0.160	0.840	0.000	0.655
30	0.144	0.856	0.000	0.655
40	0.135	0.865	0.000	0.655
50	0.129	0.871	0.000	0.655
60	0.126	0.874	0.000	0.655
70	0.123	0.877	0.000	0.655
80	0.121	0.879	0.000	0.655
90	0.119	0.881	0.000	0.655
100	0.117	0.883	0.000	0.655
150	0.113	0.887	0.000	0.655
200	0.111	0.889	0.000	0.655
300	0.109	0.891	0.000	0.655

5.7 Capillary Pressure Curves

Nine capillary pressure curves were calculated for drainage and imbibition for nine RQI values based on a recently patented formula (SMH reference No: 1002061-0002). The formula constitutes a function for the shape of Pc curves and functions for the end points that are entry pressure (P_{entry}) and irreducible water saturation (Swir). The end points are correlated to RQI. P_{entry} was calculated from entry radius (R15) and Winland (R35). There is a relationship

between R35 and R15 and a relationship between P_{entry} and R15; therefore, P_{entry} can be calculated from R15 derived from R35. Swir was calculated from the NMR log at a Pc equal to 20 bars (290 psi). To calculate imbibition curves, a residual CO_2 saturation (CO_{2r}) value was needed. CO_{2r} was calculated from a relationship between initial CO_2 saturation and CO_{2r} as discussed above. The capillary pressure curves for drainage and imbibition for RQI of 0.35 are presented in fig. 12. The capillary pressure data for the full set of RQI values are presented in Appendix B.
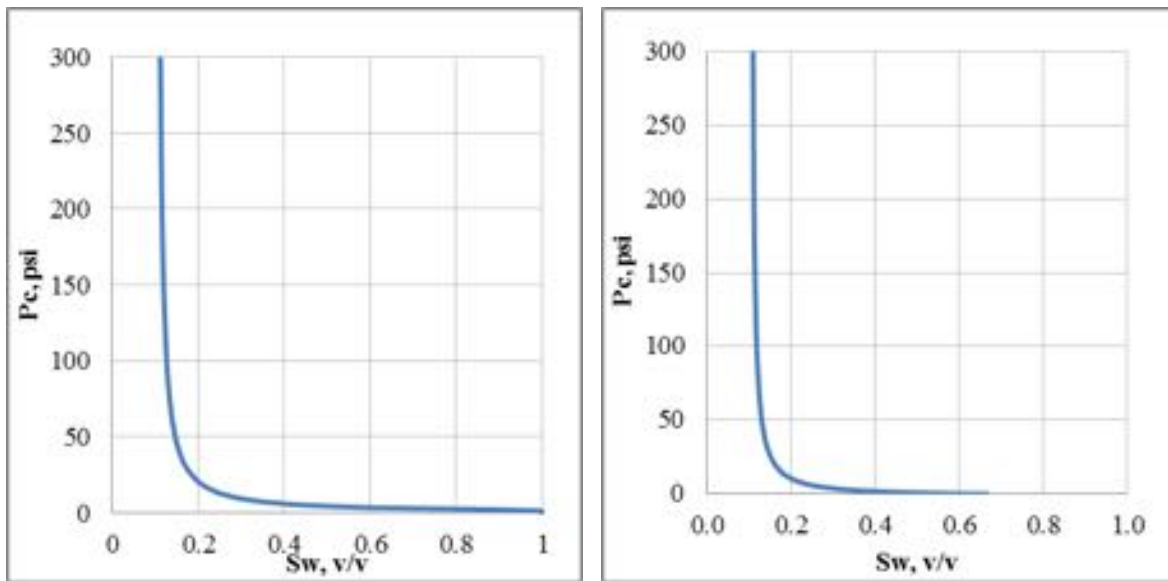
Figure 12. Capillary pressure curves for drainage (left) and imbibition (right) for an RQI value of 0.35.

5.8   Validation of the Capillary Pressure and Relative Permeability Methods

The capillary pressure and relative permeability curves were estimated in the laboratory for the Mississippian Reservoir as part of the Wellington Mississippian Enhanced Oil Recovery (EOR) project located approximately a mile southwest of the Wellington CO_2 storage site. The laboratory-derived curves were used to validate the relative permeability and capillary pressure approach for the Arbuckle discussed above and this was deemed reasonable since the same approach that was used in the Mississippian was also used for the Arbuckle.

Two core plug samples with similar RQI values were sent to Core Laboratories for capillary pressure and relative permeability measurements. The relative permeability and capillary pressure curves were calculated twice for the Mississippian reservoir—before and after the core results were obtained from the laboratory. The initial estimation of Pc curves was based on the end points that were calculated from the NMR log. As shown in fig. 13a, there is a

slight difference between the calculated Pc and measured Pc before calibration. However, there is an excellent match between the calculated Pc and the measured Pc after calibration using the core measured end points. Similarly, as shown in fig. 13b, there is a slight difference between the initial calculated relative permeability and measured relative permeability, but the match is excellent after calibration.
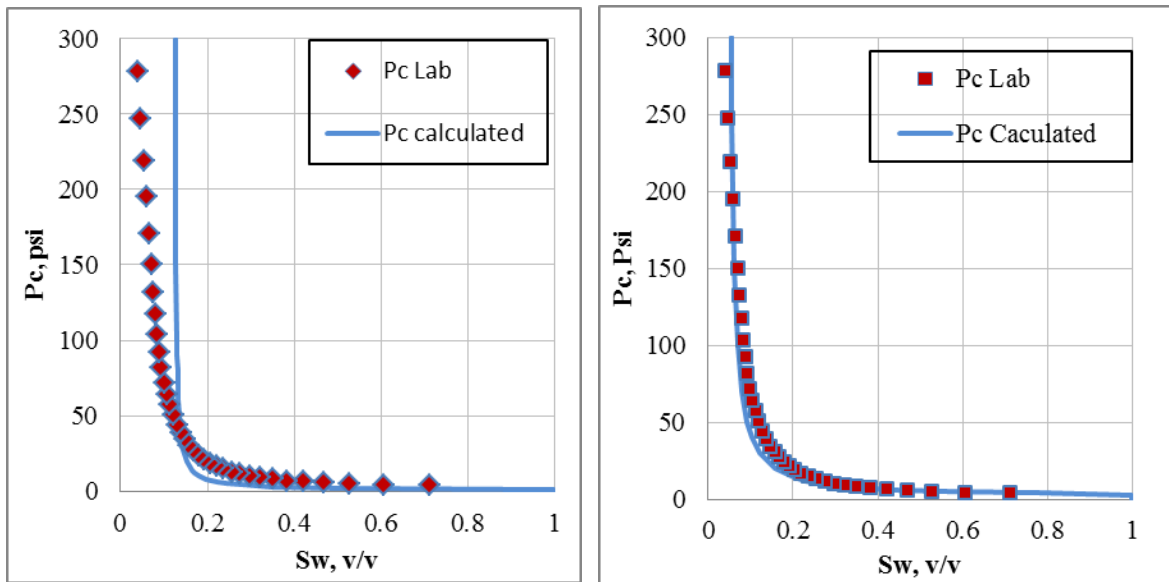
Figure 13a. Capillary pressure curves for an RQI value of 0.2 before calibration (left) and after calibration (right).
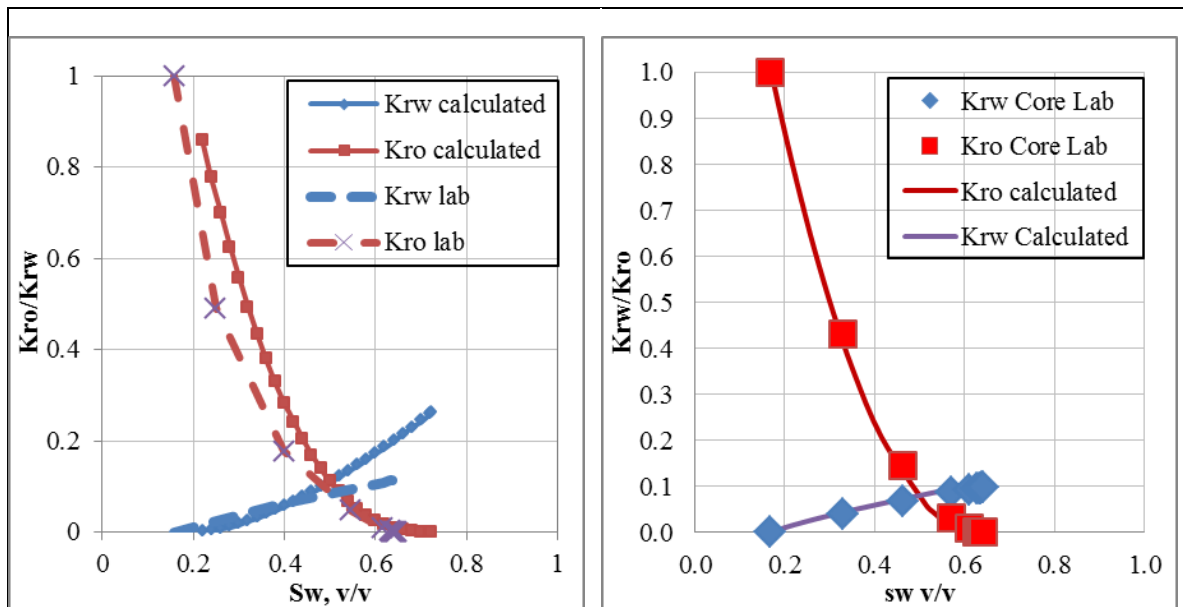
Figure 13b. Relative permeability curves for an RQI value of 0.16 before calibration (left) and after calibration (right).

5.9 Initial Conditions and Injection Rates

Table 6 lists the initial conditions specified in the reservoir model. The simulations were conducted assuming isothermal conditions, but a thermal gradient of 0.008 °C/ft was considered for specifying petrophysical properties that vary with layer depth and temperature such as CO_2 relative permeability, CO_2 dissolution in formation water, etc. The original static pressure in the injection zone (at a reference depth of 4,960 ft) was set to 2,093 psi and the Arbuckle pressure gradient of 0.48 psi/ft was assumed for specifying petrophysical properties. A 140 ft thick perforation zone in well KGS 1-28 was specified between 4,910 and 5,050 ft. A constant brine density of 68.64 lbs/ft^3 (specific gravity of 1.1) was assumed. A total of 40,000 metric tons (MT) of CO_2 was injected in the Arbuckle formation over a period of nine months at an average injection rate of 150 tons/day.

Table 6. Model input specification and CO_2 injection rates.

Temperature	60 °C (140 °F)
Temperature Gradient	0.008 °C/ft
Pressure	2,093 psi (14.43 MPa) @ 4,960 ft RKB
Perforation Zone	4,910-5,050 ft
Perforation Length	140 ft (model layers 54 to 73)
Injection Period	9 months
Injection Rate	150 tons/day
Total CO_2 injected	40,000 MT

5.10 Permeability and Porosity Alternative Models

The base-case reservoir model has been carefully constructed using a sophisticated geomodel as discussed in Section 5.3, which honors site-specific hydrogeologic information obtained from laboratory tests and log-based analyses. However, to account and test for sensitivity of hydrogeologic uncertainties, a set of alternate parametric models were developed by varying the porosity and horizontal hydraulic permeability. Specifically, the porosity and permeability were increased and decreased by 25% following general industry practice (FutureGen Industrial Alliance, 2013). This resulted in nine alternative models, listed in table 7. Simulation results based on all nine models were evaluated to derive the worst-case impacts on

pressure and migration of the plume front for purposes of establishing the AoR and ensuring that operational constraints are not exceeded.

Table 7. Nine alternative permeability-porosity combination models (showing multiplier of base-case permeability and porosity distribution assigned to all model cells).

Alternative Models	Base Porosity x 0.75	Base Porosity	Base Porosity x 1.25
Base Permeability x 0.75	K-0.75/Phi-0.75	K-0.75/Phi-1.0	K-0.75/Phi-1.25
Base Permeability	K-1.0/Phi-0.75	K-1.0/Phi-1.0	K-1.0/Phi-1.25
Base Permeability x 1.25	K-1.25/Phi-0.75	K-1.25/Phi-1.0	K-1.25/Phi-1.25

6.   Reservoir Simulation Results

For the simulations, 40,000 MT of CO_2 were injected into the KGS 1-28 well at a constant rate of approximately 150 tons per day for a period of nine months. Although Berexco is seeking a permit for injecting 40,000 tons, it is likely that only 26,000 tons will be injected due to budgetary constraints. At the request of the EPA, an alternate set of simulations were conducted with a total injection volume of only 26,000 tons. All simulation results presented below for 40,000 tons are repeated for an injection volume of 26,000 tons in Appendix A. Note that only the simulation result figures are provided in Appendix A; the context for each figure is the same as provided in the following description for an injection volume of 40,000 tons. For example, fig. A.6a (in Appendix A), which shows the extent of the free-phase CO_2 plume at six months from commencement of injection for an injection volume of 26,000 tons is equivalent to fig. 14a below, which shows the plume extent at six months from the start of injection for an injection volume of 40,000 tons.

A total of nine models representing three sets of alternate permeability-porosity combinations as specified in table 7 were simulated with the objective of bracketing the range of expected pressures and extent of CO_2 plume migration.

The extent of lateral plume migration depends on the particular combination of permeability-porosity in each of the nine alternative models. These two parameters are independently specified in CMG as they are assumed to be decoupled. A high-permeability value results in farther travel of the plume due to gravity override, bouyancy, and updip migration. Similarly, a low effective porosity for the same value of permeability results in farther travel for the plume as compared to high porosity as the less-connected pore volume

results in faster pore velocity. The high-permeability/low-porosity combination (k-1.25/phi-0.75) resulted in the largest horizontal plume dimension. In contrast, the highest induced pressures were obtained for the alternative model with the lowest permeability and the lowest porosity (k-0.75/phi-0.75).

6.1 CO_2 Plume Migration

Figure 14a–f shows the maximum lateral migration of the CO_2 plume in the injection interval (elevation 5,010 ft) for the largest areal migration case (k-1.25/phi-0.75). The plume grows rapidly during the injection phase (fig. 14a–c) and is largely stabilized by the end of the second year (fig. 14d). The plume at the end of 100 years (fig. 14f) has spread only minimally since cessation of injection and has a maximum lateral spread of approximately 2,150 ft from the injection well. It does not intercept any well other than the proposed Arbuckle monitoring well KGS 2-28, will be constructed in compliance with Class VI injection well guidelines.

The evolution of the maximum lateral extent of the free phase plume is shown in fig. 15 for the maximum plume spread case (k-1.25/phi-0.75) The plume grows rapidly during the injection period and up to the second year from commencement of injection. Thereafter, the plume has stabilized to a maximum lateral extent of approximately 2,150 ft. The plume only intercepts the proposed Arbuckle monitoring well KGS 2-28, which will be built to be in compliance with Class VI design and construction requirements. There are no additional natural or artificial penetrations that will allow CO_2 to escape upward from the Arbuckle injection zone.

Figure 16 shows the extent of vertical plume migration for the fast vertical migration case (k-1.25/phi-0.75), the base case (k-1.00/phi-1.00), and the high pressure case (k-0.75/phi-0.75). The free-phase plume remains confined in the injection interval (lower Arbuckle) because of the presence of the low-permeability baffle zones above the injection interval. This same information is shown in fig. 14 a—f, which shows the maximum extent of vertical migration. For all three cases, the plume remains confined in the injection interval in the lower Arbuckle.

To account for uncertainties of CO_2 movement in the vertical direction, an alternate vertical permeability model was also developed in which the vertical permeability parameter was increased by 50% along with a porosity of 75% (k-1.50/phi-0.75). Figure 16 presents the

extent of vertical migration of the free phase plume for this case in addition to the three cases already described. The figure shows that the CO_2 migrates approximately 30 ft higher for the altered vertical permeability case, but it does not penetrate the low permeability baffle zone in the middle of the Arbuckle and stays contained within the lower Arbuckle injection zone.

The simulation results discussed above are expected to represent conservative estimates of plume migration because the present CMG simulations neglect mineral sequestration trapping. Additionally, the modeling results presented in this document do not simulate convection cells, which as demonstrated recently by Pau et al. (2010) can greatly accelerate the dissolution rate. Because of time and computational constraints, these mechanisms were ignored, and therefore the storage rates and quantities are likely to be underestimated, thus ensuring that the projections presented in this application provide a "worst-case" scenario.
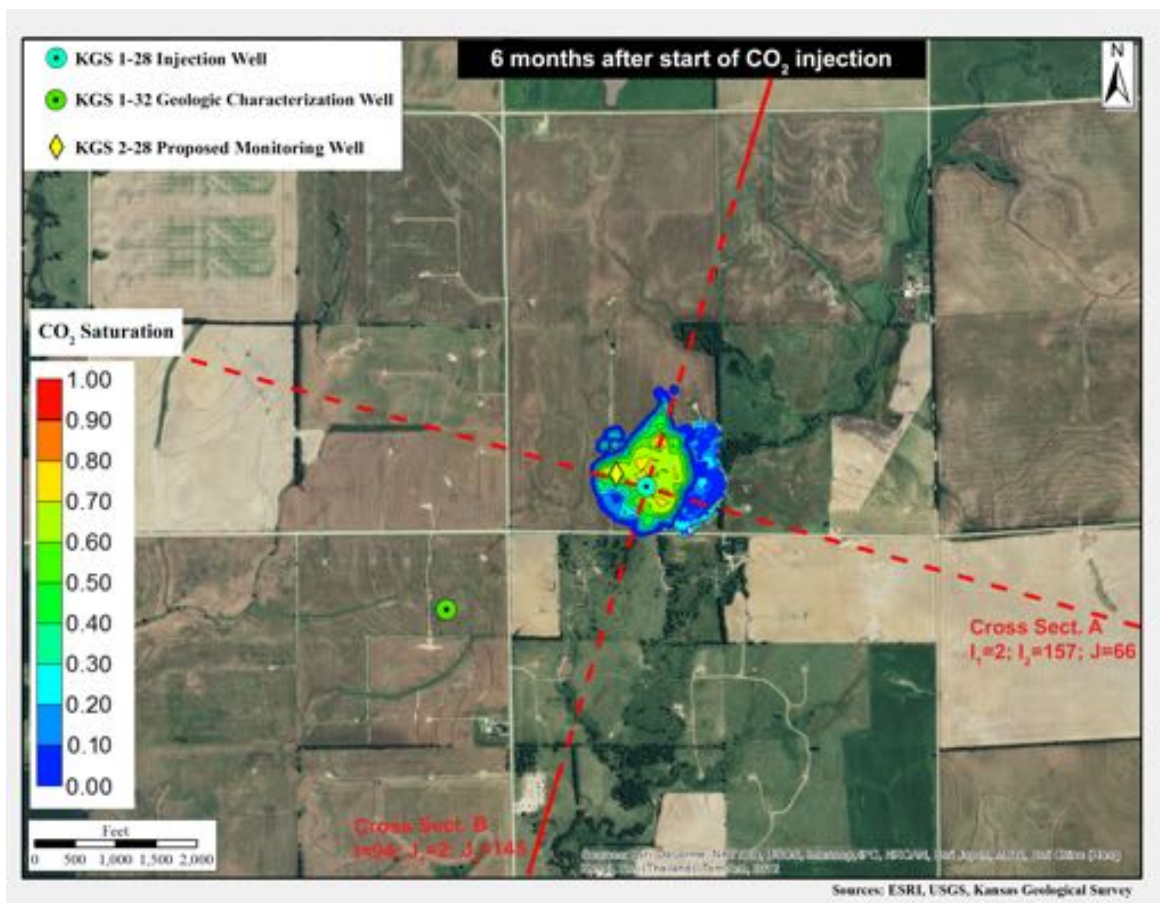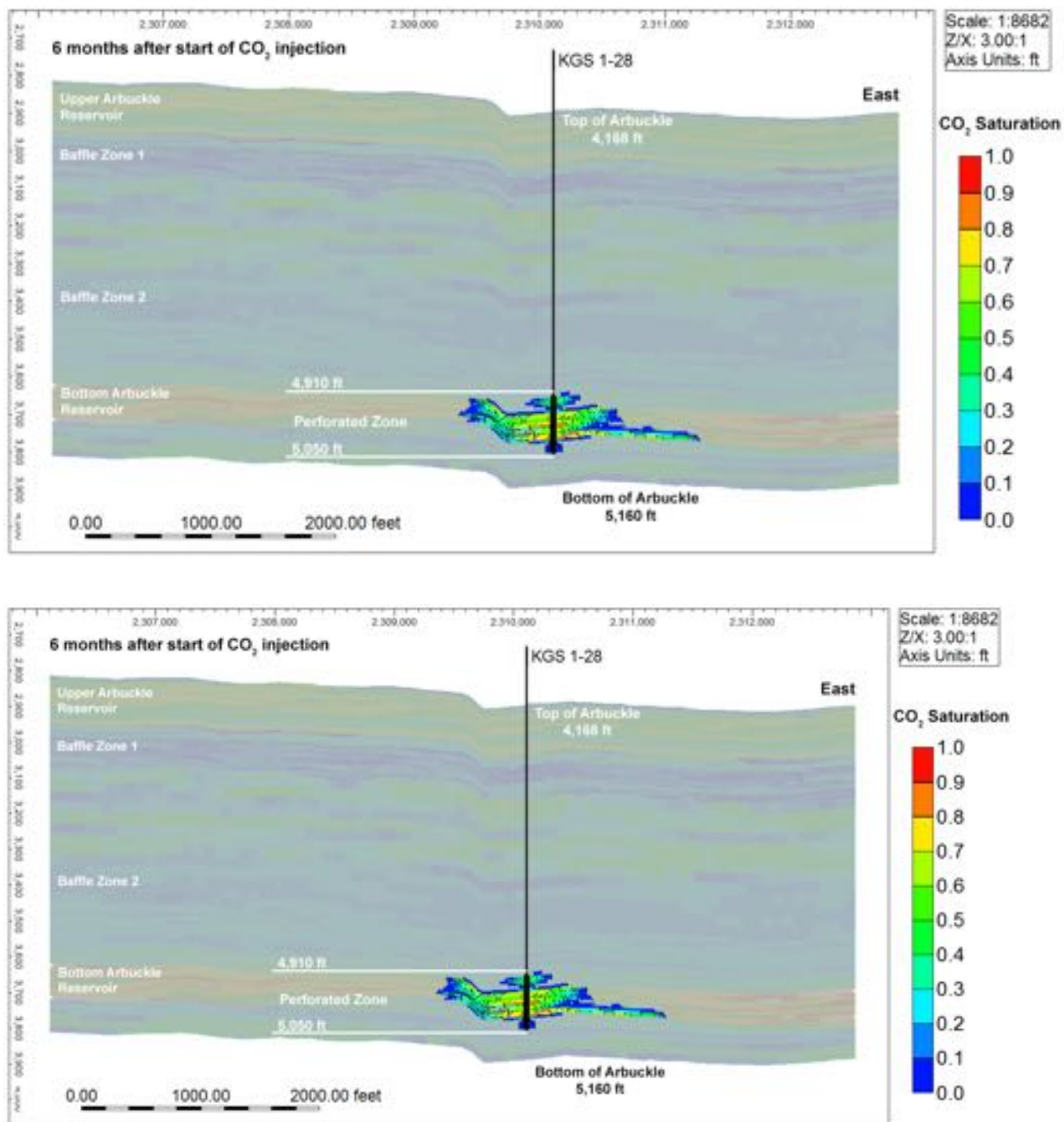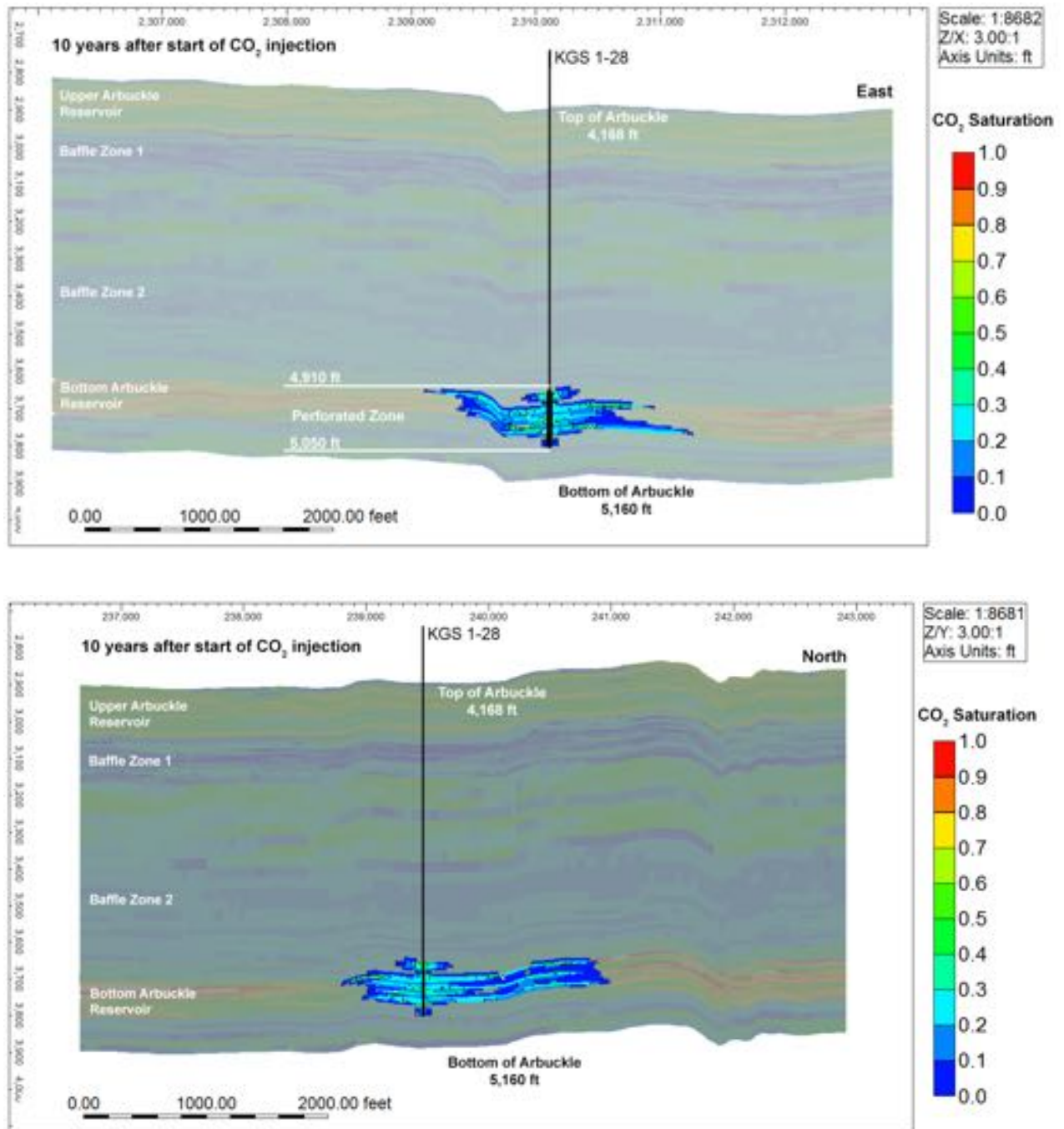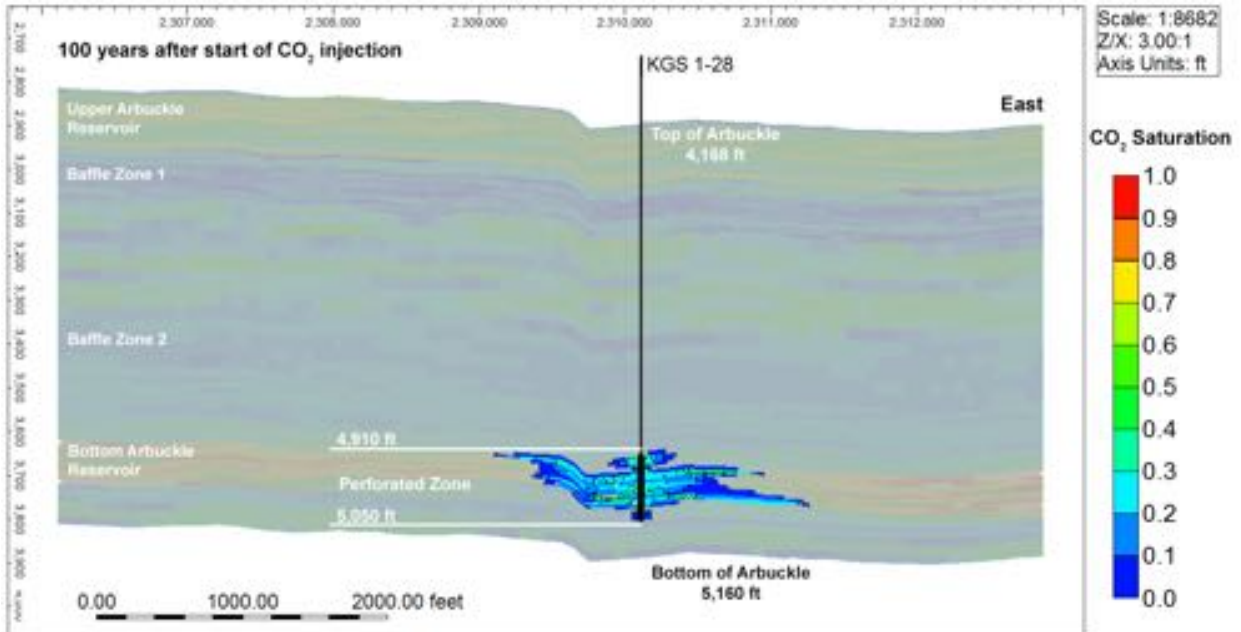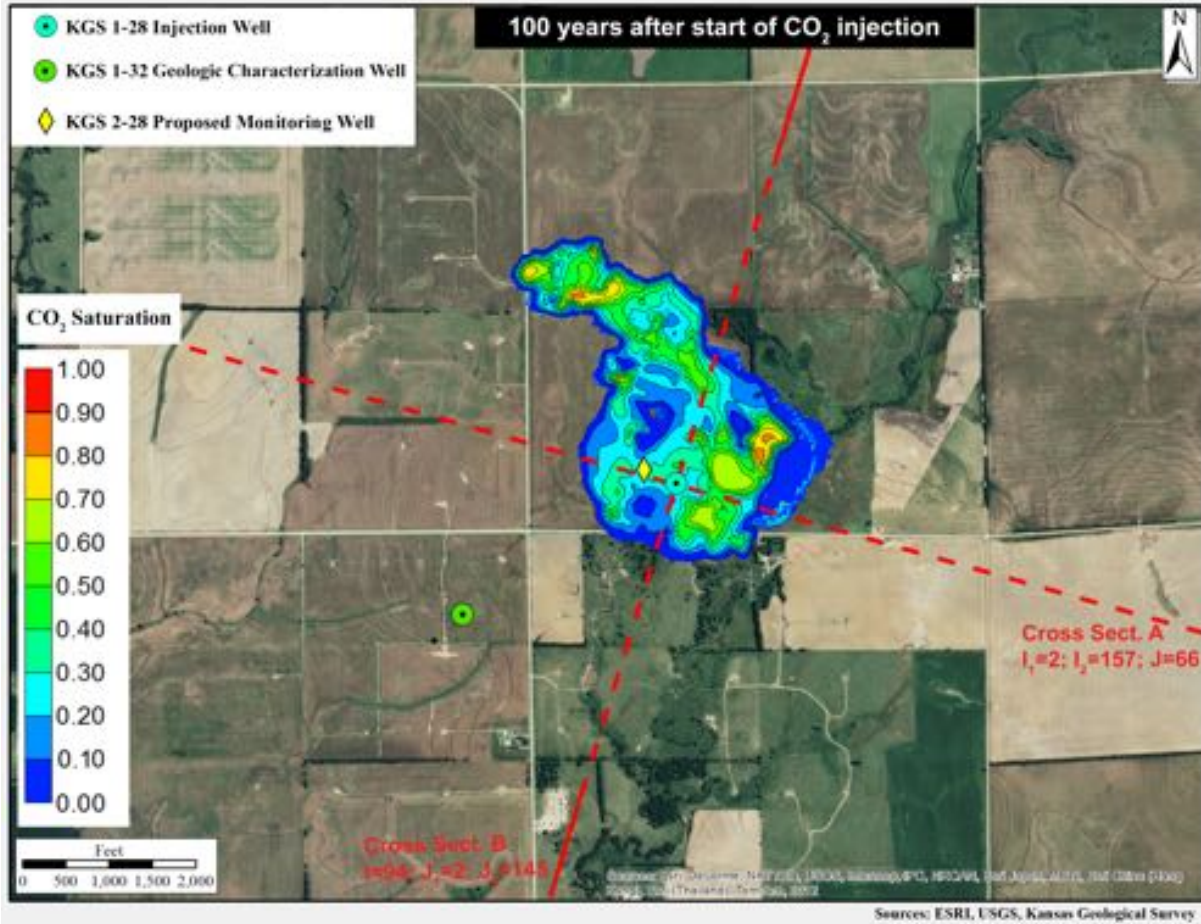
Figure 14a. Free-phase CO_2 plume in aerial and cross-sectional view for the largest migration alternative model (k-1.25/phi-0.75) at six months from start of injection.
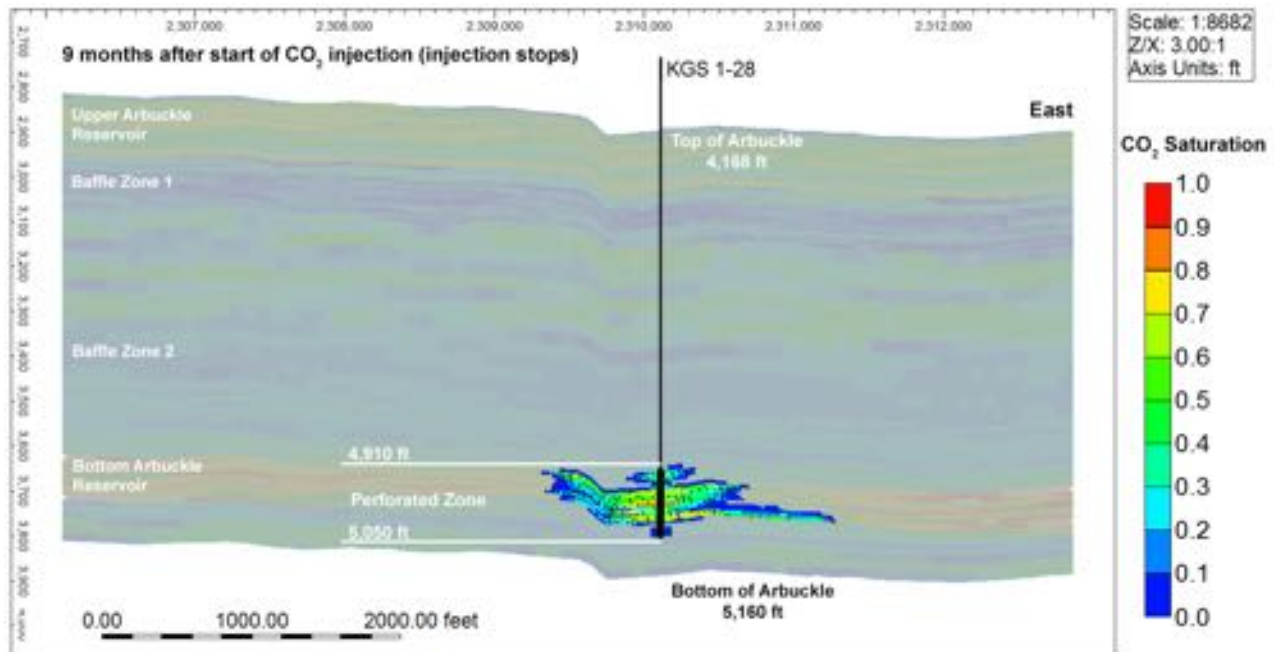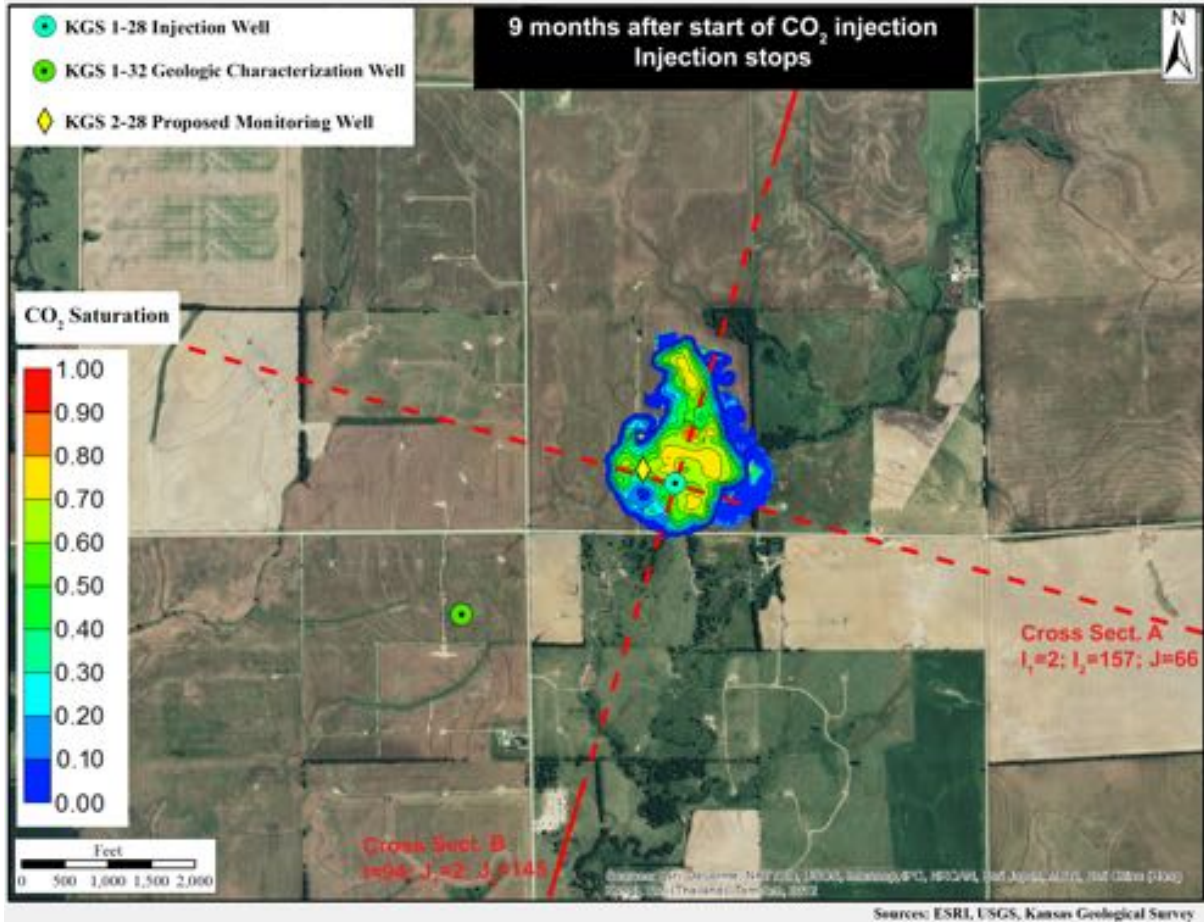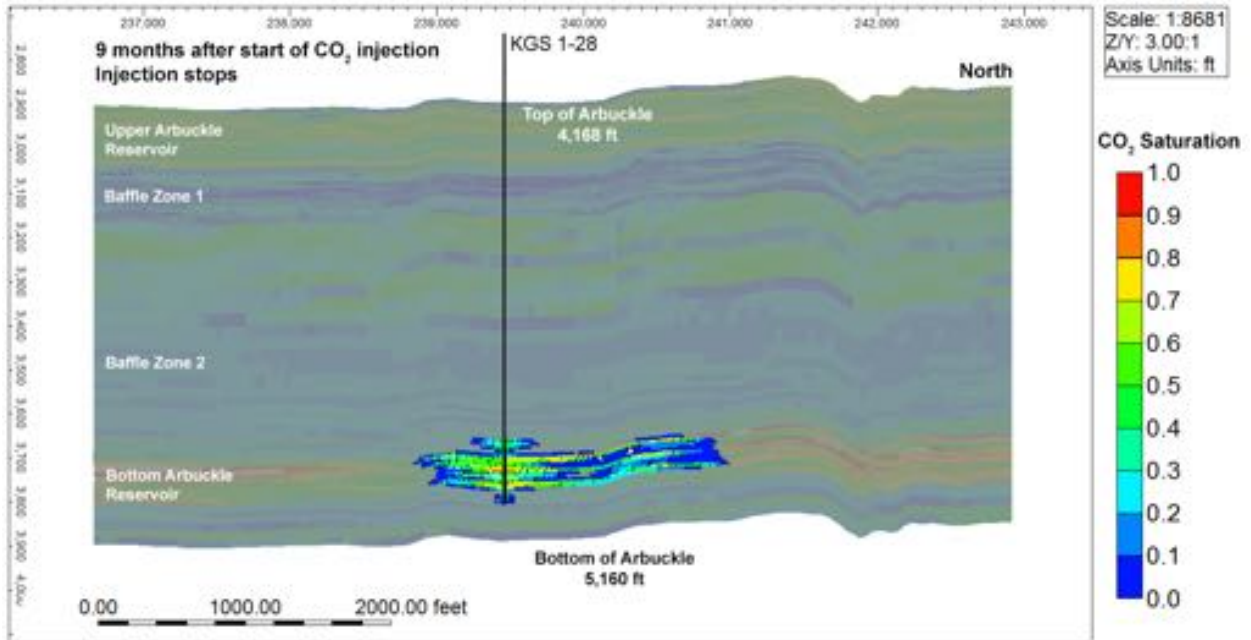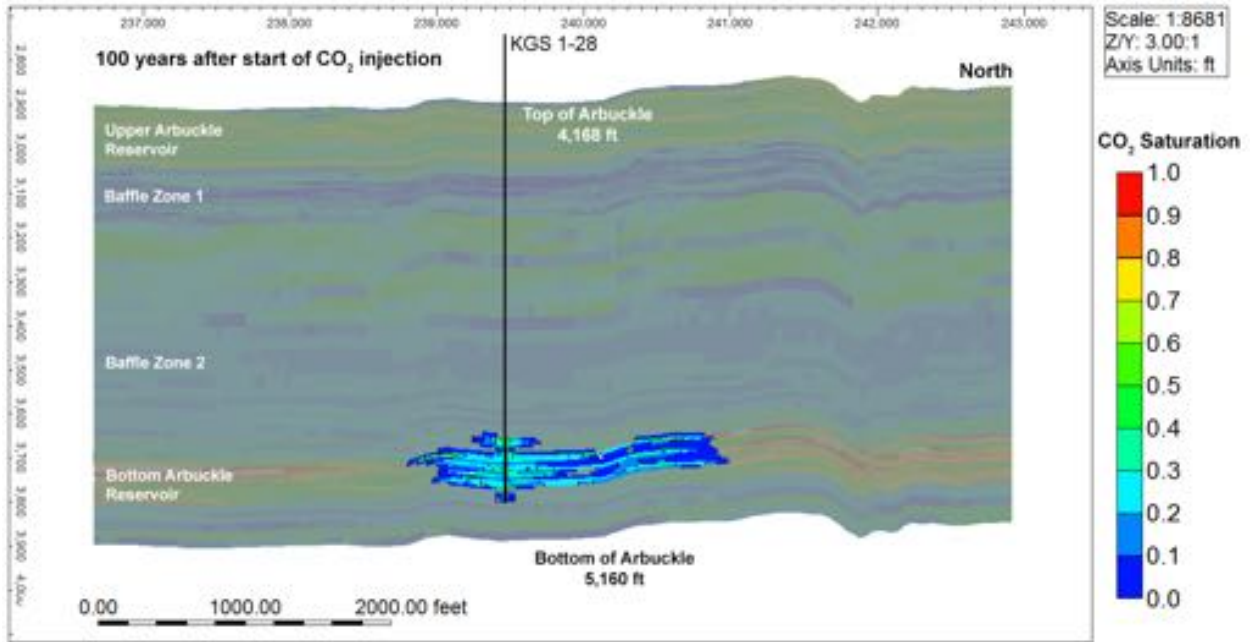
Figure 14b. Free-phase CO$_2$ plume in aerial and cross-sectional view for the largest migration alternative model (k-1.25/phi-0.75) at nine months from start of injection.
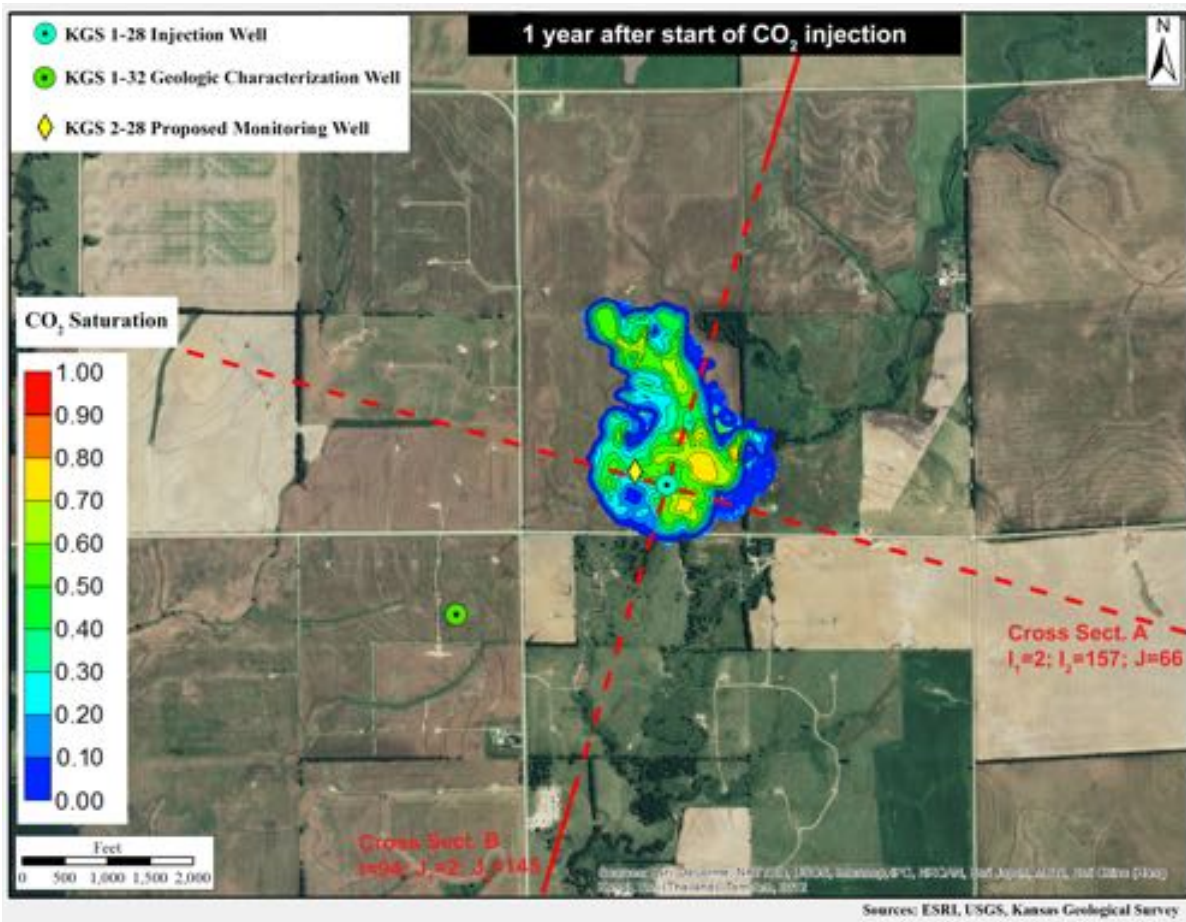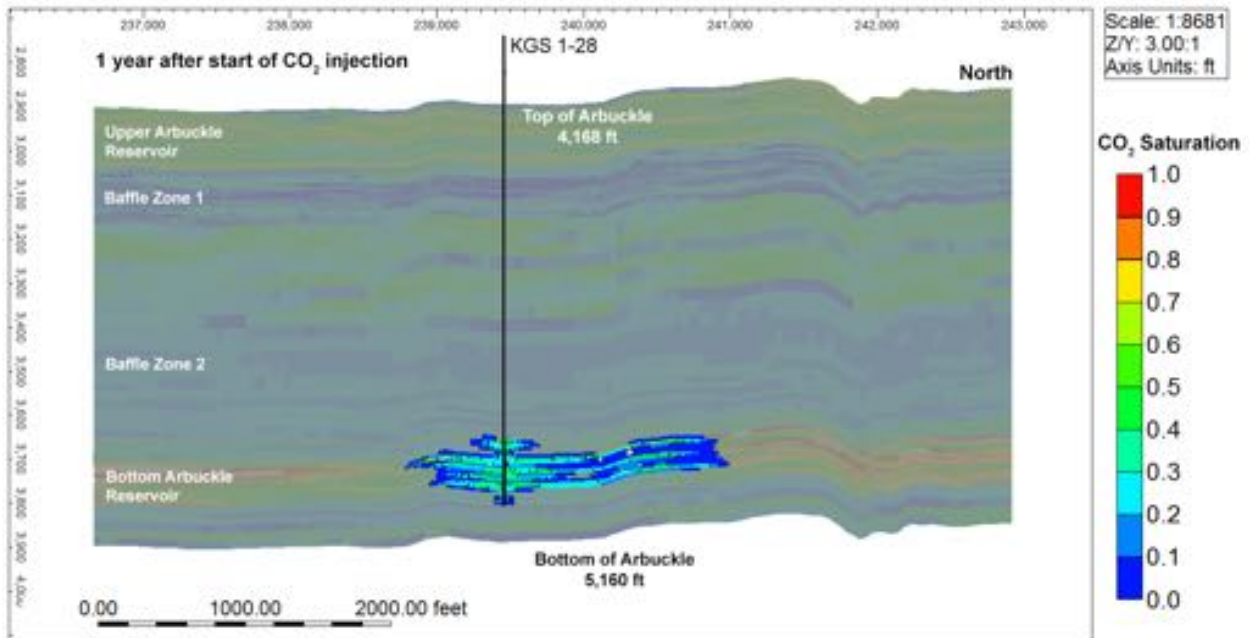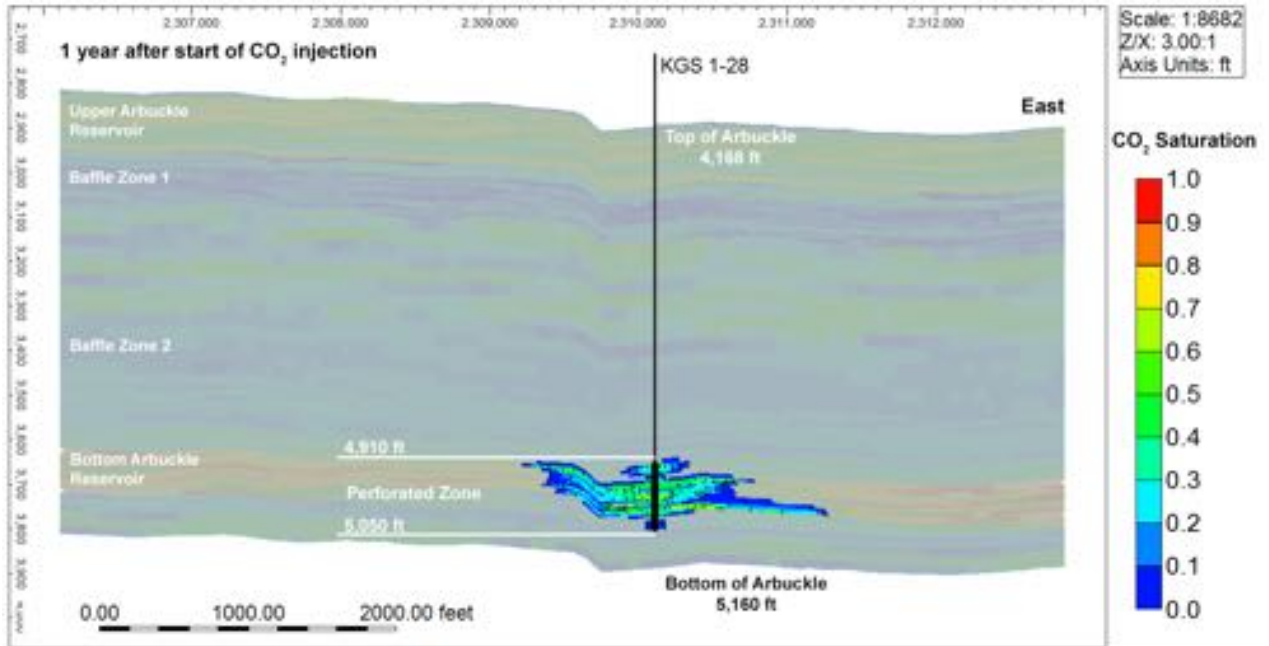
Figure 14c. Free-phase CO$_2$ plume in aerial and cross-sectional view for the largest migration alternative model (k-1.25/phi-0.75) at one year from start of injection.

2 years after start of CO$_2$ injection

2 years after start of CO$_2$ injection
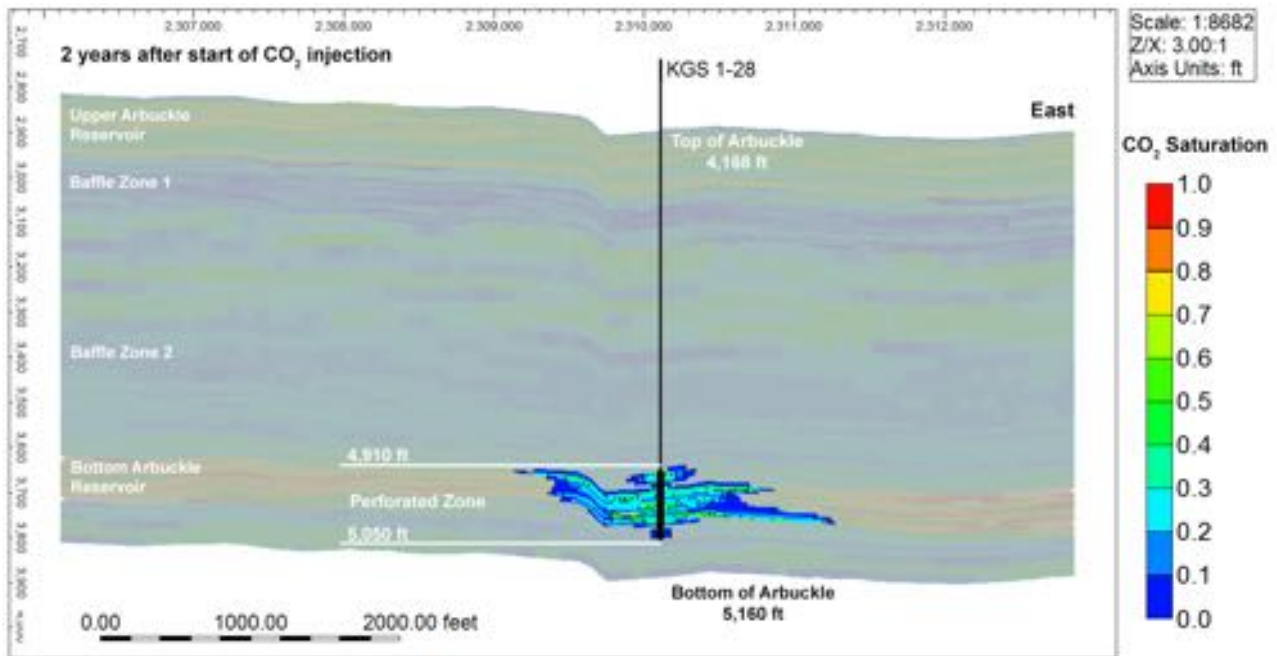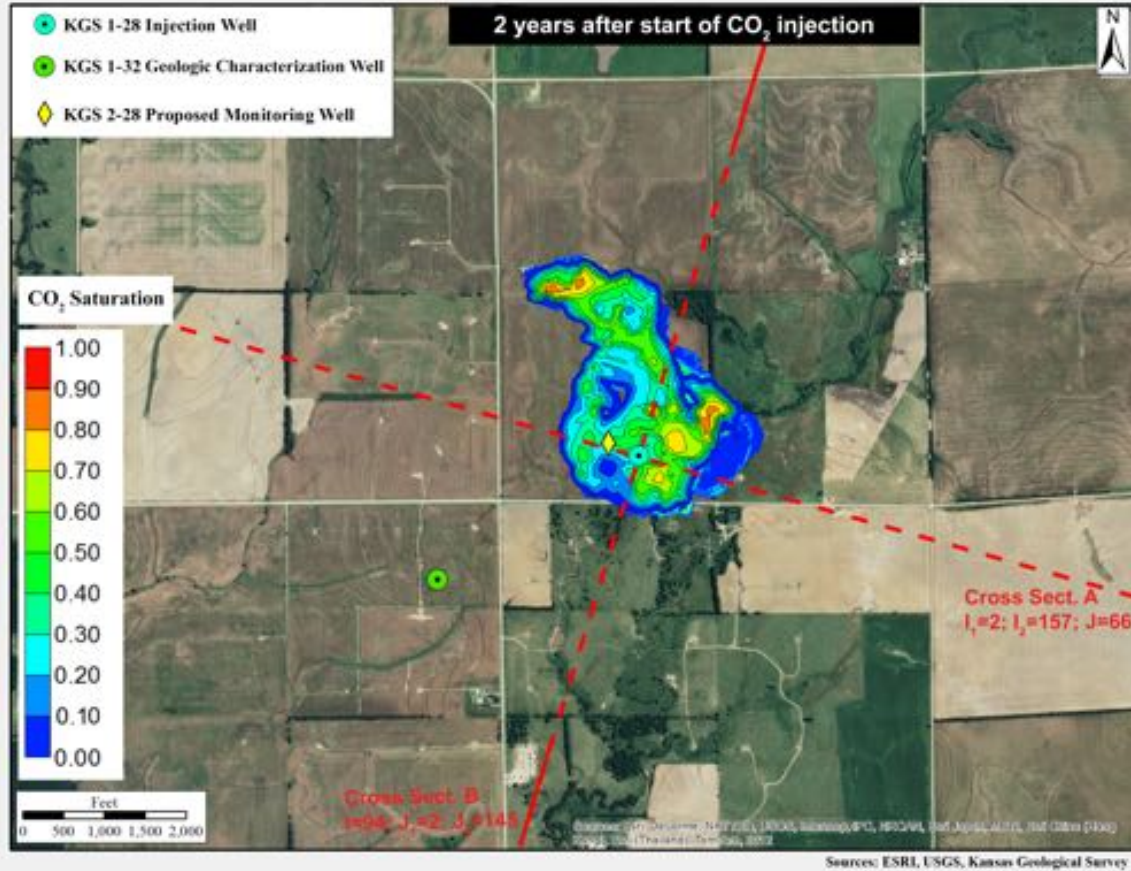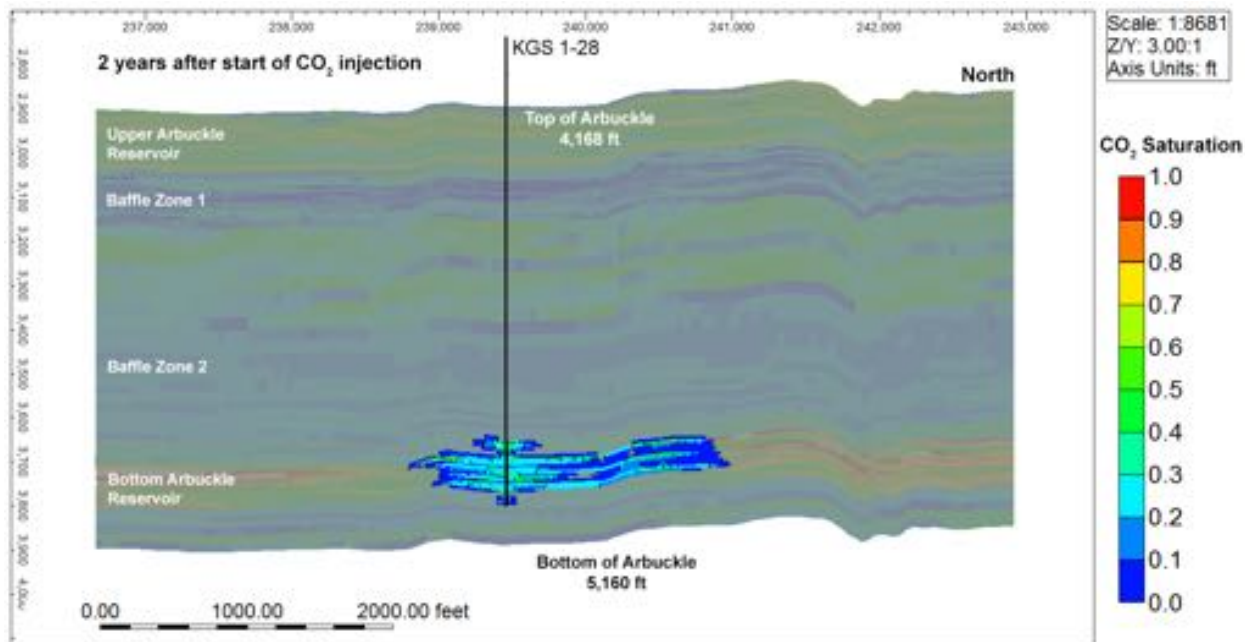
Figure 14d. Free-phase CO₂ plume in aerial and cross-sectional view for the largest migration alternative model (k-1.25/phi-0.75) at two years from start of injection.
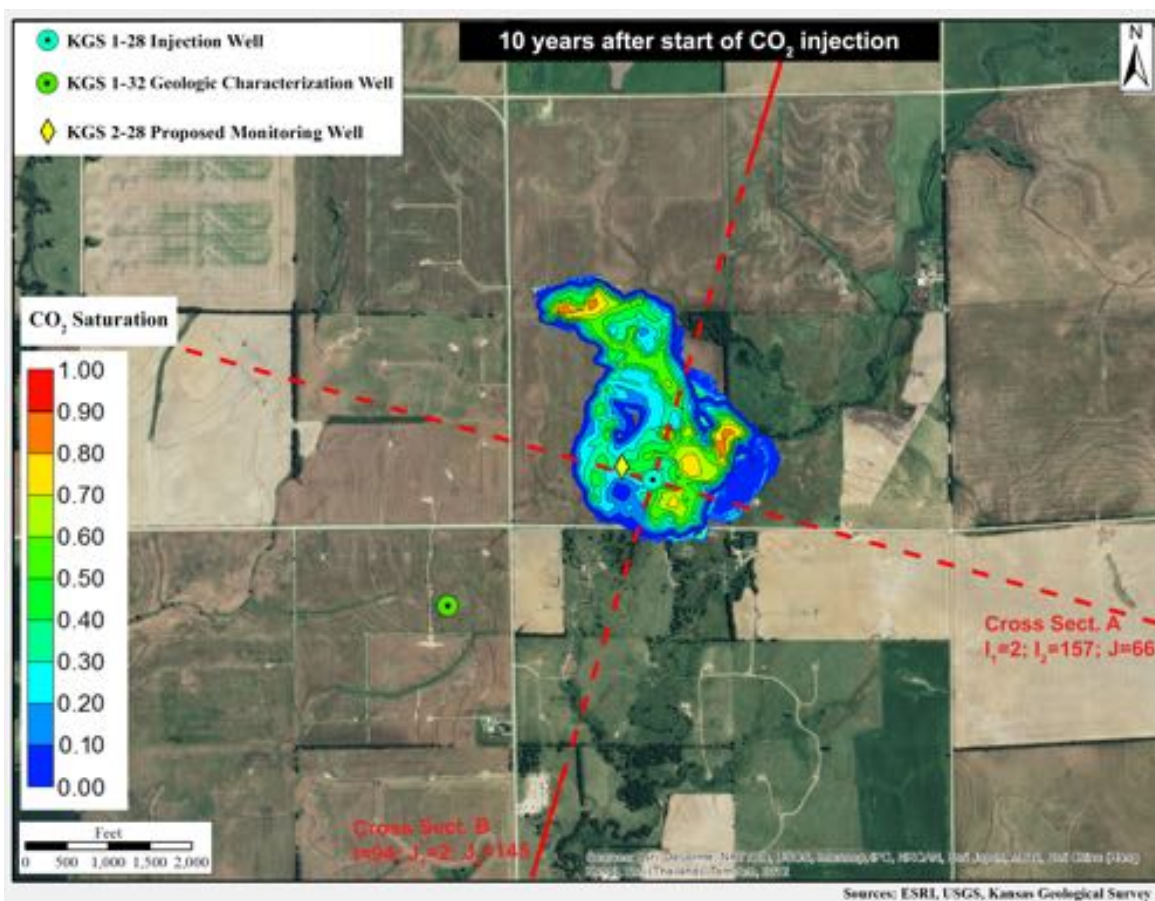
Figure 14e. Free-phase CO$_2$ plume in aerial and cross-sectional view for the largest migration alternative model (k-1.25/phi-0.75) at 10 years from start of injection.

100 years after start of CO₂ injection

100 years after start of CO₂ injection

Figure 14f. Free-phase CO₂ plume in aerial and cross-sectional view for the largest migration alternative model (k-1.25/phi-0.75) at 100 years from start of injection.
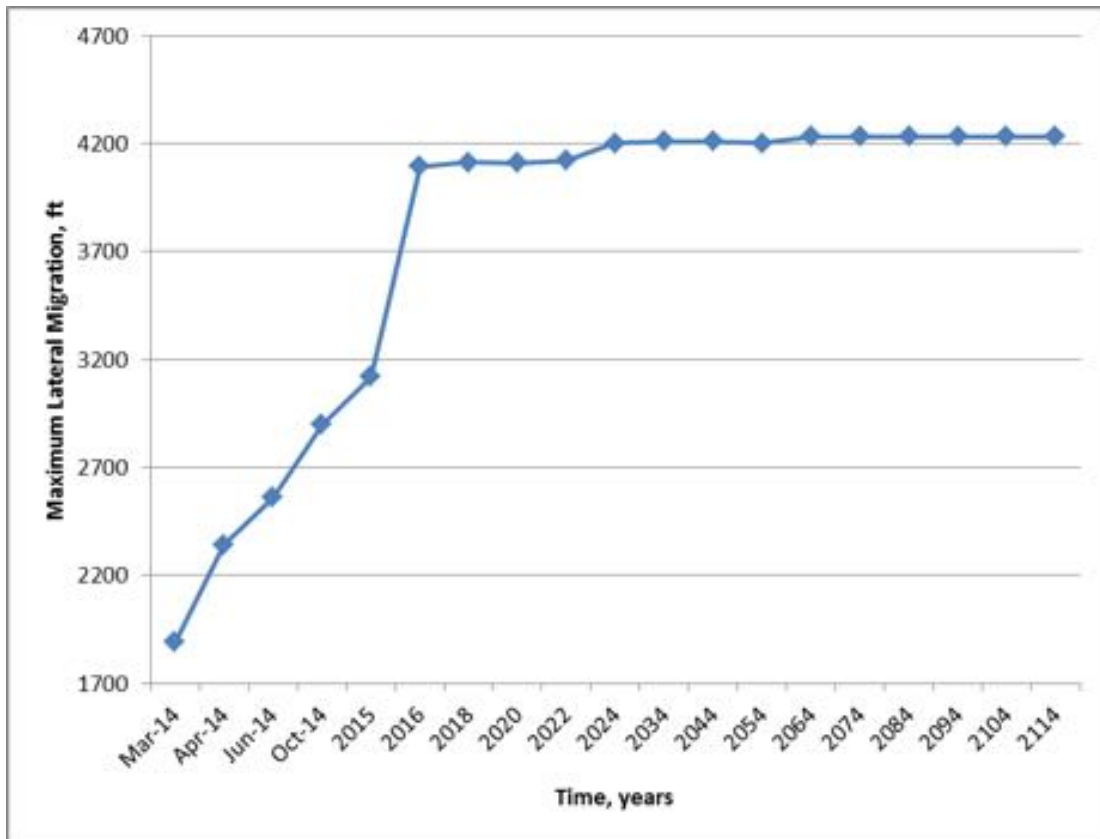
Figure 15. Maximum lateral extent of CO₂ plume migration (as defined by the 0.5% CO₂ saturation isoline) for the largest plume migration case k-1.25/phi-0.75.
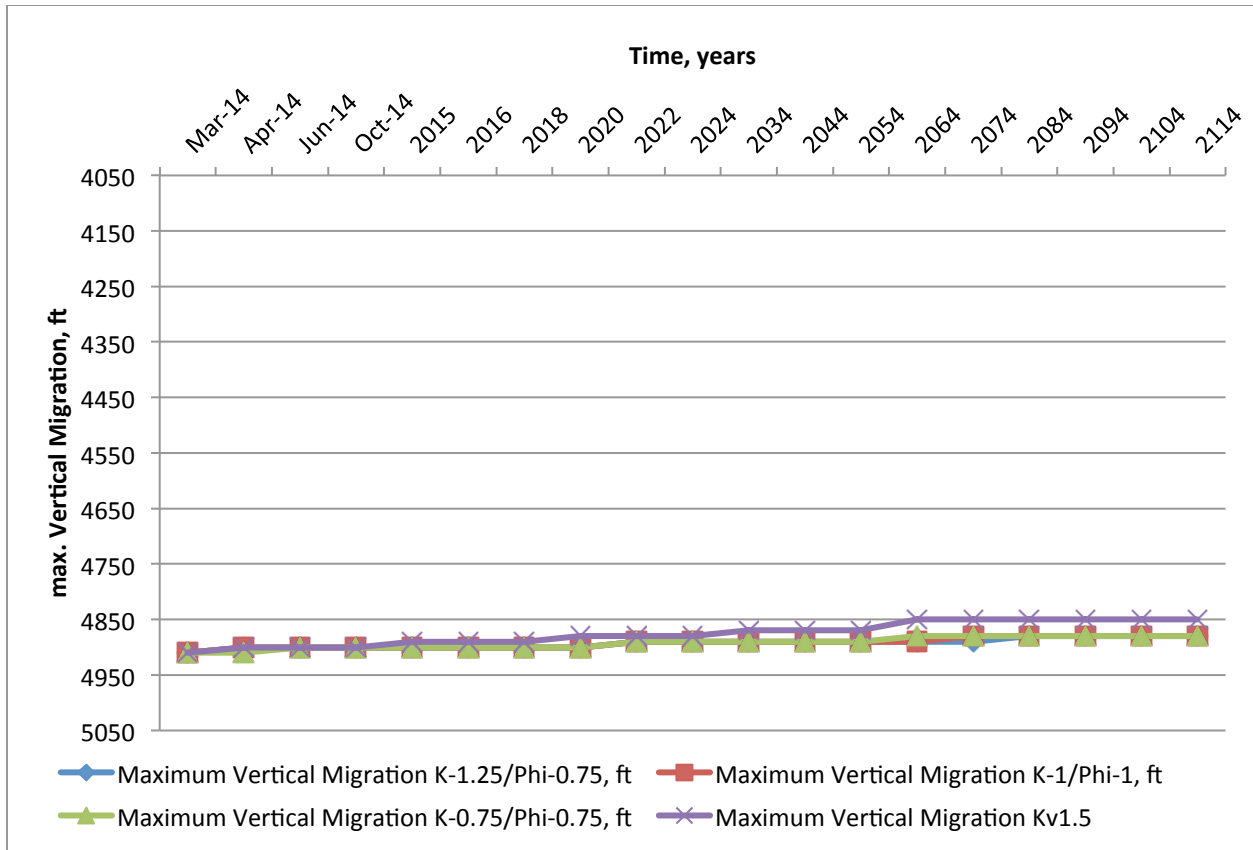
Figure 16. Maximum vertical extent of free-phase CO_2 migration for the two alternative cases that result in the maximum plume spread (k-1.25/phi-0.75) and the maximum induced pressure (k-0.75/phi-0.75) along with base case (k-1.0/phi-1.0) and vertical permeability sensitivity case (k-1.25/phi-0.75).

6.2   Simulated Total and Dissolved CO_2 Spatial Distribution

Figure 17a–l shows the maximum lateral and vertical migration of the CO_2 plume in total concentration and in dissolved phase at the injection interval (elevation 5,010 ft) for the largest areal migration case (k-1.25/phi-0.75). The areal extent of total and dissolved CO_2 plumes is larger than the extent of the CO_2 plume in free phase; however, these delineations are not used for the AoR definition, since the CO_2 in dissolved and other than supercritical and gaseous phases is considered to be immobile. The total and dissolved CO_2 plumes do not intercept any well other than the proposed Arbuckle monitoring well KGS 2-28 will be constructed in compliance with Class VI injection well guidelines. The extent of vertical CO_2 plume migration in total and dissolved states is similar to the vertical migration of the free phase CO_2. The CO_2 remains confined in the injection interval (lower Arbuckle) because of the presence of the low-permeability baffle zones above the injection interval.
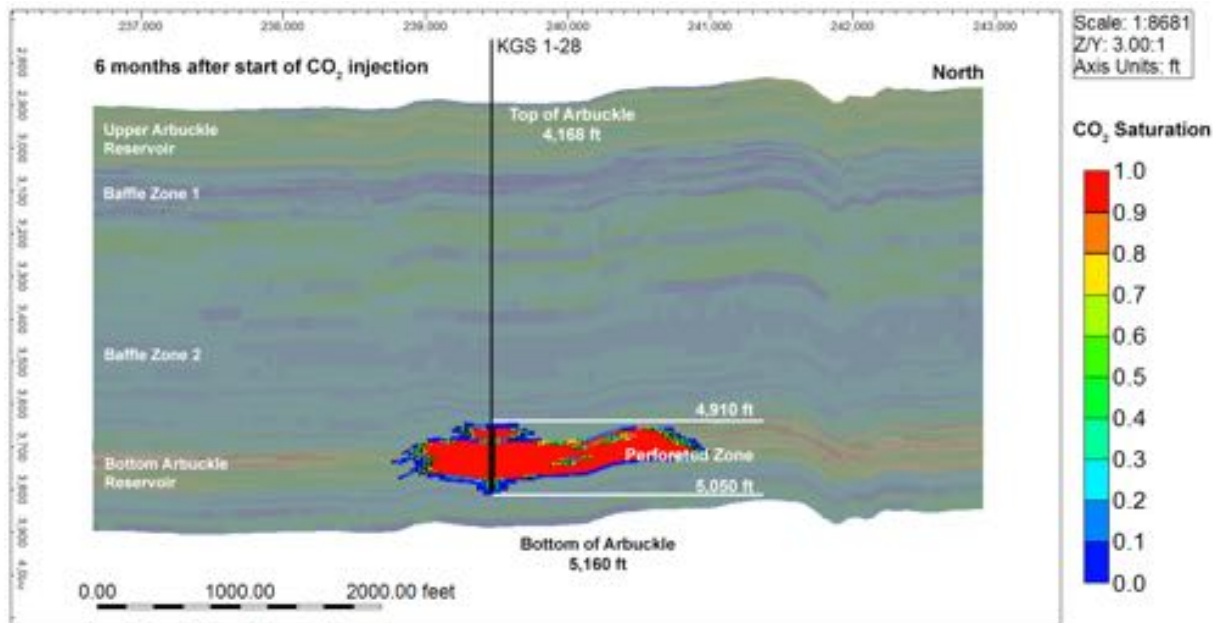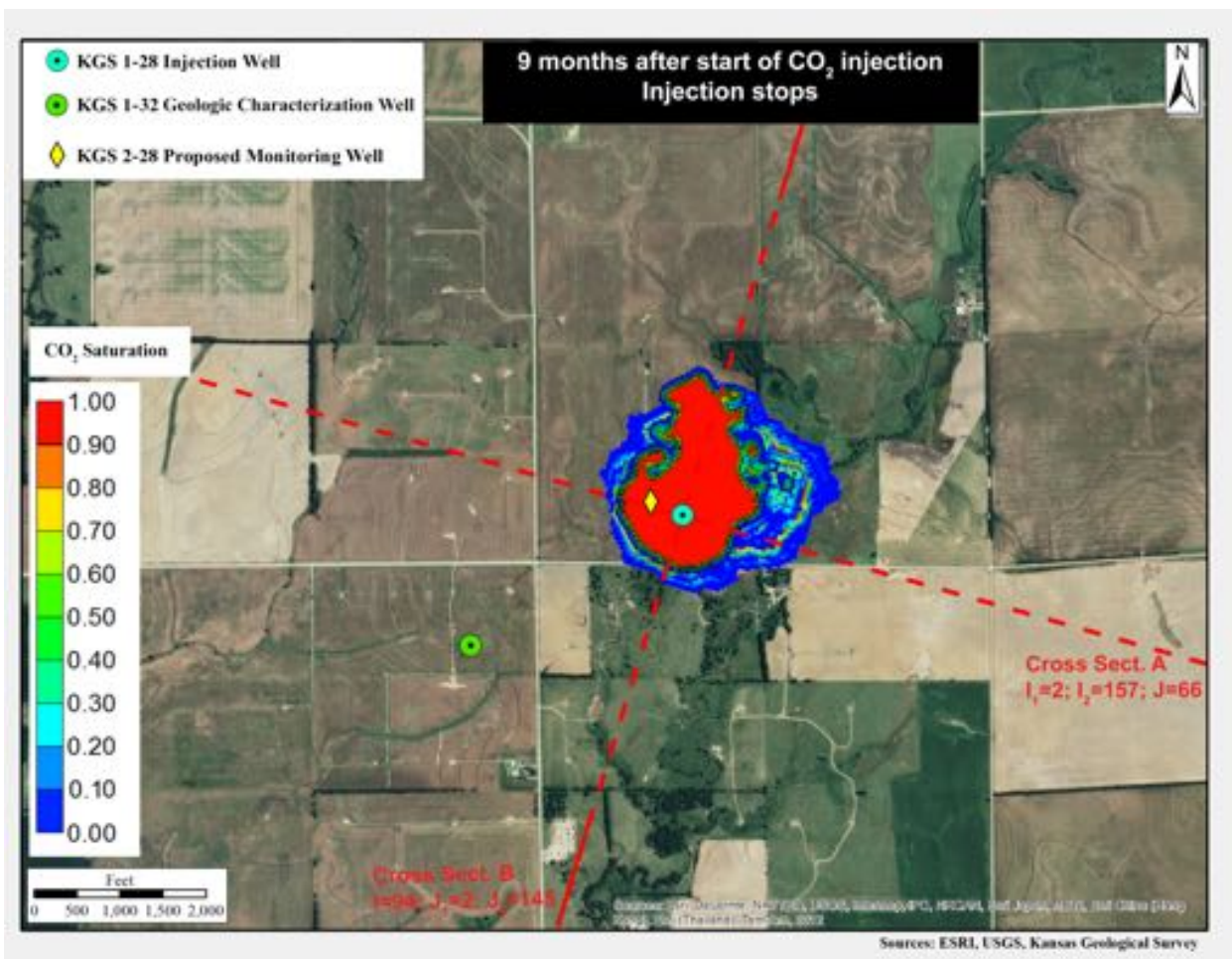
6 months after start of CO_2 injection

6 months after start of CO_2 injection
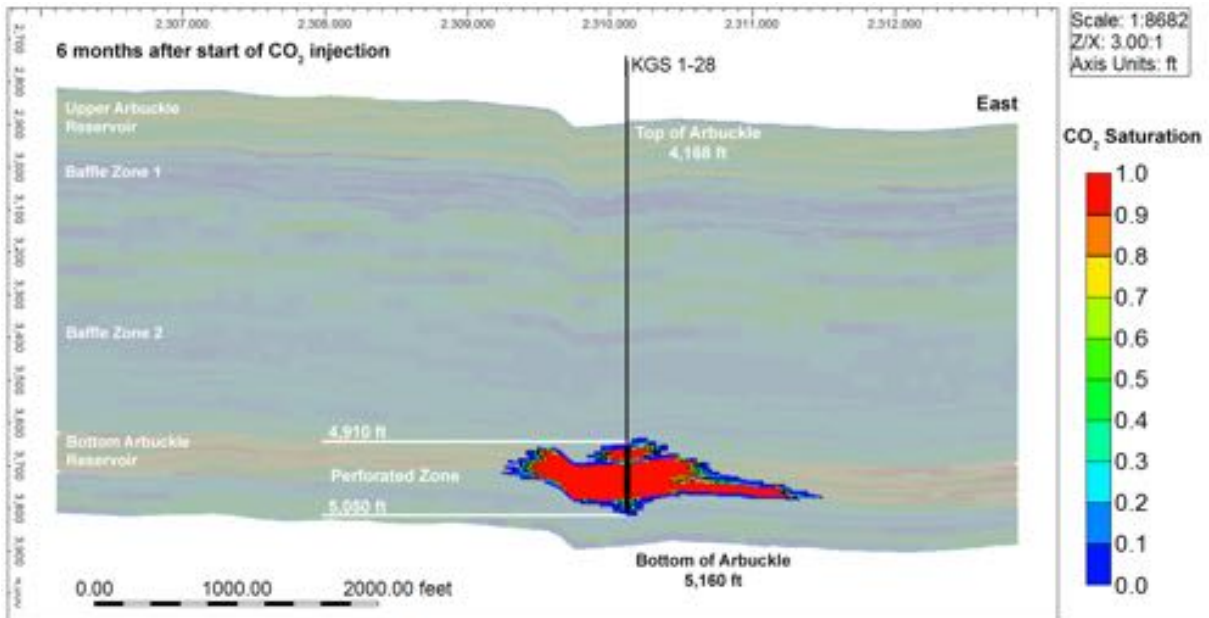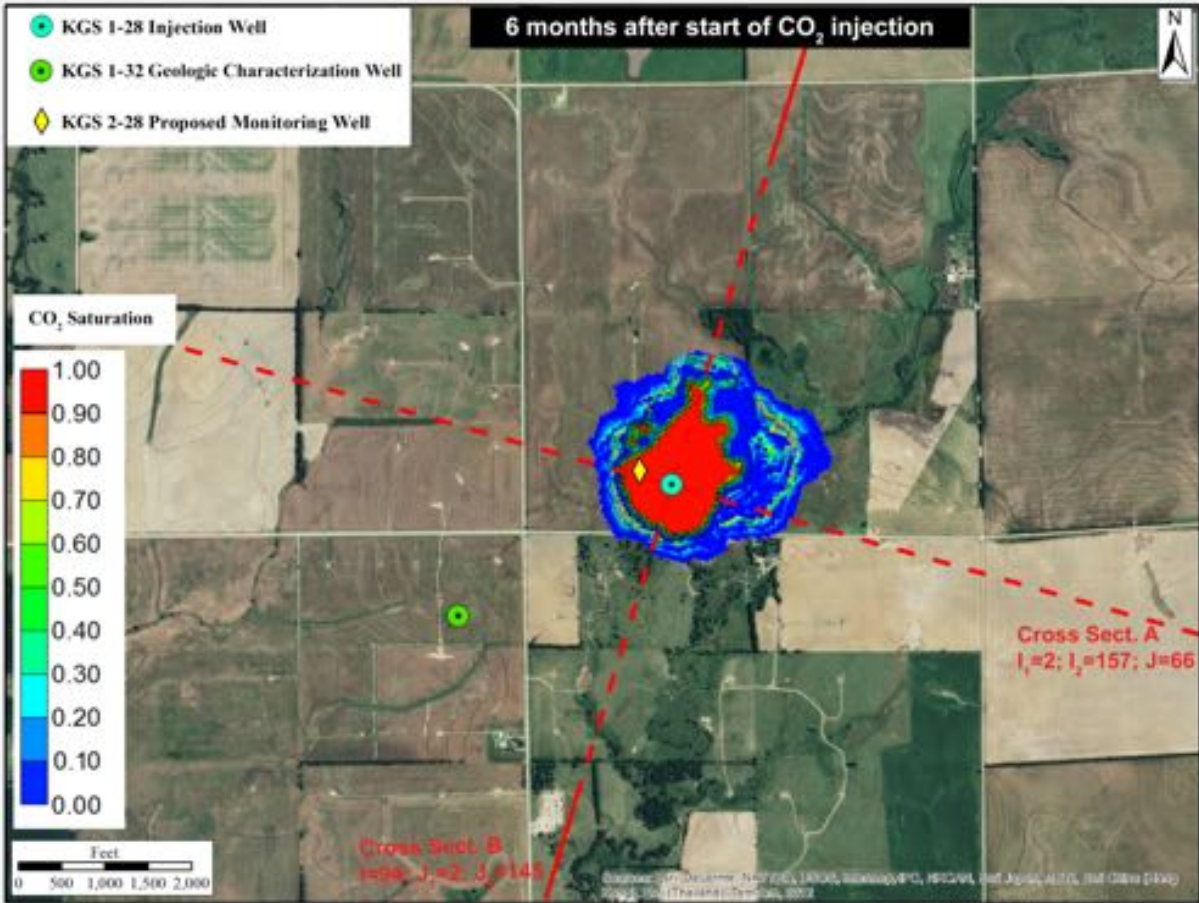
Figure 17a. Total CO₂ spatial distribution in aerial and cross-sectional view for the largest migration alternative model (k-1.25/phi-0.75) at six months from start of injection.
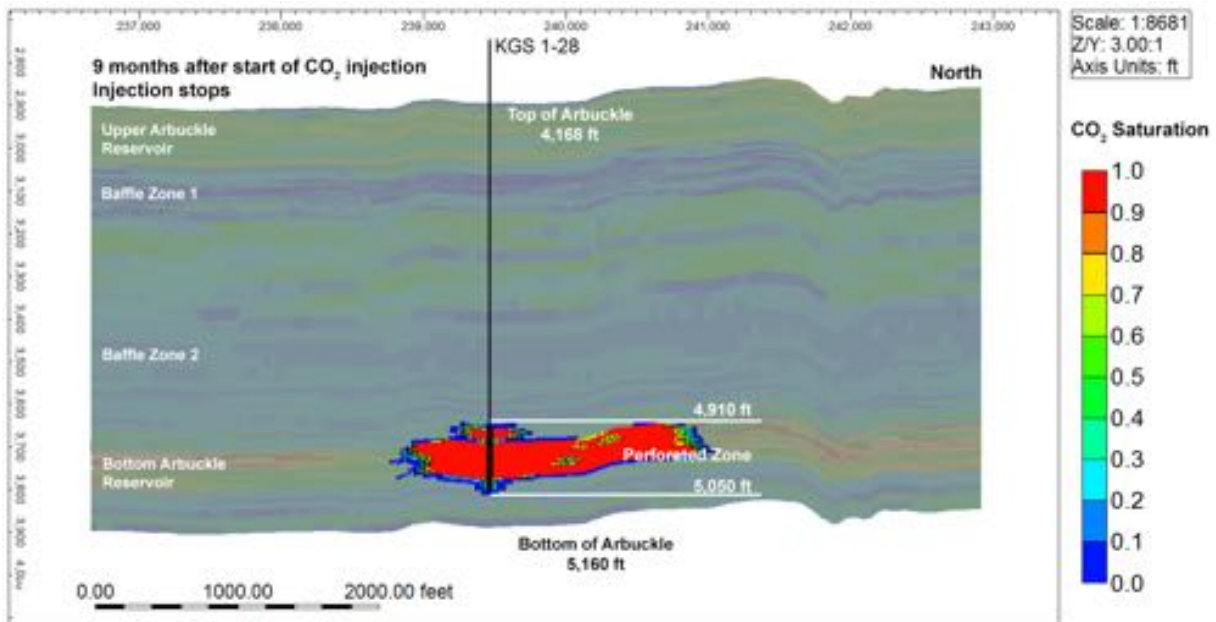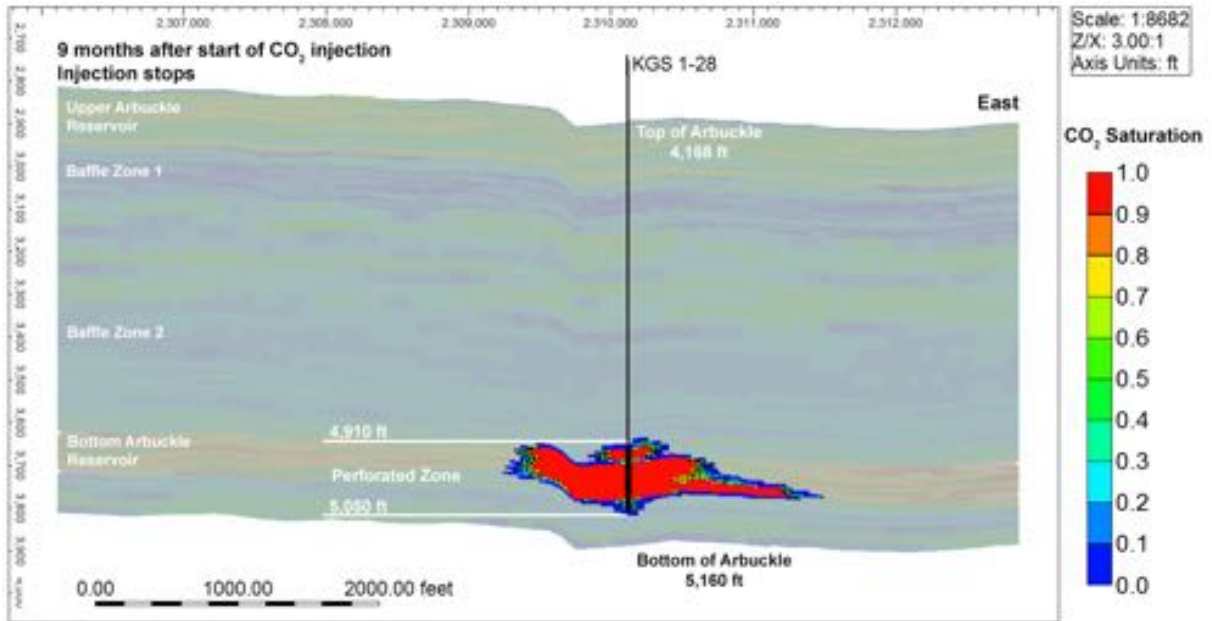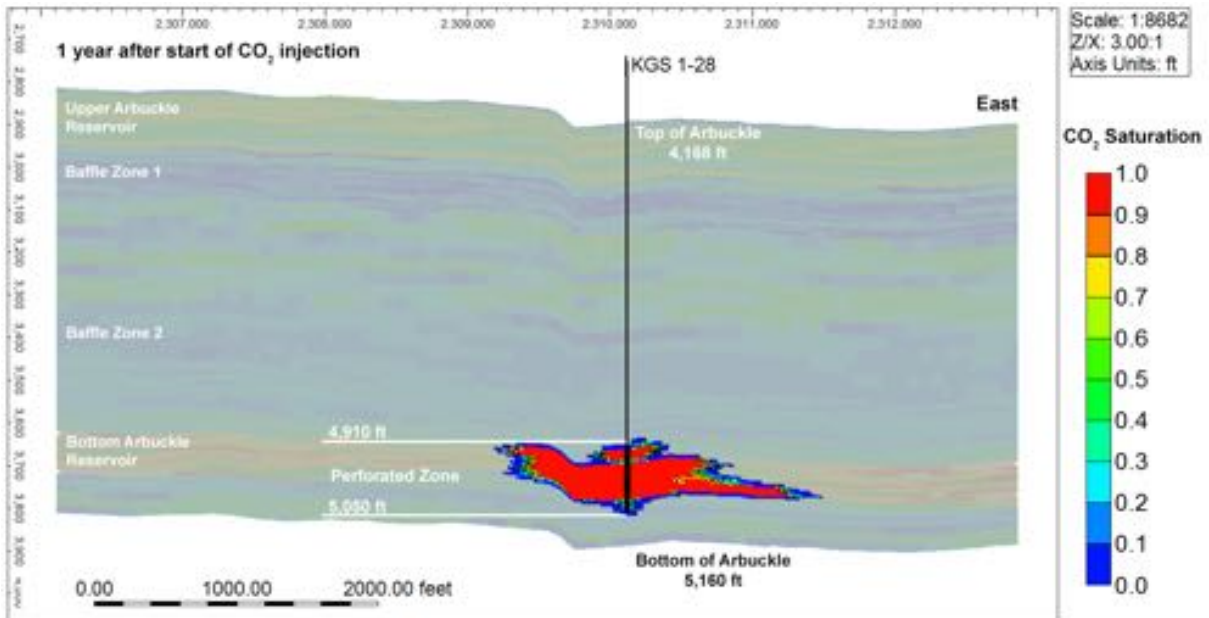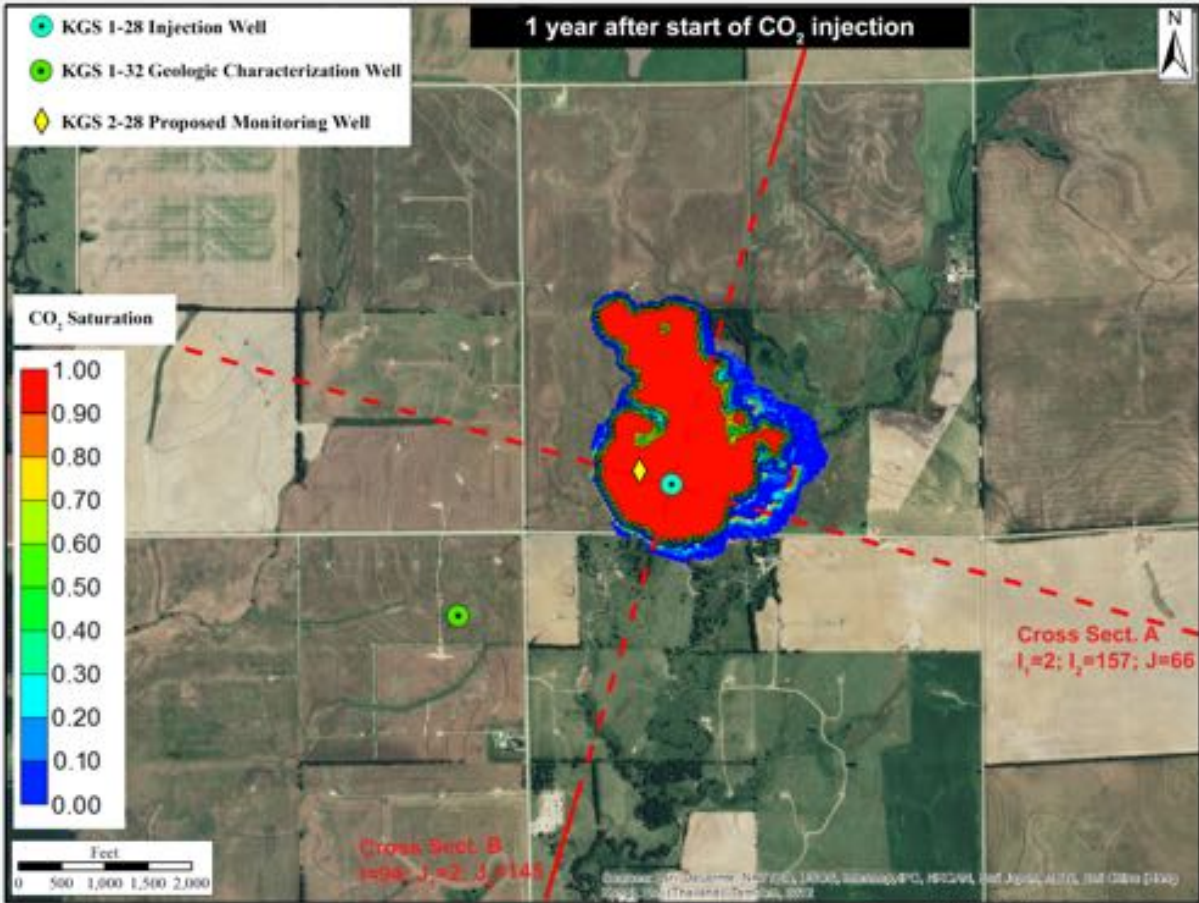
Figure 17b. Total CO₂ spatial distribution in aerial and cross-sectional view for the largest migration alternative model (k-1.25/phi-0.75) at nine months from start of injection. Injection stops at the end of this month.
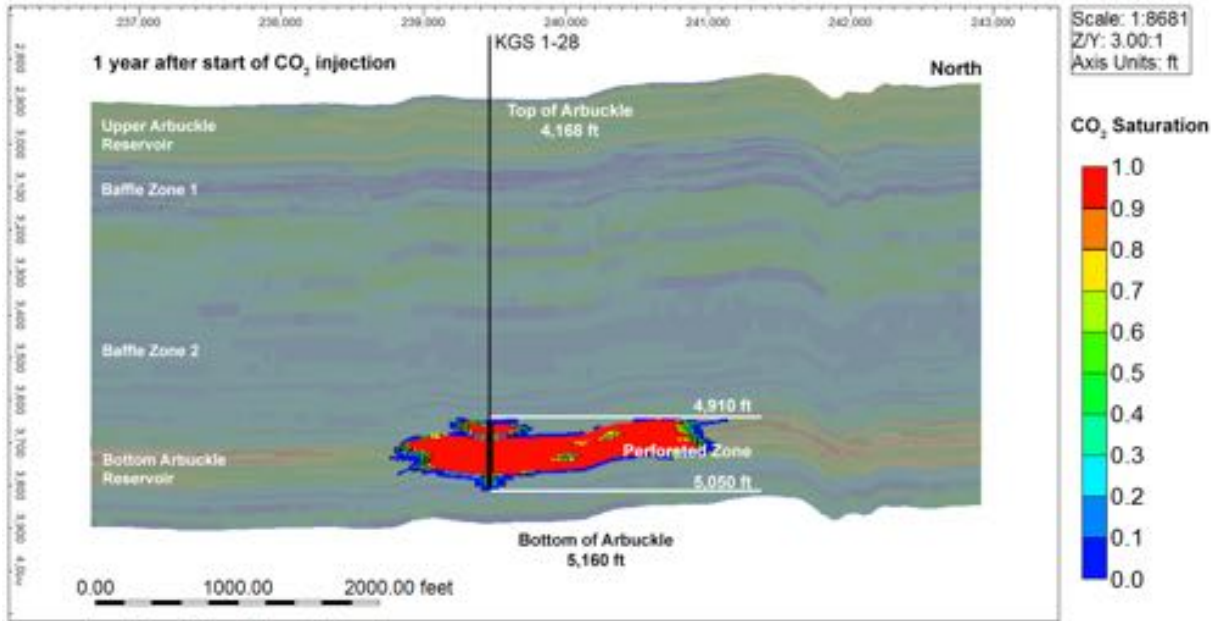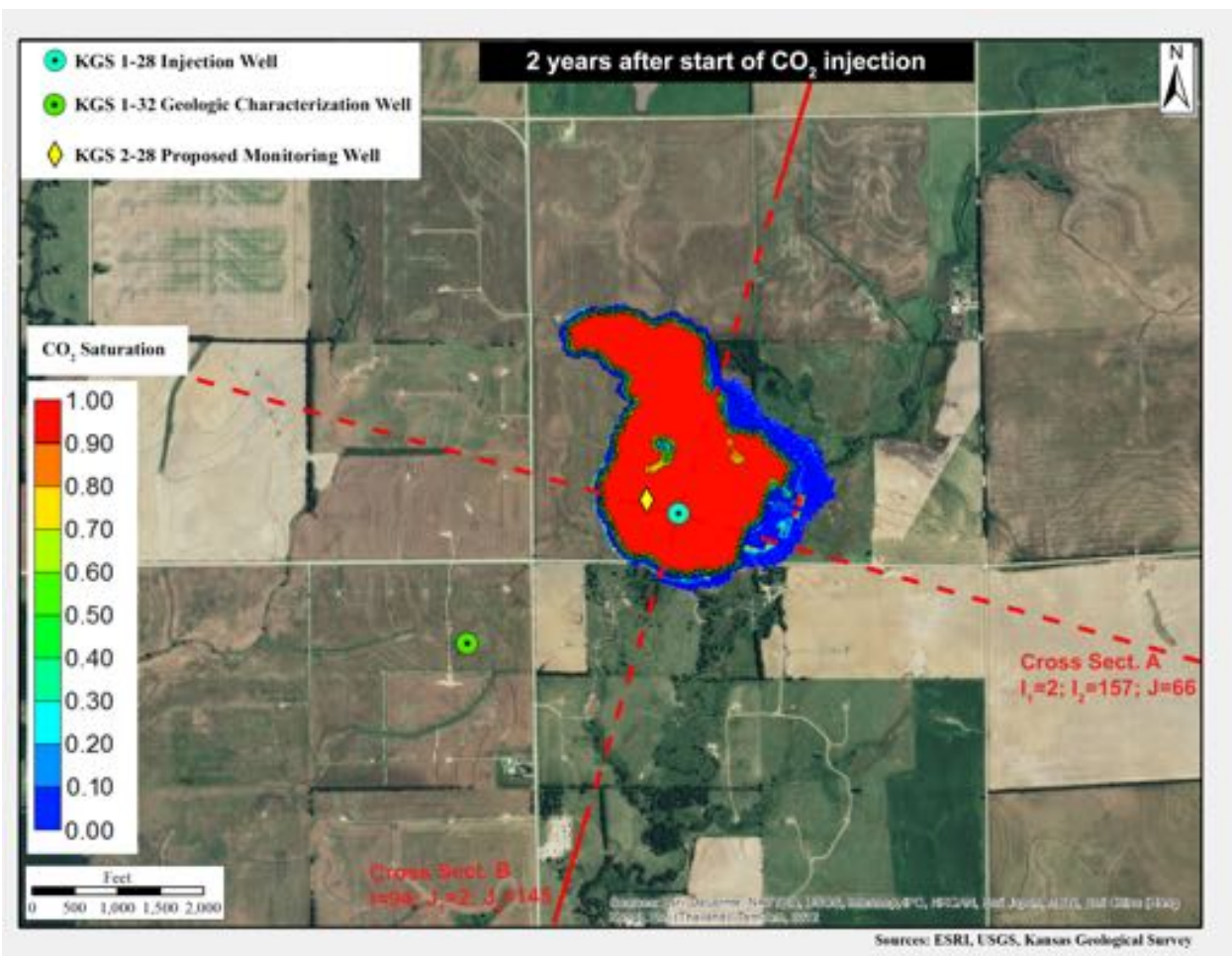
Figure 17c. Total CO$_2$ spatial distribution in aerial and cross-sectional view for the largest migration alternative model (k-1.25/phi-0.75) at one year from start of injection.

Figure 17d. Total CO₂ spatial distribution in aerial and cross-sectional view for the largest migration alternative model (k-1.25/phi-0.75) at two years from start of injection.

Figure 17e. Total CO$_2$ spatial distribution in aerial and cross-sectional view for the largest migration alternative model (k-1.25/phi-0.75) at 10 years from start of injection.

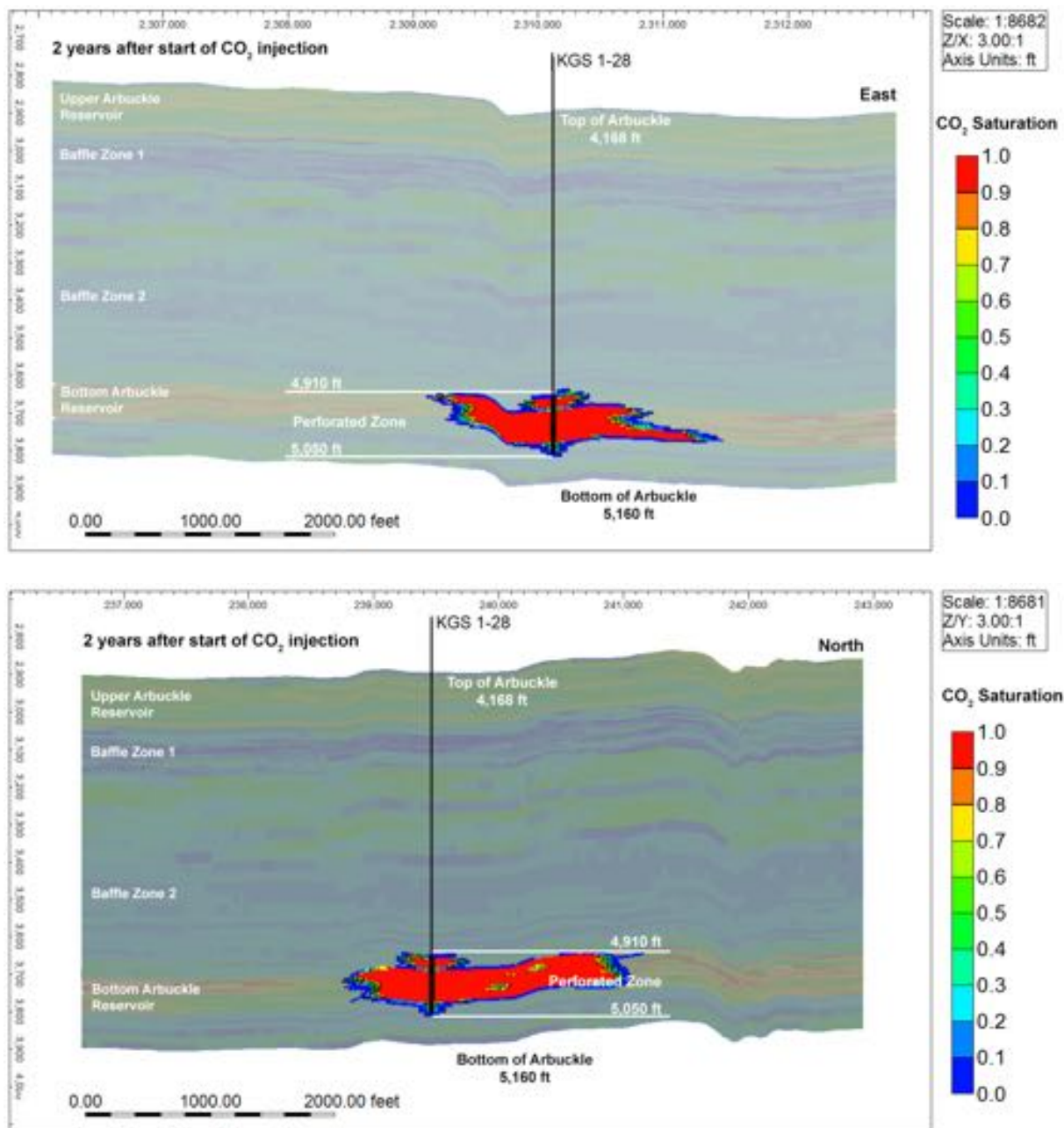*Figure 17f. Total CO_2 spatial distribution in aerial and cross-sectional view for the largest migration alternative model (k-1.25/phi-0.75) at 100 years from start of injection.*

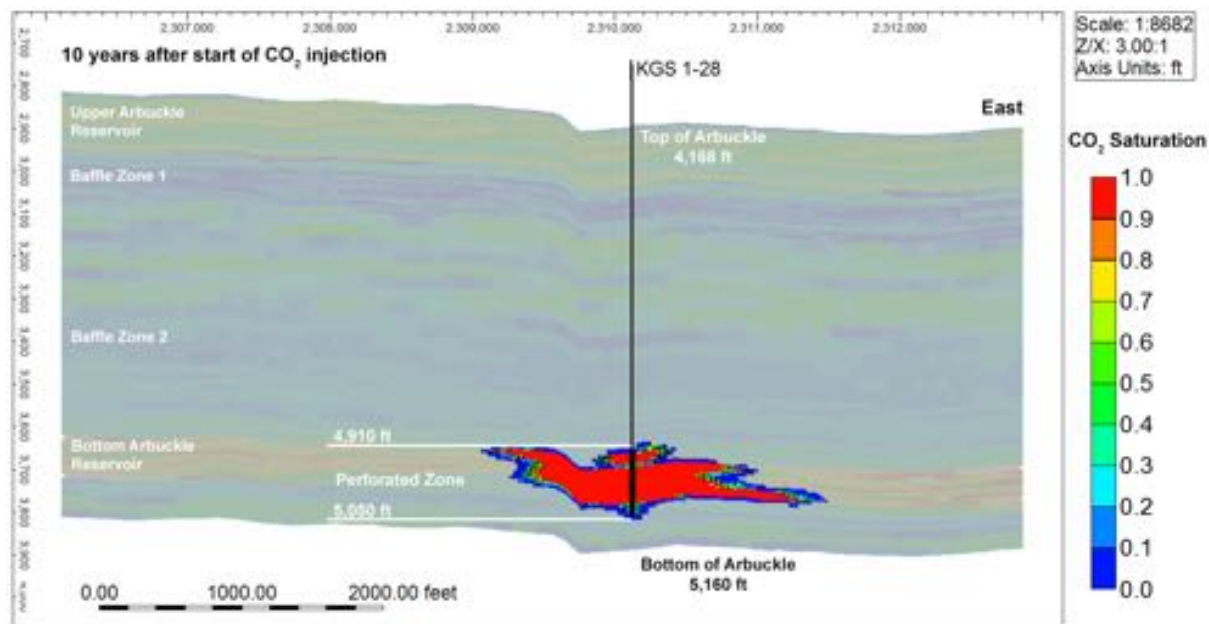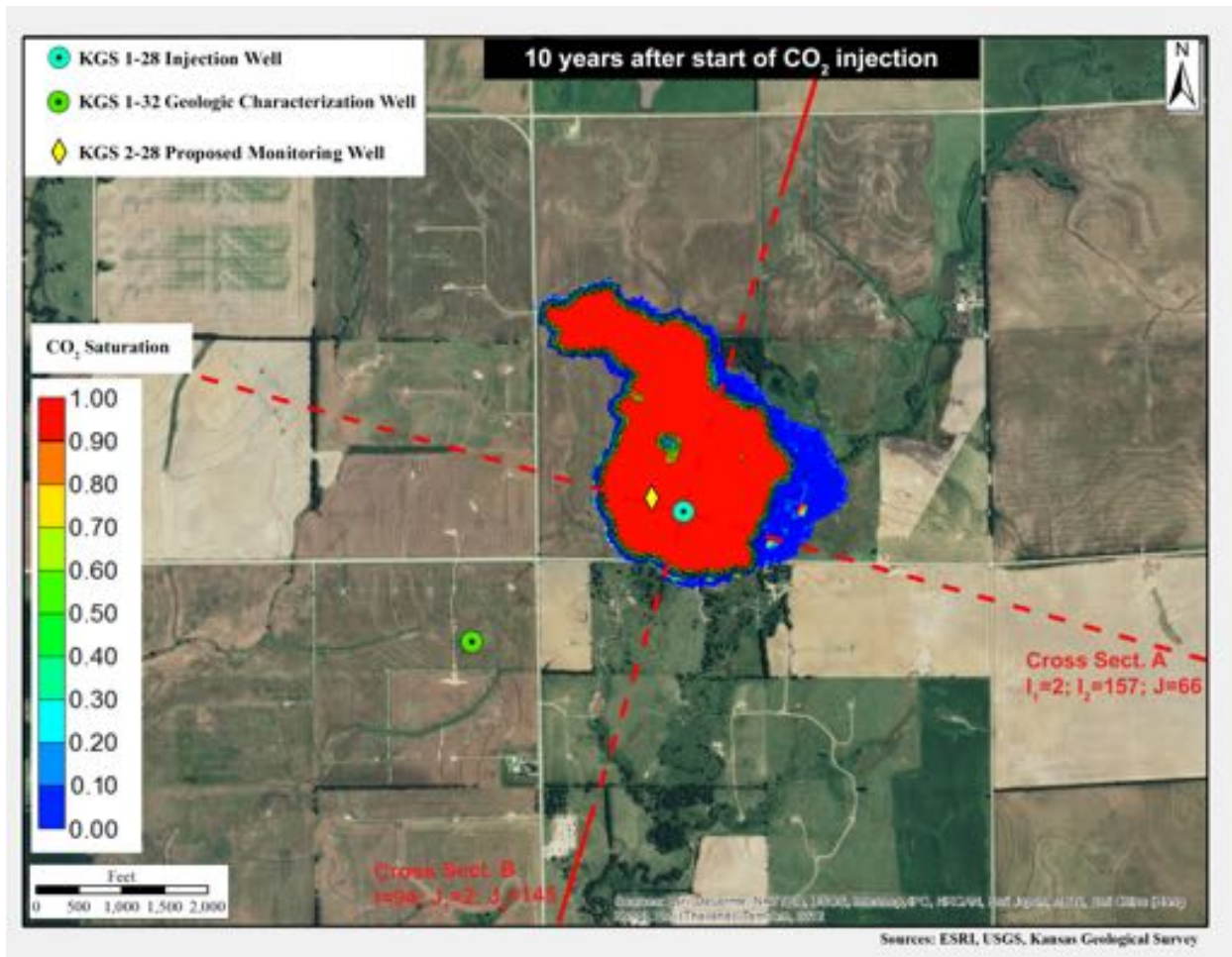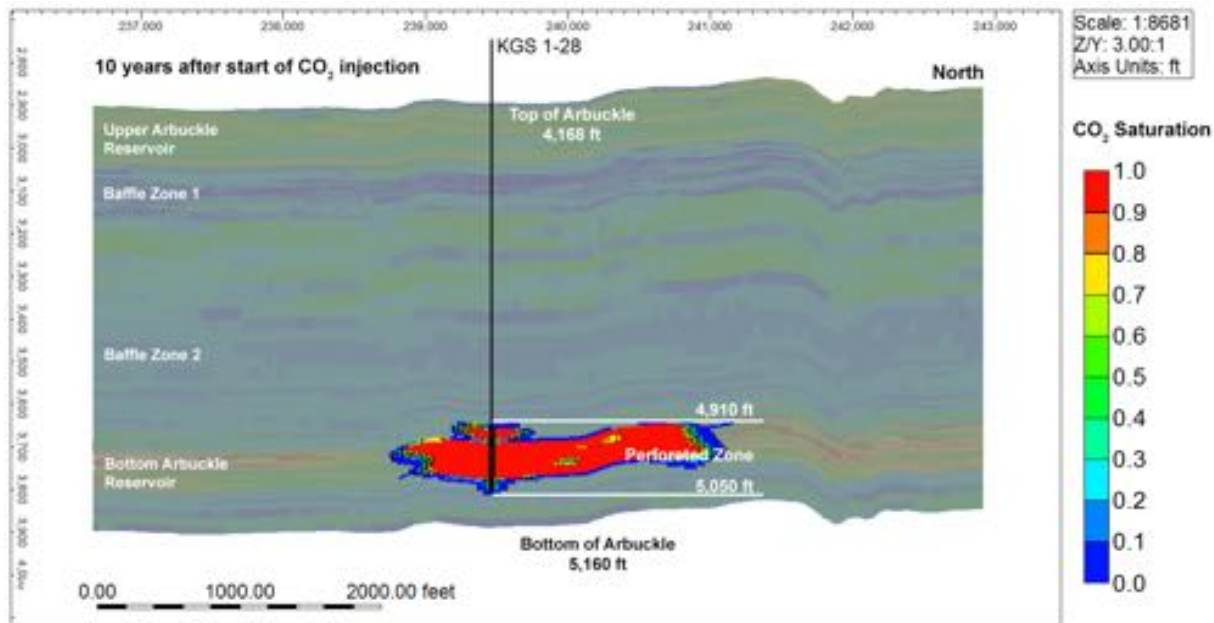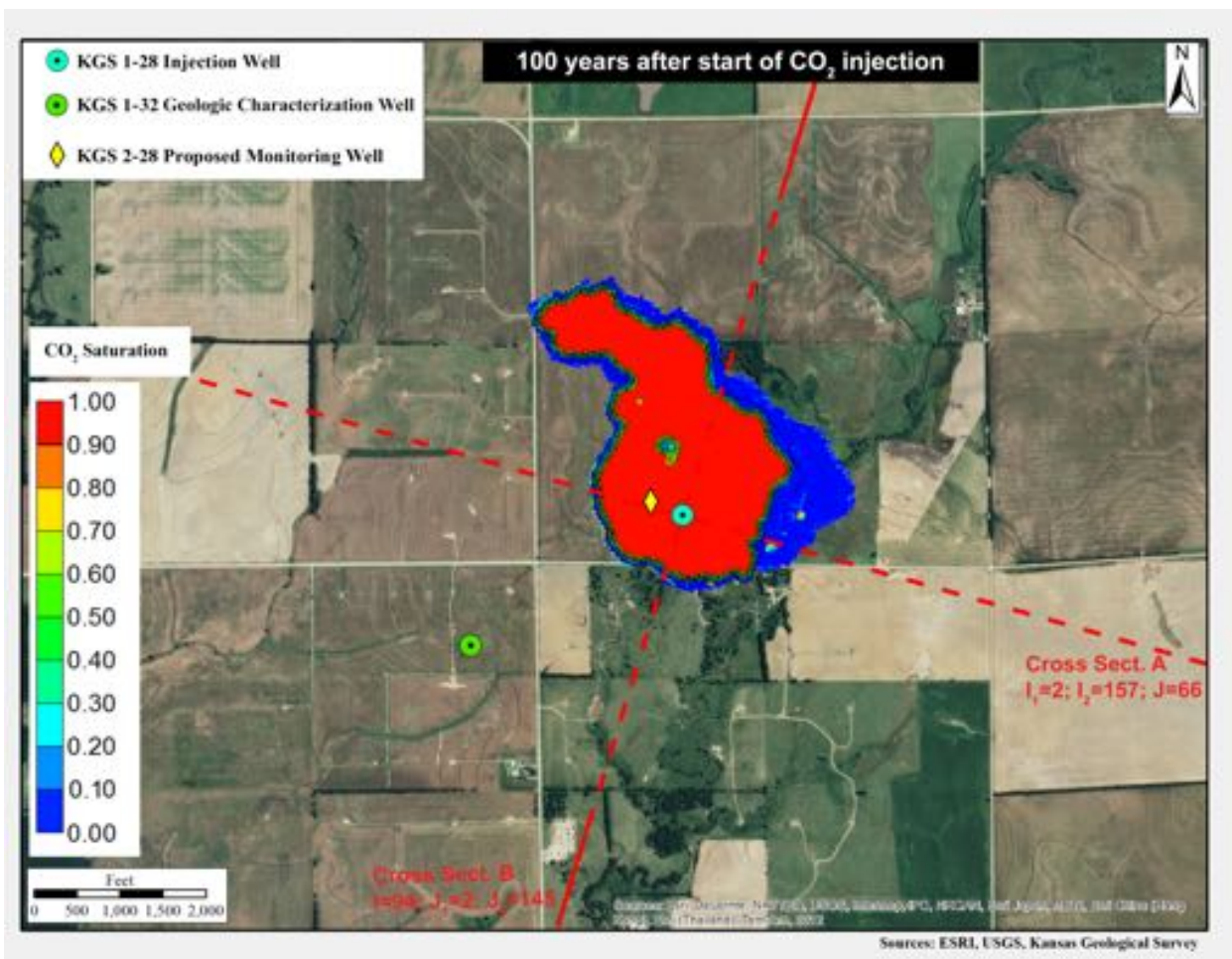6 months after start of CO_2 injection

CO₂ Saturation legend: 1.00, 0.90, 0.80, 0.70, 0.60, 0.50, 0.40, 0.30, 0.20, 0.10, 0.00

KGS 1-28 Injection Well
KGS 1-32 Geologic Characterization Well
KGS 2-28 Proposed Monitoring Well

Cross Sect. A
I₁=2; I₂=157; J=66

Cross Sect. B
I=98; J₁=2; J₂=145

Sources: ESRI, USGS, Kansas Geological Survey

6 months after start of CO_2 injection

Scale: 1:8682
Z/X: 3.00:1
Axis Units: ft

KGS 1-28

East

Upper Arbuckle Reservoir
Baffle Zone 1
Top of Arbuckle 4,168 ft
Baffle Zone 2
Bottom Arbuckle Reservoir
4,910 ft
Perforated Zone
5,050 ft
Bottom of Arbuckle 5,160 ft

CO₂ Saturation: 1.0, 0.9, 0.8, 0.7, 0.6, 0.5, 0.4, 0.3, 0.2, 0.1, 0.0

Figure 17g. Dissolved CO$_2$ spatial distribution in aerial and cross-sectional view for the largest migration alternative model (k-1.25/phi-0.75) at six months from start of injection.
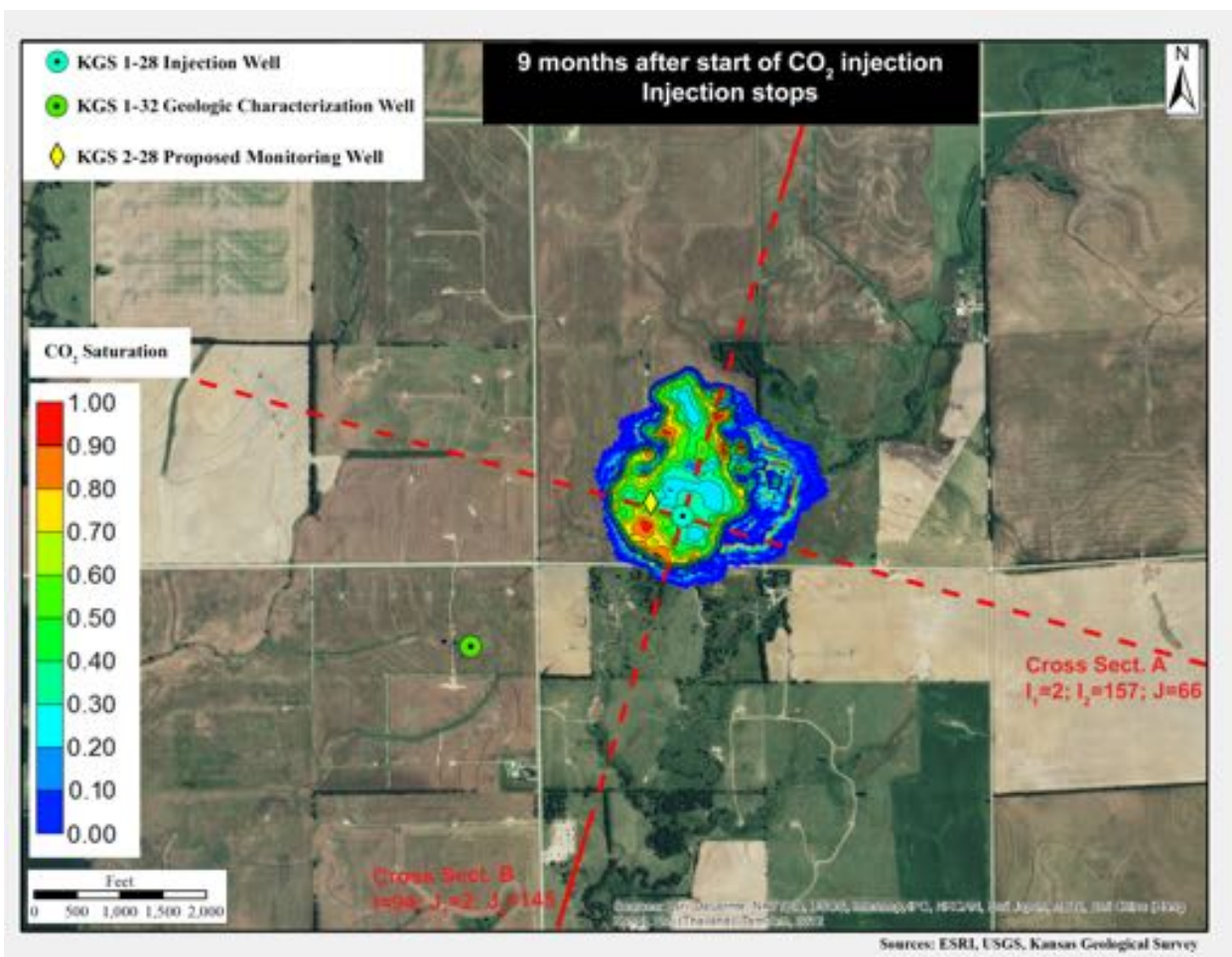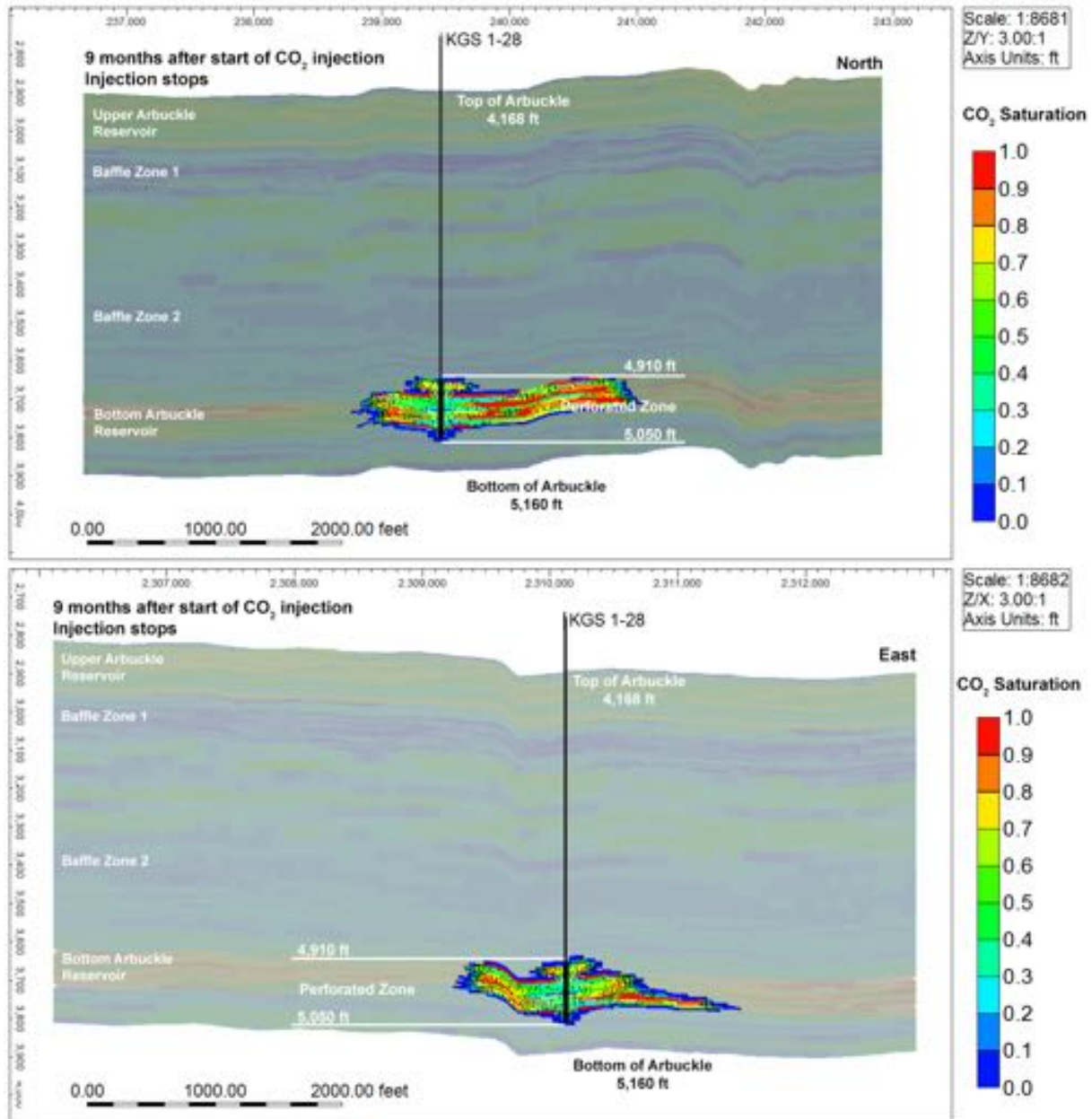
Figure 17h. Dissolved CO₂ spatial distribution in aerial and cross-sectional view for the largest migration alternative model (k-1.25/phi-0.75) at nine months from start of injection. Injection stops at the end of this month.
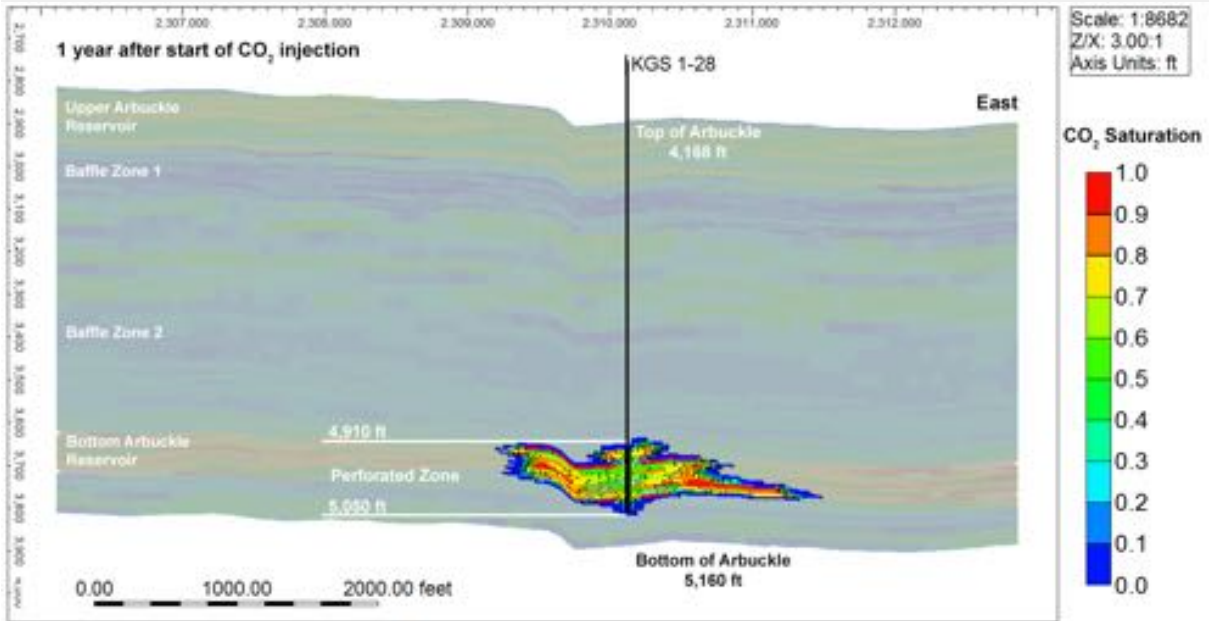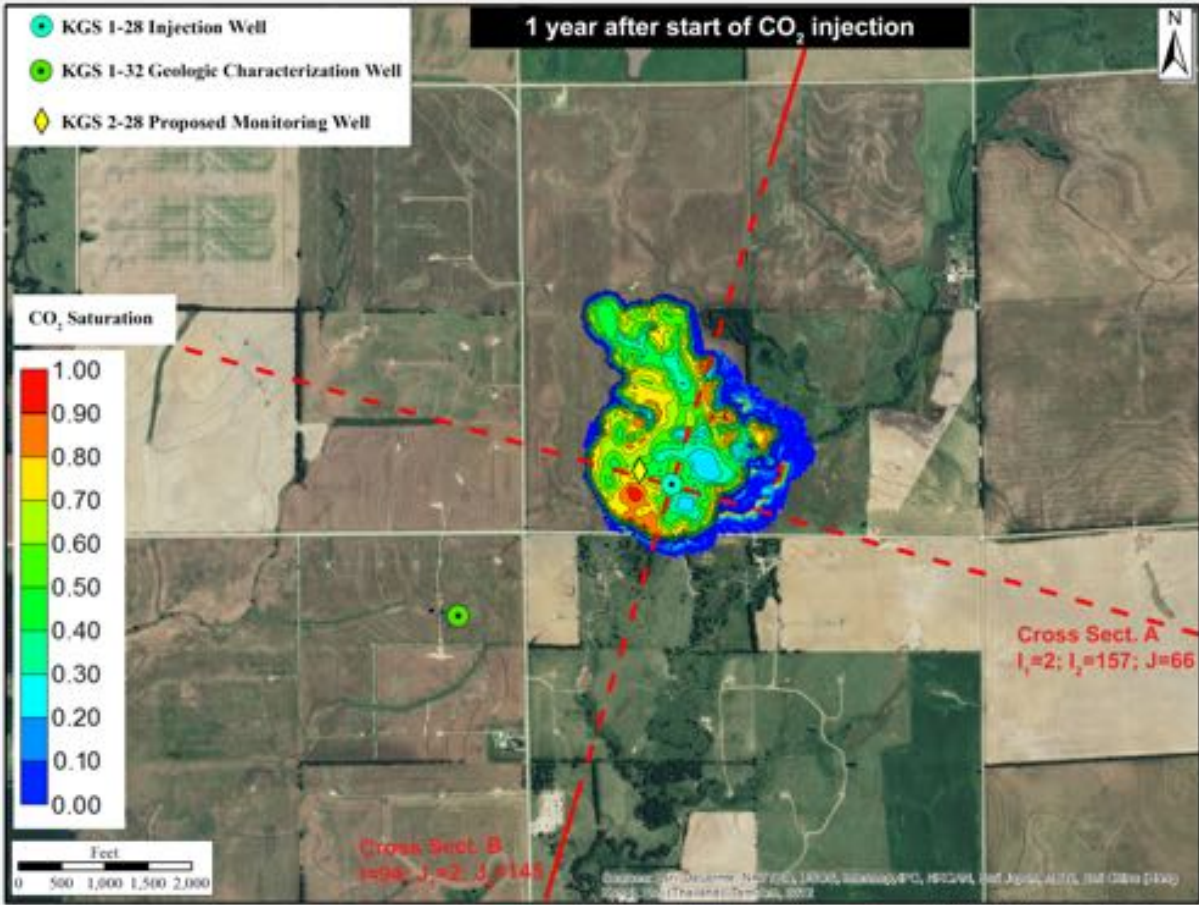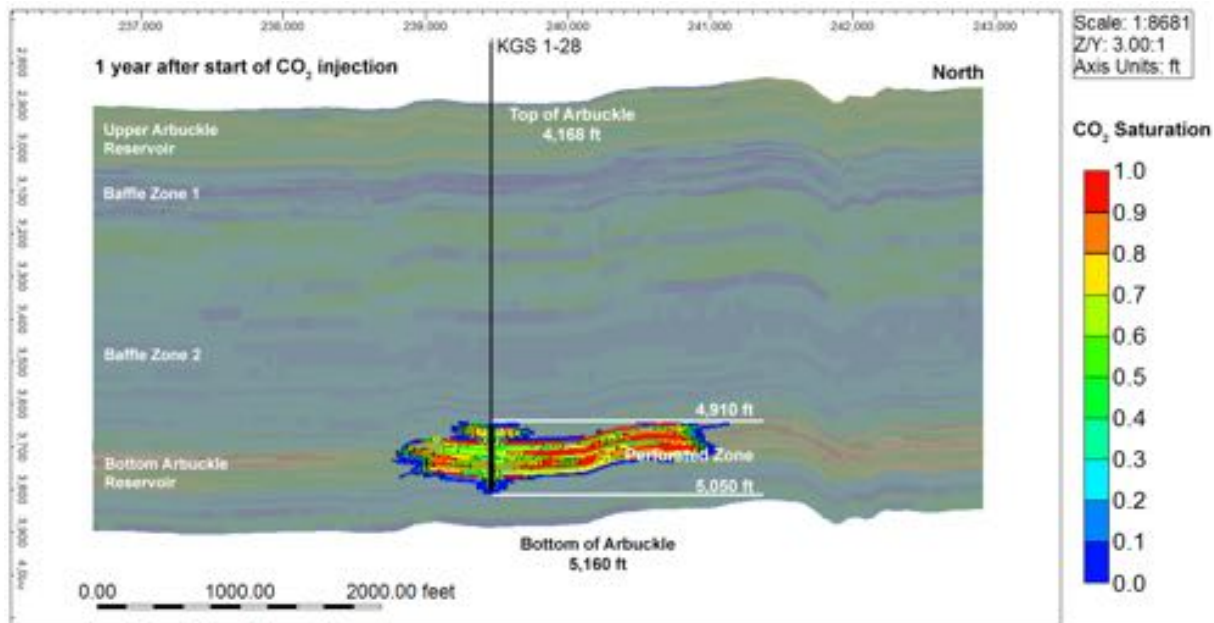
Figure 17i. Dissolved CO₂ spatial distribution in aerial and cross-sectional view for the largest migration alternative model (k-1.25/phi-0.75) at one year from start of injection.
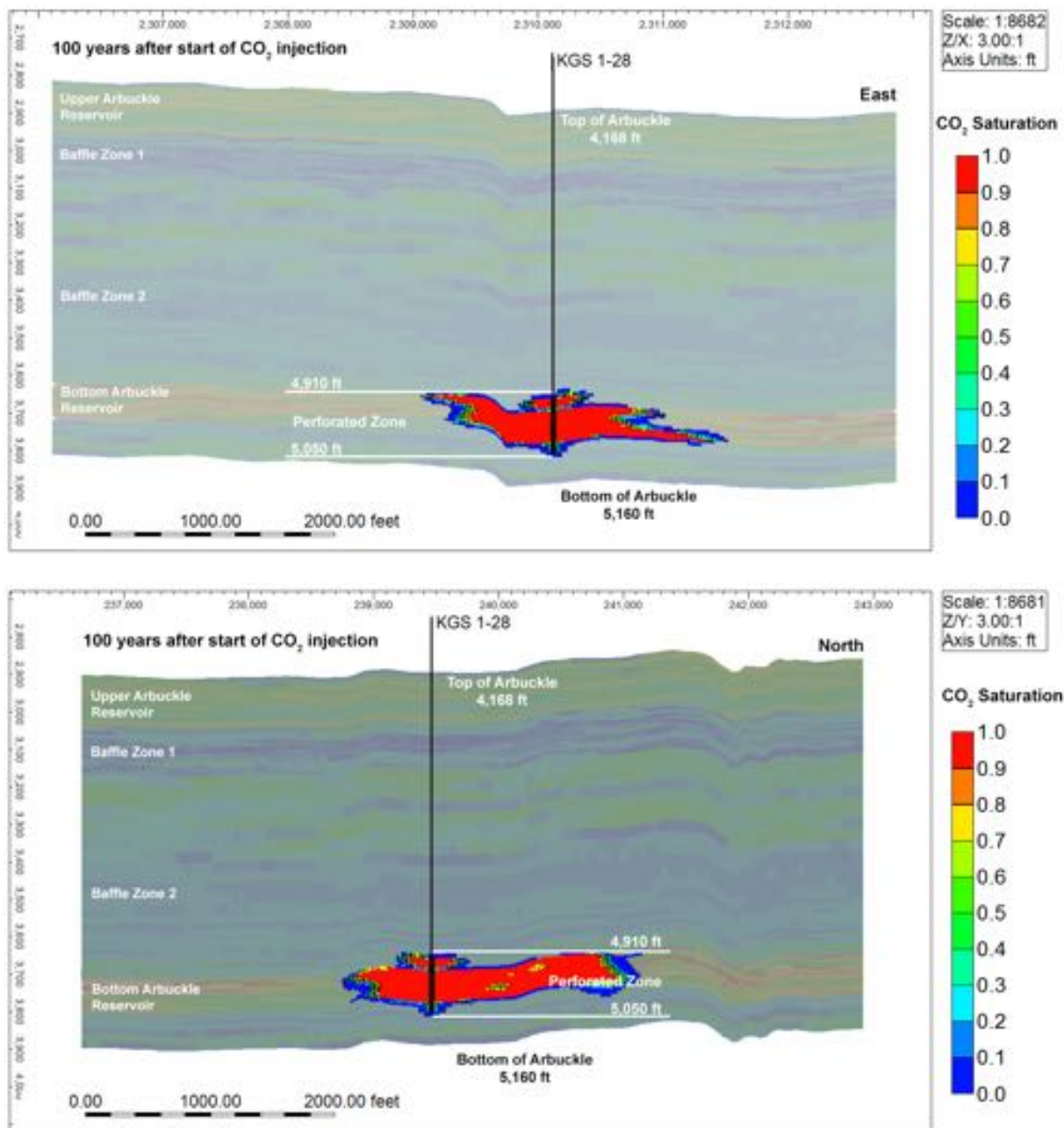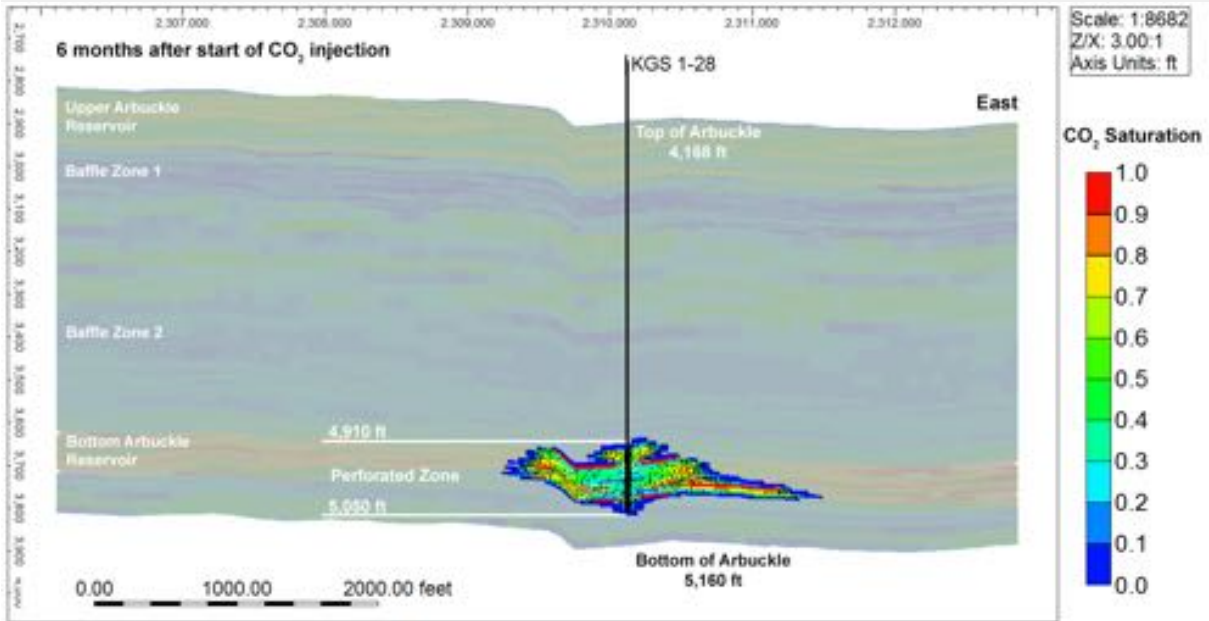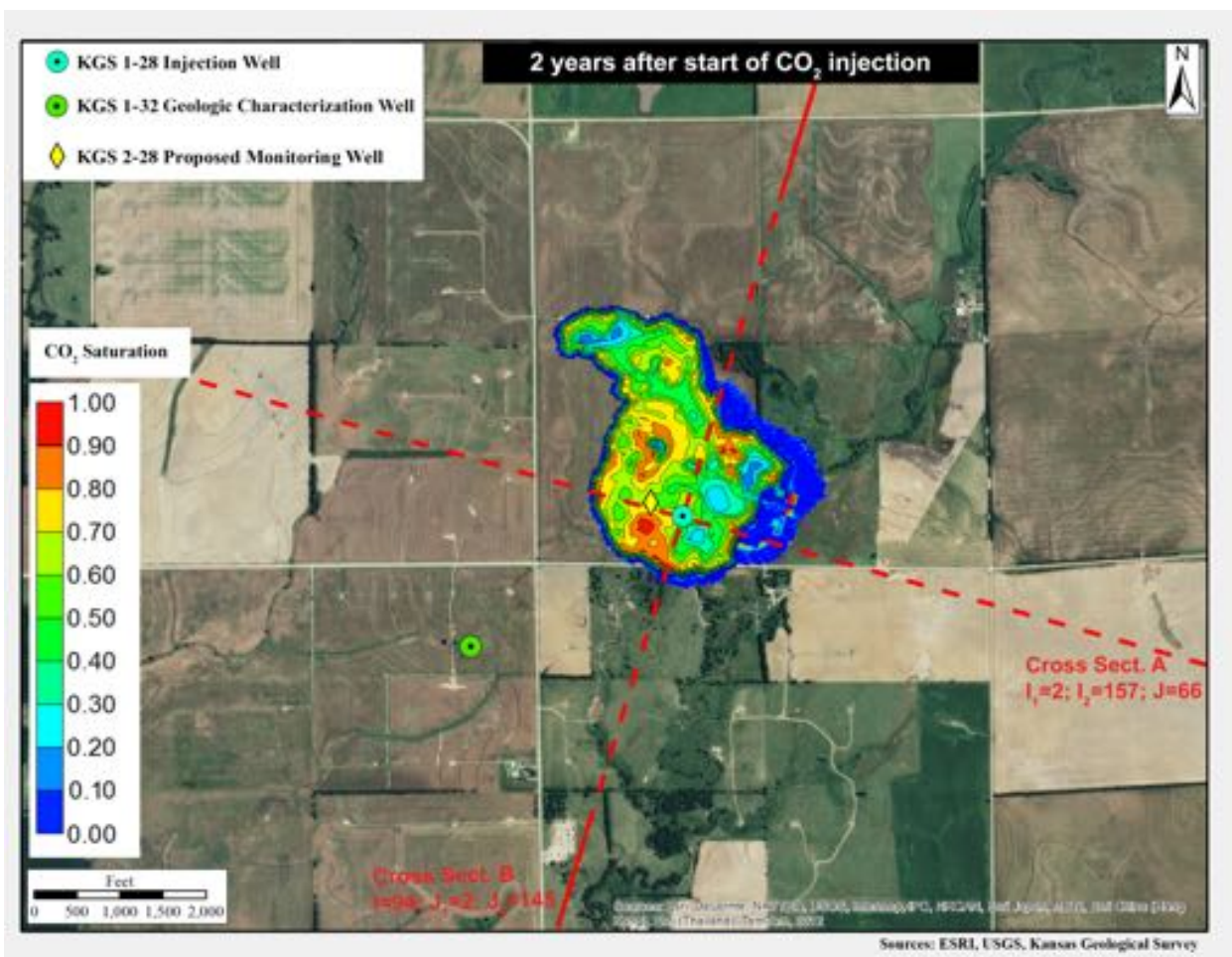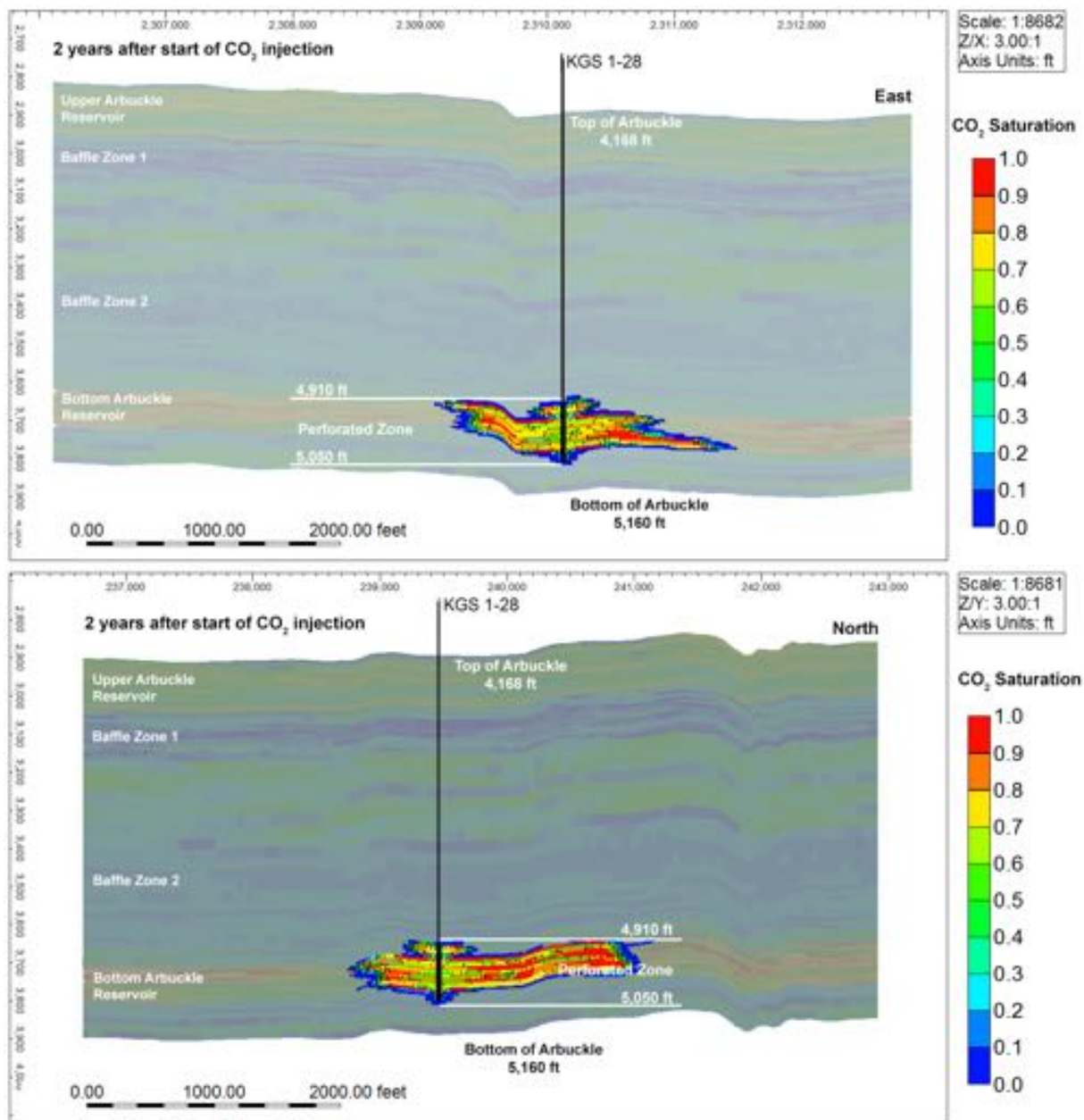
Figure 17j. Dissolved CO₂ spatial distribution in aerial and cross-sectional view for the largest migration alternative model (k-1.25/phi-0.75) at two years from start of injection.
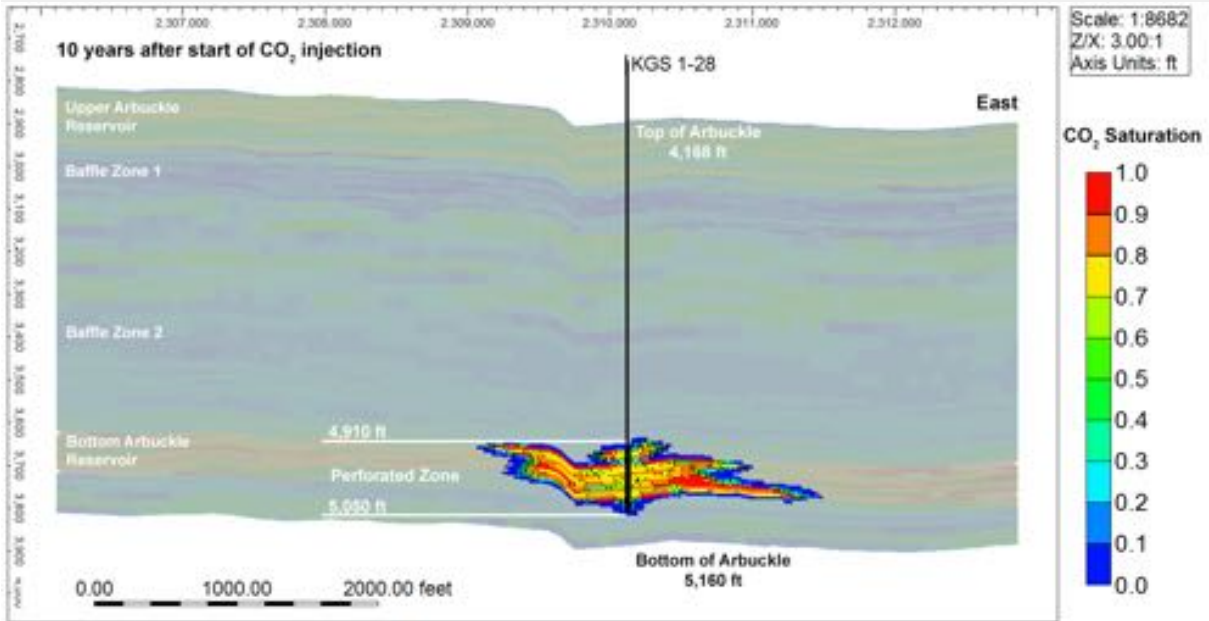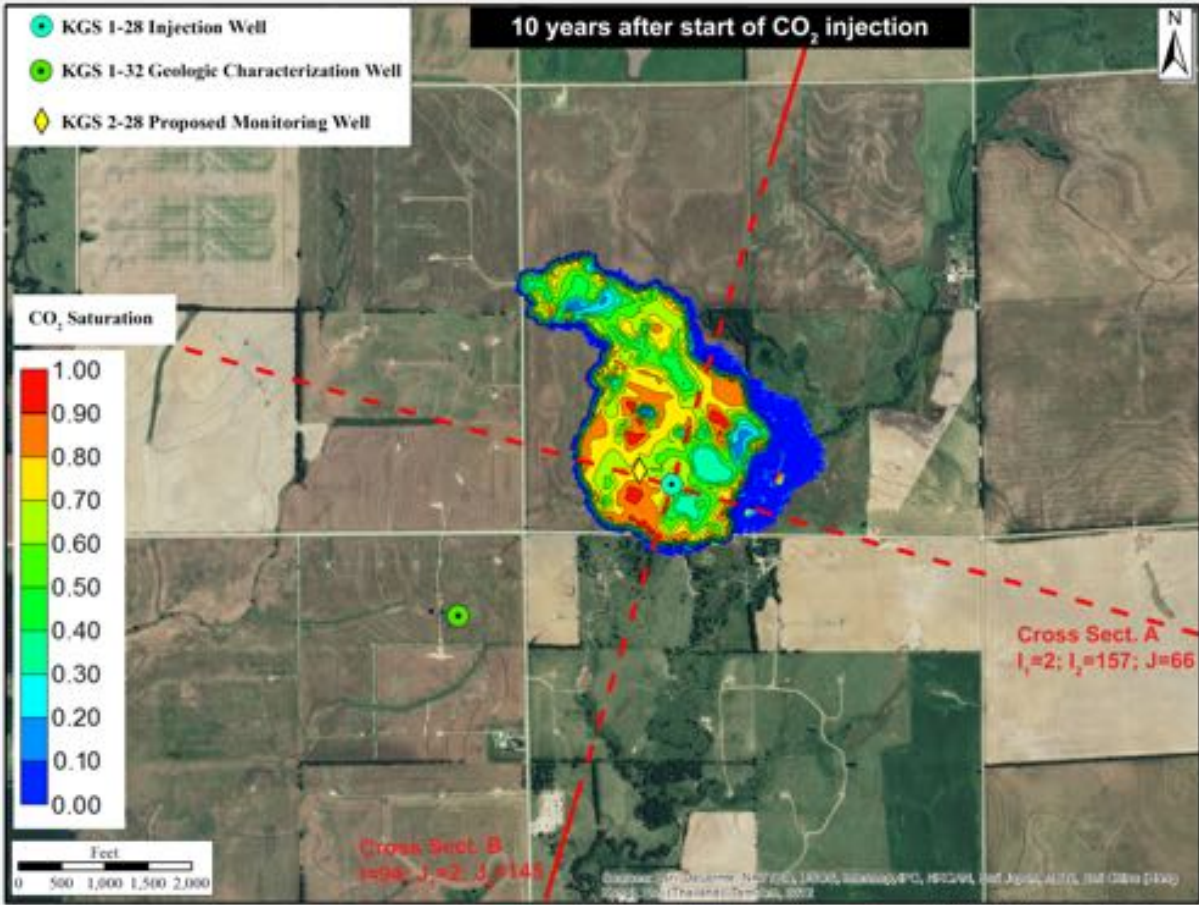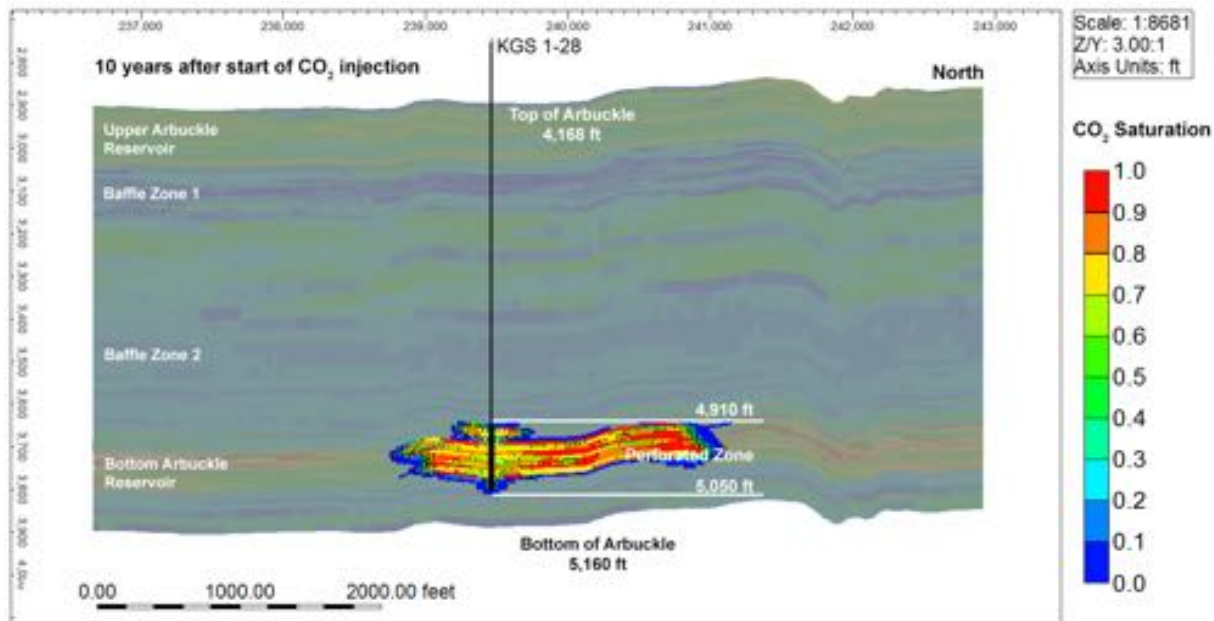
Figure 17k. Dissolved CO_2 spatial distribution in aerial and cross-sectional view for the largest migration alternative model (k-1.25/phi-0.75) at 10 years from start of injection.
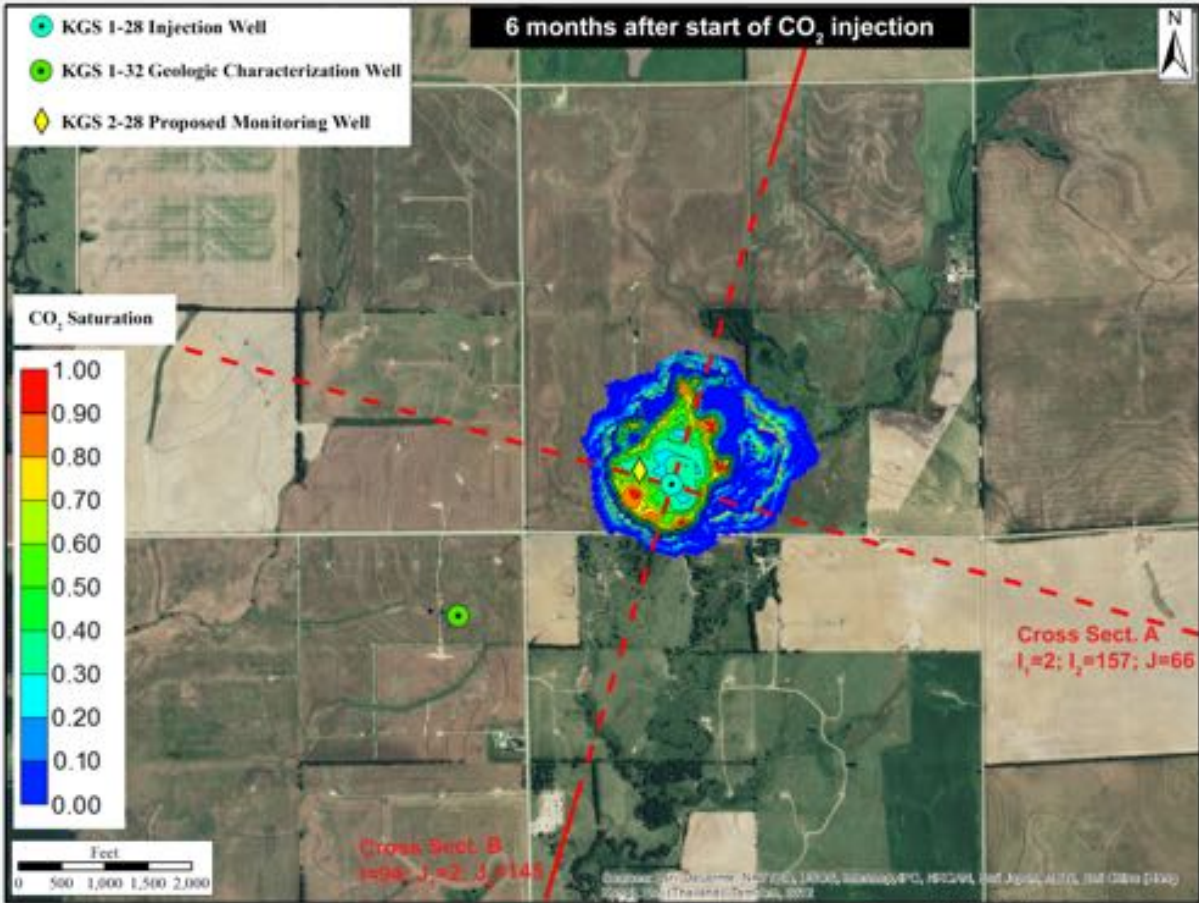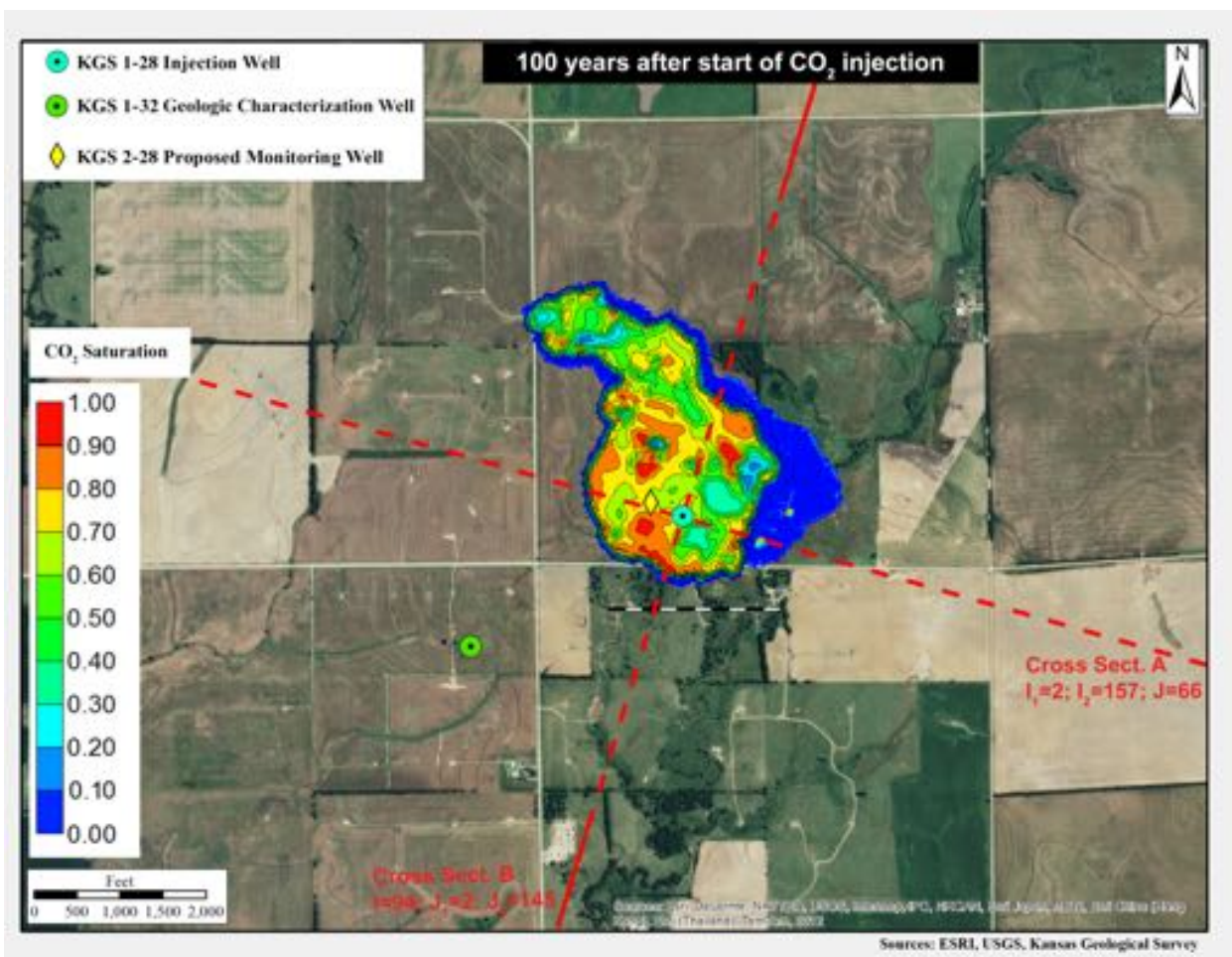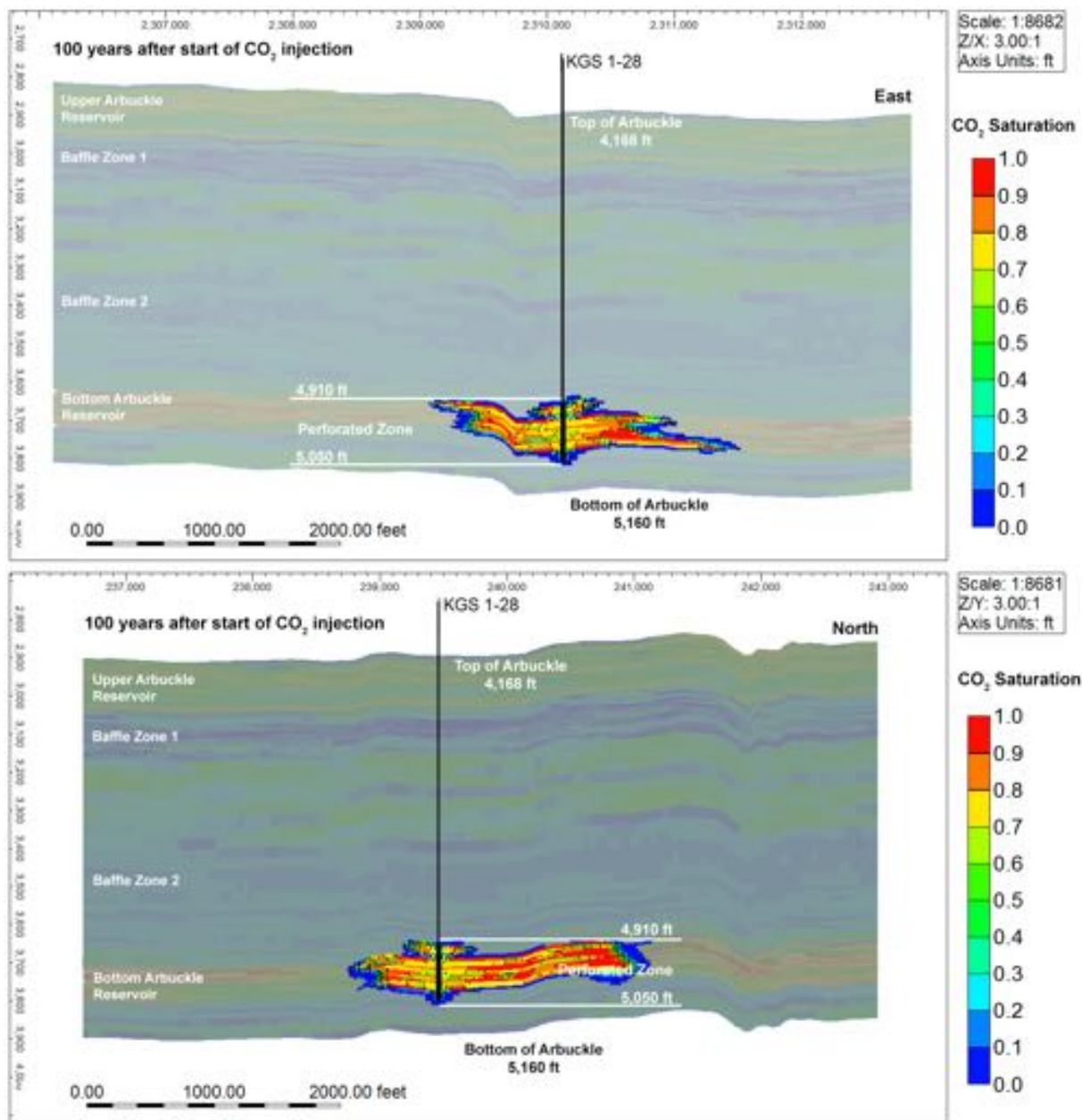
Figure 17l. Dissolved CO₂ spatial distribution in aerial and cross-sectional view for the largest migration alternative model (k-1.25/phi-0.75) at 100 years from start of injection.
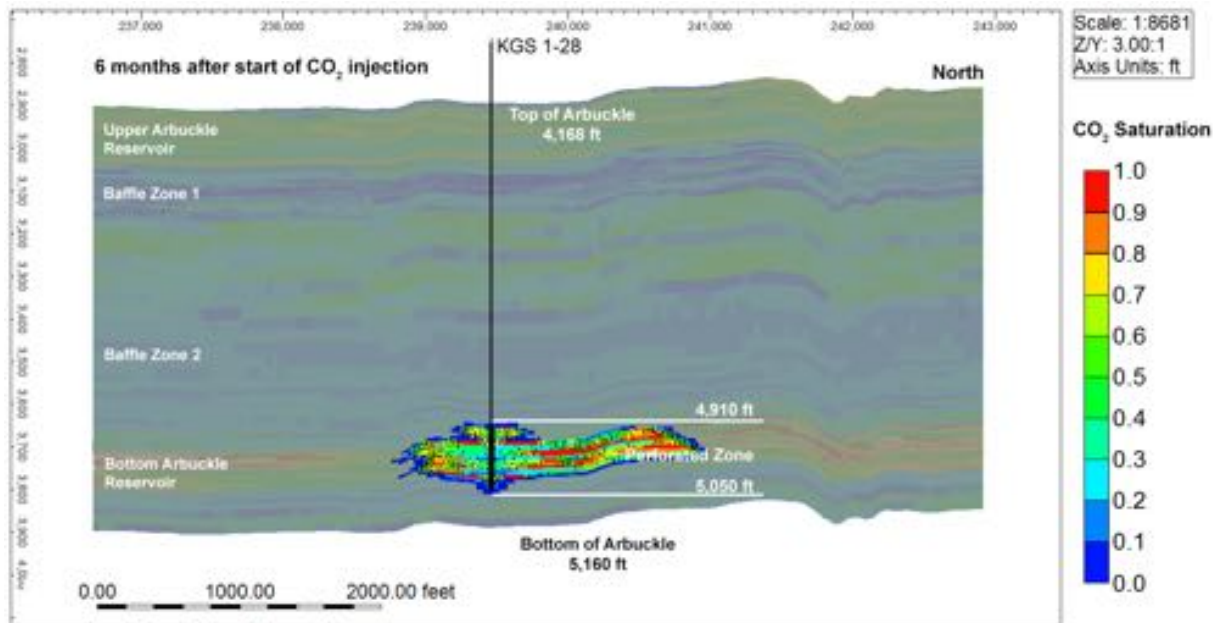
6.3   Simulated Pressure Distribution

Figure 18 presents the bottomhole pressure (at a reference depth of 5,050 ft) for the highest pressures alternative model (k-0.75/phi-0.75). The pressure increases to 2,485 psi upon commencement of injection and then gradually drops during the injection period as the capillary effects are overcome. The pressure decreases to pre-injection levels upon cessation of injection. The rise in pressure to 2,485 psi upon commencement of injection represents an increase of 392 psi

over pre-injection levels and results in a pressure gradient of 0.515 psi/ft, which is less than the maximum allowable pressure gradient of 0.675 psi/ft corresponding to 90% of the fracture gradient (0.75 psi/ft).
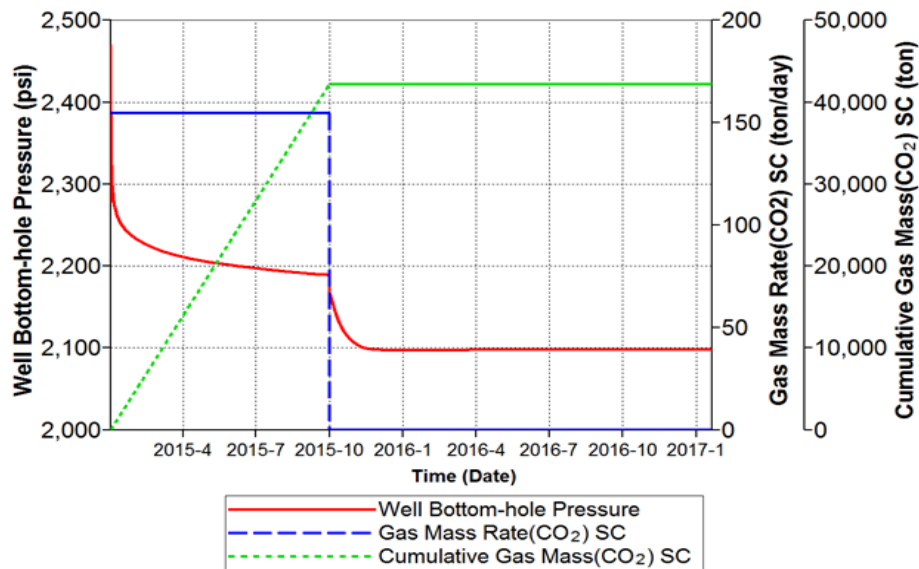
Figure 18. Maximum well bottomhole pressure at a depth of 5,050 ft for the minimum porosity and minimum permeability case (k-0.75/phi-0.75).

Figure 19 presents the change in pore pressure at the base of the confining zone (Simpson Group) for the k-0.75/phi-0.75 alternate model that resulted in the highest pressures. The maximum pressure increase at the end of the injection period of approximately 1.15 psi is fairly small and well below the entry pressure of 956 psi for the confining zone.

Figure 20a–e presents the lateral distribution of pressure in the Arbuckle injection interval (at an elevation of 4,960 ft) for the k-0.75/phi-0.75 case, which resulted in the maximum induced pore pressures. The pressures increase from commencement of injection to nine months and then drop significantly by the end of the first year (three months after operations stop). The pressures also drop very rapidly at short distances from the injection well at the end of the nine-month injection period, as shown in fig. 21. The pressures at the end of the nine-month injection period drop from about 120 psi a short distance from the injection well to less than 15 psi at the geologic characterization well, KGS 1-32, which is approximately 3,500 ft southwest of the injection well. The maximum induced pressure at the model boundary is only 7–12 psi.

Figure 21a–e also shows the vertical pressure distribution for the maximum induced

pressure case (k-0.75/phi-0.75). The confining effect of the mid-Arbuckle baffle zones is evident in the plots as the large pressure increases are mostly restricted to the injection interval. The pressures decline rapidly at a short distance from the injection well. The pressures throughout the model subside to nearly pre-injection levels soon after injection stops, as shown in the one-year pressure plot in fig. 20e.
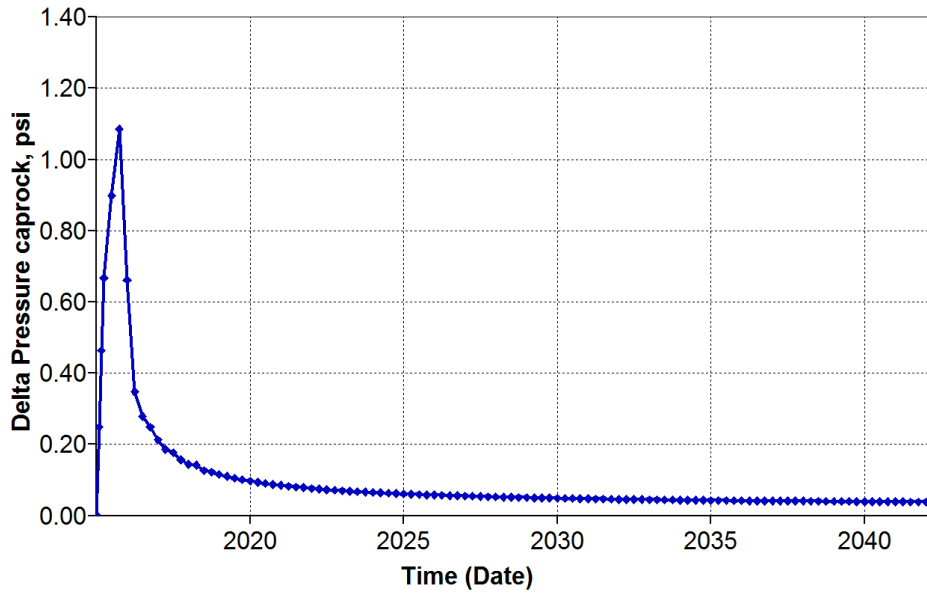
Figure 19. Change in pore pressure at the base of the confining zone (i.e., base of Simpson Group) at the injection well site for the maximum induced pressure (k-0.75/phi-0.75).
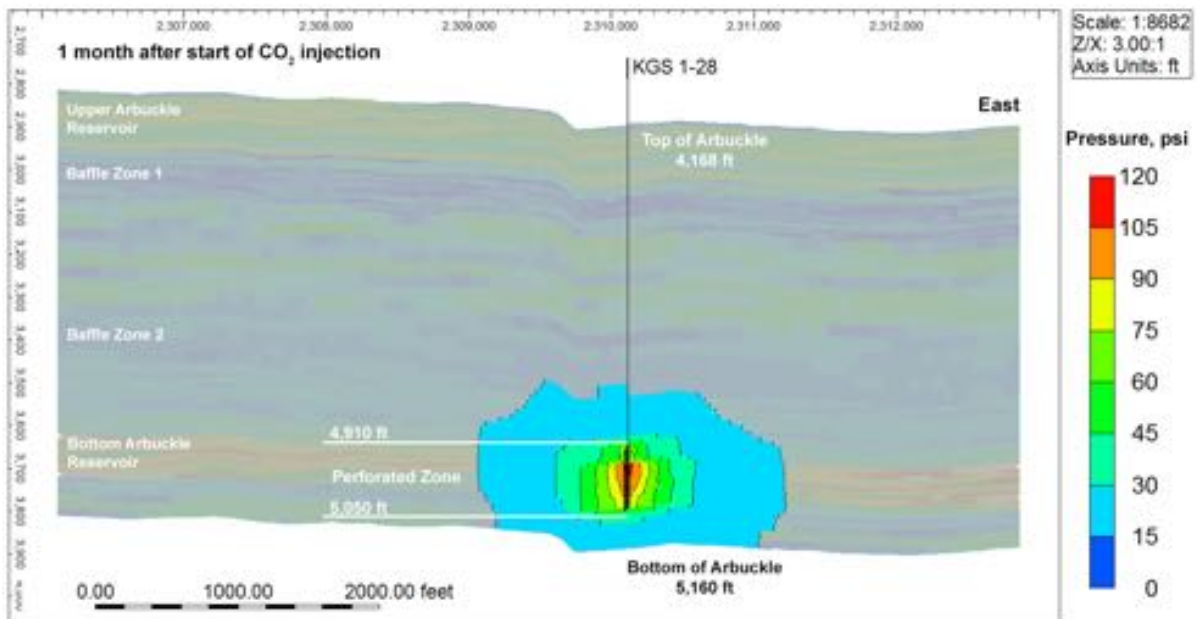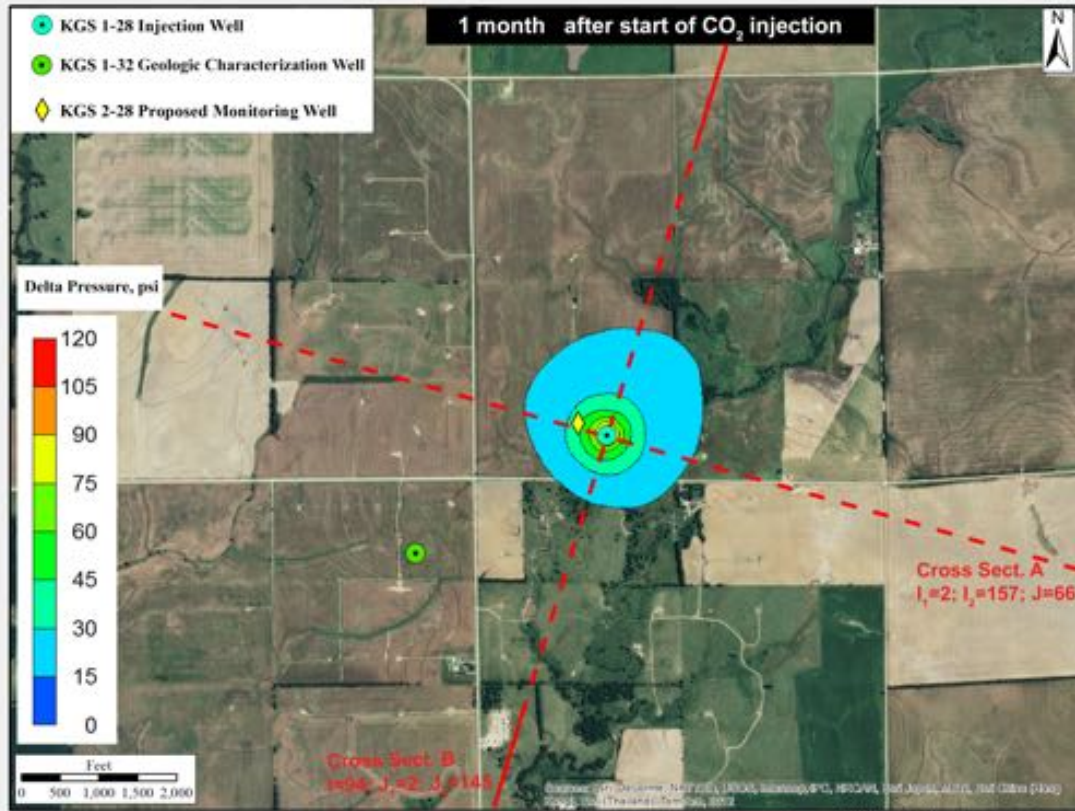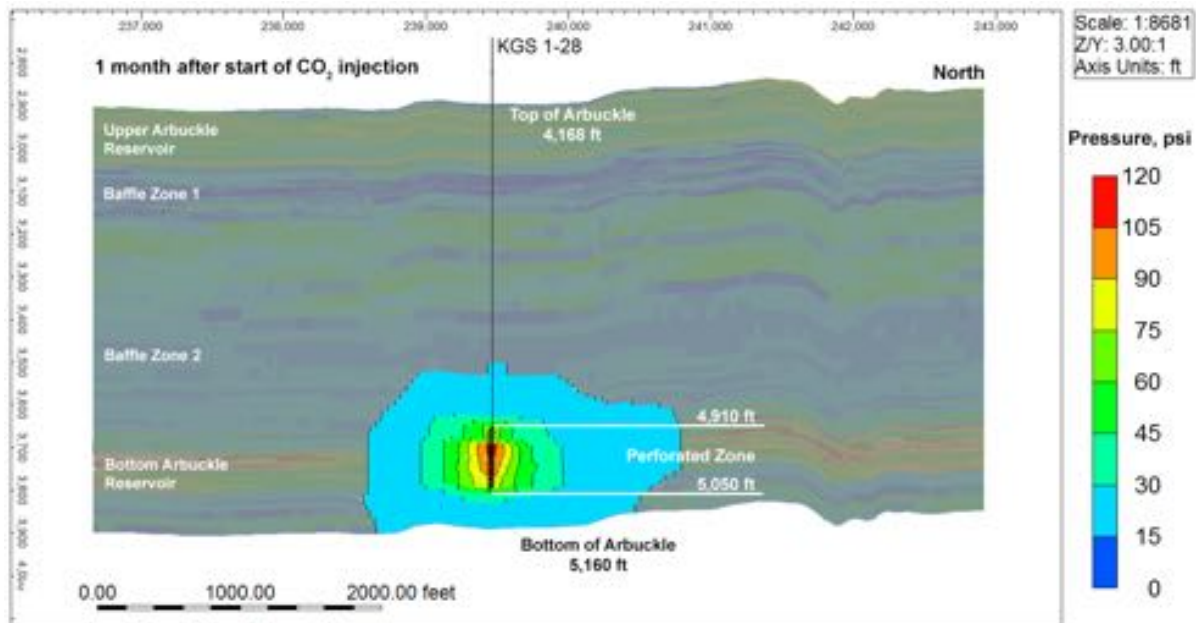
Figure 20a. Simulated increase in pressure in aerial and cross-sectional view at one month from start of injection for the low permeability–low porosity (k-0.75/phi-0.75) alternative case, which resulted in the largest simulated pressures.
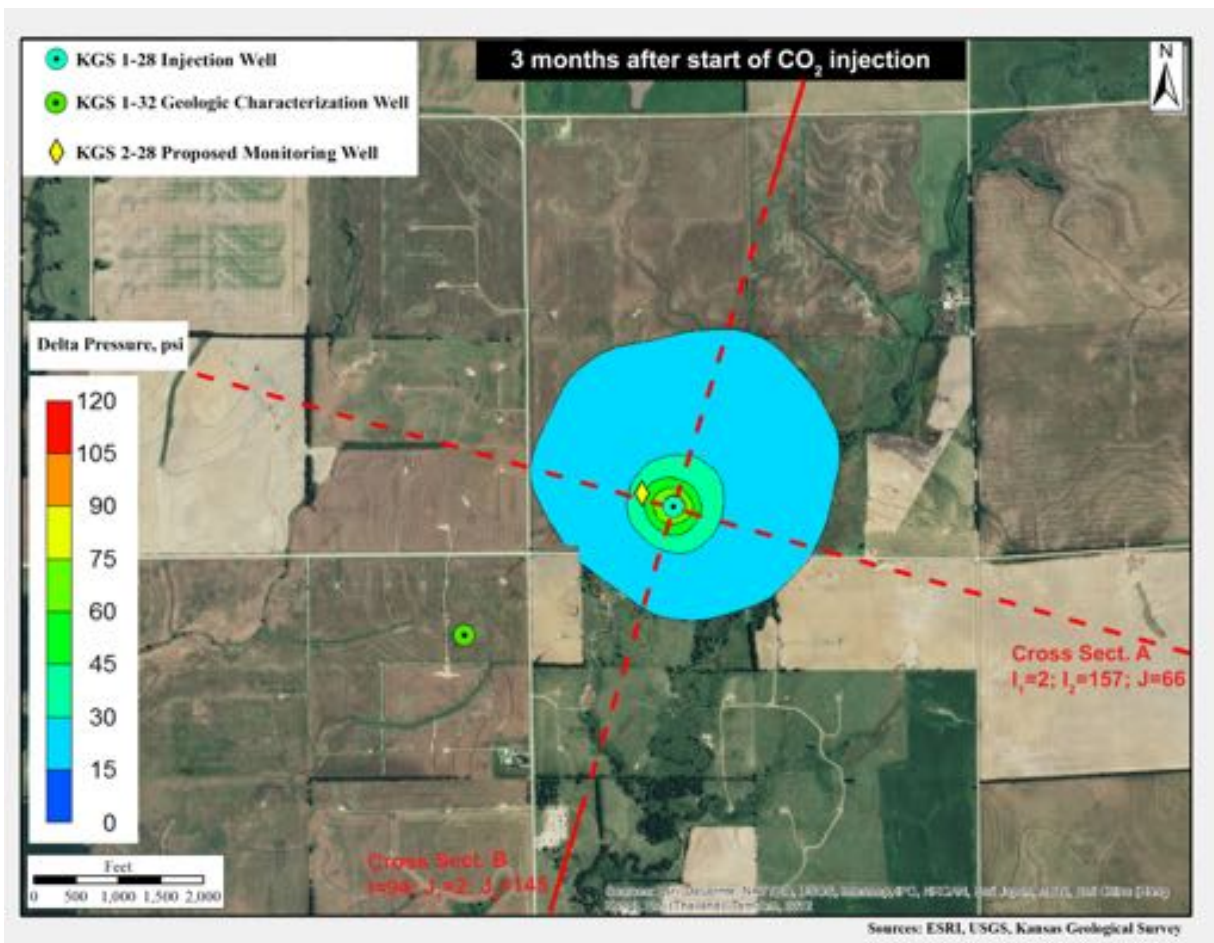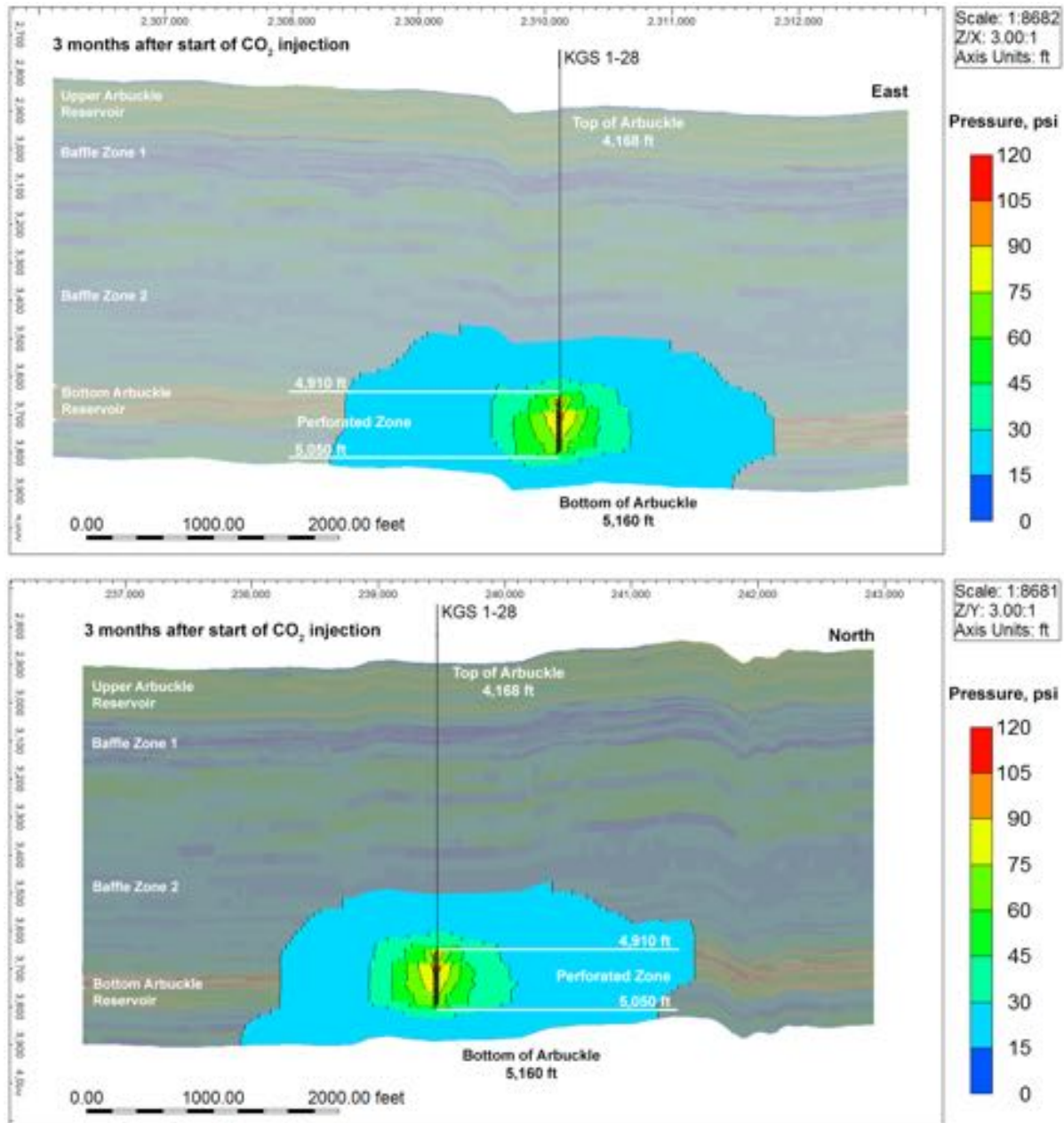
Figure 20b. Simulated increase in pressure in aerial and cross-sectional view at three months from start of injection for the low permeability–low porosity (k-0.75/phi-0.75) alternative case, which resulted in the largest simulated pressures.

6 months after start of CO_2 injection

6 months after start of CO_2 injection
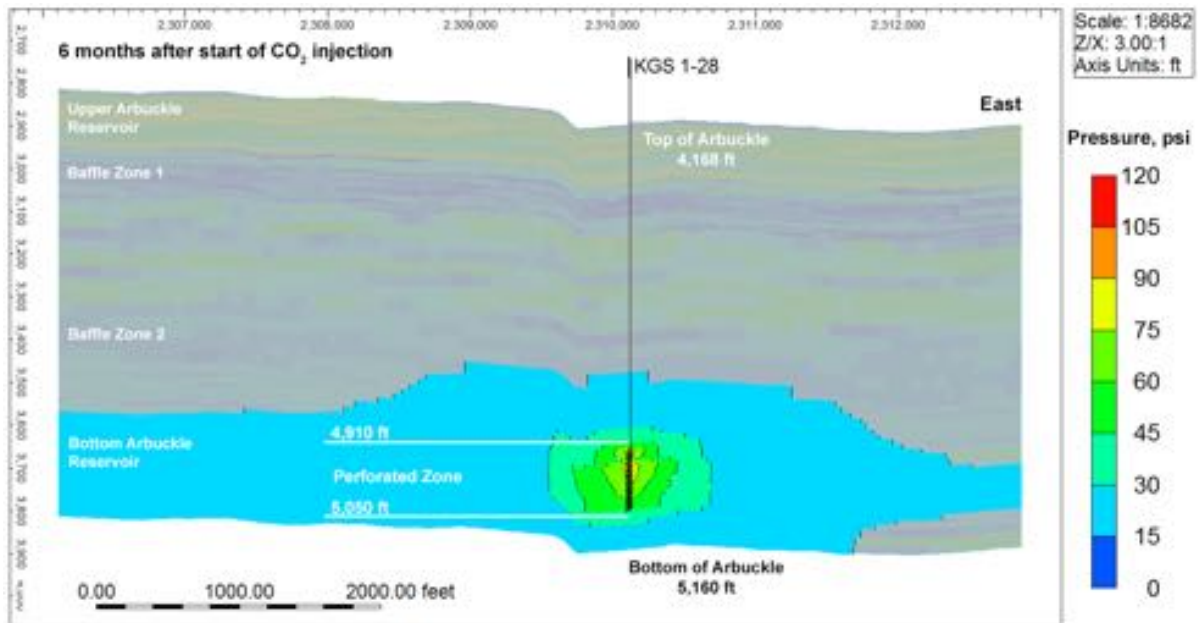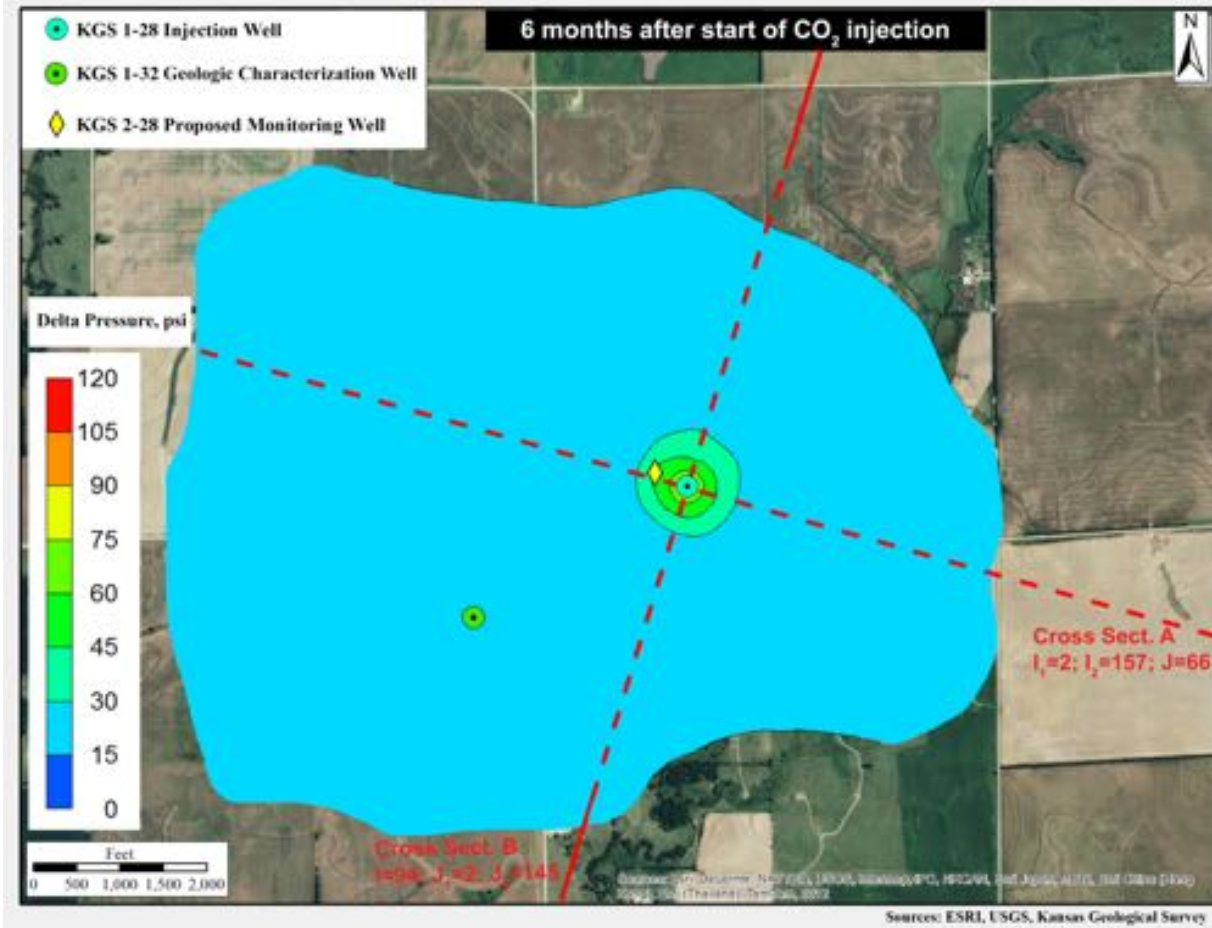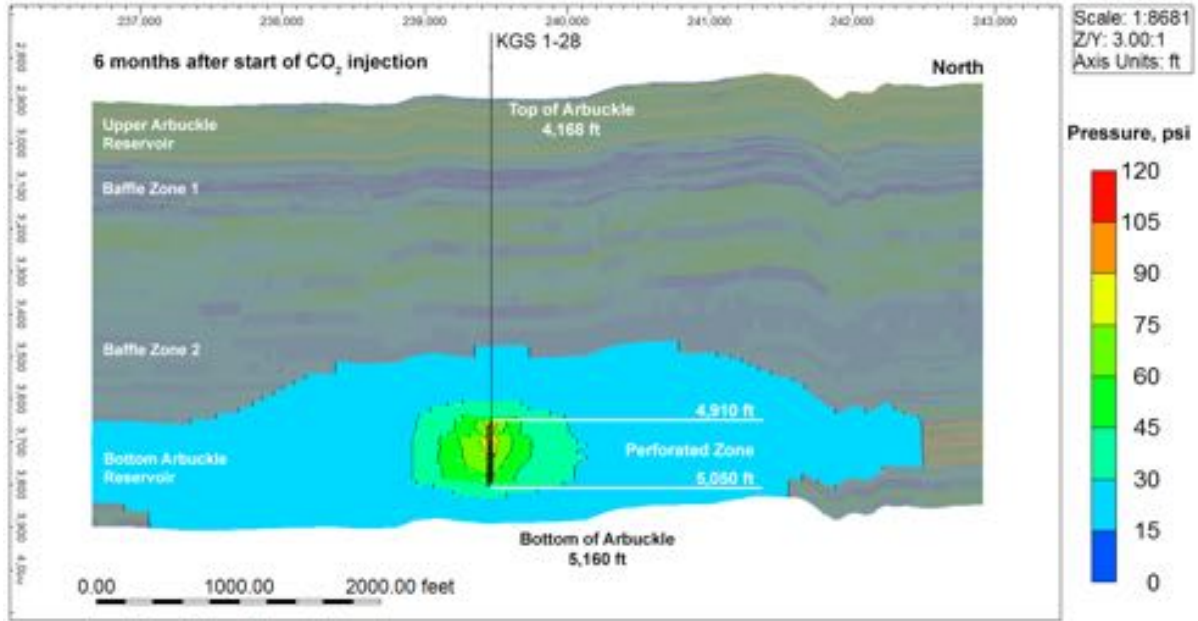
Figure 20c. Simulated increase in pressure in aerial and cross-sectional view at six months from start of injection for the low permeability–low porosity (k-0.75/phi-0.75) alternative case, which resulted in the largest simulated pressures.
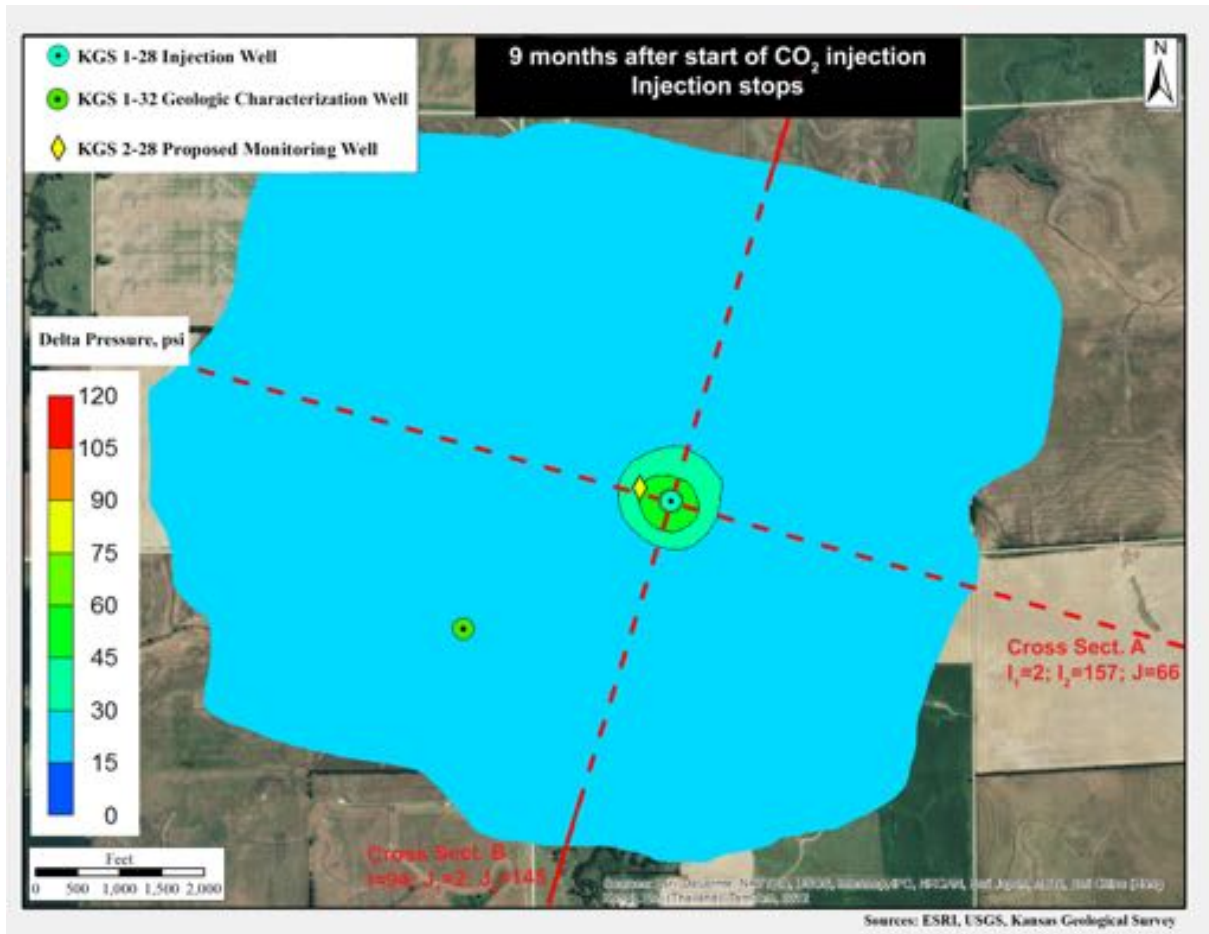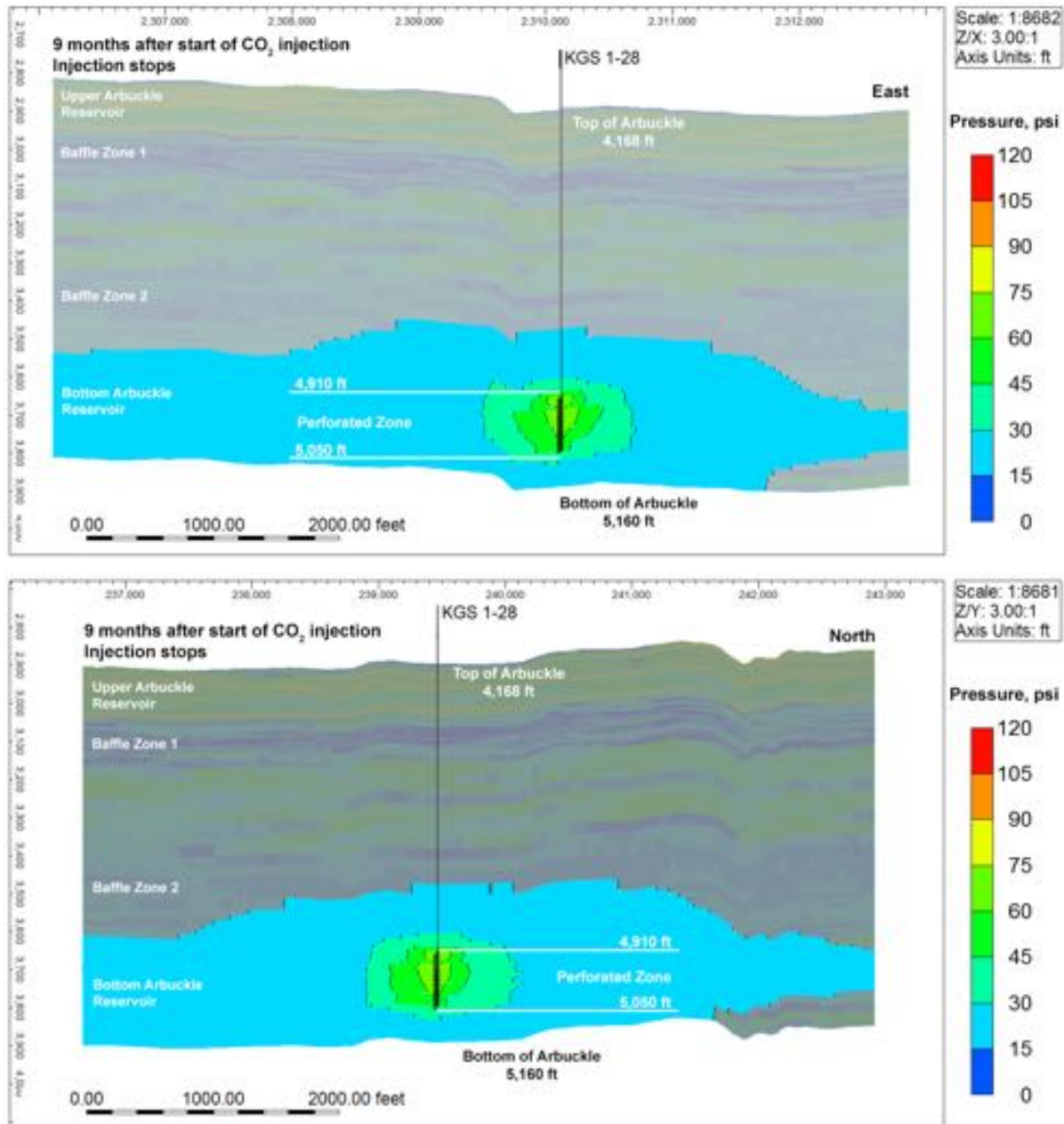
Figure 20d. Simulated increase in pressure in aerial and cross-sectional view at nine months from start of injection for the low permeability–low porosity (k-0.75/phi-0.75) alternative case, which resulted in the largest simulated pressures.

1 year after start of CO₂ injection

Delta Pressure, psi

1 year after start of CO₂ injection

KGS 1-28
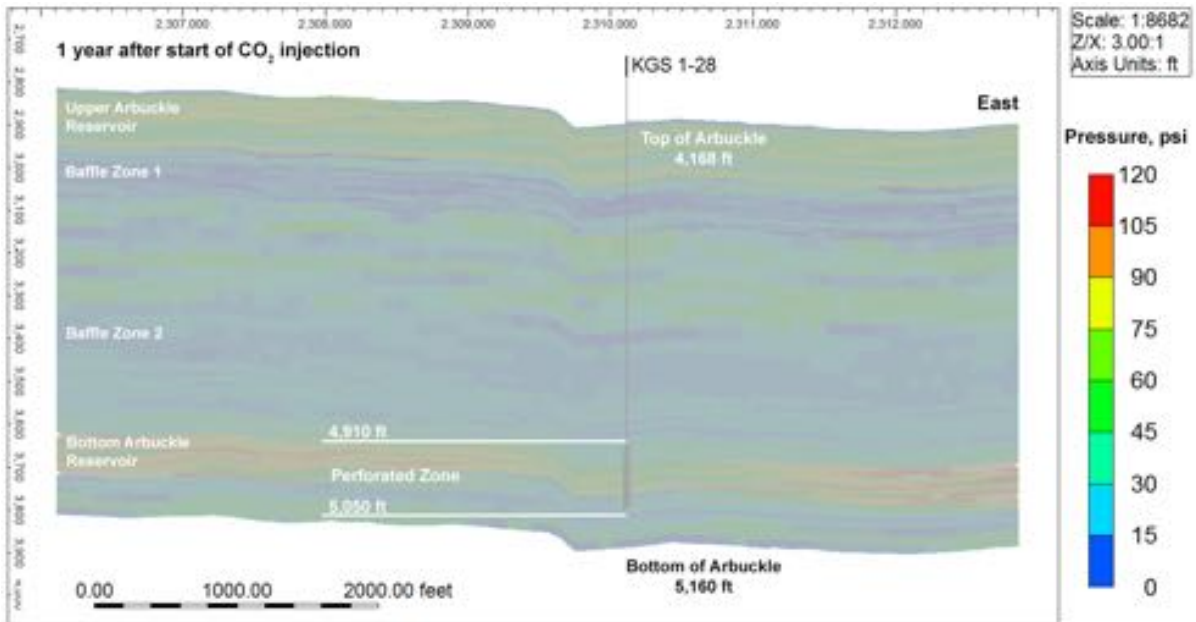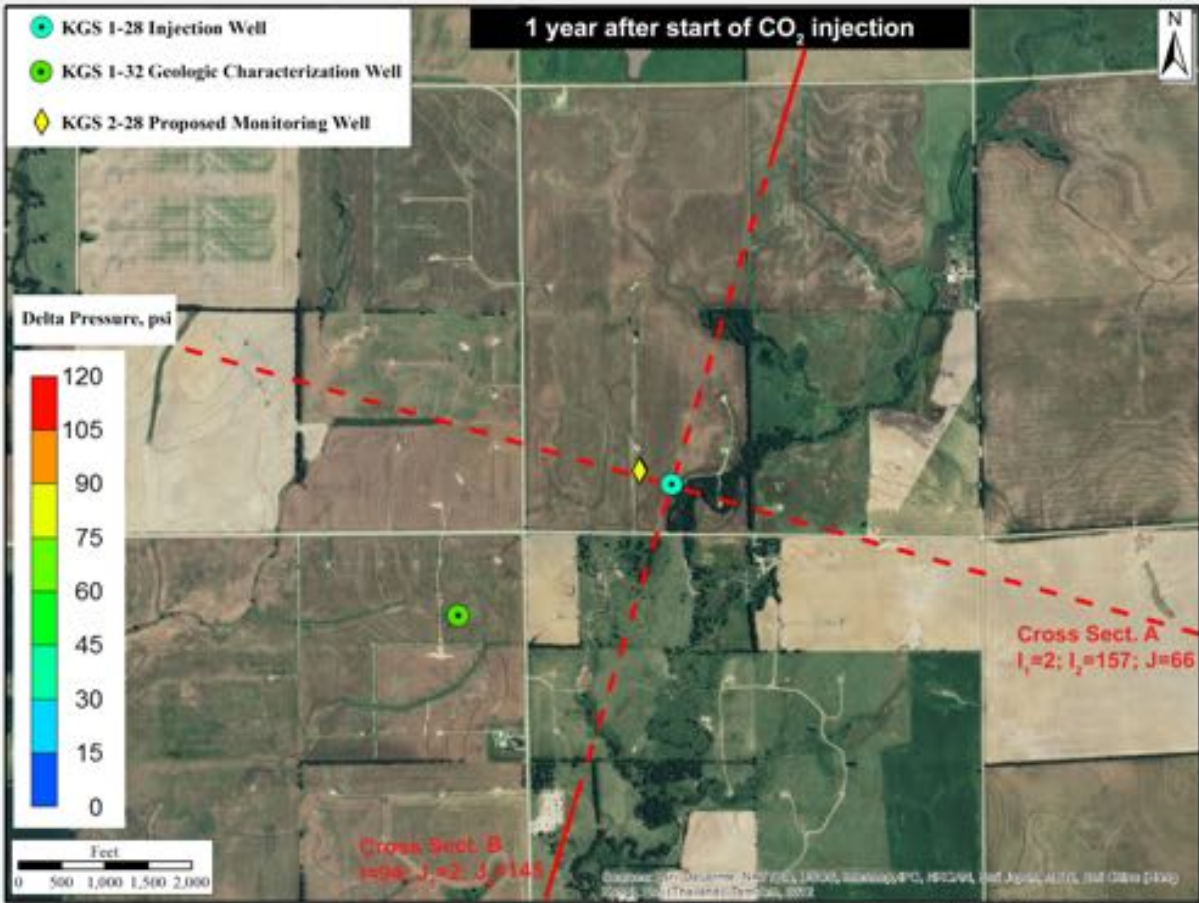
Pressure, psi

Figure 20e. Simulated increase in pressure in aerial and cross-sectional view at one year from start of injection for the low permeability–low porosity (k-0.75/phi-0.75) alternative case, which resulted in the largest simulated pressures.
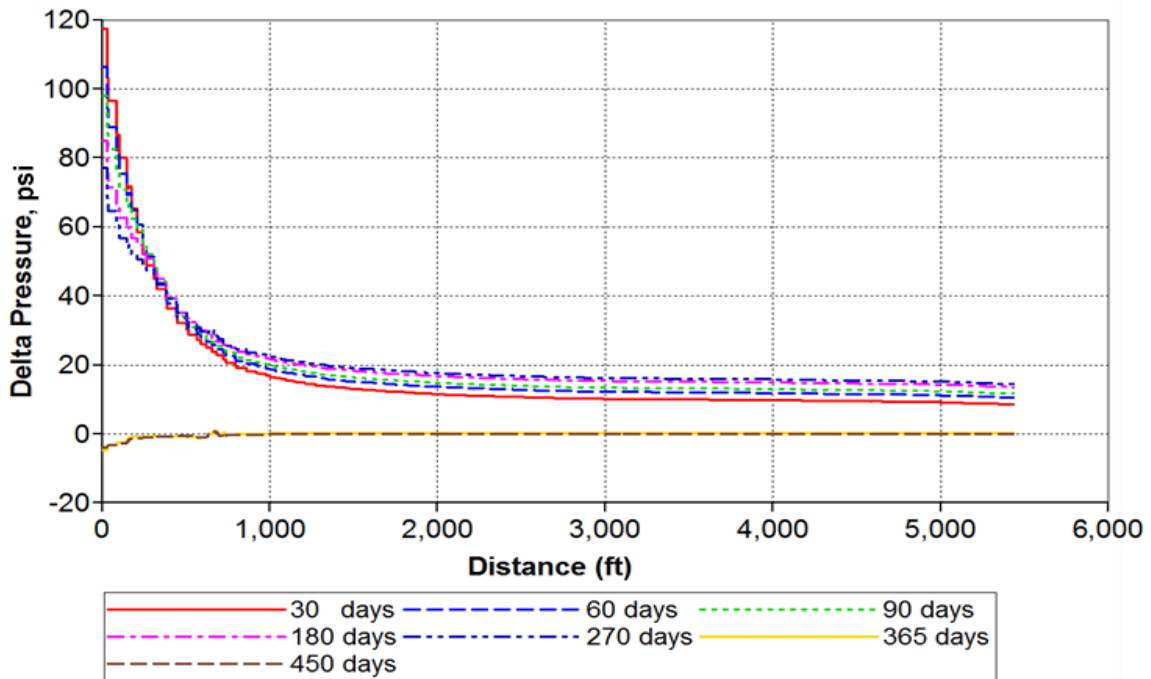
Figure 21. Pore pressure as a function of lateral distance from the injection well (KGS 1-28) at seven time intervals for the highest induced pressure case (k-0.75/phi-0.75).

Appendix A

Repeat of CMG simulations with total injected volume of 26,000 metric tons (MT) instead of 40,000 MT

For the base case simulation results presented in Section 6, 40,000 metric tons (MT) of CO_2 were injected into the KGS 1-28 well at a constant rate of approximately 150 tons per day for a period of nine months. Although Berexco is seeking a permit for injecting 40,000 tons, it is likely that only 26,000 tons will be injected due to budgetary constraints. At the request of the EPA, alternate simulations were conducted with a total injection volume of only 26,000 tons. All simulations described in Section 6 for 40,000 tons were repeated for an injection volume of 26,000 tons, and the results are presented in this appendix. Only the simulation result figures are provided in this appendix; the context for each figure is the same as provided in the description for an injection volume of 40,000 tons. For example, fig. A.6a (in this appendix), which shows the extent of the plume at six months from commencement of injection for an injection volume of 26,000 tons, is equivalent (for comparison purposes) to fig. 14a in Section 6, which shows the plume extent at the end of six months for an injection volume of 40,000 tons.

A1. CO_2 Plume Migration

A1.1 Short-Term CO_2 Arrival Forecast at (Planned) Observation Well KGS 2-28

It is projected that the dissolved CO_2 will be detected and monitored with a U-Tube sampling device at the projected observation well KGS 2-28 sometime between the first and second month from the start of CO_2 injection as indicated in fig. A.2a–b. The free phase CO_2 will arrive at the projected observation well between the fourth and fifth month after the start of the CO_2 injection (fig. A.1d–e).

It is anticipated to detect a pore-pressure response in the projected observation well KGS 2-28 in the first seconds from the start of CO_2 injection (fig. A.3a & A4). It is projected that the maximum observed delta pore pressure at the observation well will be about 40 psi. The pressure is projected to fall to the ambient levels within two or three months after CO_2 injection has commenced.

A.1.2 Short-Term Free-Phase CO₂
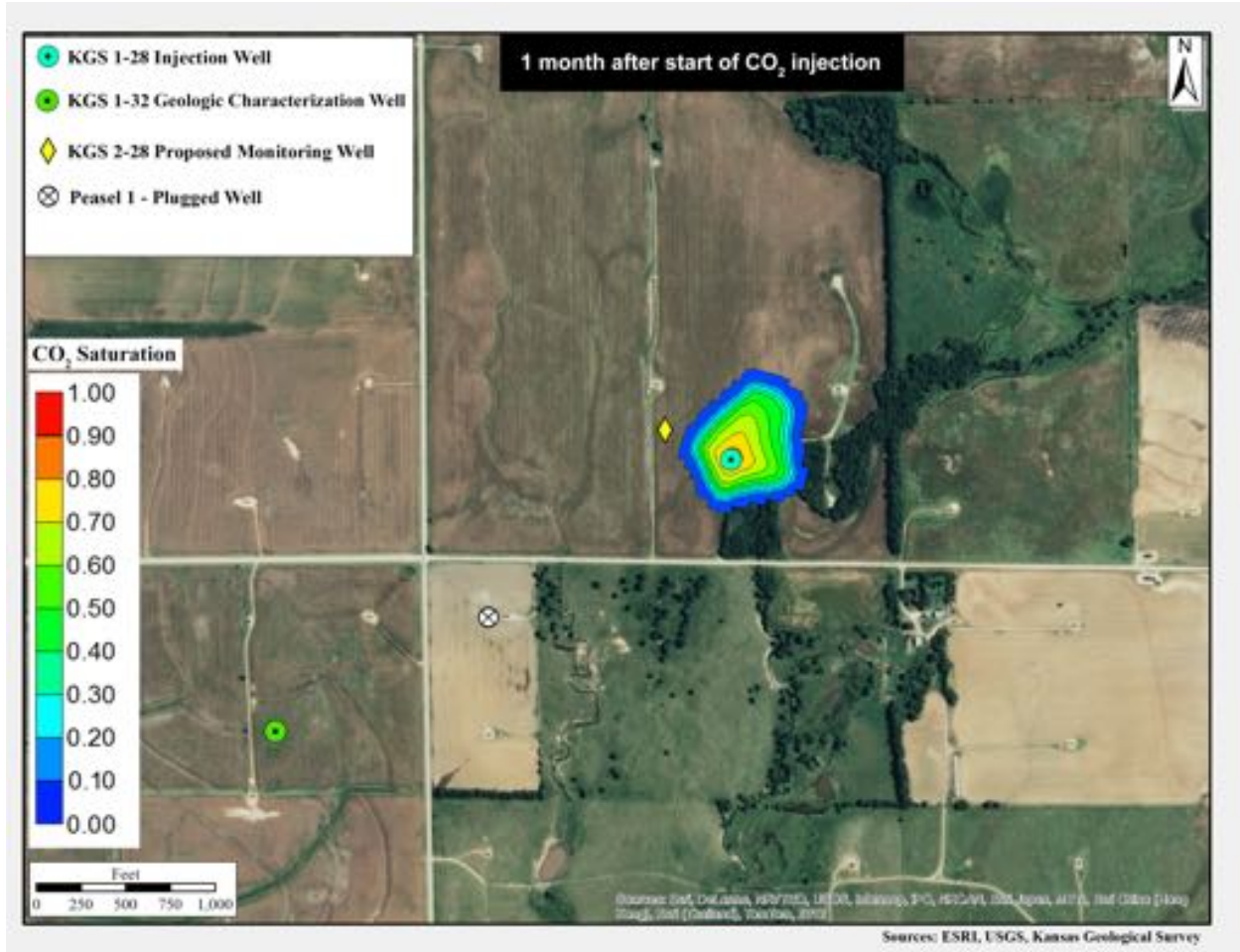
Figure A.1a. Free-phase CO₂ plume in aerial view for the largest migration alternative model (k-1.25/phi-0.75) at one month from start of injection.
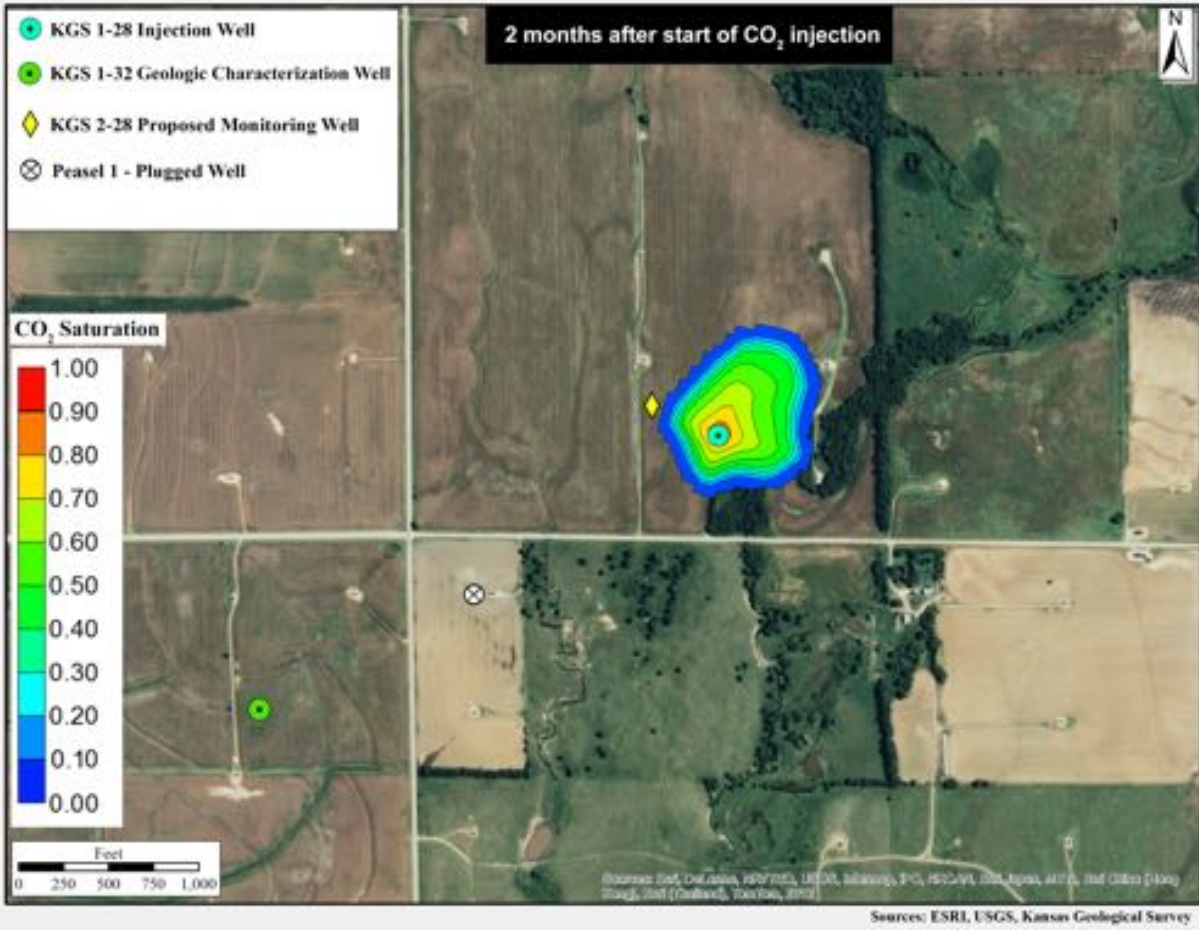
Figure A.1b. Free-phase CO$_2$ plume in aerial view for the largest migration alternative model (k-1.25/phi-0.75) at two months from start of injection.
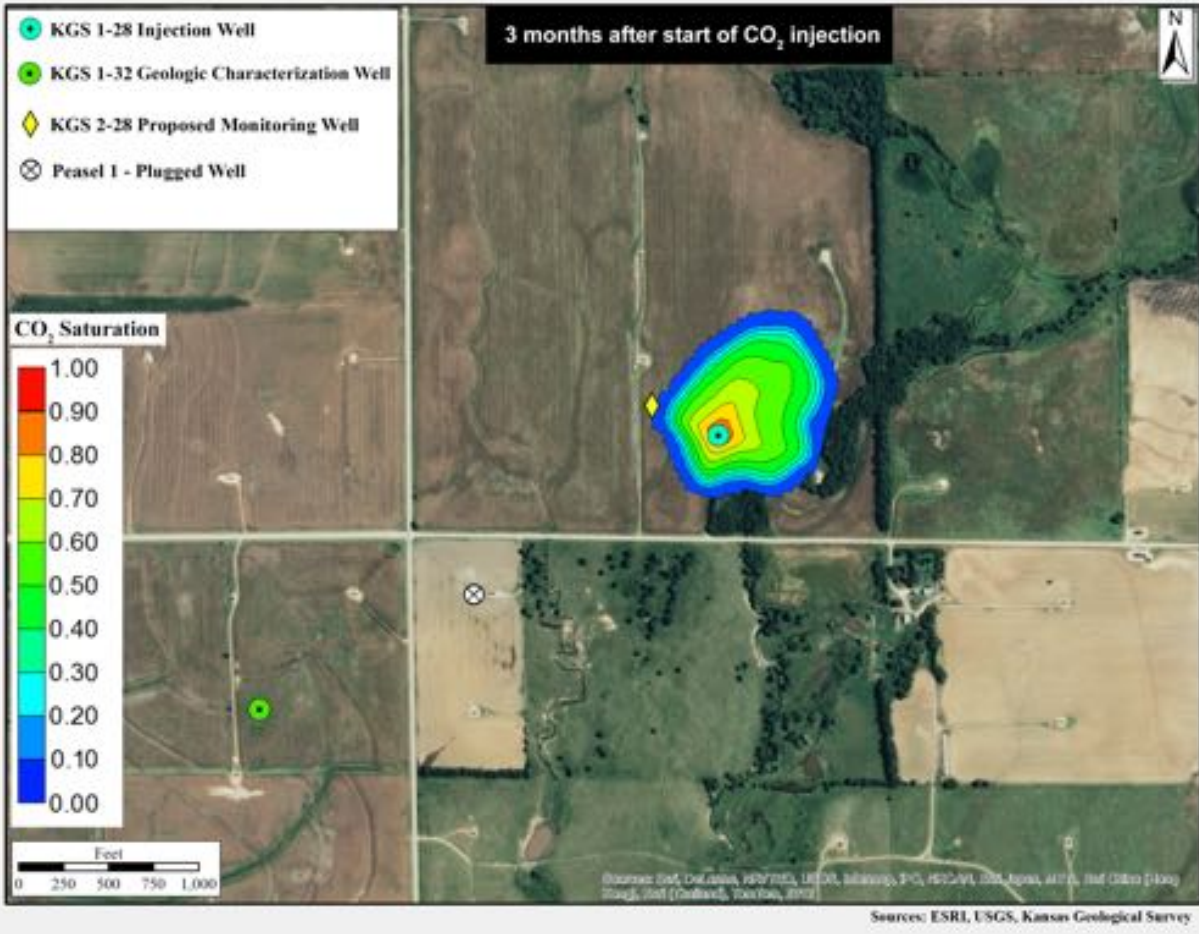
Figure A.1c. Free-phase CO$_2$ plume in aerial view for the largest migration alternative model (k-1.25/phi-0.75) at three months from start of injection.
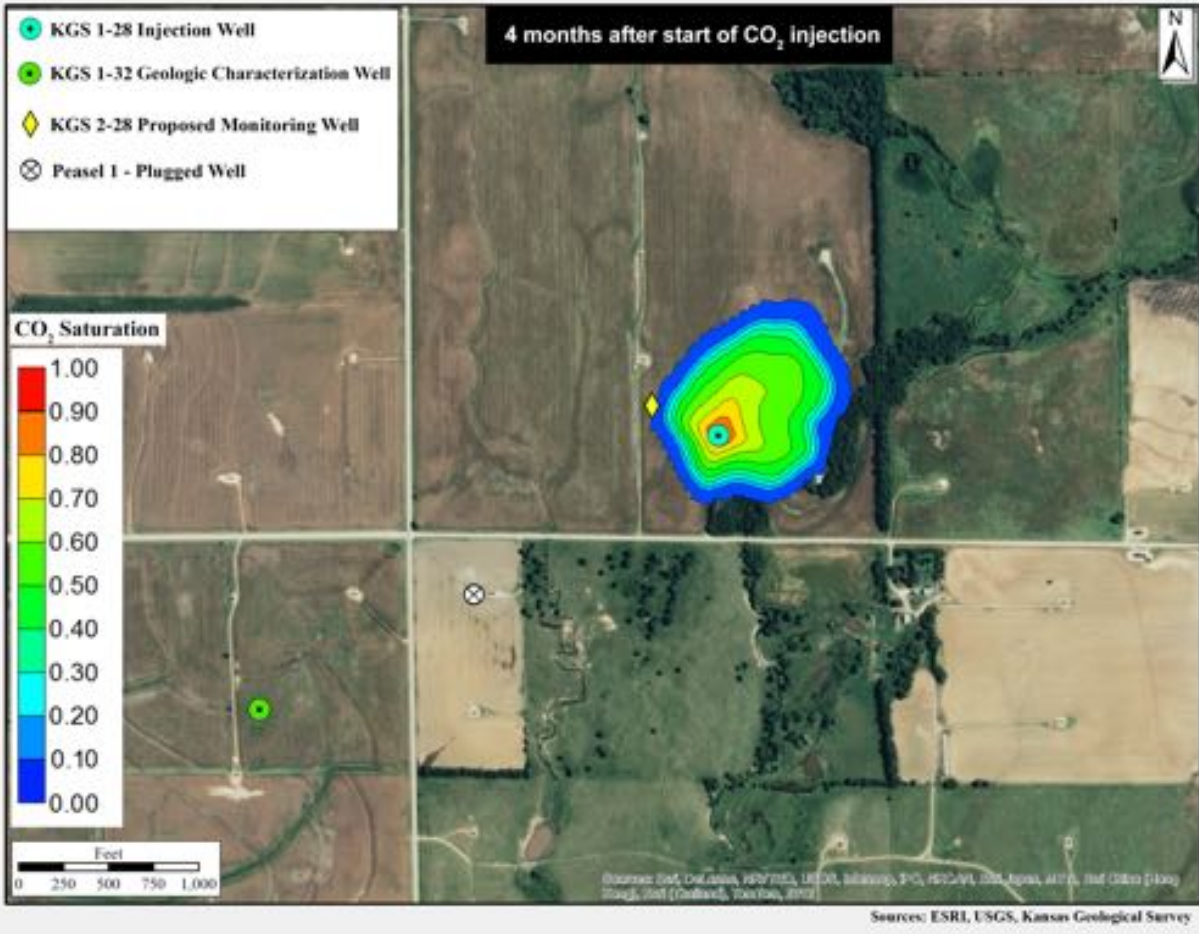
Figure A.1d. Free-phase CO$_2$ plume in aerial view for the largest migration alternative model (k-1.25/phi-0.75) at four months from start of injection.
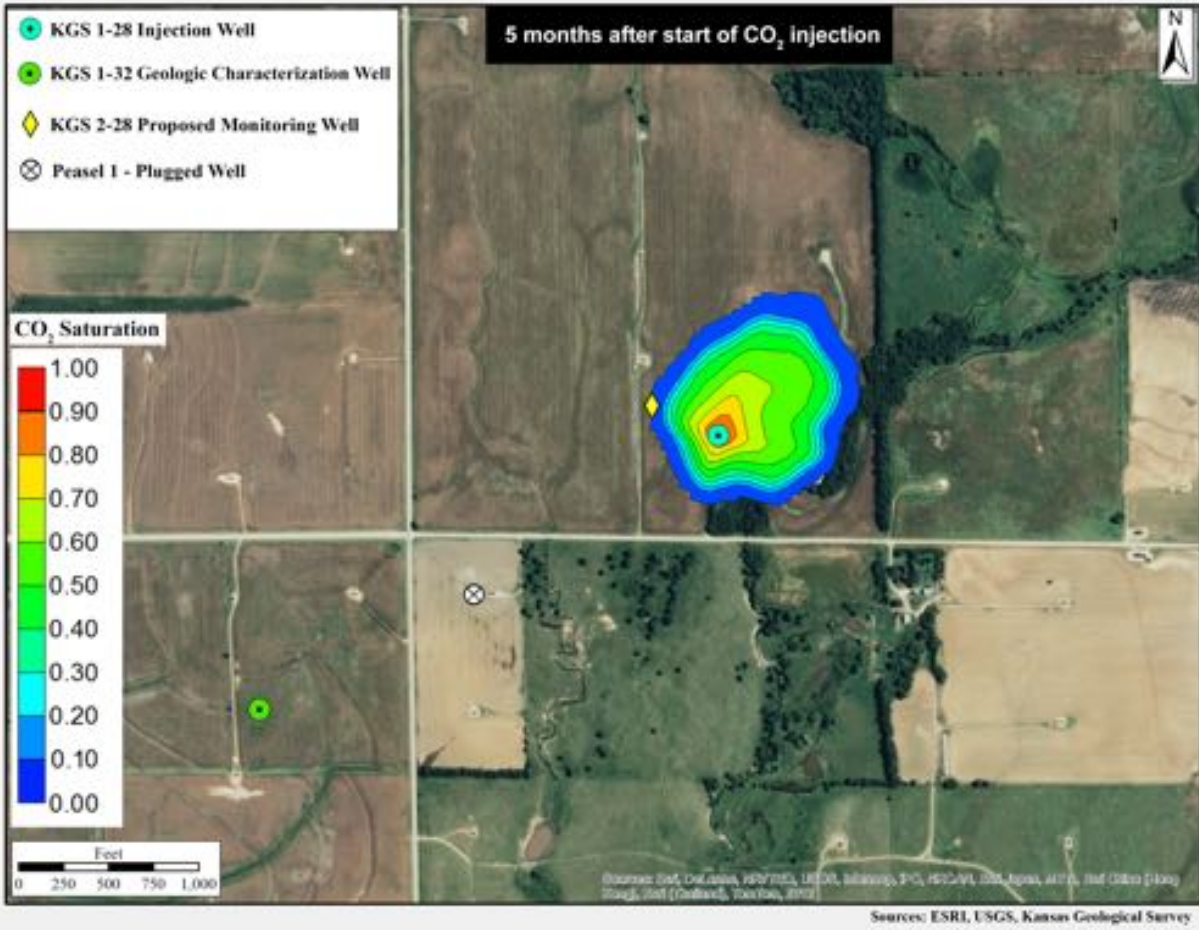
Figure A.1e. Free-phase CO$_2$ plume in aerial view for the largest migration alternative model (k-1.25/phi-0.75) at five months from start of injection.

A1.3 Short-Term Total CO$_2$ Spatial Distribution

Figure A.2a. Total CO$_2$ spatial distribution in aerial view for the largest migration alternative model (k-1.25/phi-0.75) at one month from start of injection.
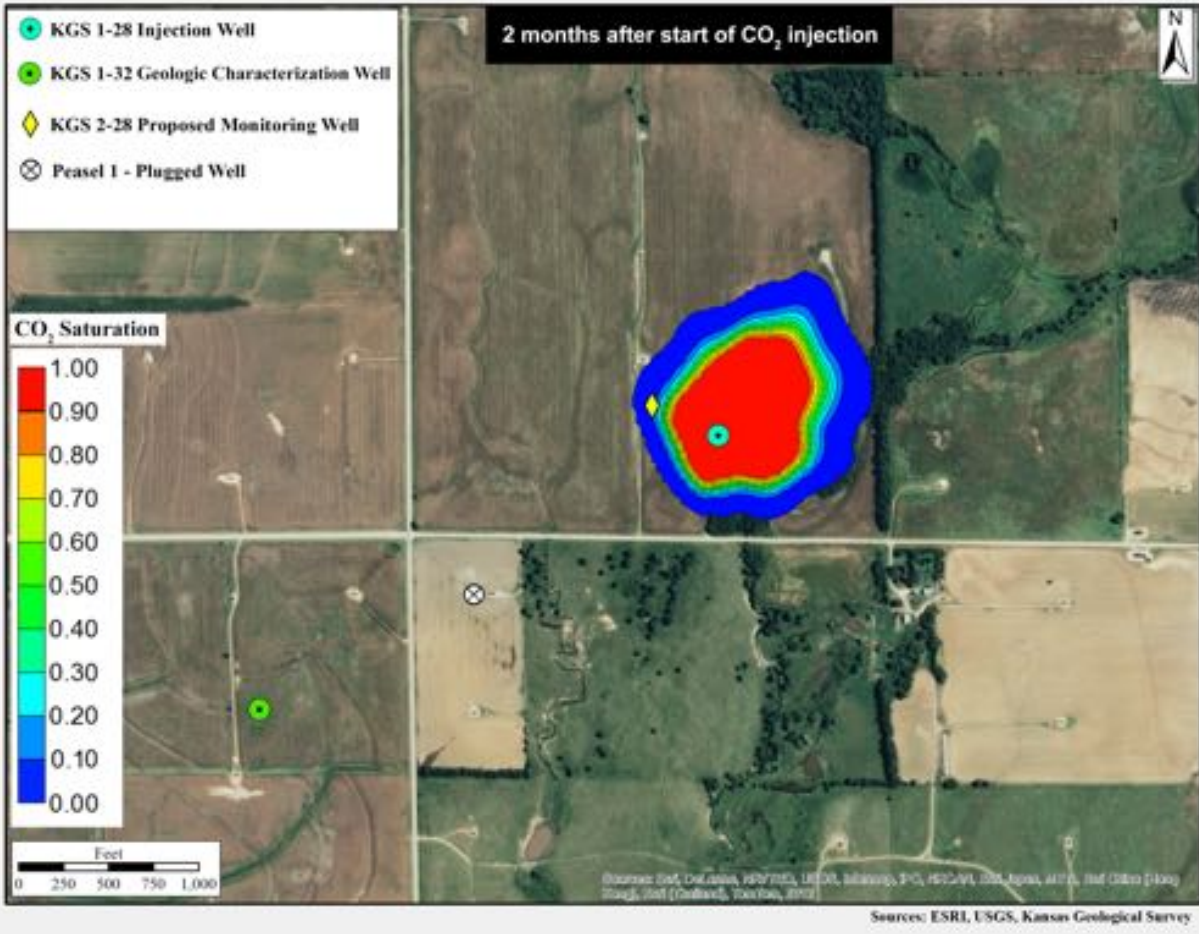
Figure A.2b. Total CO$_2$ spatial distribution in aerial view for the largest migration alternative model (k-1.25/phi-0.75) at two months from start of injection.
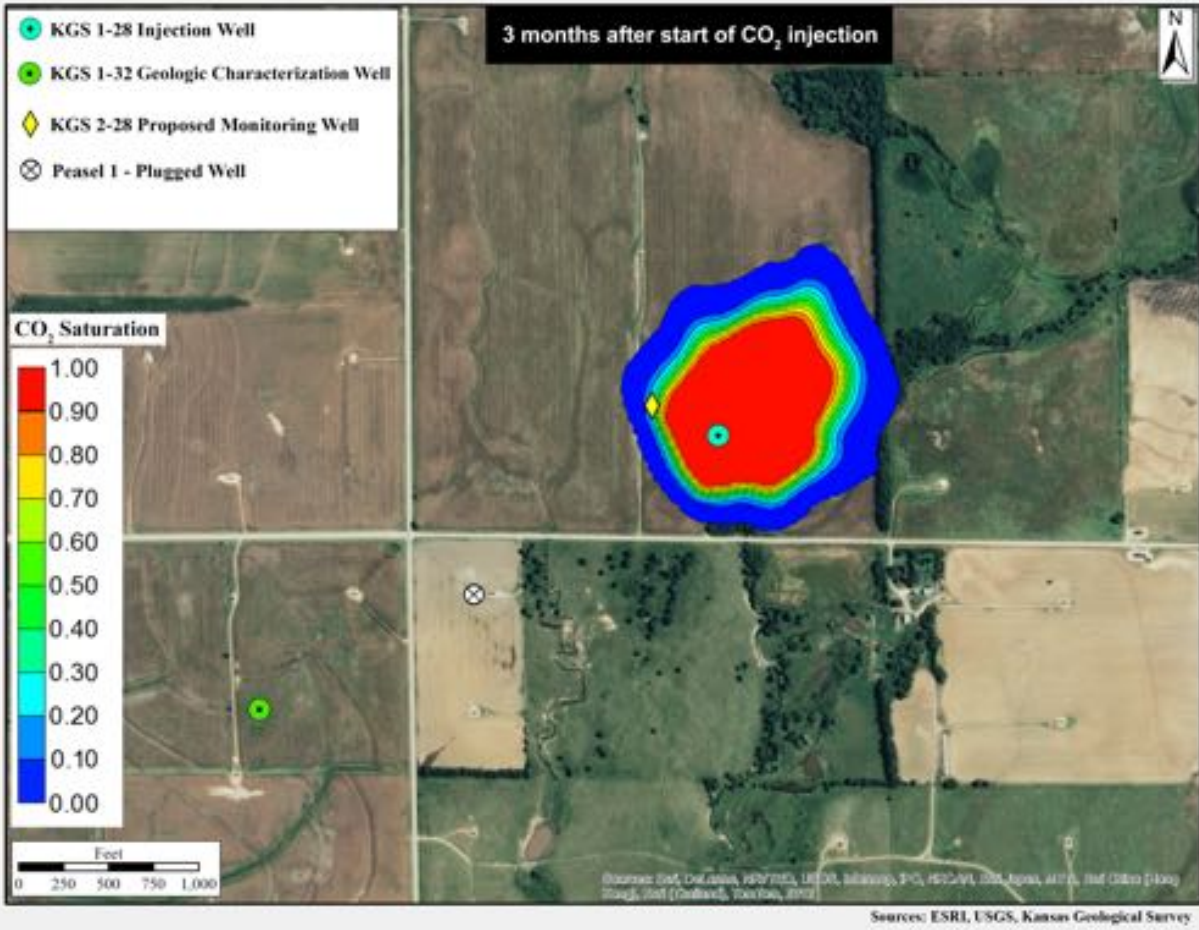
Figure A.2c. Total CO$_2$ spatial distribution in aerial view for the largest migration alternative model (k-1.25/phi-0.75) at three months from start of injection.
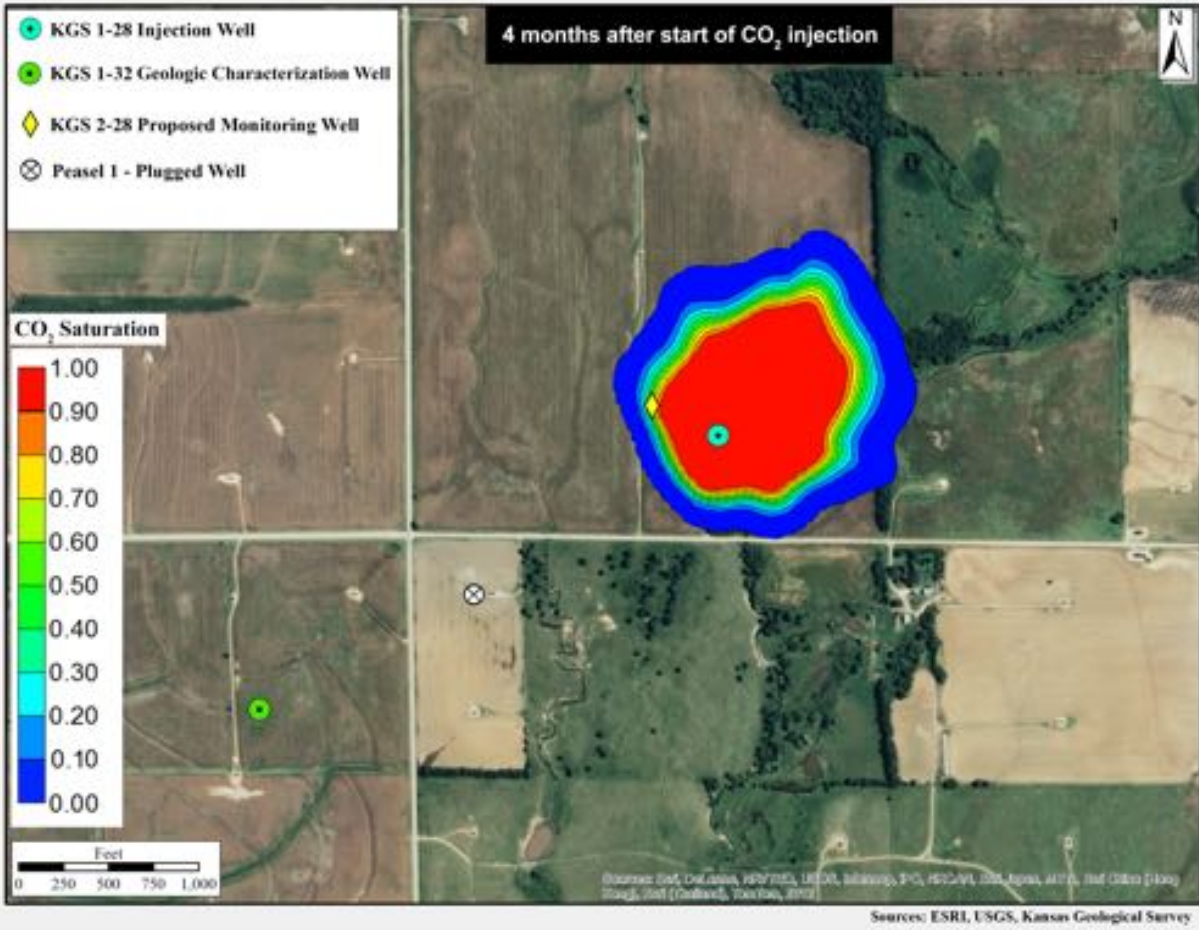
Figure A.2d. Total CO$_2$ spatial distribution in aerial view for the largest migration alternative model (k-1.25/phi-0.75) at four months from start of injection.
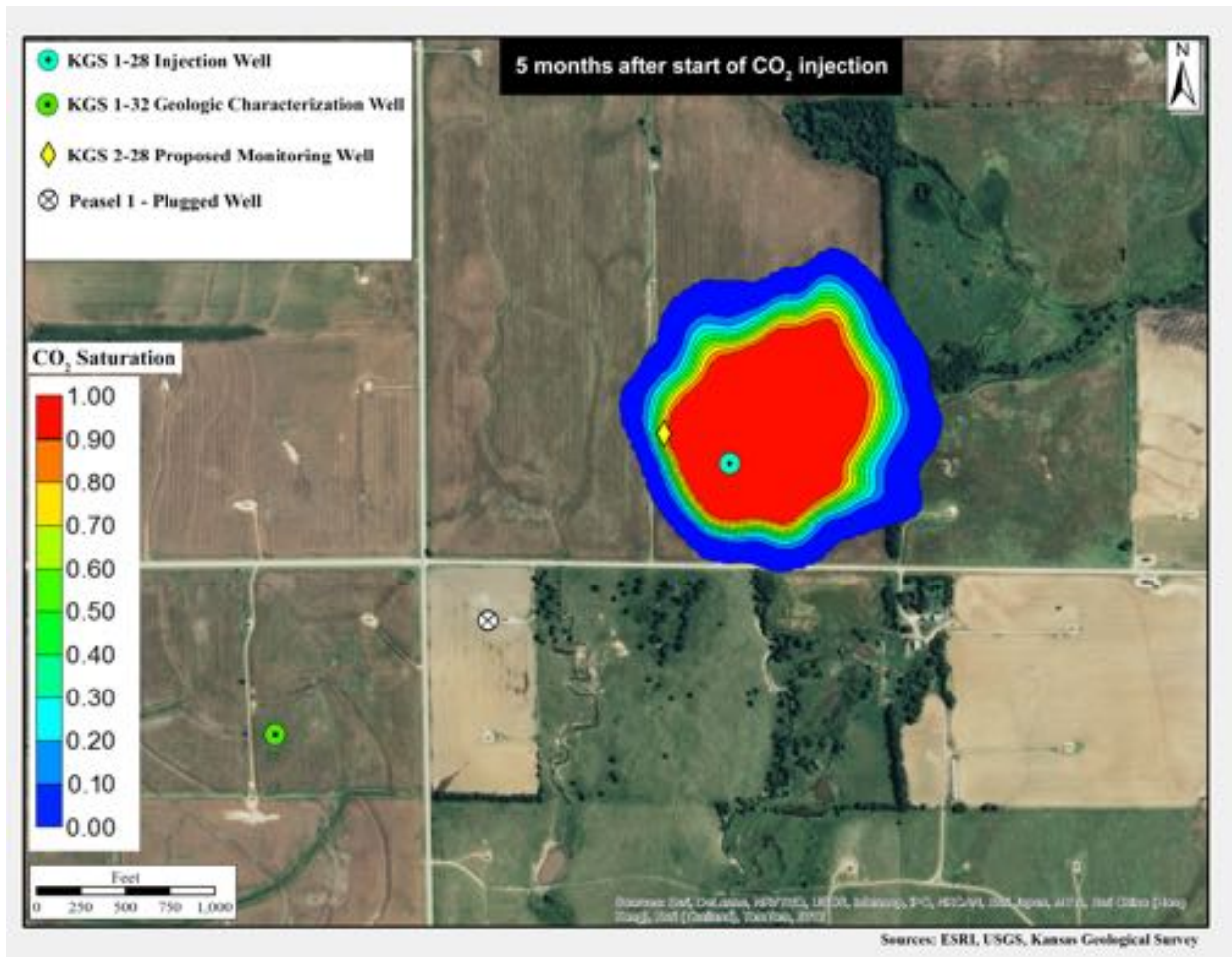
Figure A.2e. Total CO$_2$ spatial distribution in aerial view for the largest migration alternative model (k-1.25/phi-0.75) at five months from start of injection.

A1.4 Short-Term Simulated Pressure Increase
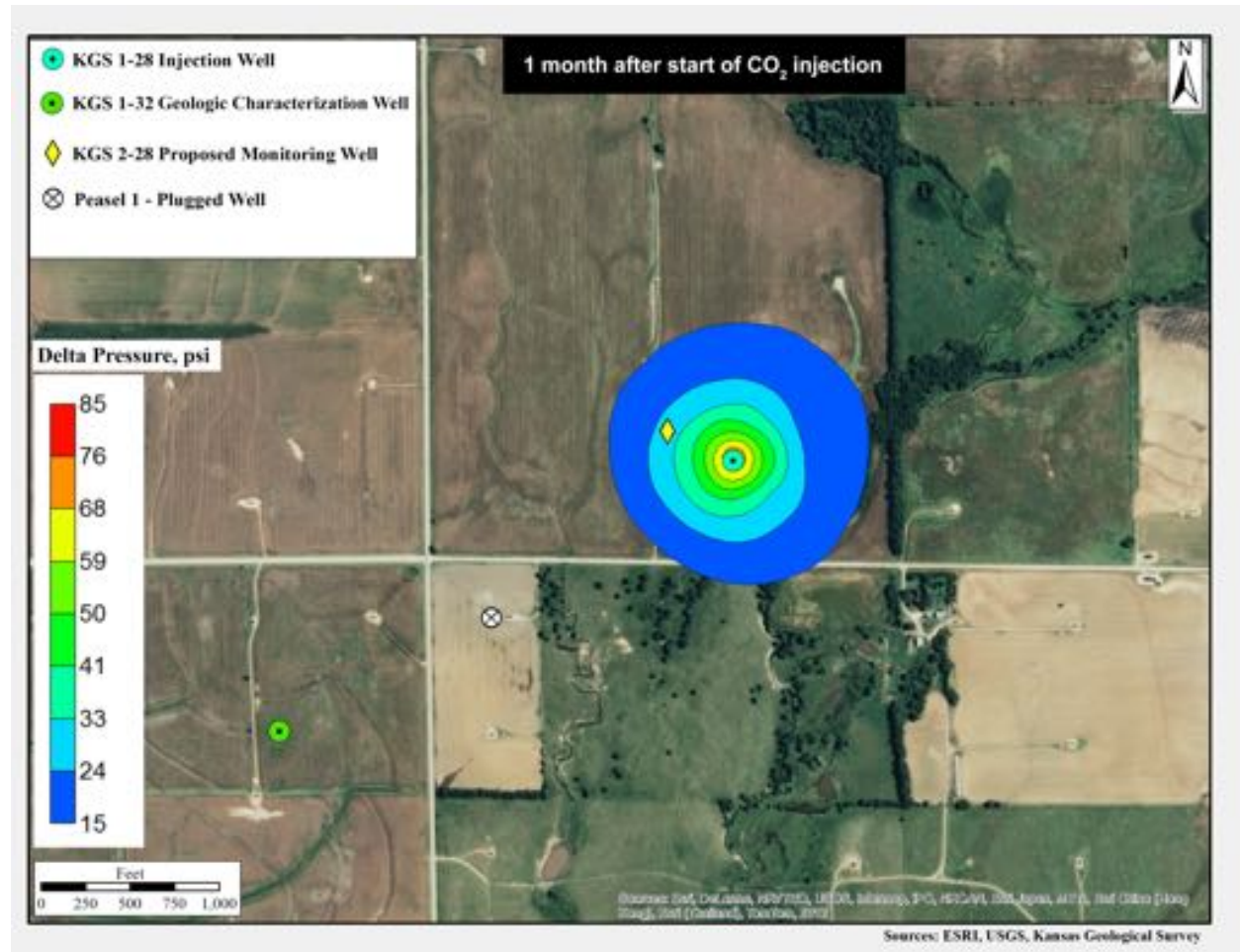
Figure A.3a. Simulated increase in pressure in aerial view at one month from start of injection for the low permeability–low porosity (k-0.75/phi-0.75) alternative case, which resulted in the largest simulated pressures.
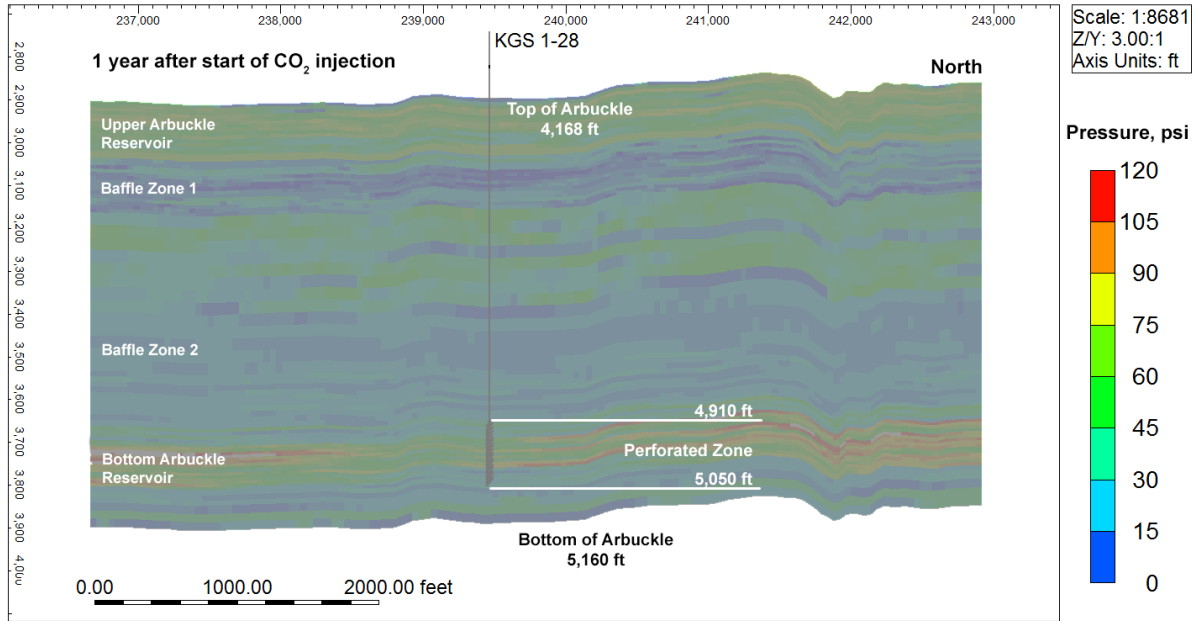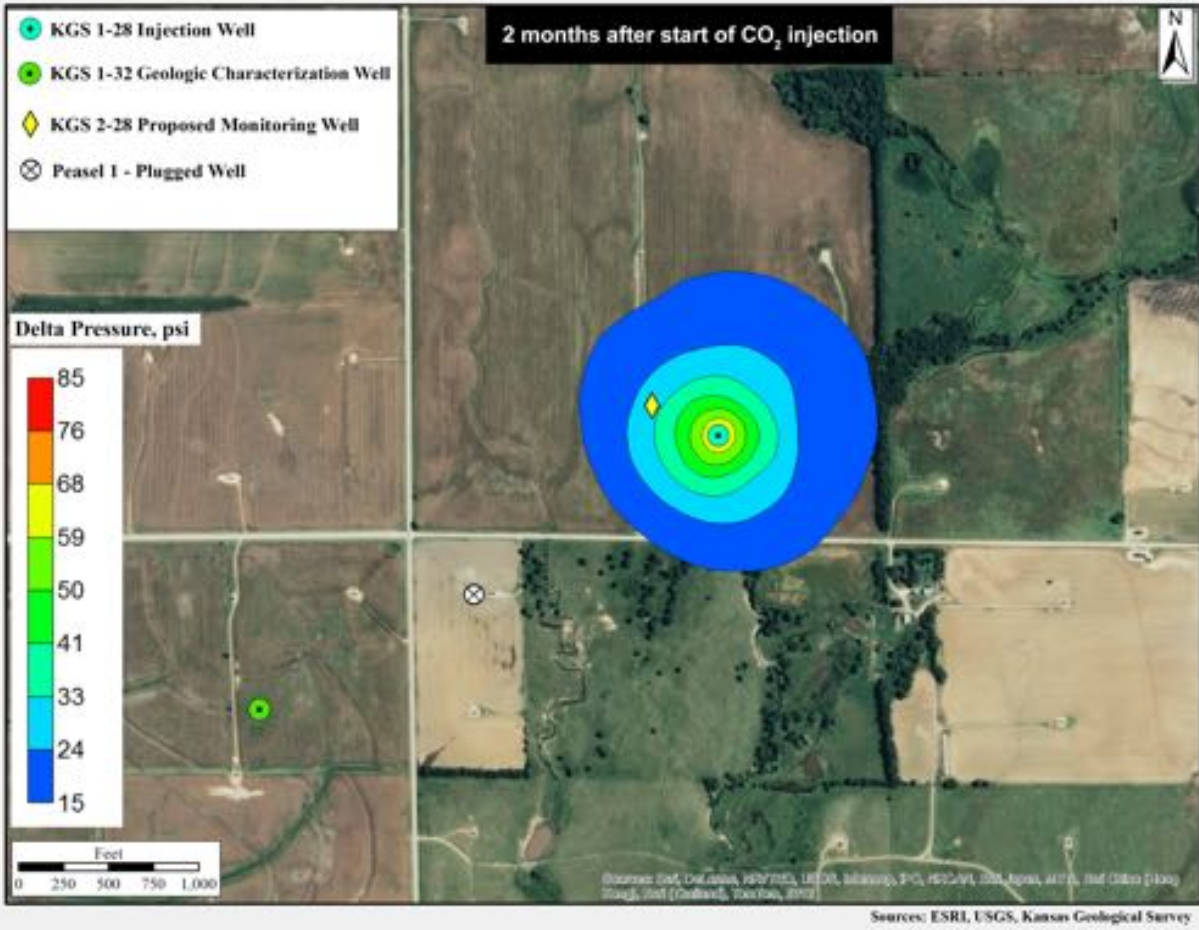
Figure A.3b. Simulated increase in pressure in aerial view at two months from start of injection for the low permeability–low porosity (k-0.75/phi-0.75) alternative case, which resulted in the largest simulated pressures.
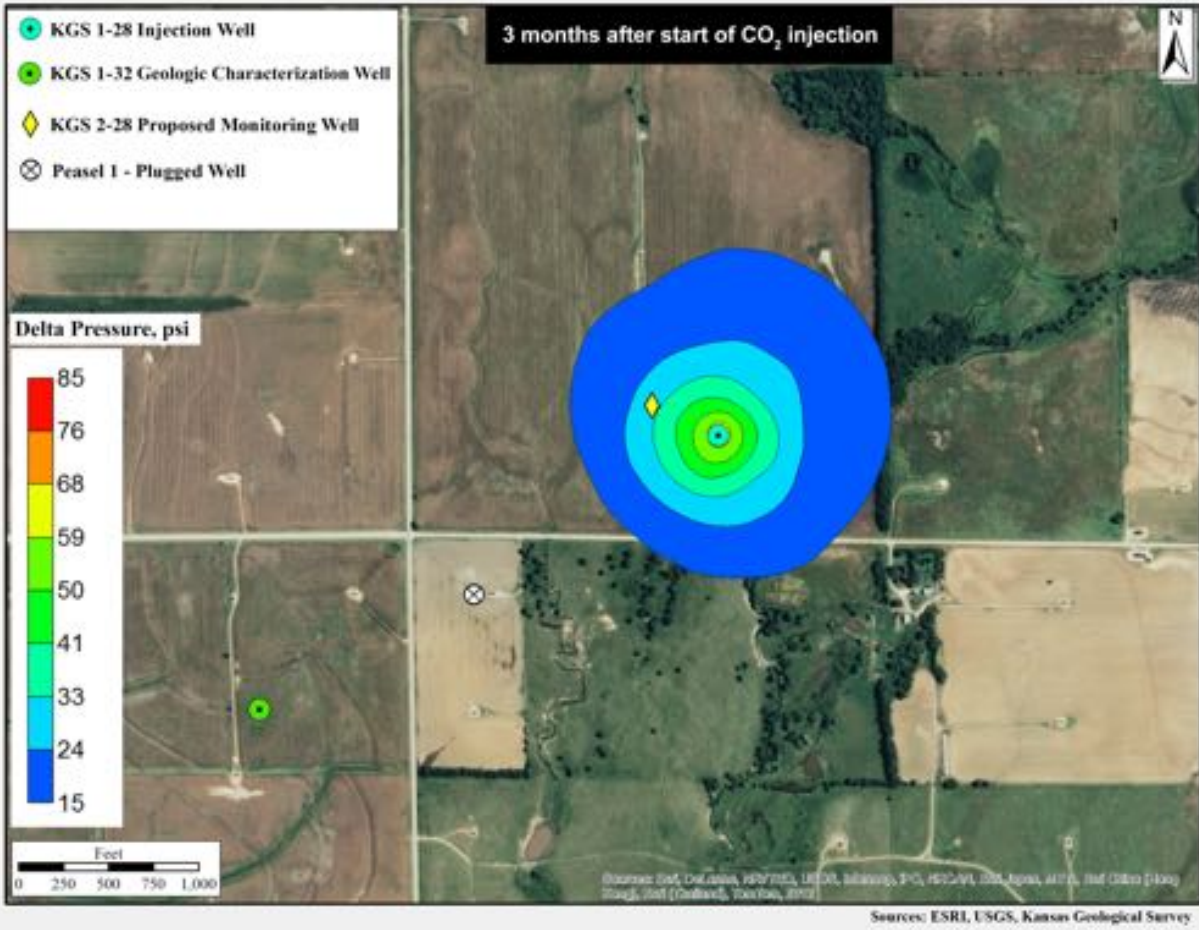
*Figure A.3c. Simulated increase in pressure in aerial view at three months from start of injection for the low permeability–low porosity (k-0.75/phi-0.75) alternative case, which resulted in the largest simulated pressures.*
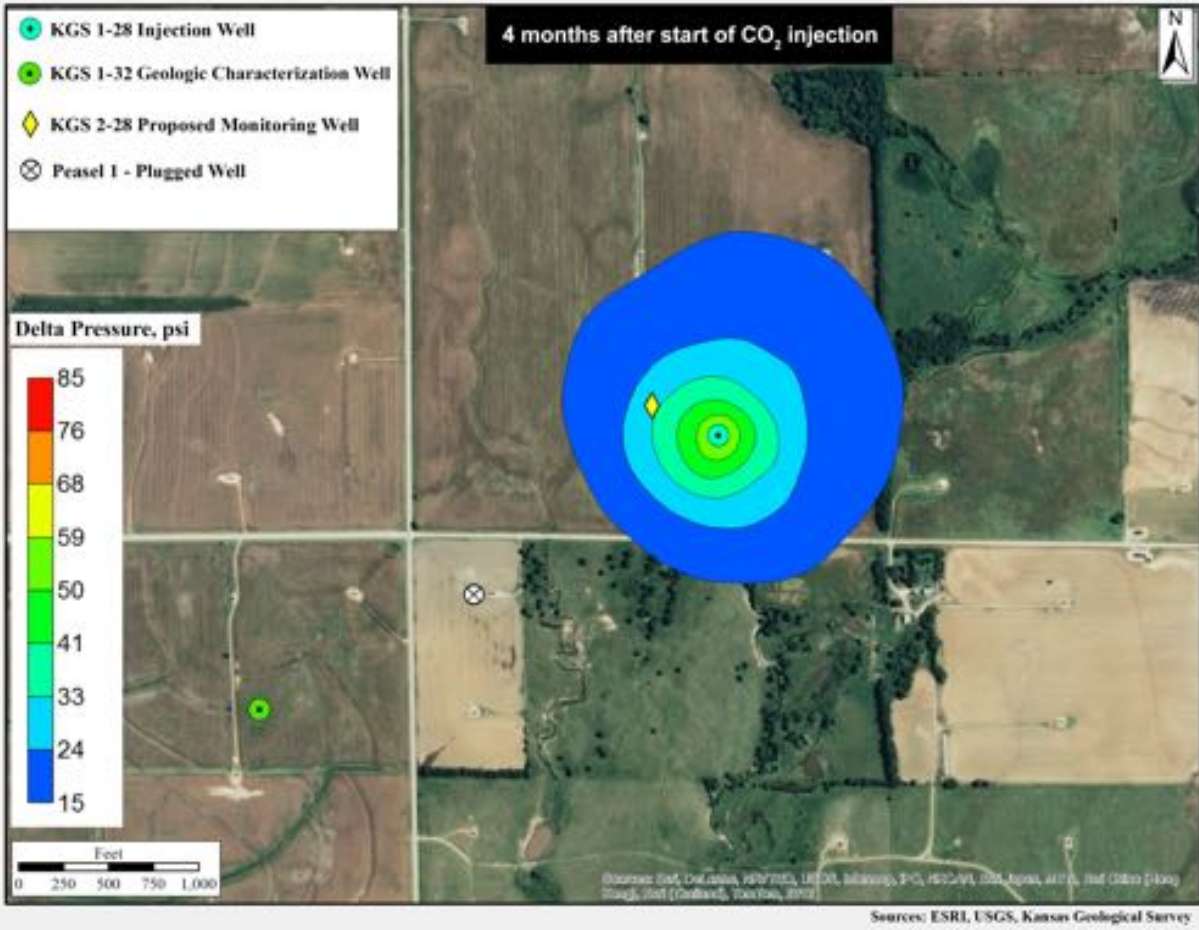
Figure A.3d. Simulated increase in pressure in aerial view at four months from start of injection for the low permeability–low porosity (k-0.75/phi-0.75) alternative case, which resulted in the largest simulated pressures.
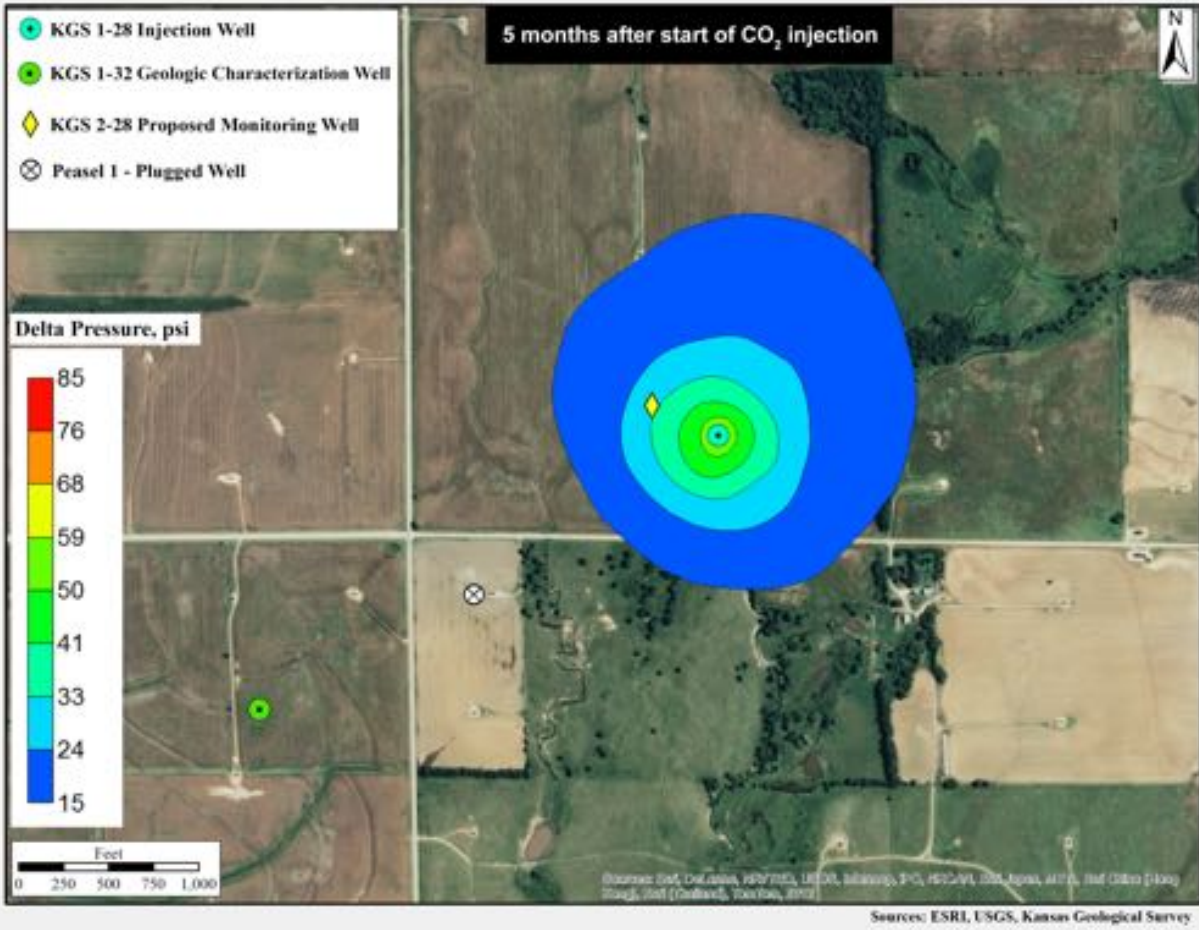
Figure A.3e. Simulated increase in pressure in aerial view at five months from start of injection for the low permeability–low porosity (k-0.75/phi-0.75) alternative case, which resulted in the largest simulated pressures.
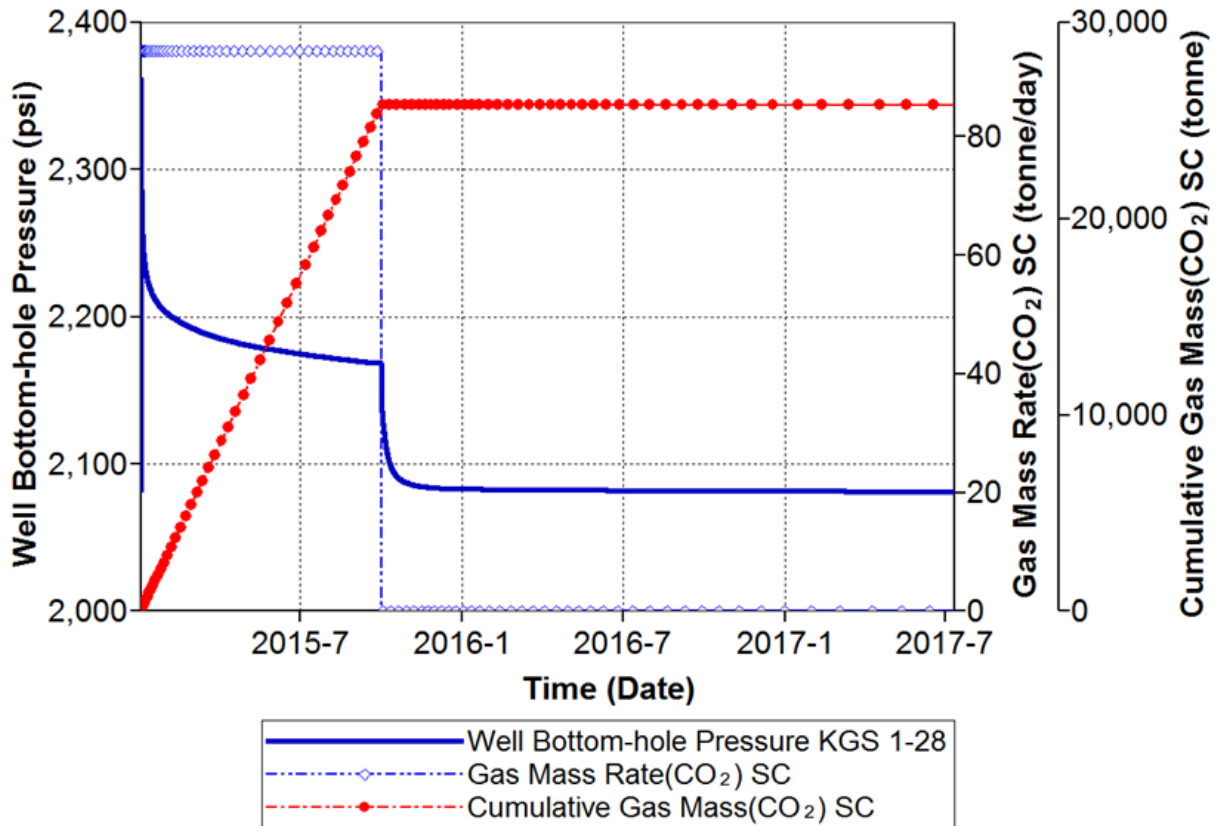
Figure A.4. Forecasted well bottomhole pressure at the depth of 5,050 ft for minimum porosity and minimum permeability case (k-0.75/phi-0.75) case.
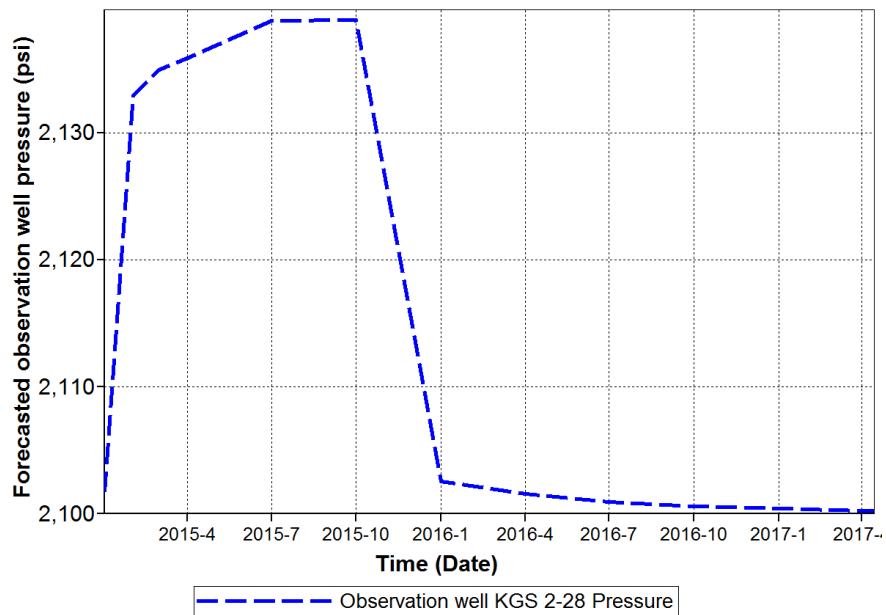
Figure A.5. Forecasted reservoir pressure at the observation well KGS 2-28 projected location at a depth of 5,050 ft for minimum porosity and minimum permeability case (k-0.75/phi-0.75) case.

A2. Long-Term Forecast for CO₂ Migration for the 26,000 tons of CO₂ Injection Scenario

A2.1 Long-Term Free-Phase

Figure A.6a–f corresponds with fig. 14a–f in Section 6 of this report. They represent simulation results for an injection volume of 26,000 MT (compared to 40,000 MT in Section 6 simulations).
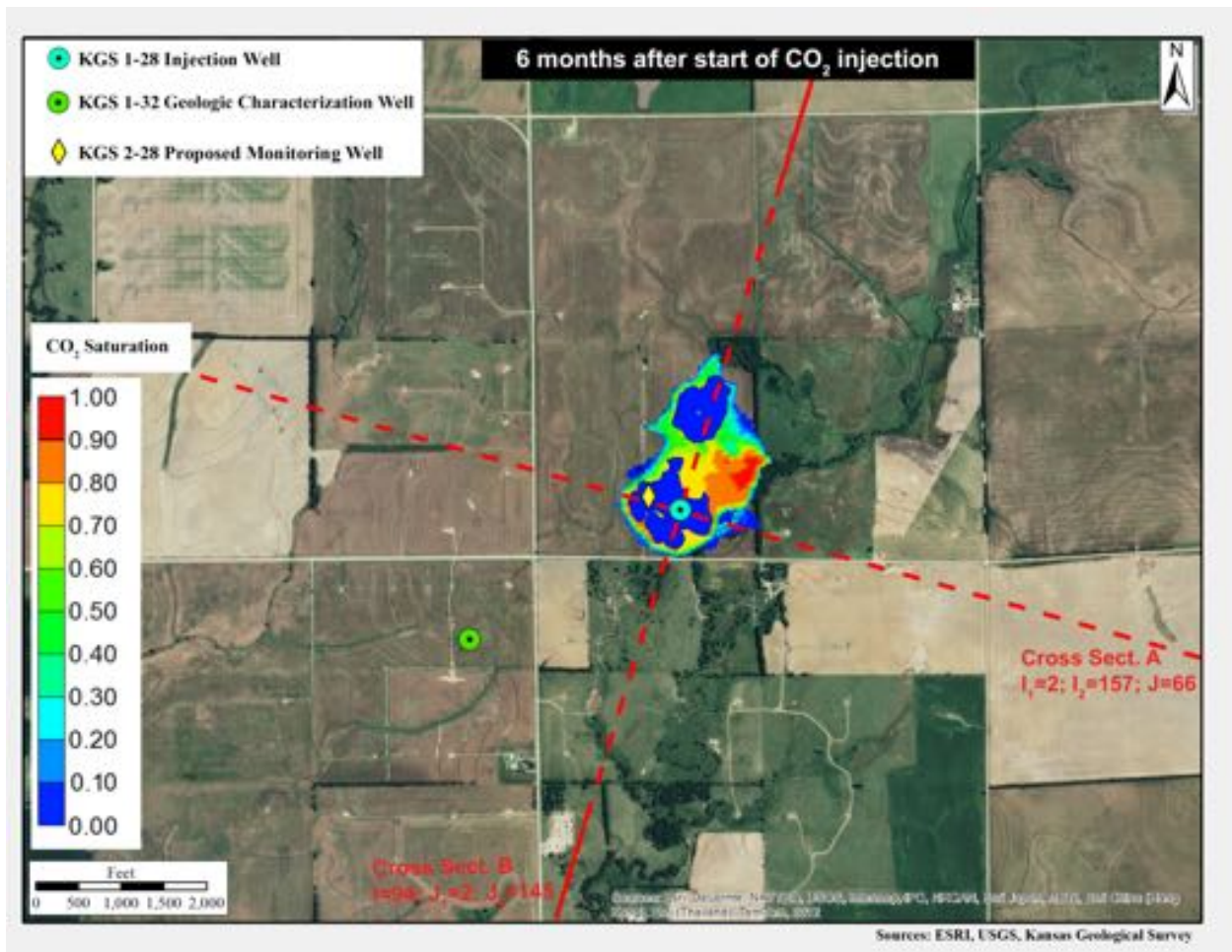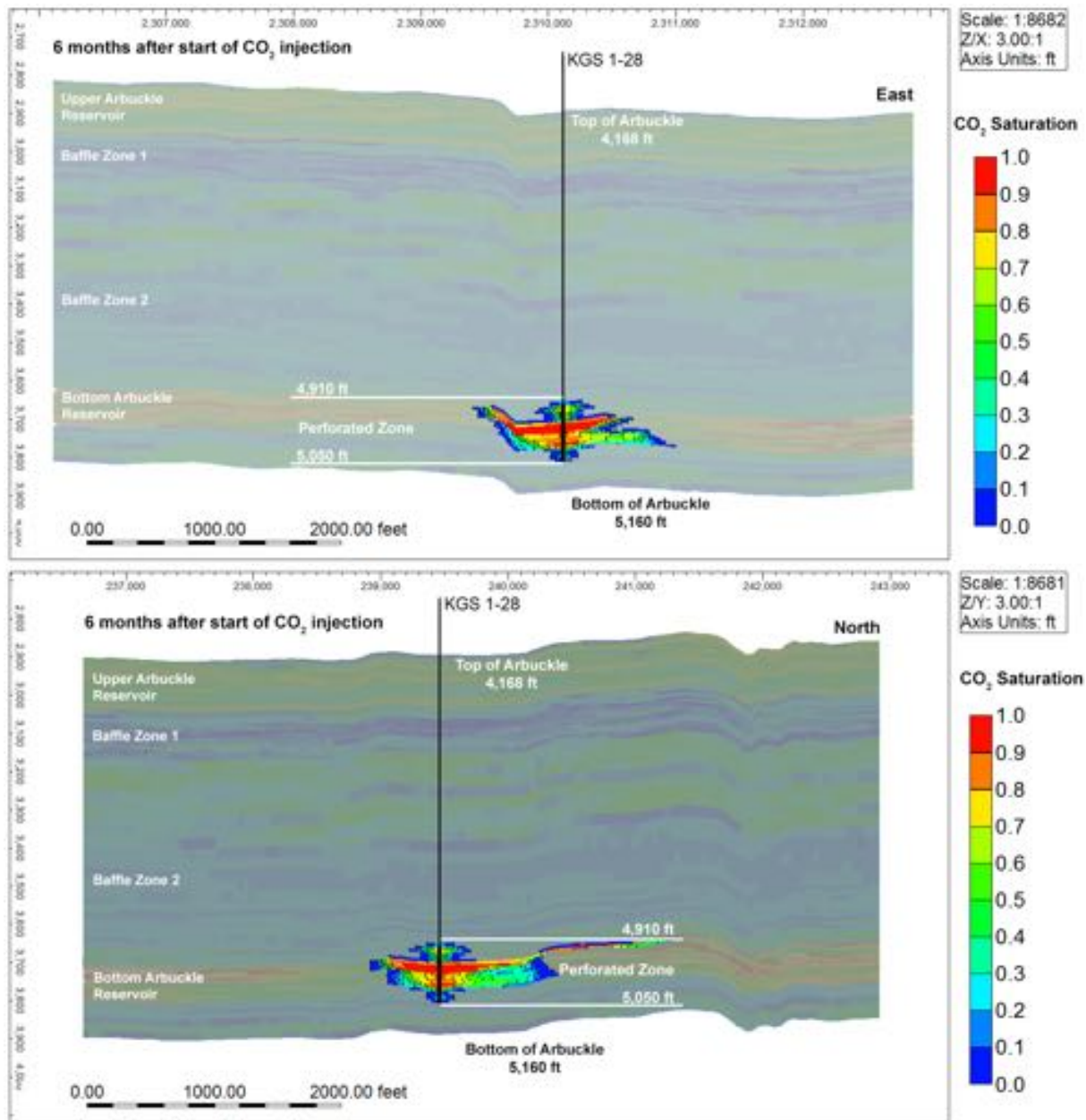
Figure A.6a. Free-phase CO₂ plume in aerial and cross-sectional view for the largest migration alternative model (k-1.25/phi-0.75) at six months from start of injection.
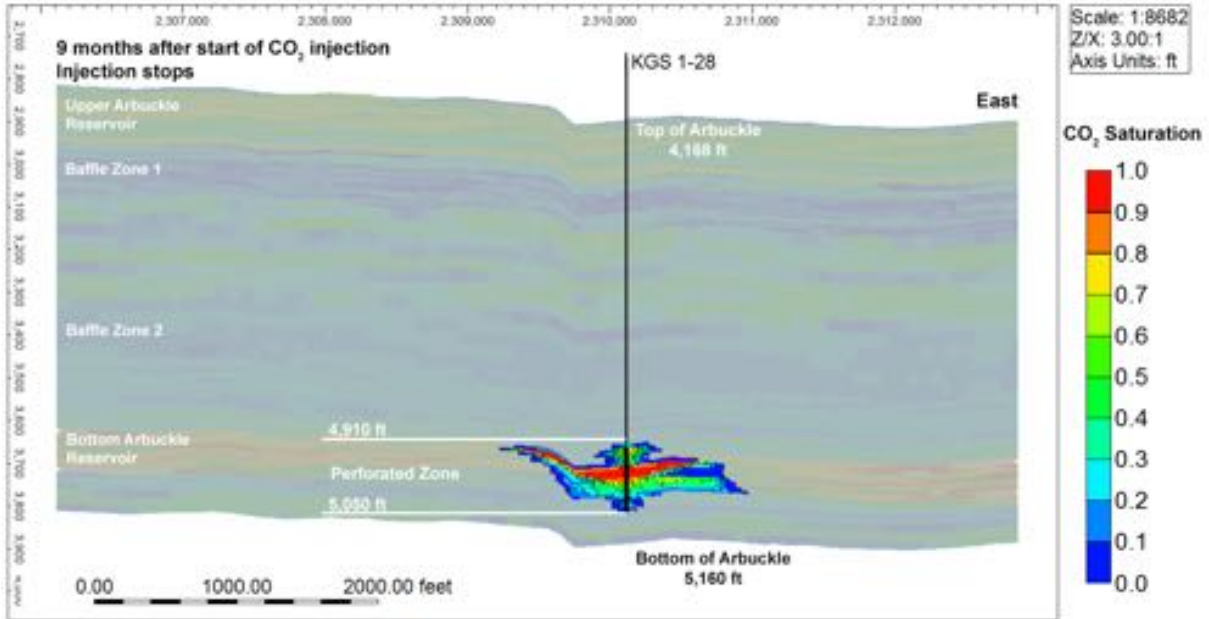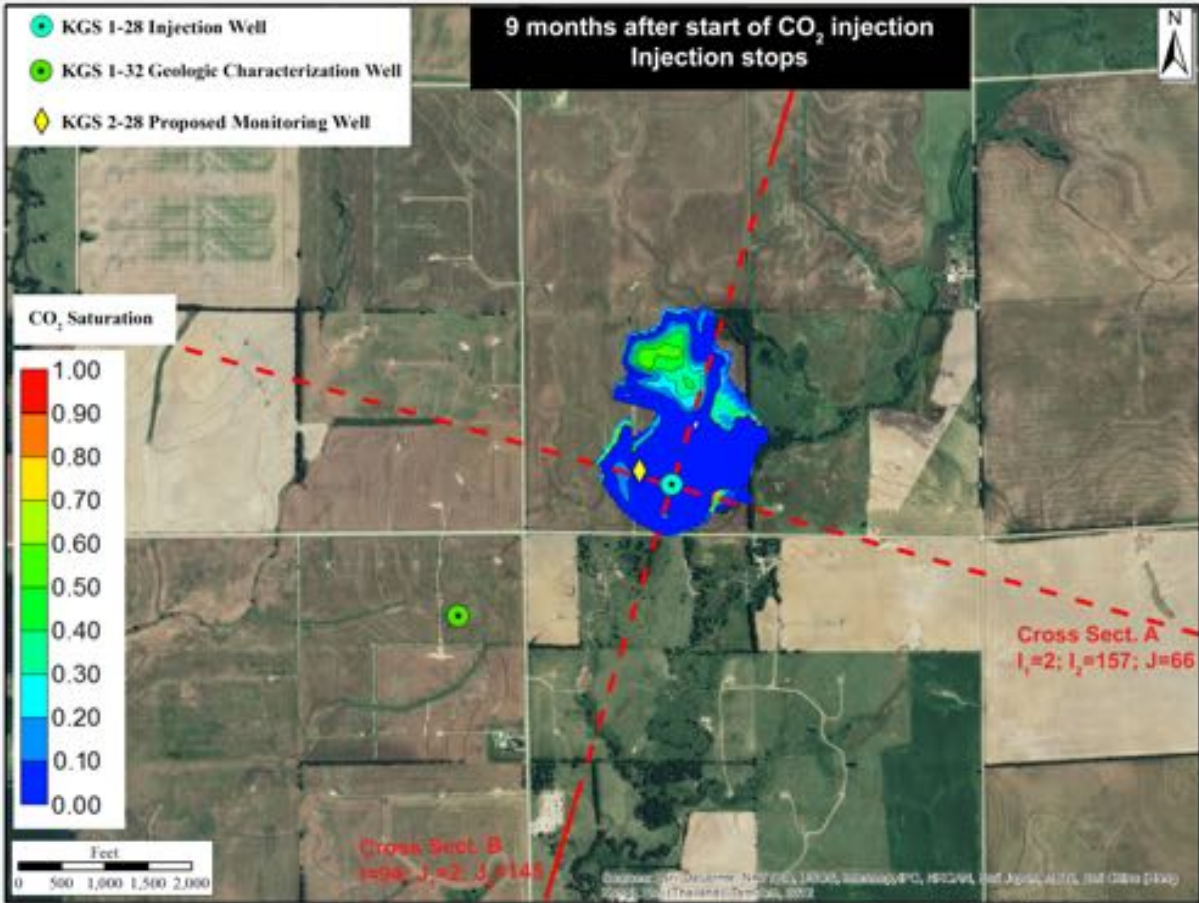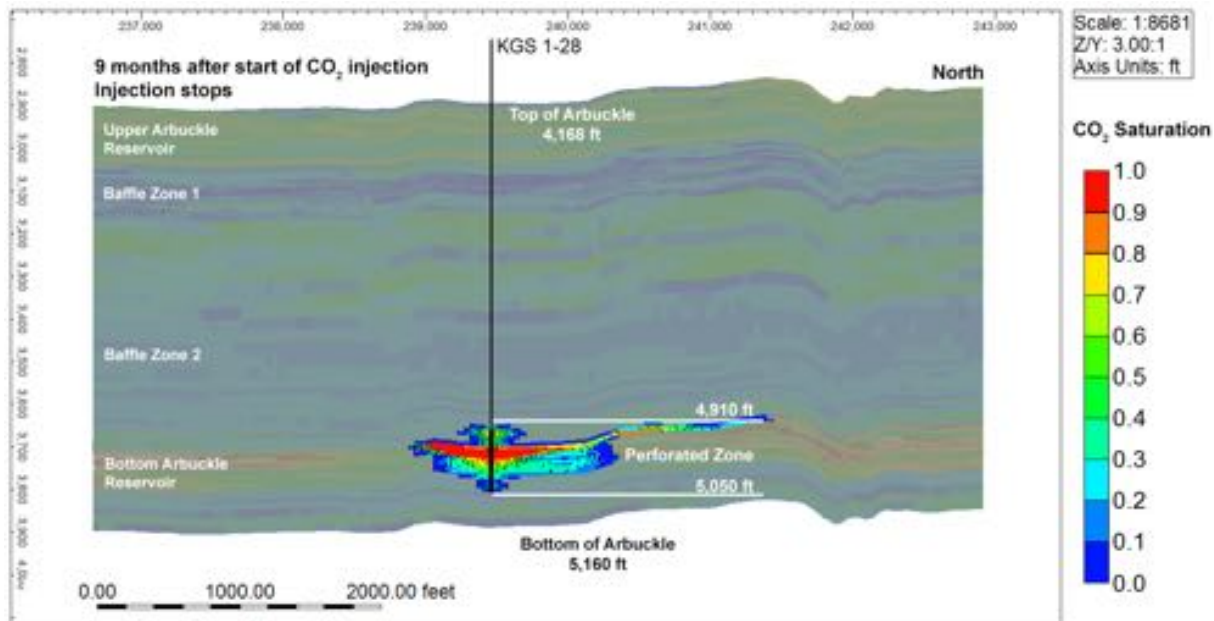
Figure A.6b. Free-phase CO$_2$ plume in aerial and cross-sectional view for the largest migration alternative model (k-1.25/phi-0.75) at nine months from start of injection. Injection stops at the end of this month.
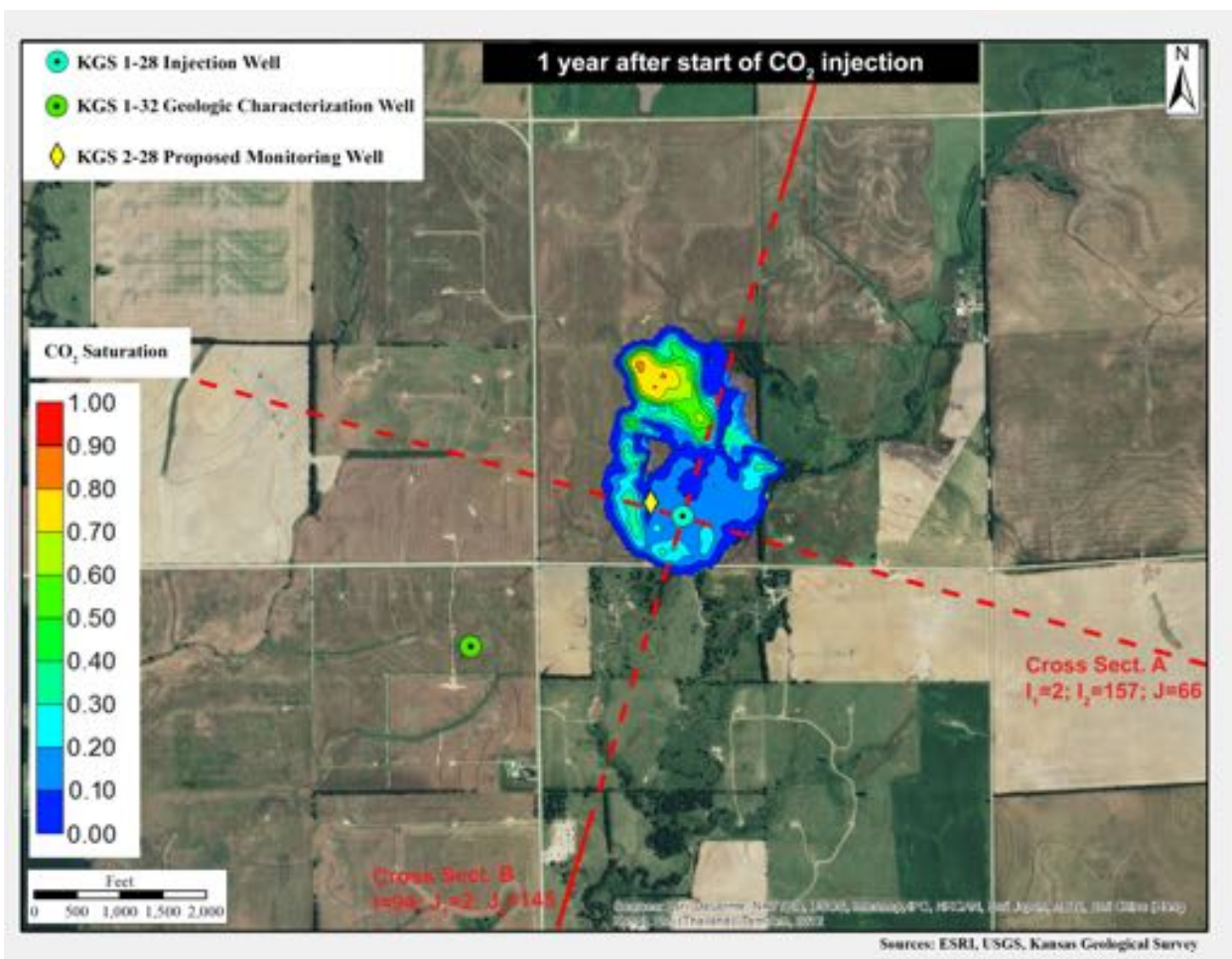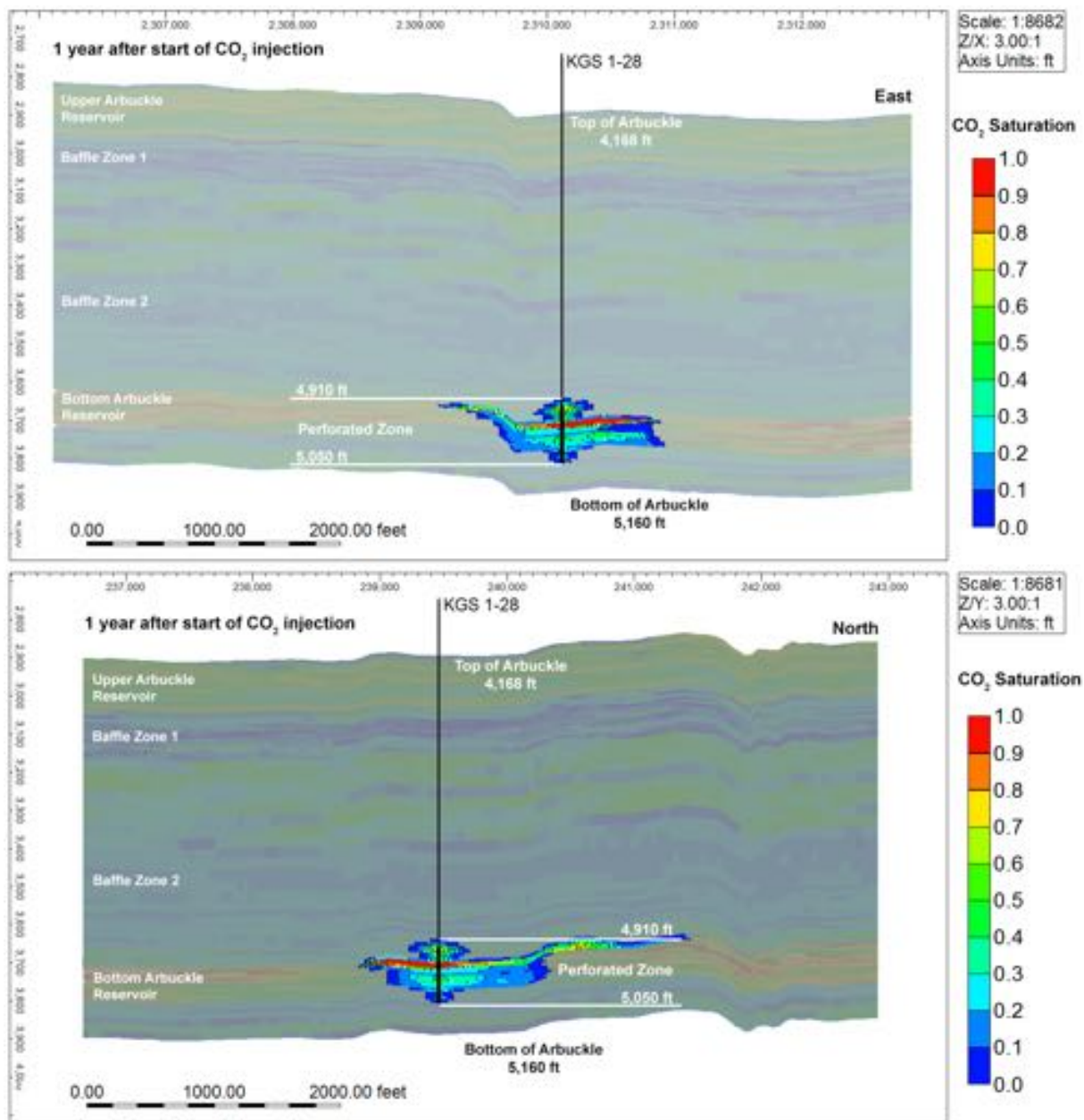
Figure A.6c. Free-phase CO₂ plume in aerial and cross-sectional view for the largest migration alternative model (k-1.25/phi-0.75) at one year from start of injection.
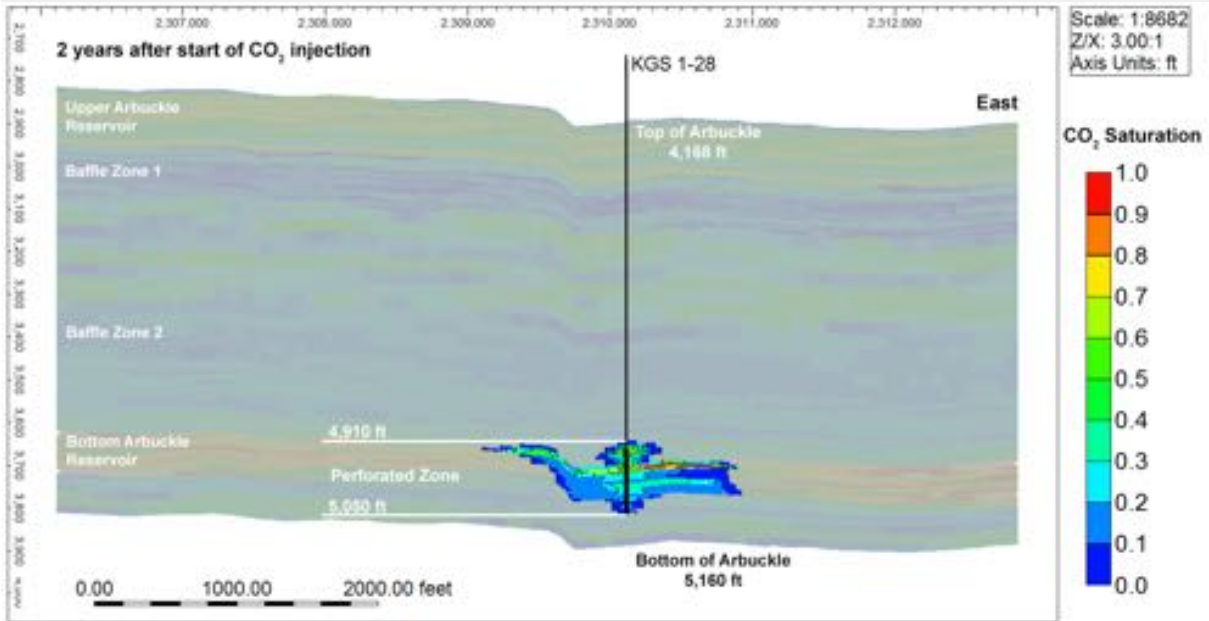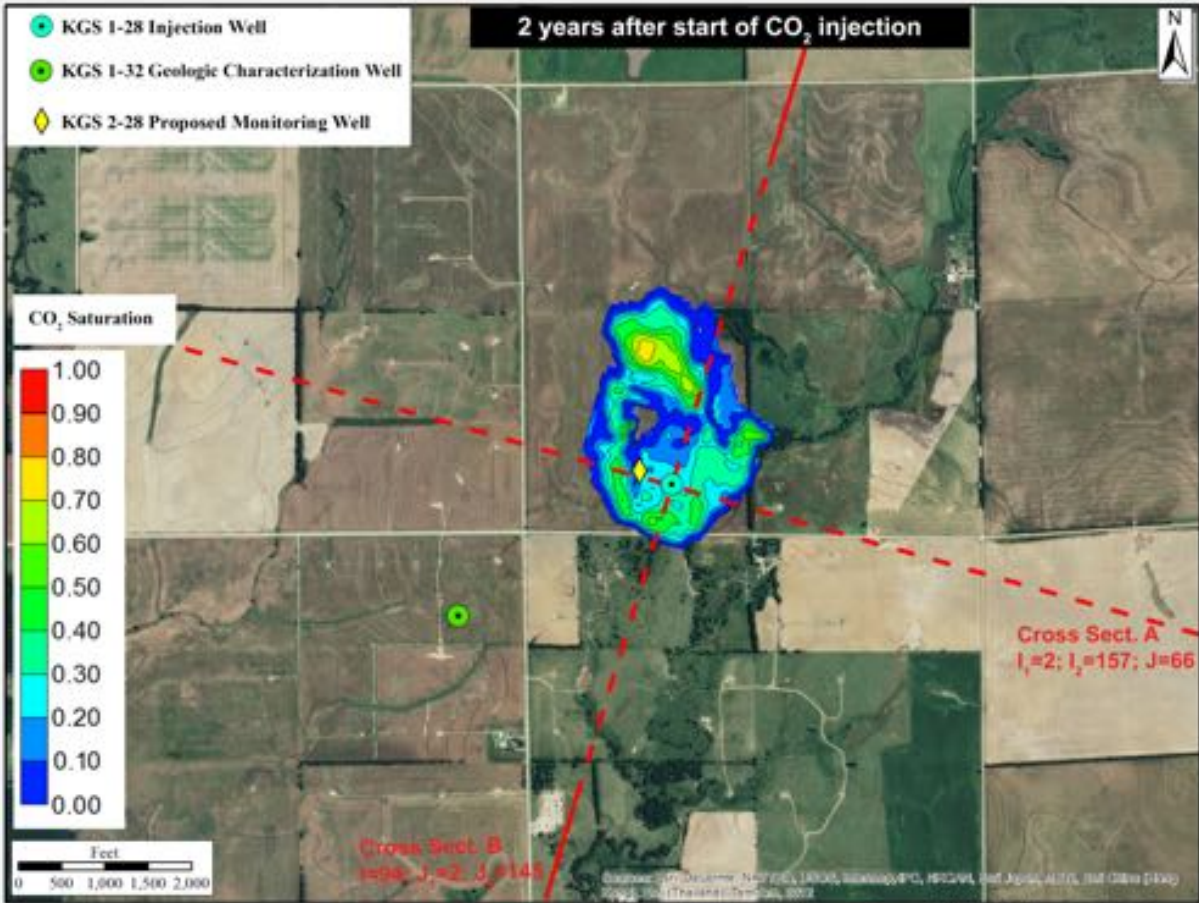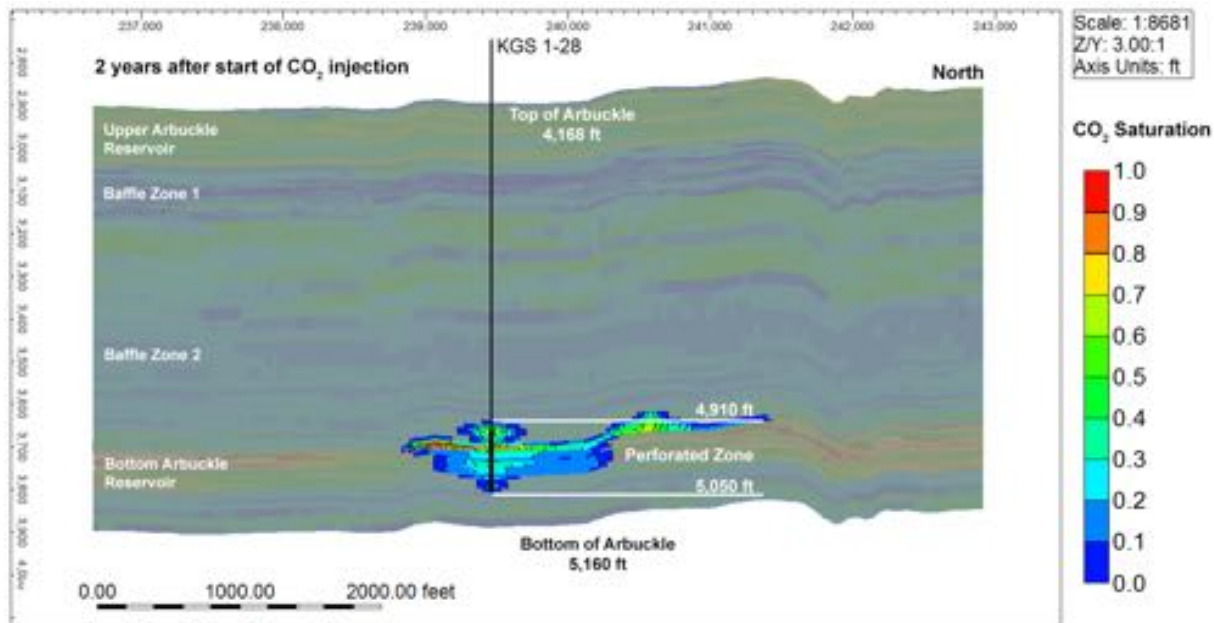
Figure A.6d. Free-phase CO₂ plume in aerial and cross-sectional view for the largest migration alternative model (k-1.25/phi-0.75) at two years from start of injection.
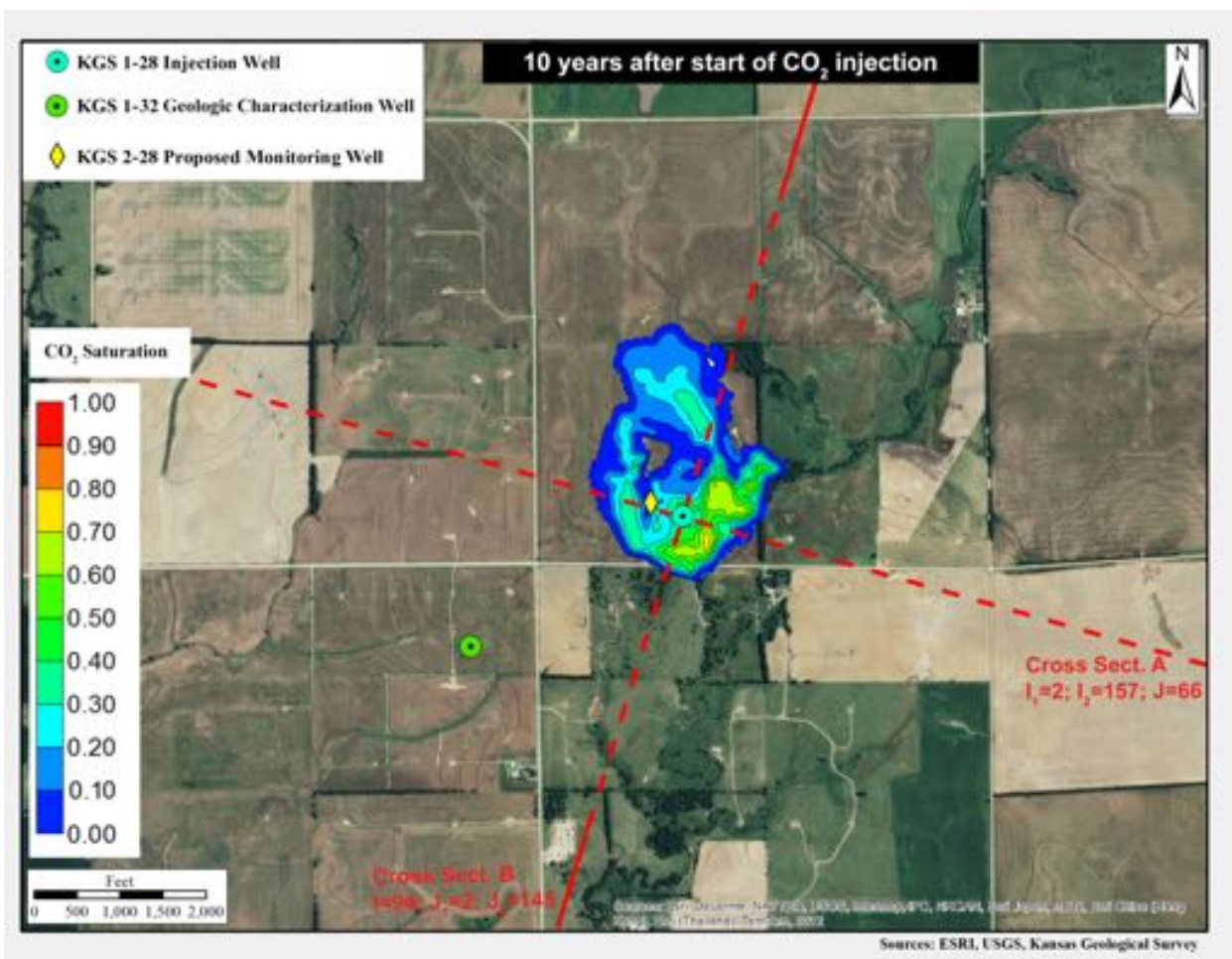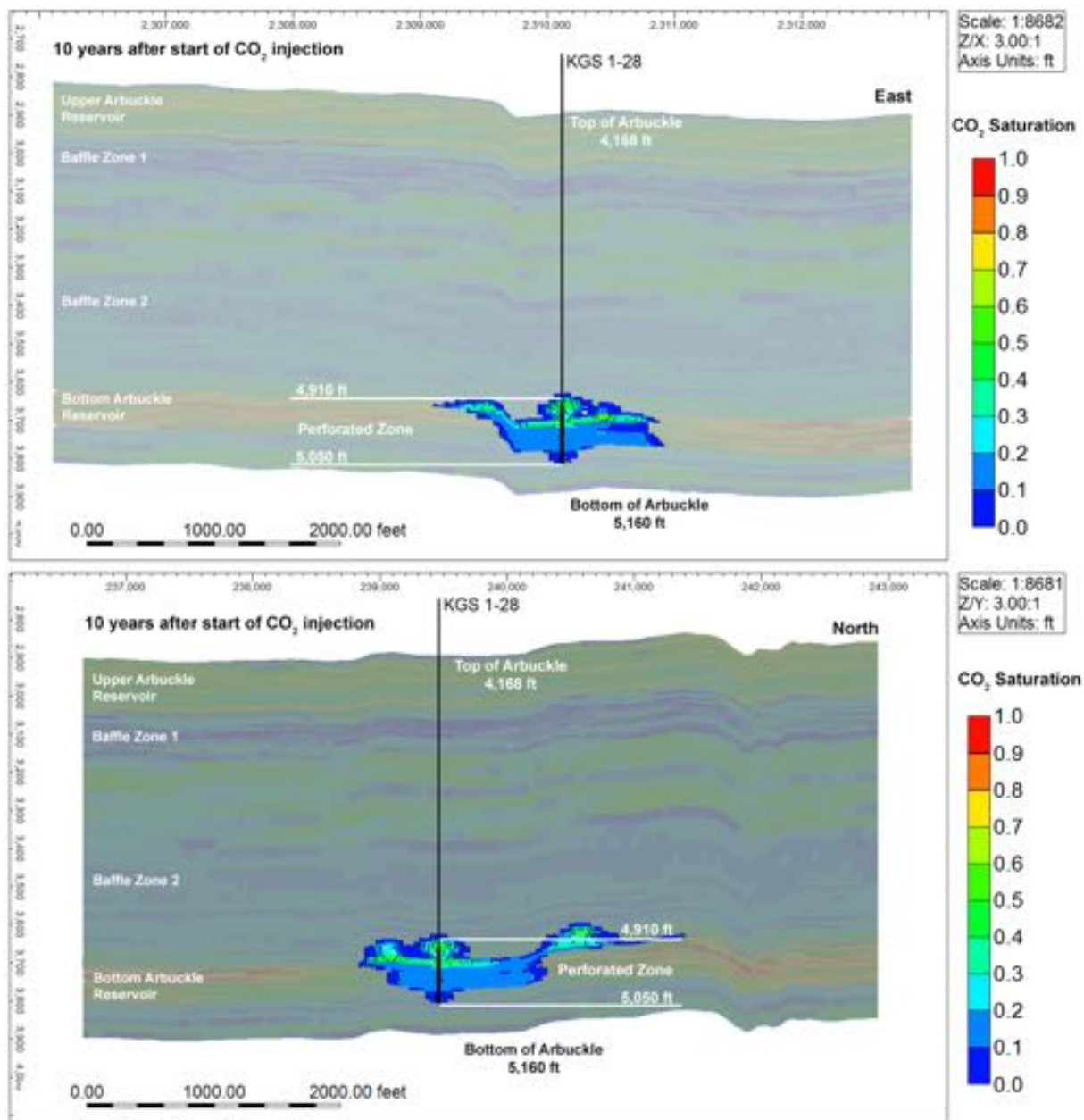
Figure A.6e. Free-phase CO₂ plume in aerial and cross-sectional view for the largest migration alternative model (k-1.25/phi-0.75) at 10 years from start of injection.

100 years after start of CO_2 injection

100 years after start of CO_2 injection
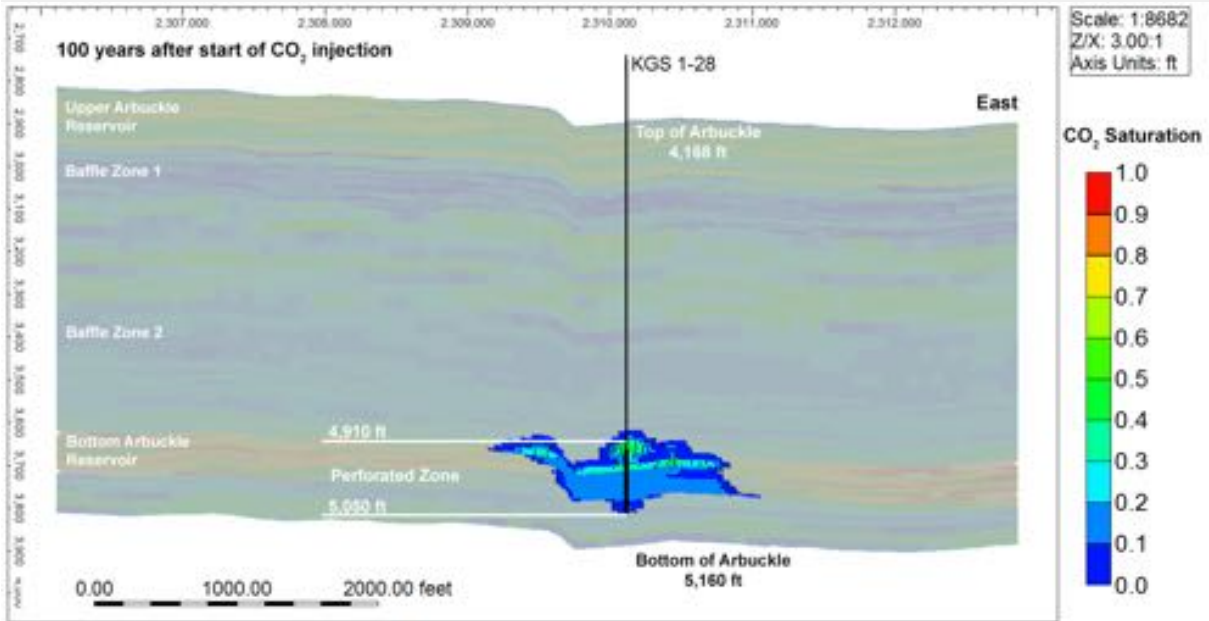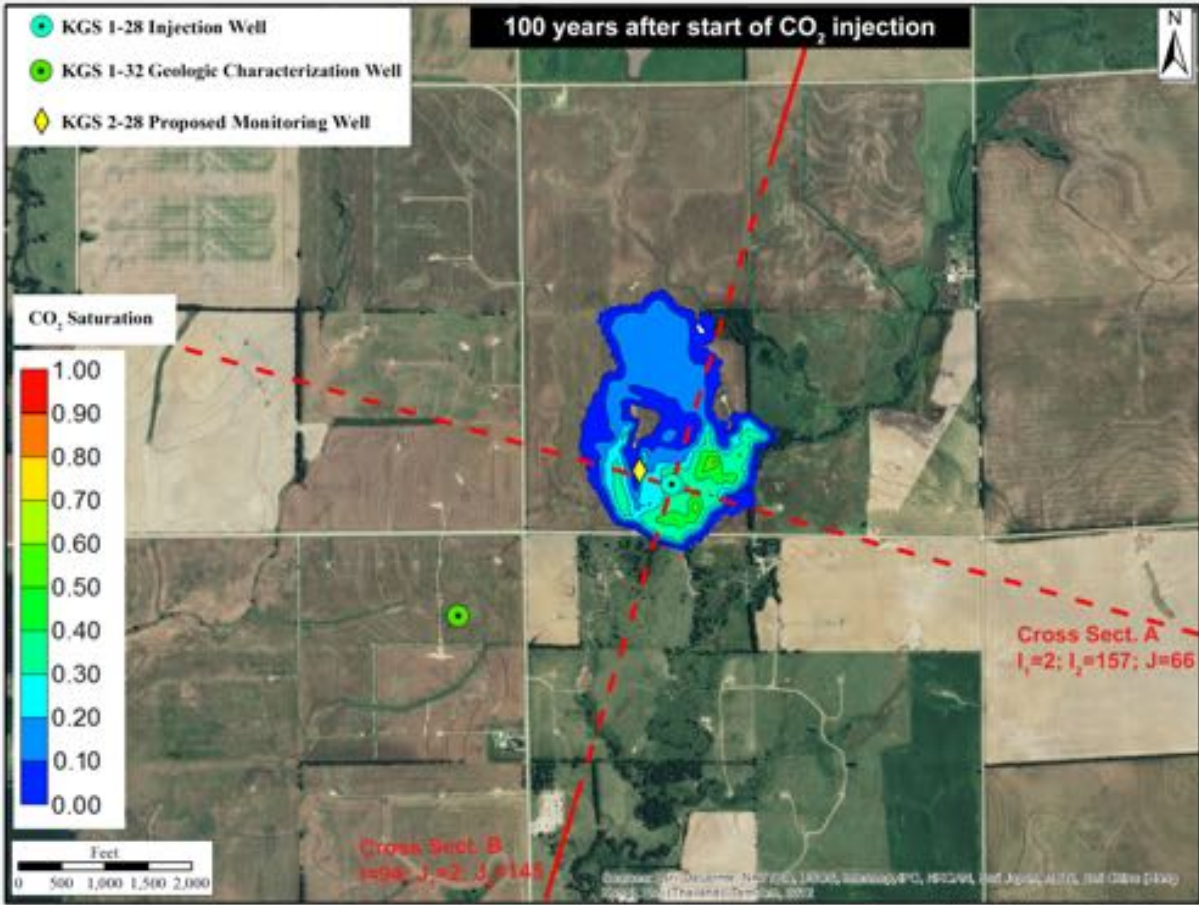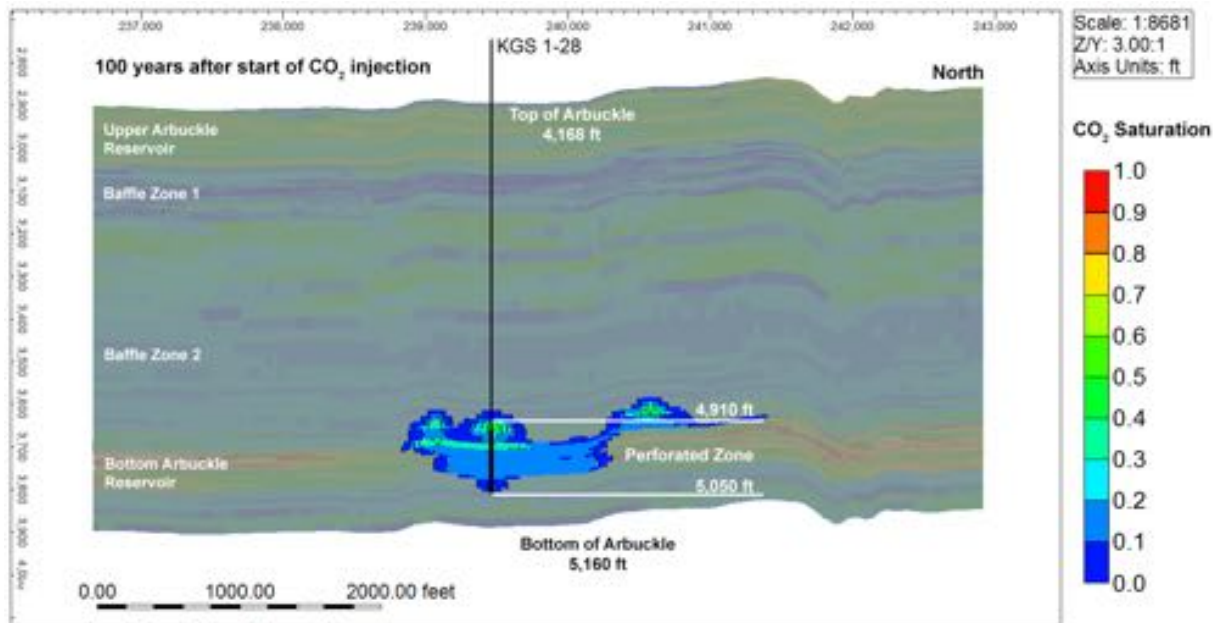
Figure A.6f. Free-phase CO₂ plume in aerial and cross-sectional view for the largest migration alternative model (k-1.25/phi-0.75) at 100 years from start of injection.
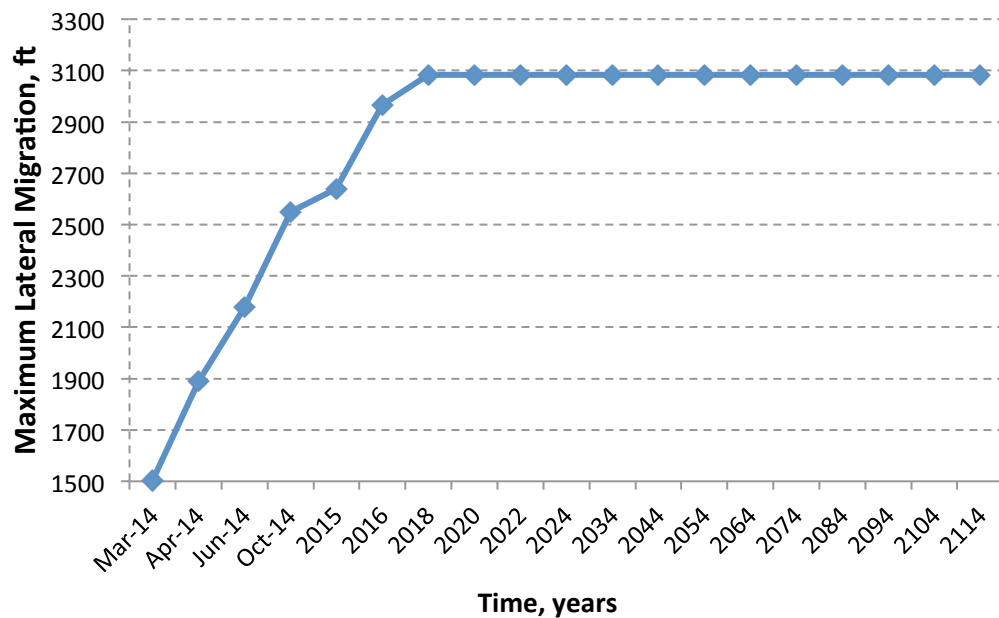
Figure A.7. Maximum lateral extent of CO_2 plume migration (as defined by the 0.5% CO_2 saturation isoline).
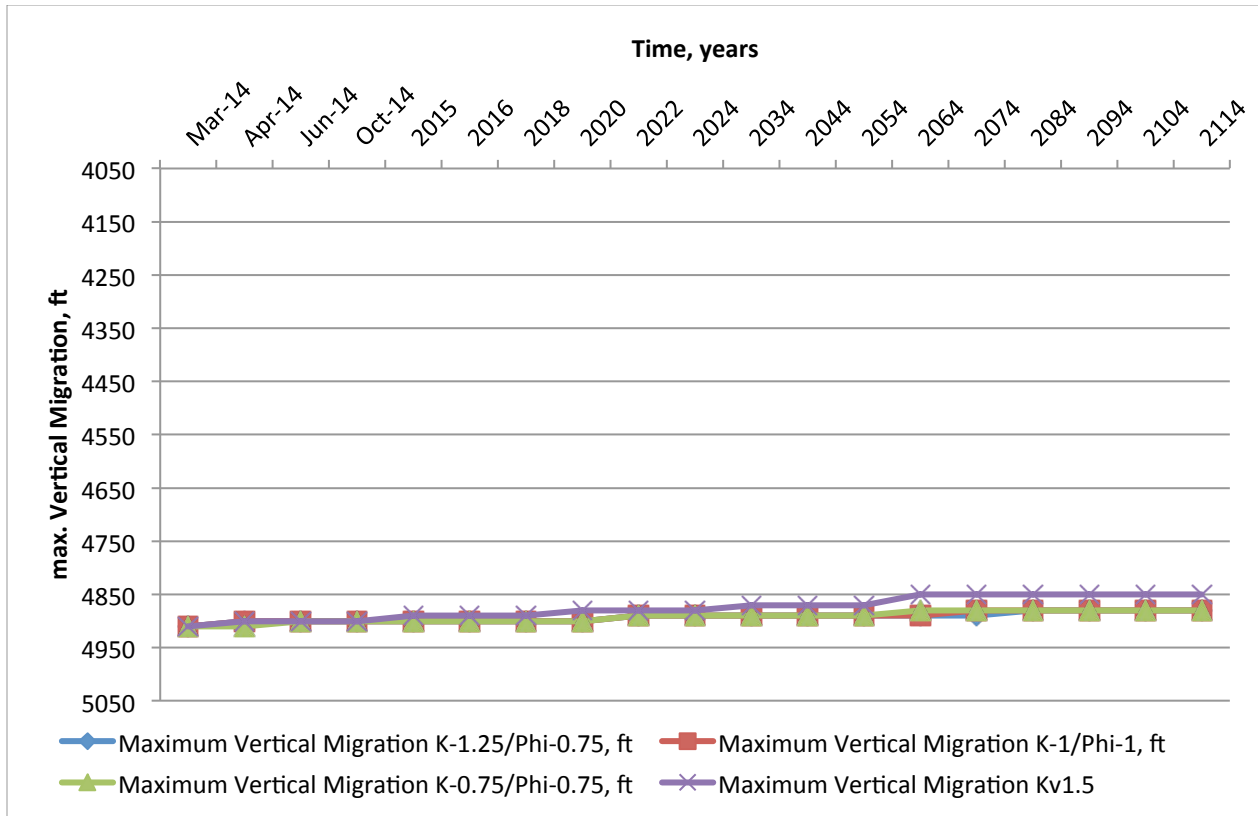
Figure A.8. Maximum vertical extent of free-phase CO_2 migration for the two alternative cases that result in the maximum plume spread (k-1.25/phi-0.75) and the maximum induced pressure (k-0.75/phi-0.75) along with base case (k-1.0/phi-1.0).

A2.2 Long-Term Simulated Total CO_2 Spatial Distribution

Figure A.9a–l corresponds with fig. 17a–l in Section 6 of this report. They represent simulation results for a CO_2 injection volume of 26,000 MT (compared to 40,000 MT in Section 6 simulations). Figure A.9a–l shows the maximum lateral and vertical migration of the CO_2 plume in total concentration and in dissolved phase at the injection interval (elevation 5,010 ft) for the largest areal migration case (k-1.25/phi-0.75).

6 months after start of CO_2 injection

CO₂ Saturation legend (top map):
1.00, 0.90, 0.80, 0.70, 0.60, 0.50, 0.40, 0.30, 0.20, 0.10, 0.00

KGS 1-28 Injection Well
KGS 1-32 Geologic Characterization Well
KGS 2-28 Proposed Monitoring Well

Cross Sect. A
I₁=2; I₂=157; J=66

Cross Sect. B
I=98; J₁=2; J₂=145

Sources: ESRI, USGS, Kansas Geological Survey

6 months after start of CO_2 injection

Scale: 1:8682
Z/X: 3.00:1
Axis Units: ft

KGS 1-28

East

Upper Arbuckle Reservoir
Baffle Zone 1
Top of Arbuckle 4,168 ft
Baffle Zone 2
Bottom Arbuckle Reservoir
4,910 ft
Perforated Zone
5,050 ft
Bottom of Arbuckle 5,160 ft

CO₂ Saturation legend (cross section):
1.0, 0.9, 0.8, 0.7, 0.6, 0.5, 0.4, 0.3, 0.2, 0.1, 0.0

Figure A.9a. Total CO$_2$ spatial distribution in aerial and cross-sectional view for the largest migration alternative model (k-1.25/phi-0.75) at six months from start of injection.

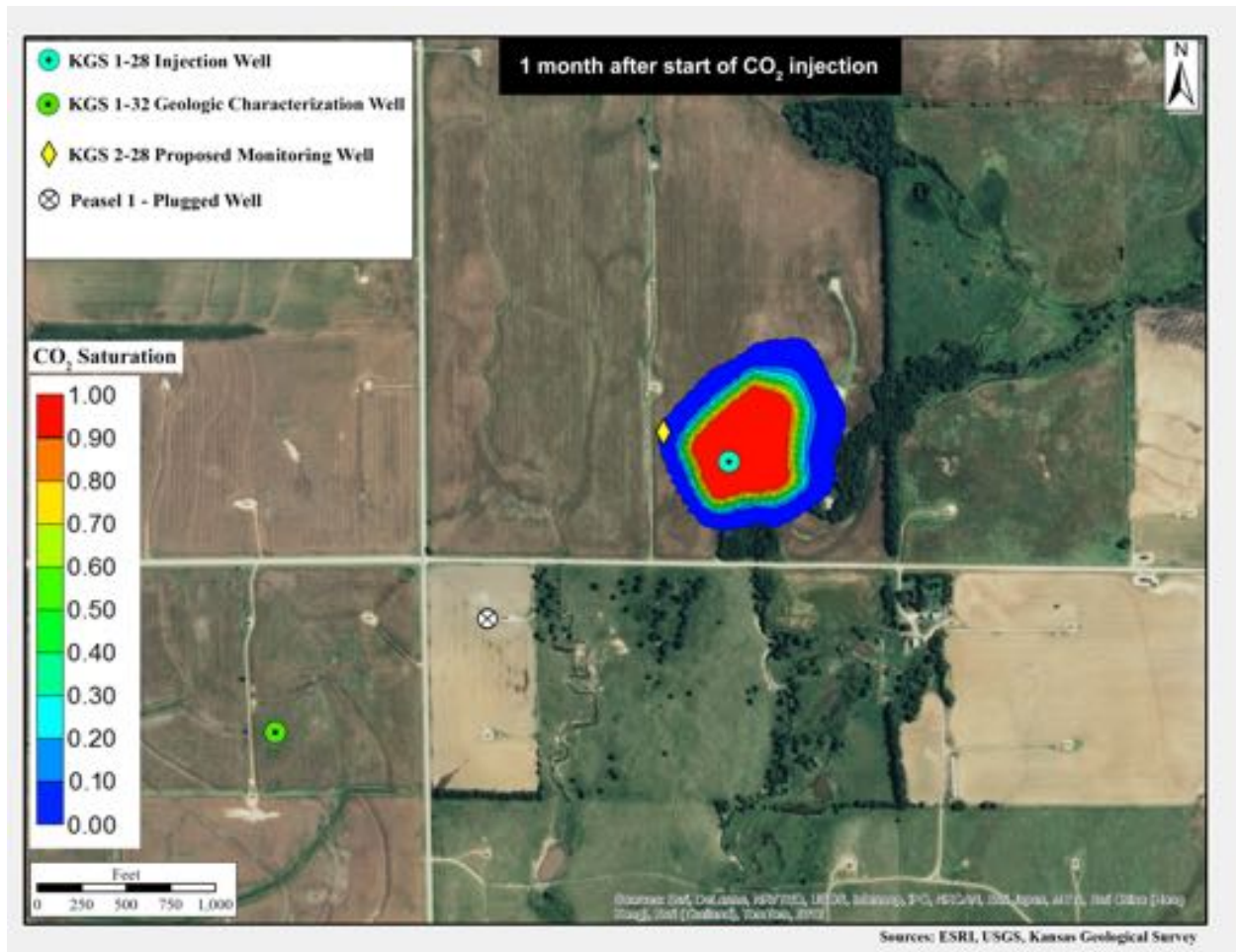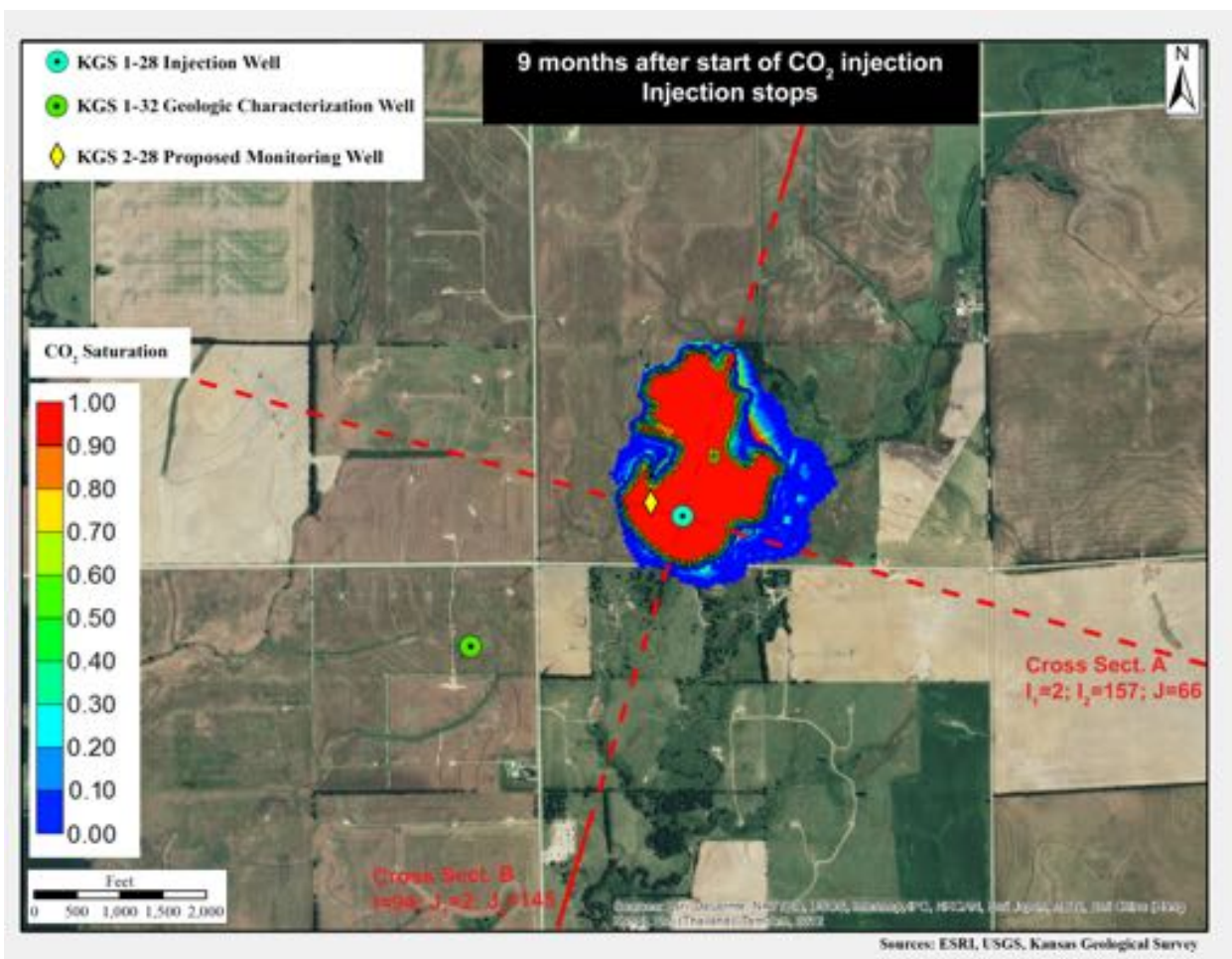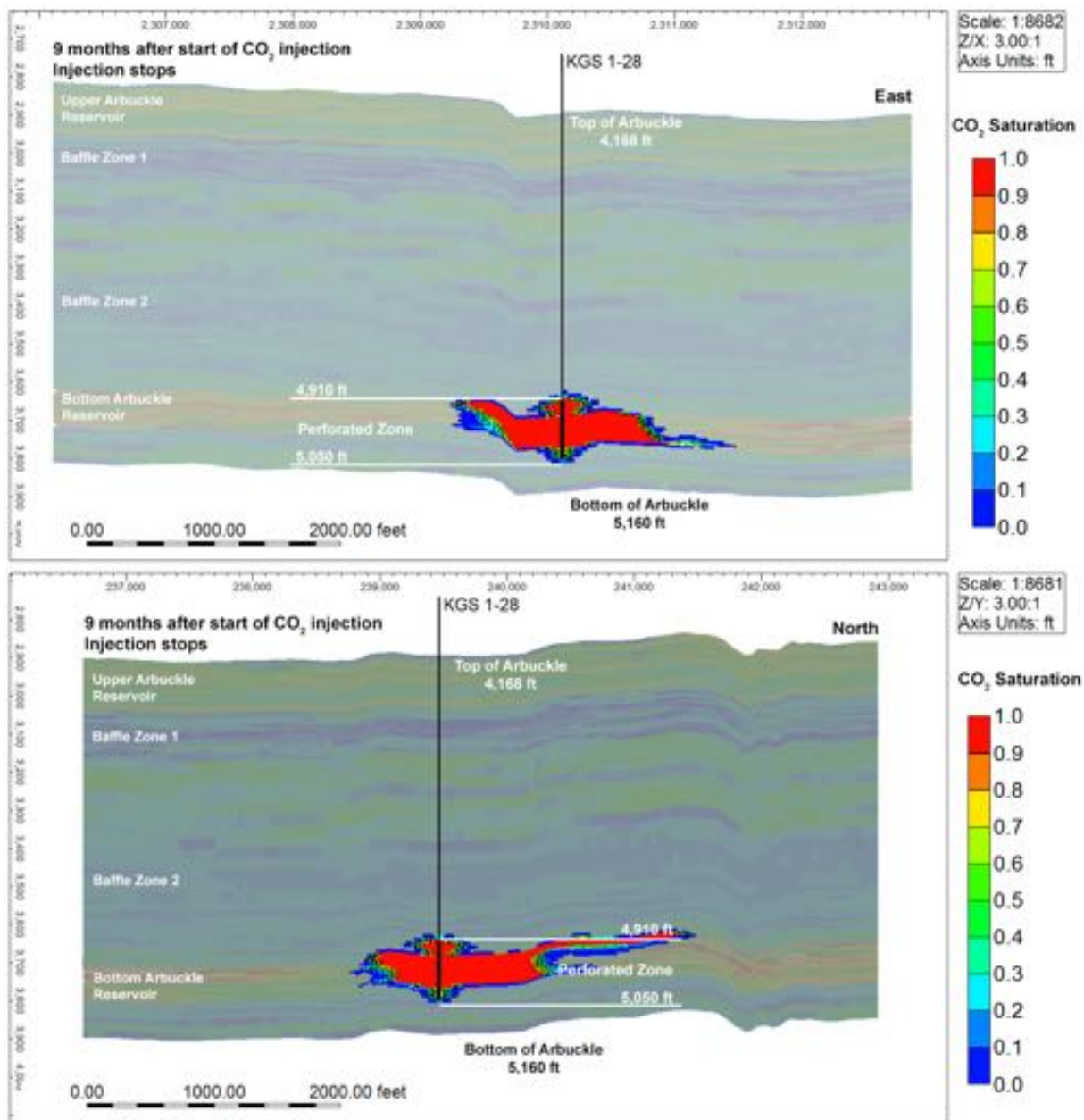*Figure A.9b. Total CO$_2$ spatial distribution in aerial and cross-sectional view for the largest migration alternative model (k-1.25/phi-0.75) at nine months from start of injection. Injection stops at the end of this month.*

1 year after start of CO_2 injection

KGS 1-28 Injection Well
KGS 1-32 Geologic Characterization Well
KGS 2-28 Proposed Monitoring Well

CO_2 Saturation

1.00
0.90
0.80
0.70
0.60
0.50
0.40
0.30
0.20
0.10
0.00

Feet
0   500 1,000 1,500 2,000

Cross Sect. A
I₁=2; I₂=157; J=66

Sources: ESRI, USGS, Kansas Geological Survey

1 year after start of CO_2 injection

KGS 1-28

East

Scale: 1:8682
Z/X: 3.00:1
Axis Units: ft

Upper Arbuckle Reservoir
Baffle Zone 1
Top of Arbuckle 4,168 ft
Baffle Zone 2
Bottom Arbuckle Reservoir
4,910 ft
Perforated Zone
5,050 ft
Bottom of Arbuckle 5,160 ft

CO_2 Saturation

1.0
0.9
0.8
0.7
0.6
0.5
0.4
0.3
0.2
0.1
0.0

0.00   1000.00   2000.00 feet

Figure A.9c. Total CO$_2$ spatial distribution in aerial and cross-sectional view for the largest migration alternative model (k-1.25/phi-0.75) at one year from start of injection.
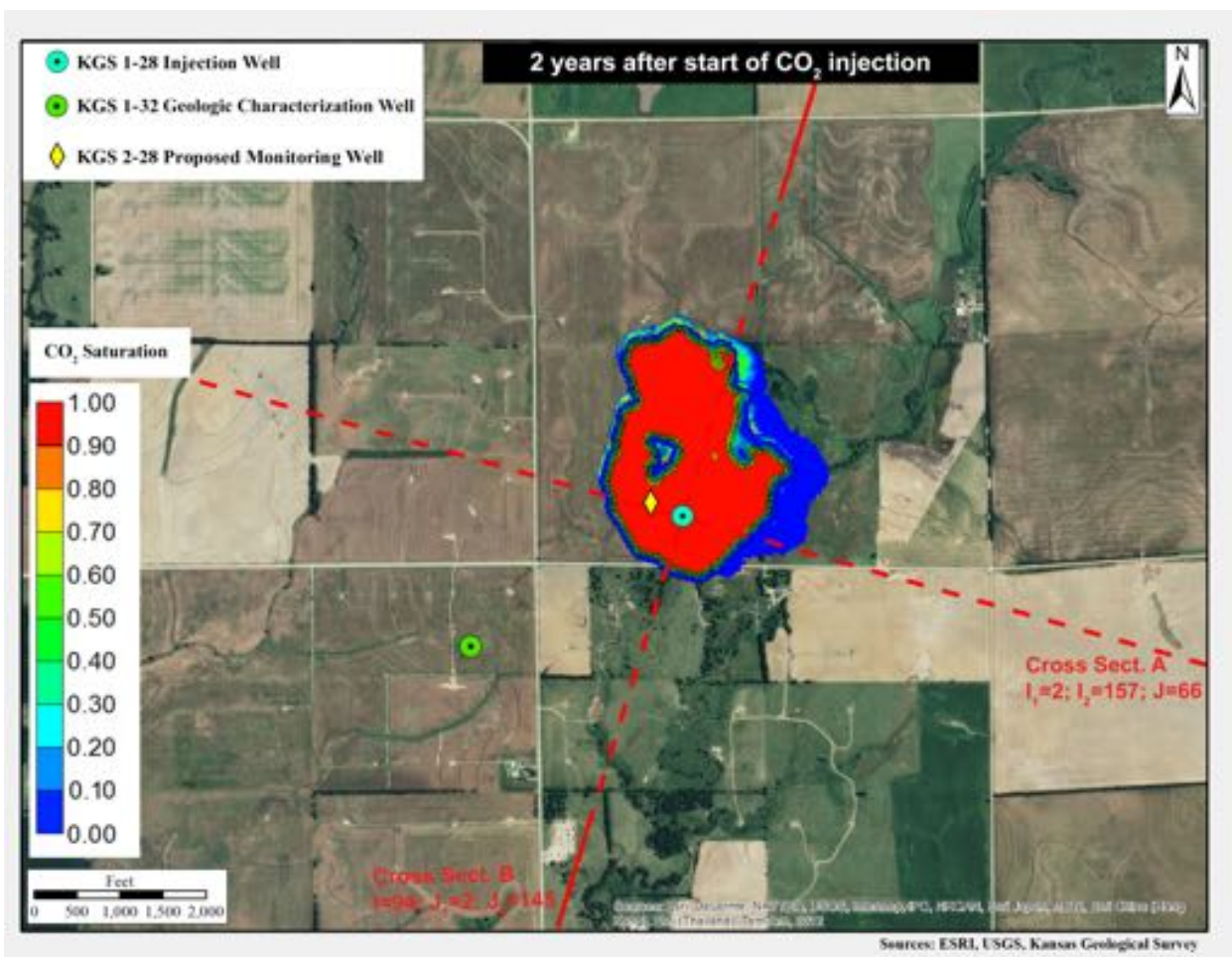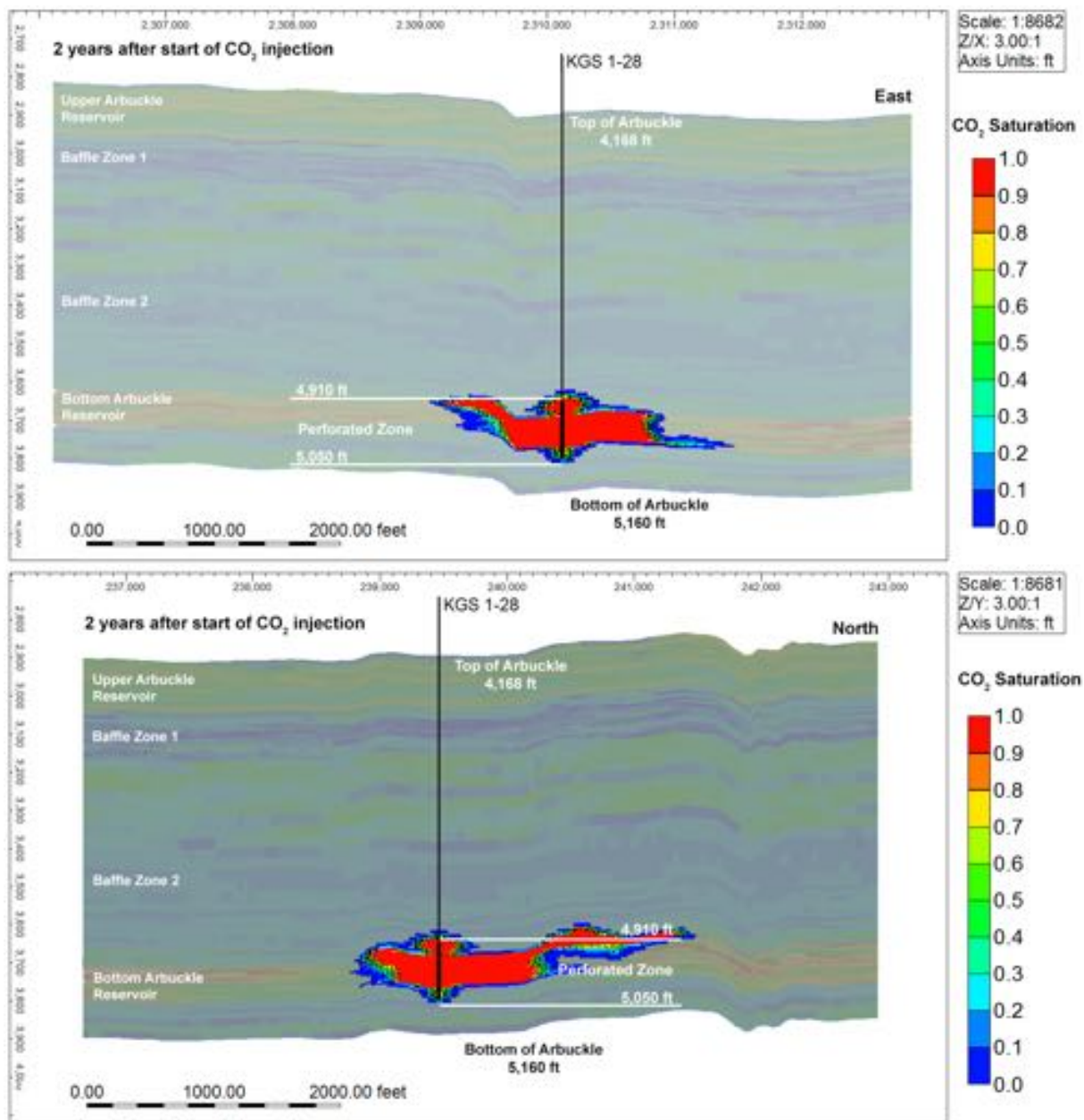
Figure A.9d. Total CO₂ spatial distribution in aerial and cross-sectional view for the largest migration alternative model (k-1.25/phi-0.75) at two years from start of injection.

10 years after start of CO_2 injection

10 years after start of CO_2 injection
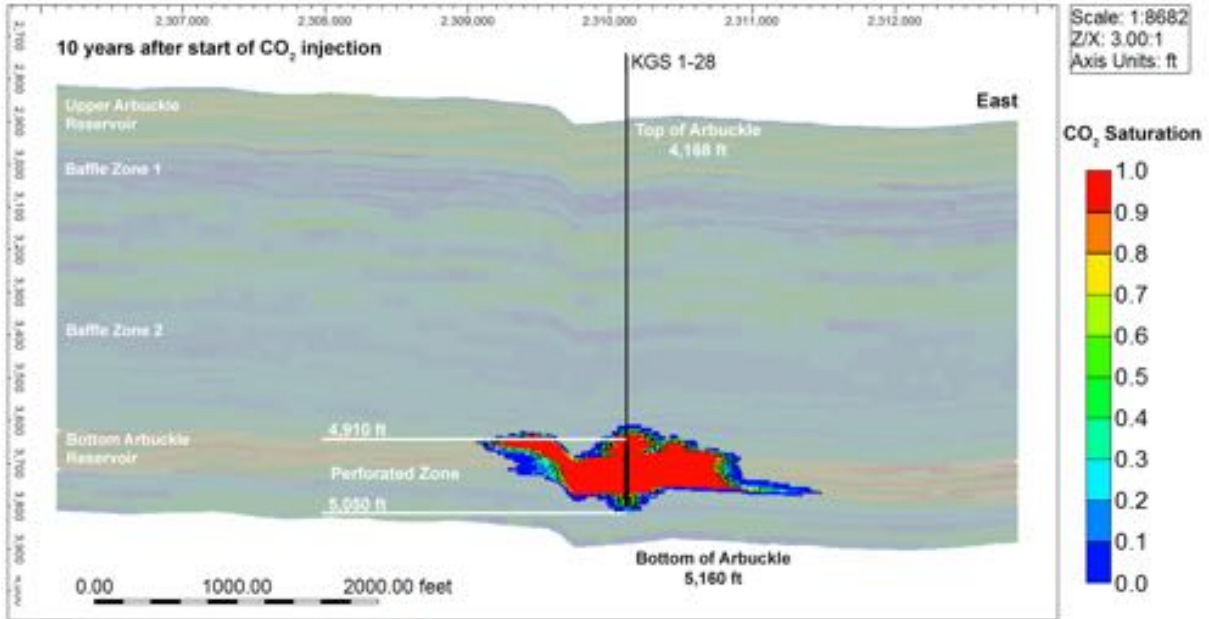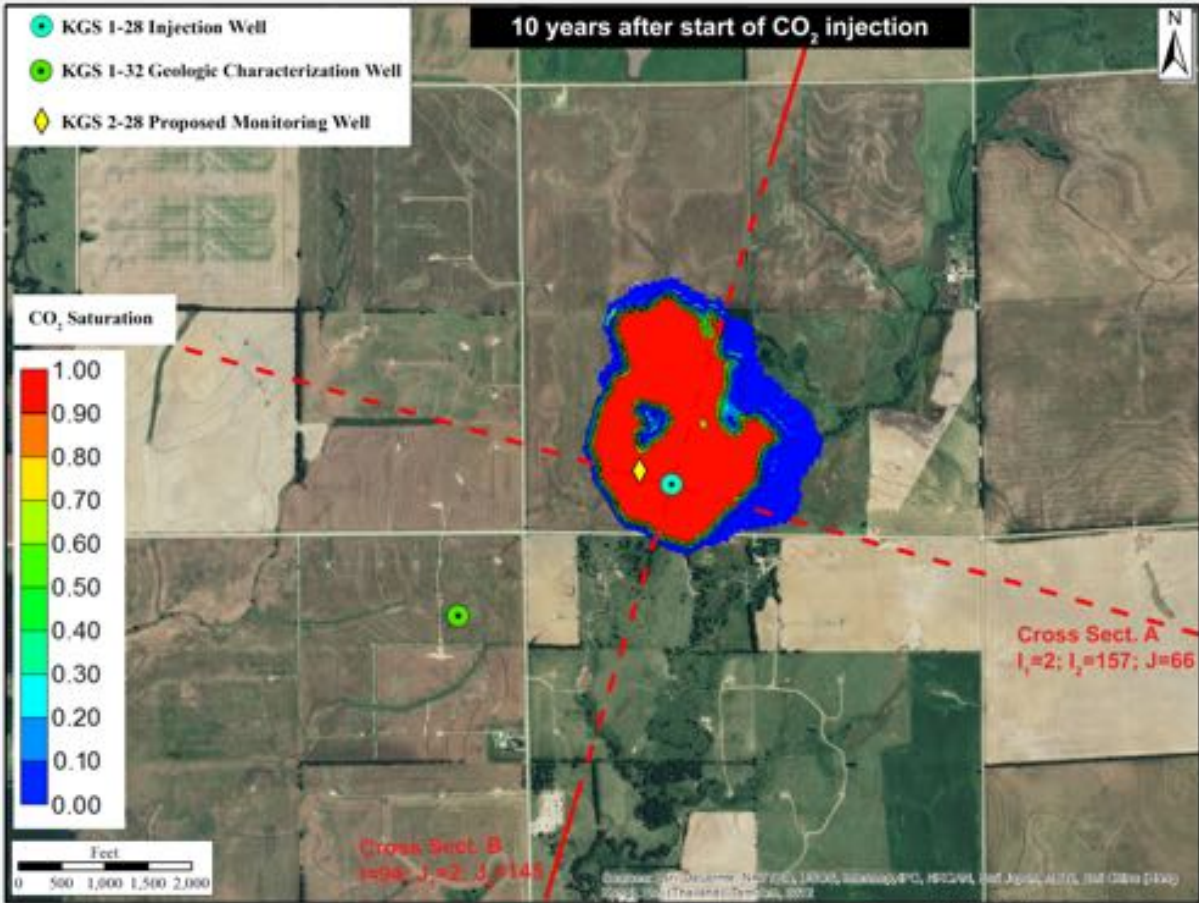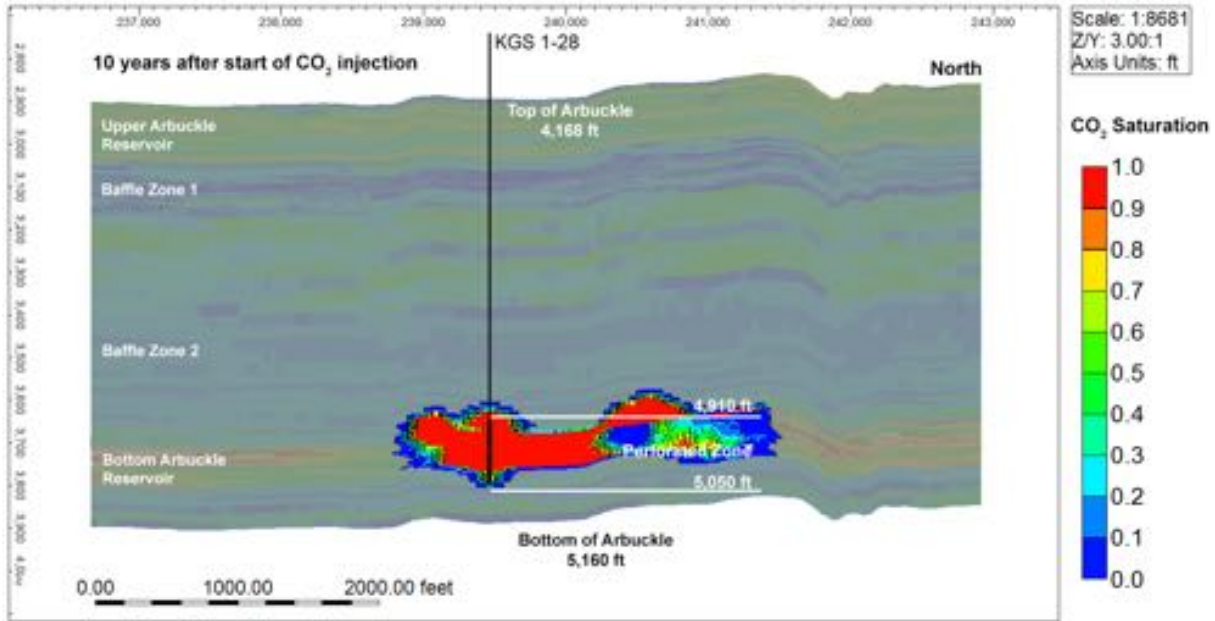
Figure A.9e. Total CO$_2$ spatial distribution in aerial and cross-sectional view for the largest migration alternative model (k-1.25/phi-0.75) at 10 years from start of injection.
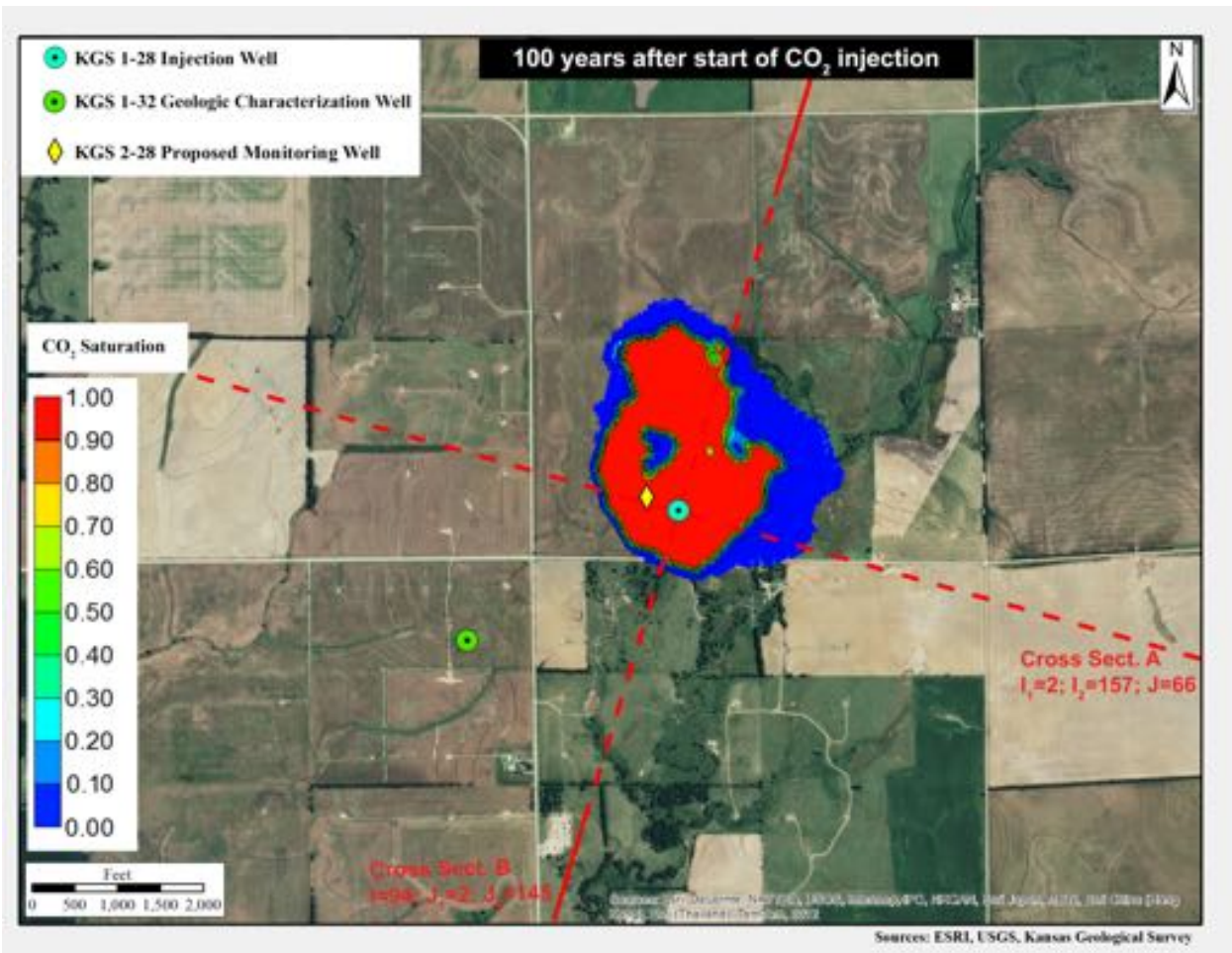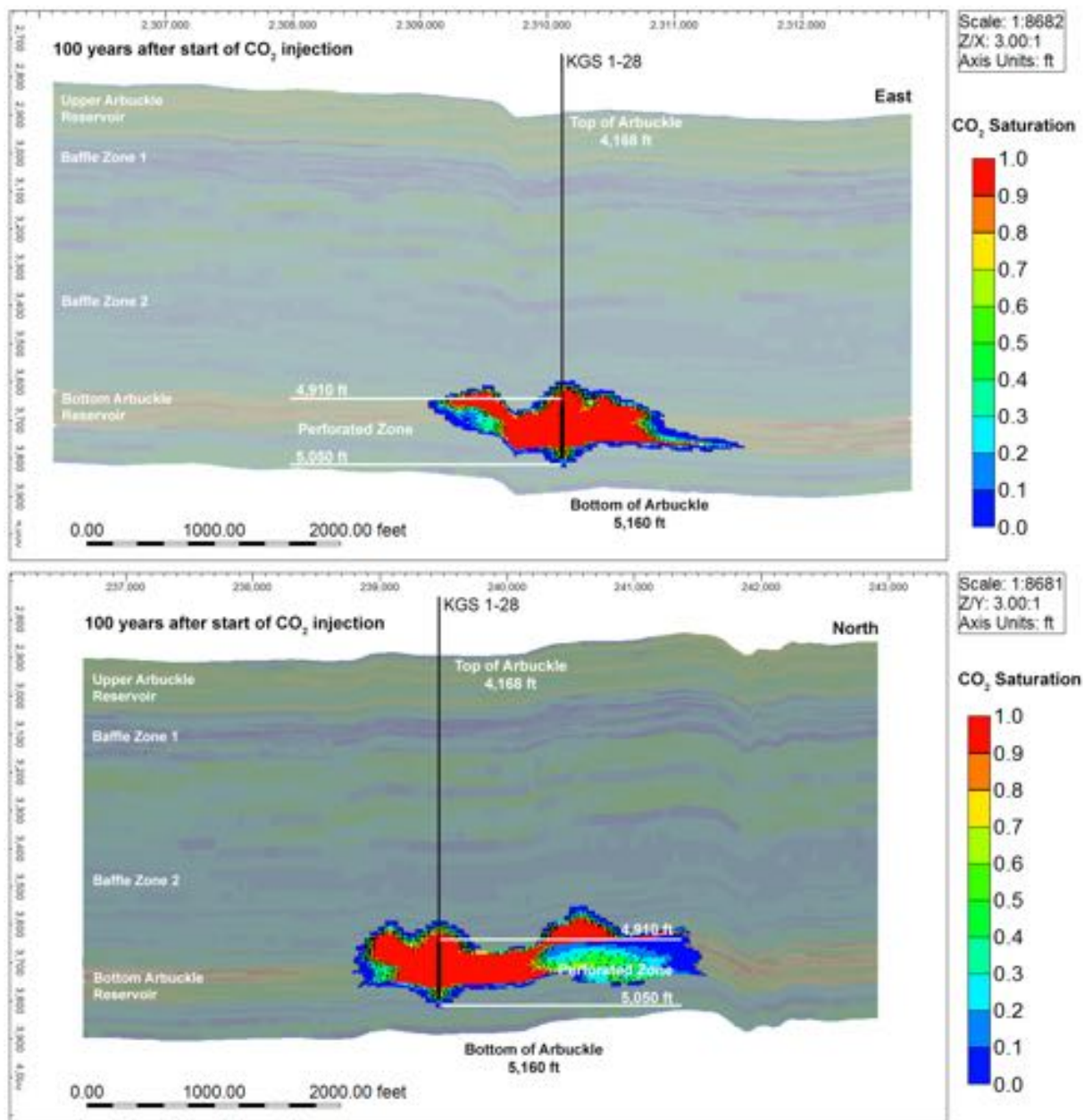
Figure A.9f. Total CO$_2$ spatial distribution in aerial and cross-sectional view for the largest migration alternative model (k-1.25/phi-0.75) at 100 years from start of injection.

6 months after start of CO₂ injection
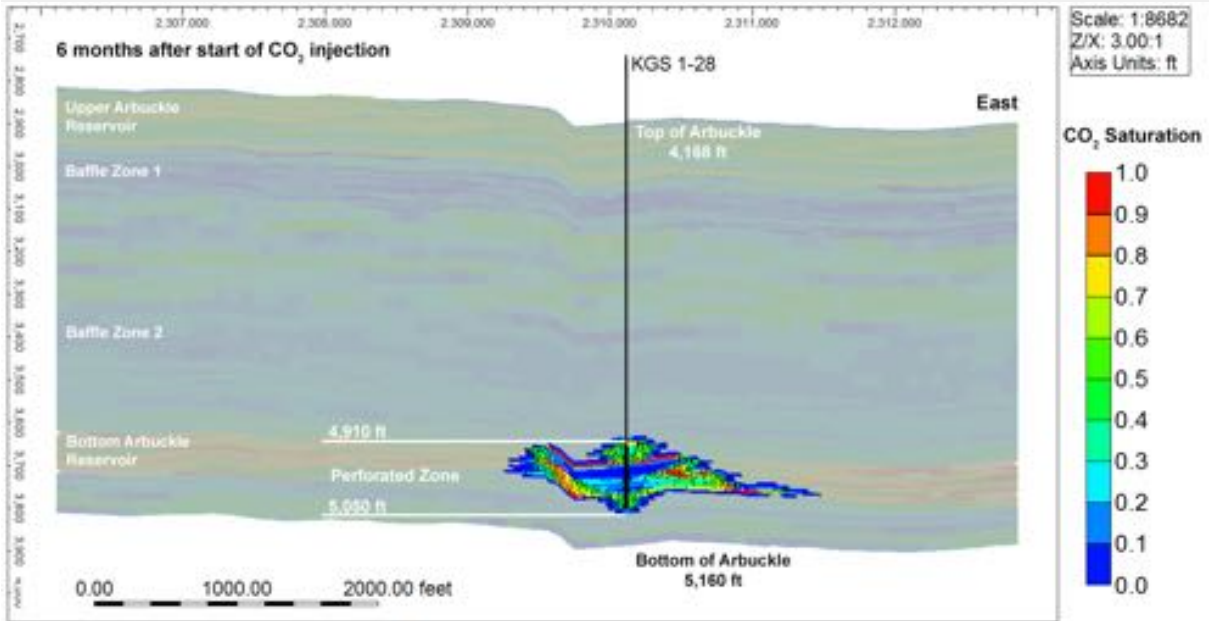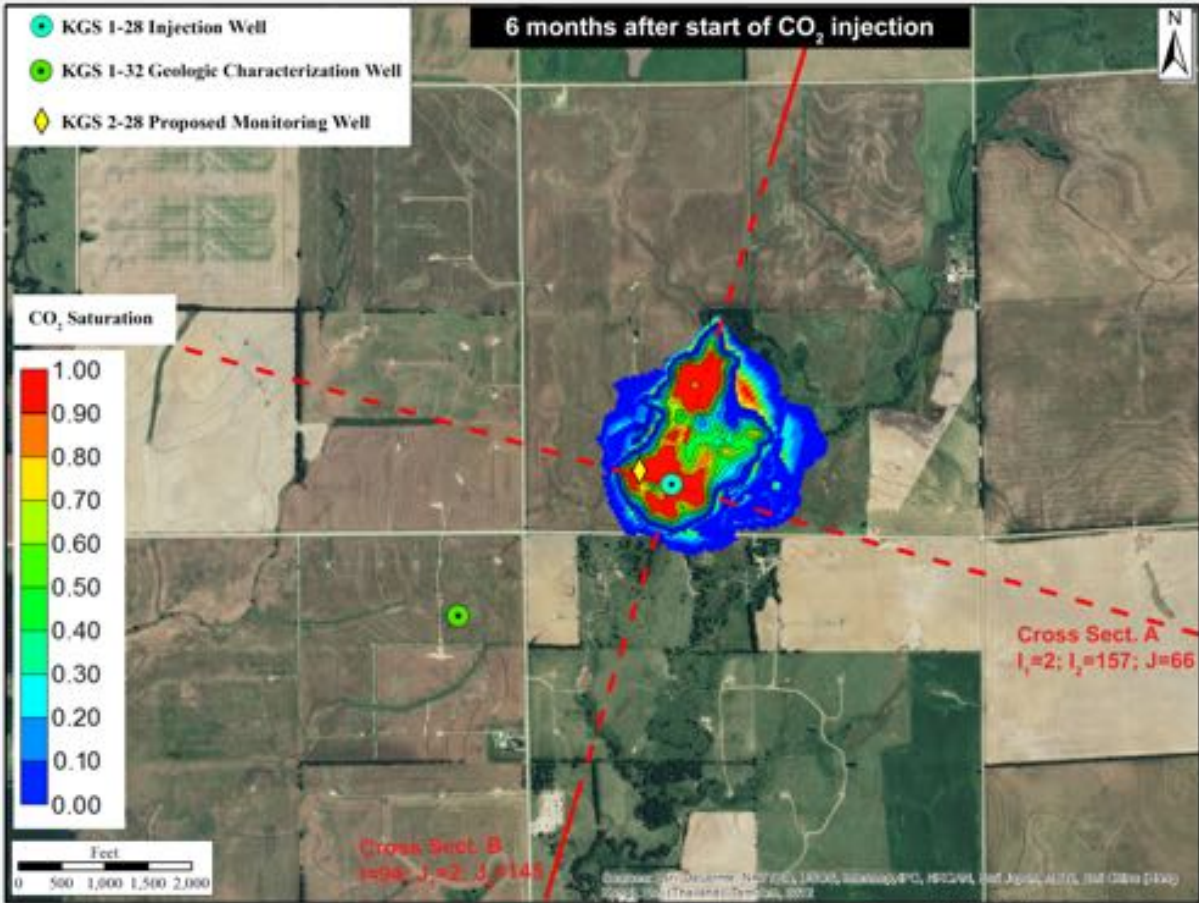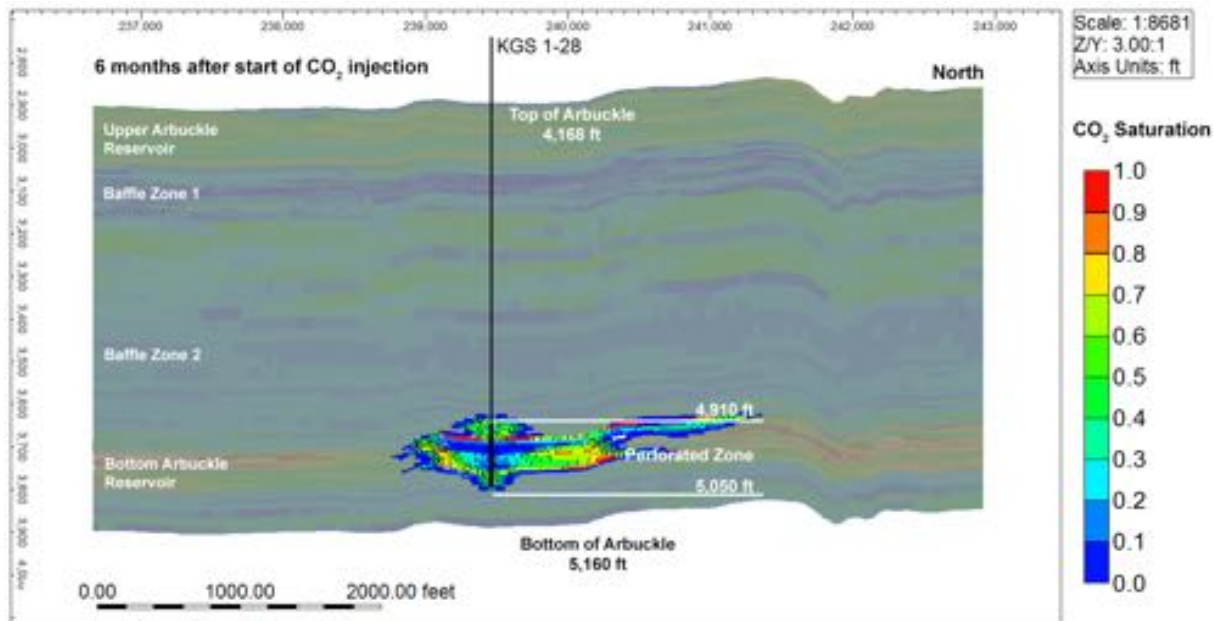
Figure A.9g. Dissolved CO_2 spatial distribution in aerial and cross-sectional view for the largest migration alternative model (k-1.25/phi-0.75) at six months from start of injection.
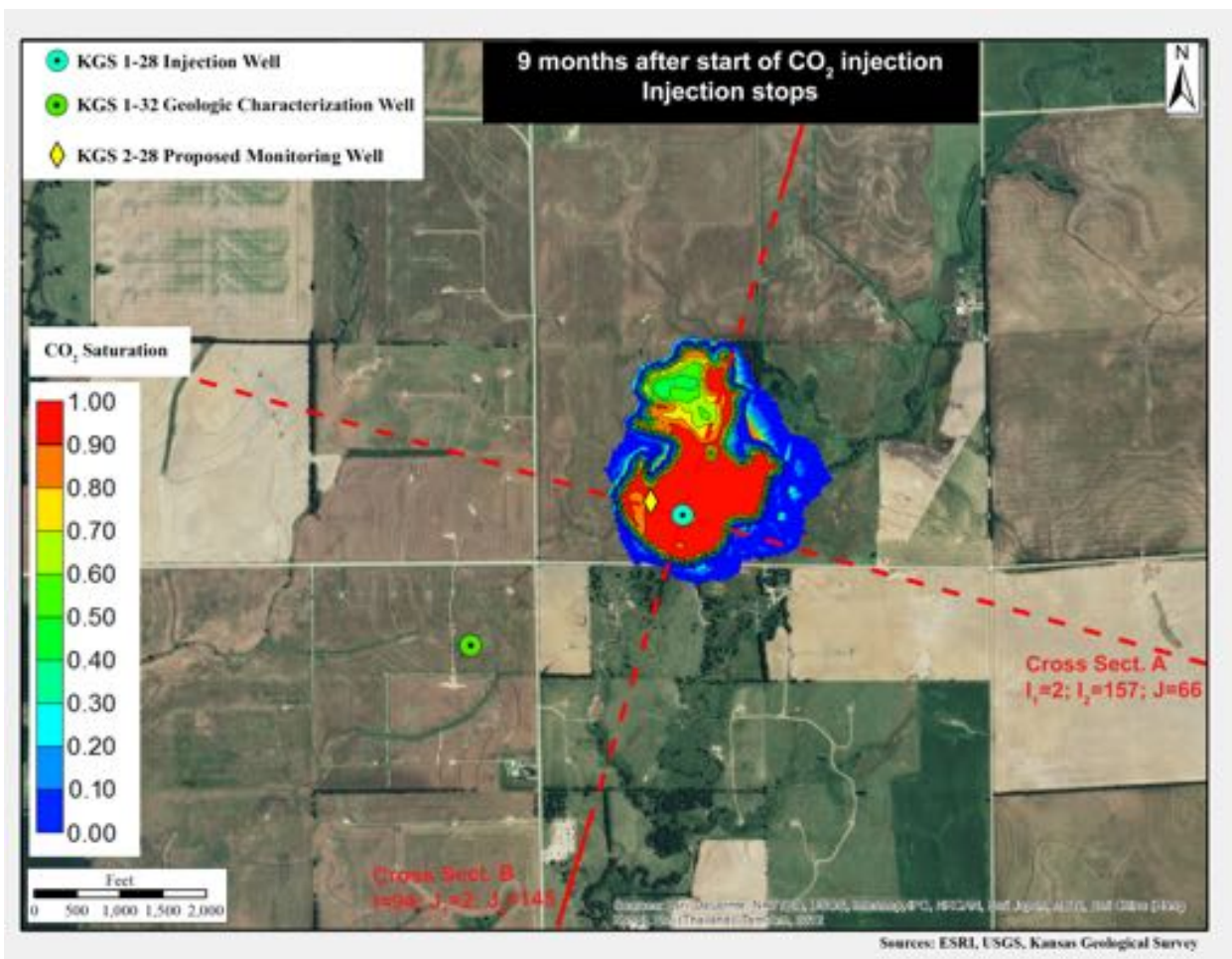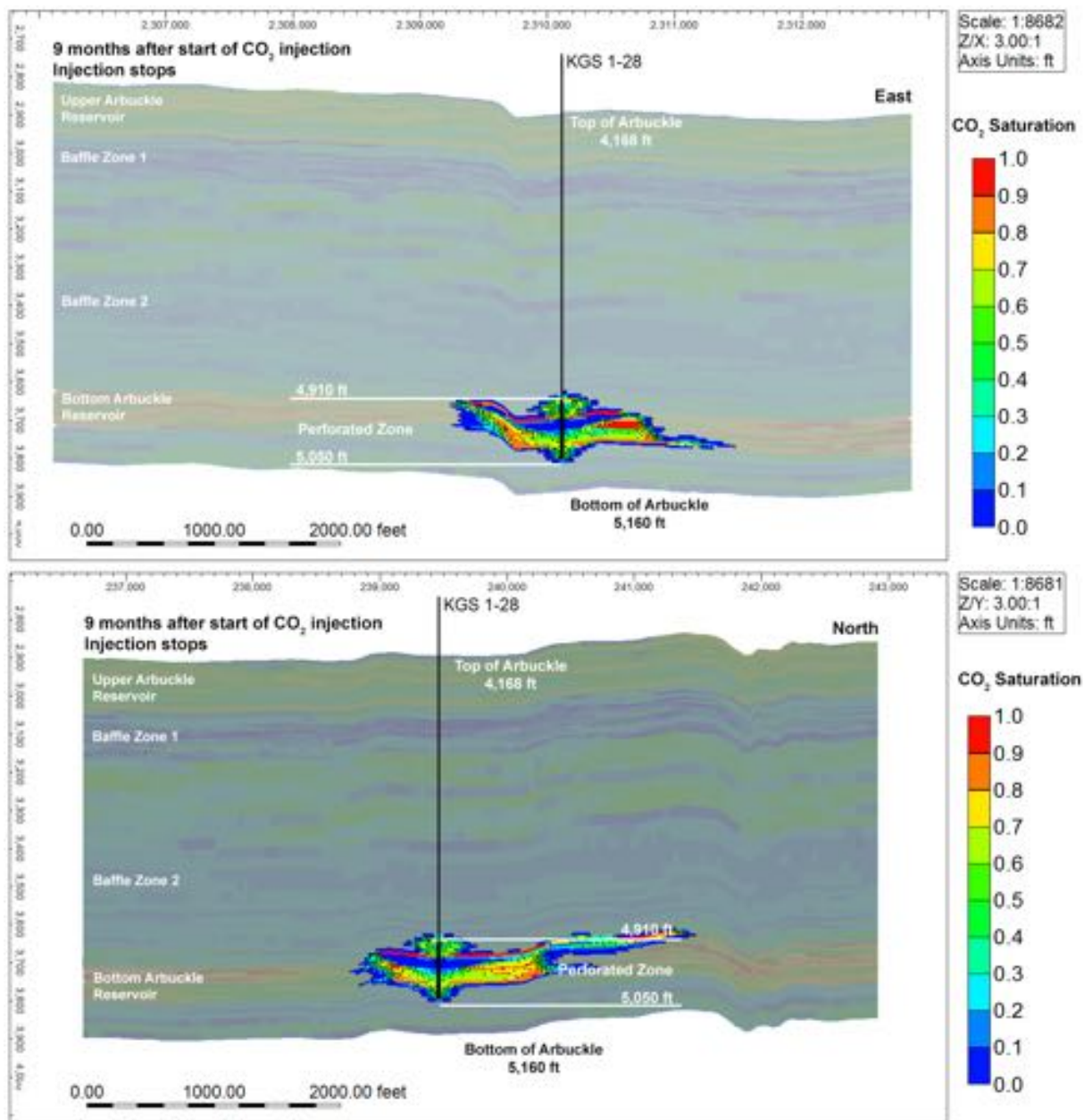
Figure A.9h. Dissolved CO_2 spatial distribution in aerial and cross-sectional view for the largest migration alternative model (k-1.25/phi-0.75) at nine months from start of injection. Injection stops at the end of this month.

1 year after start of CO₂ injection

1 year after start of CO₂ injection
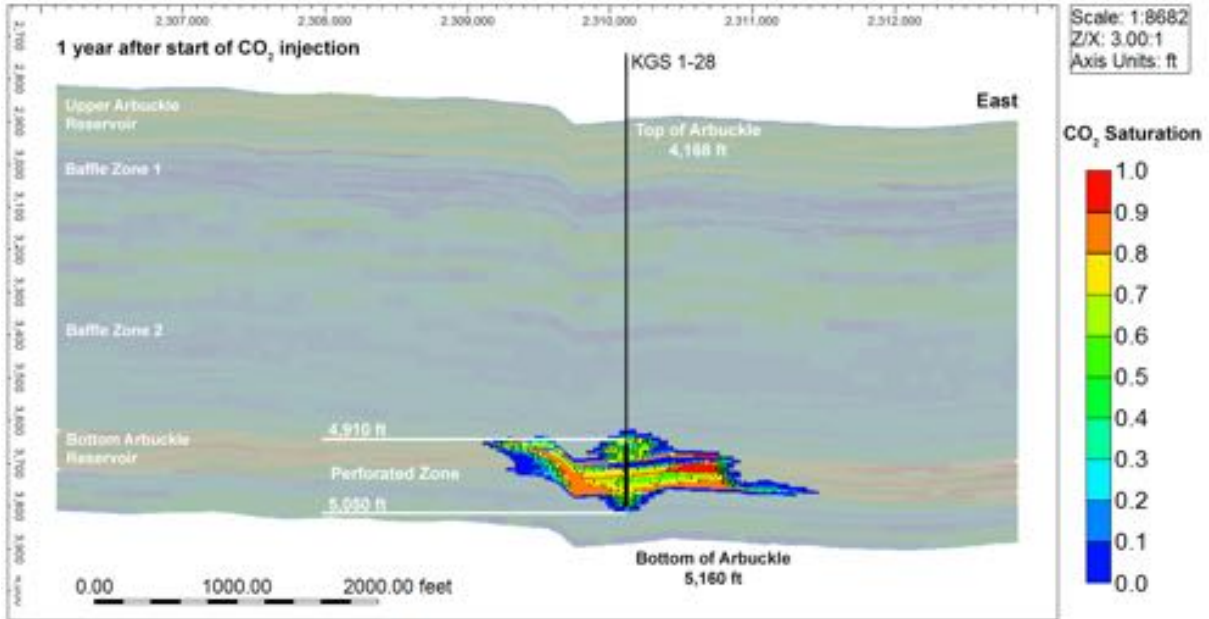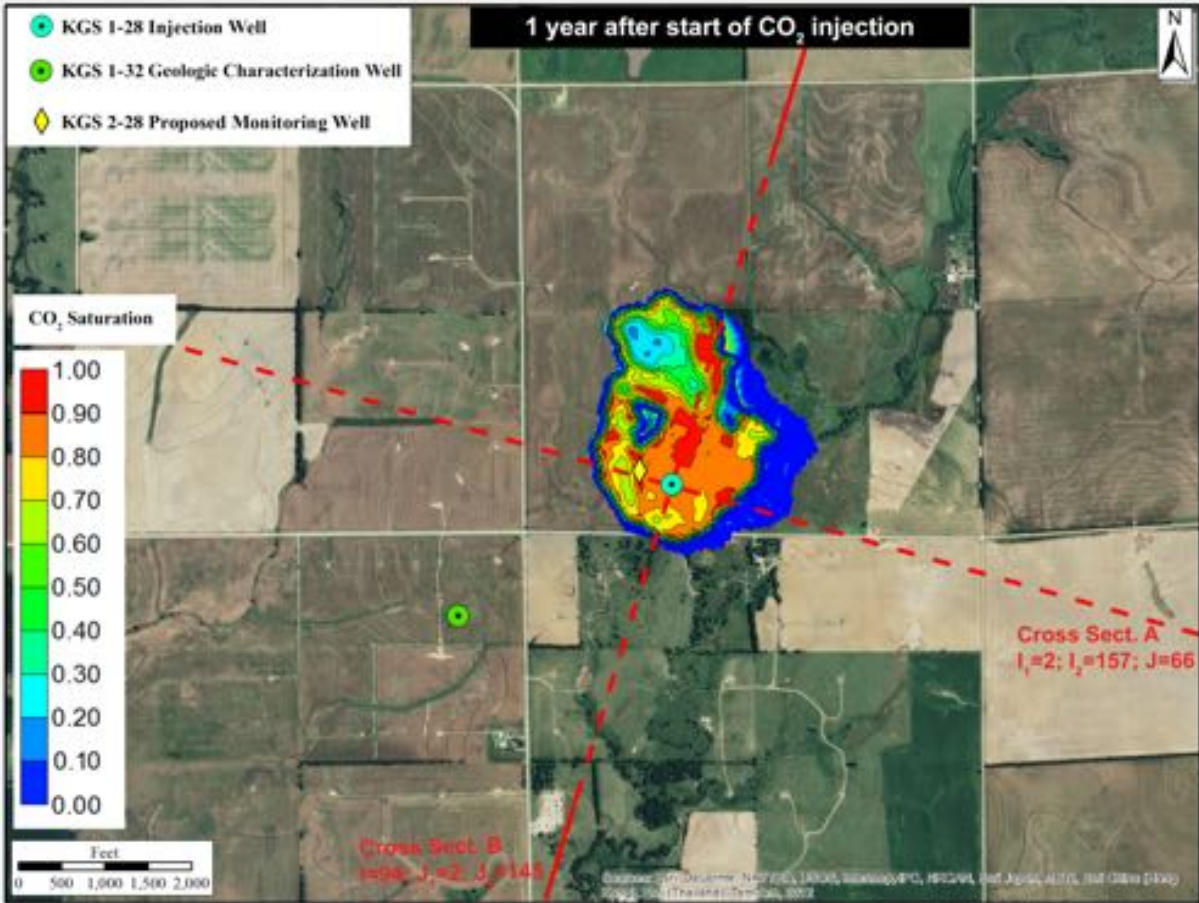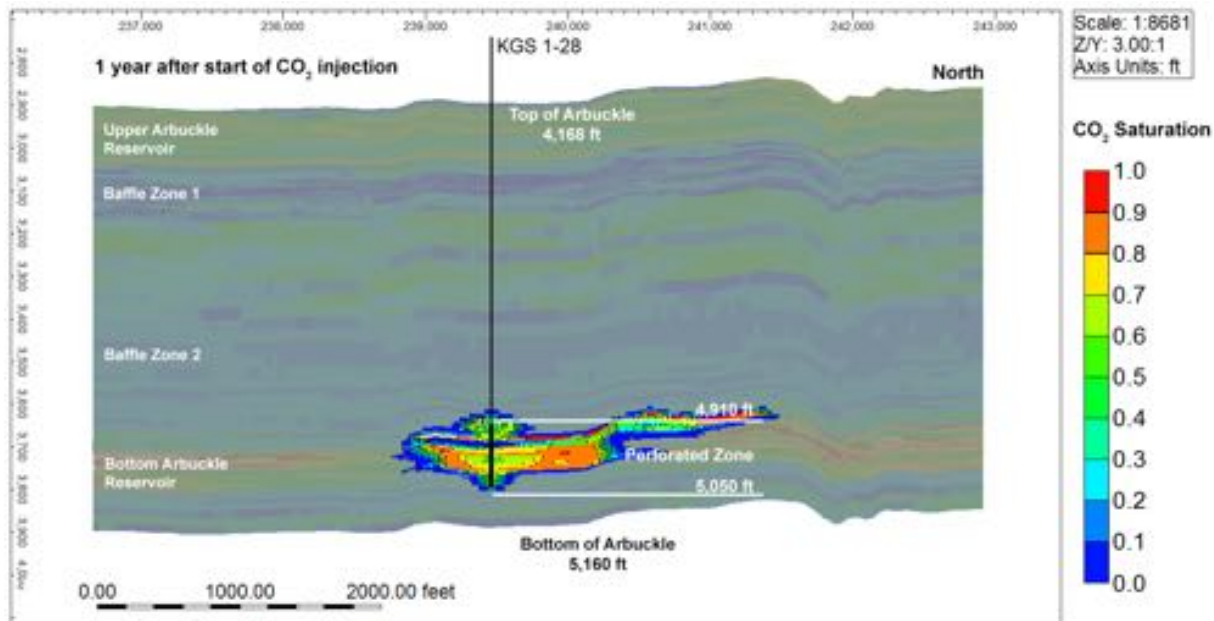
Figure A.9i. Dissolved CO₂ spatial distribution in aerial and cross-sectional view for the largest migration alternative model (k-1.25/phi-0.75) at one year from start of injection.
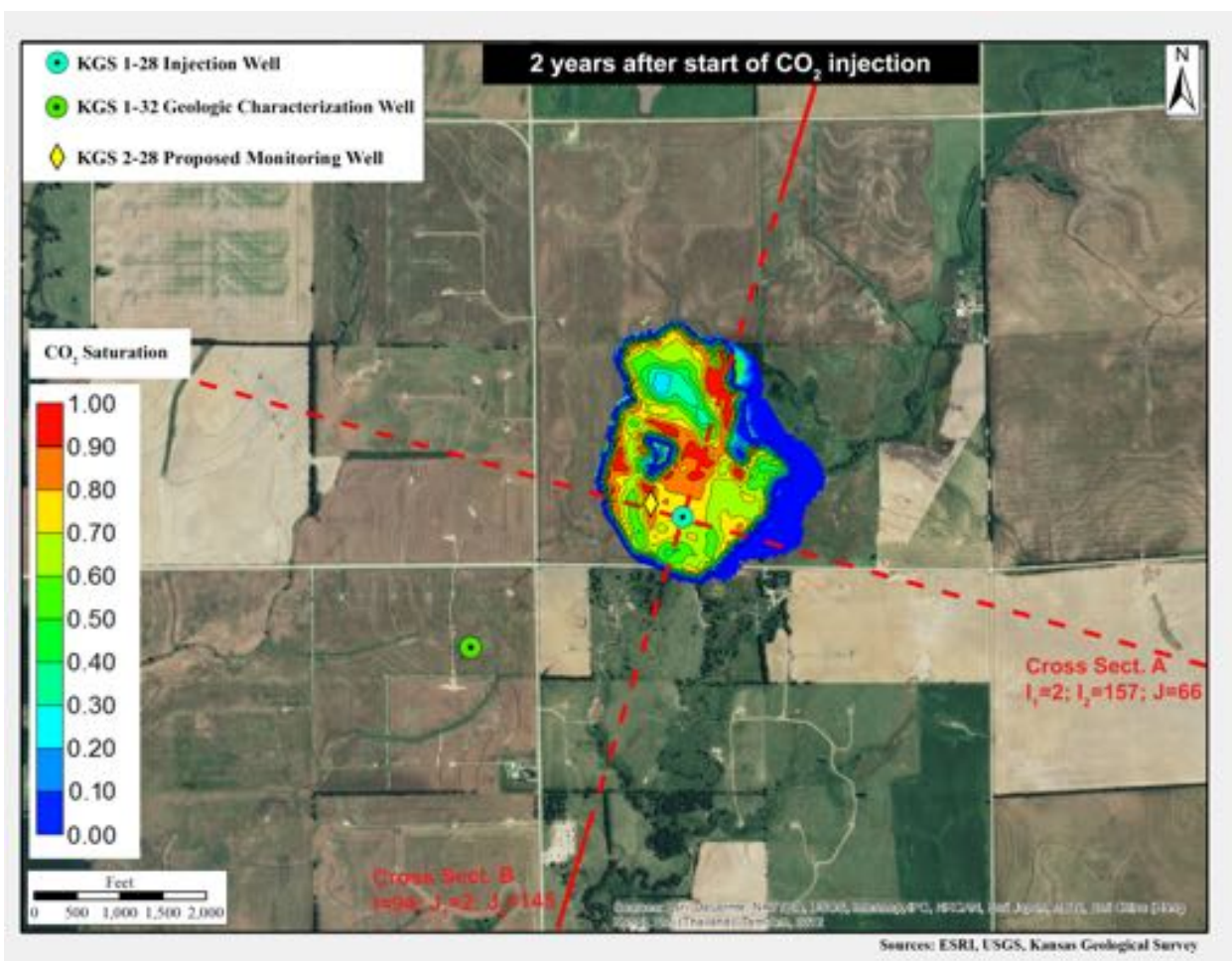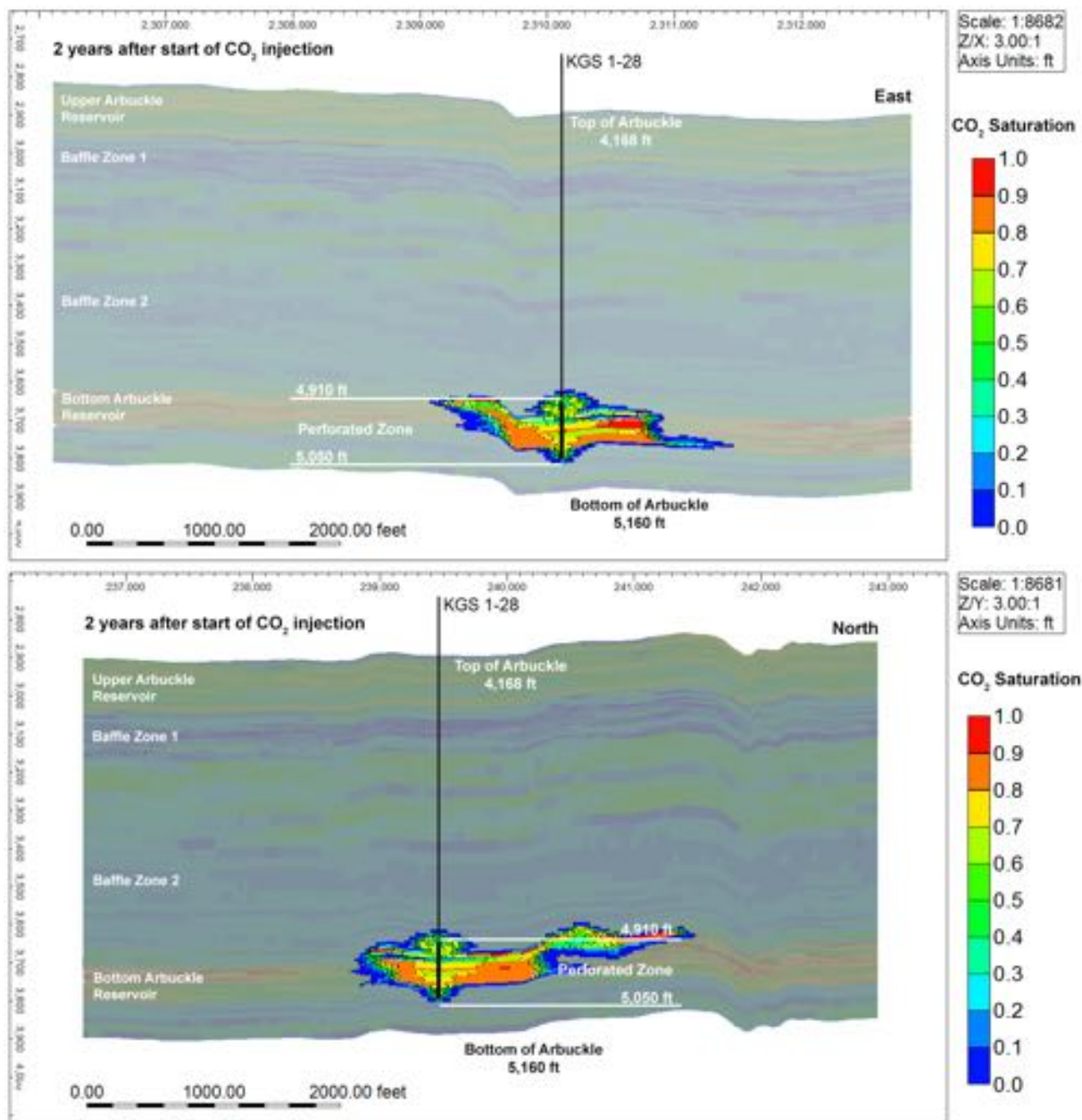
Figure A.9j. Dissolved CO₂ spatial distribution in aerial and cross-sectional view for the largest migration alternative model (k-1.25/phi-0.75) at two years from start of injection.

10 years after start of CO₂ injection

10 years after start of CO₂ injection
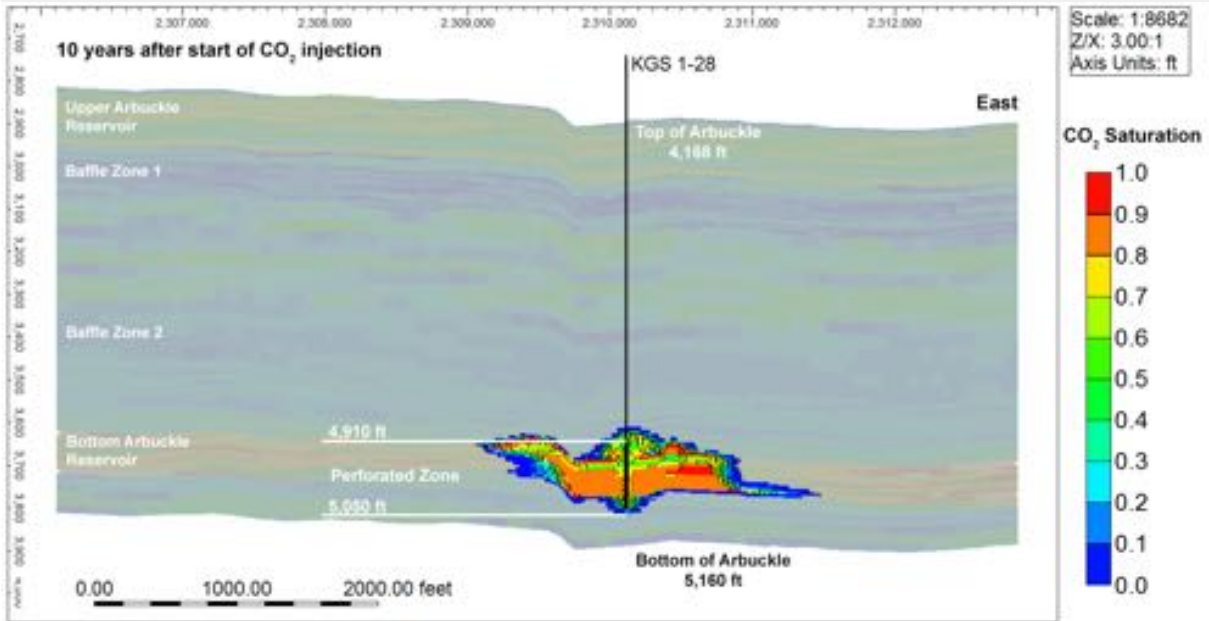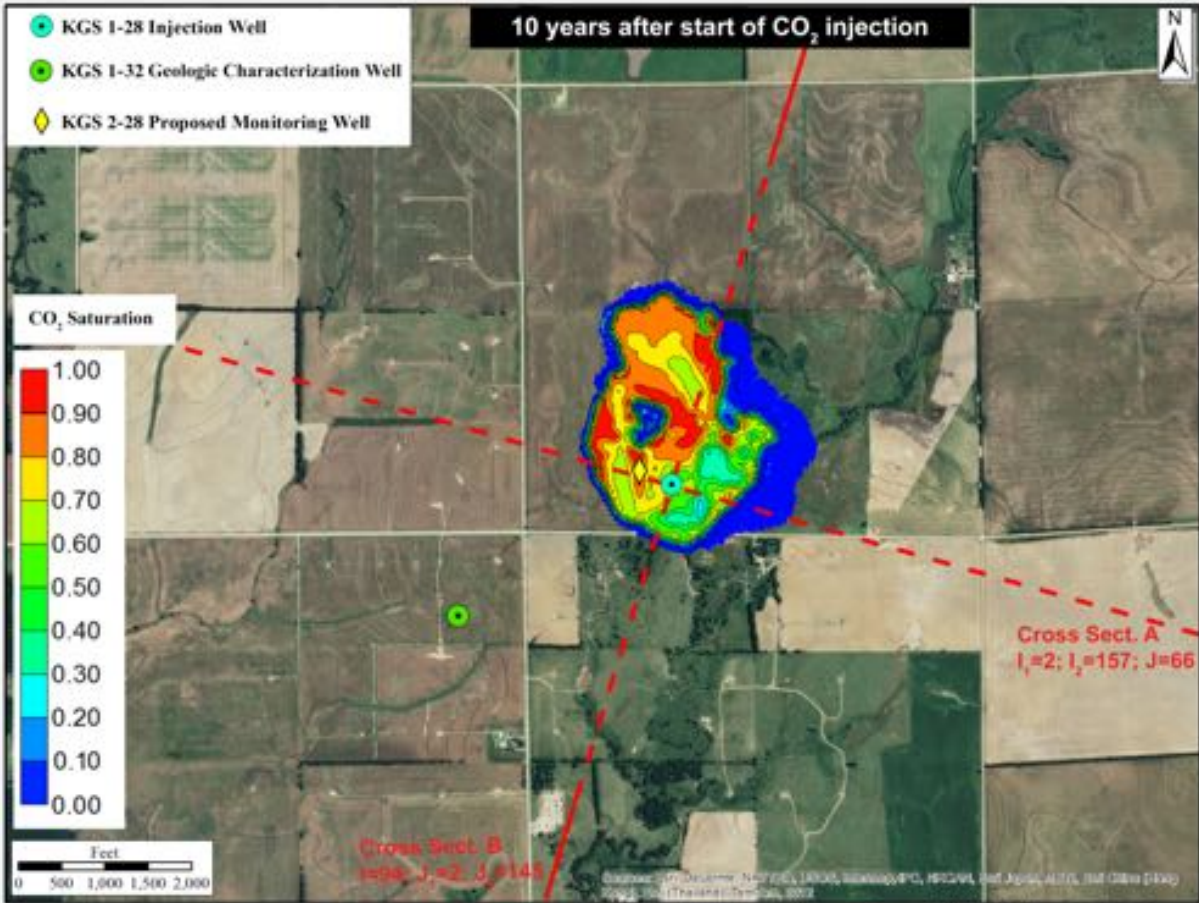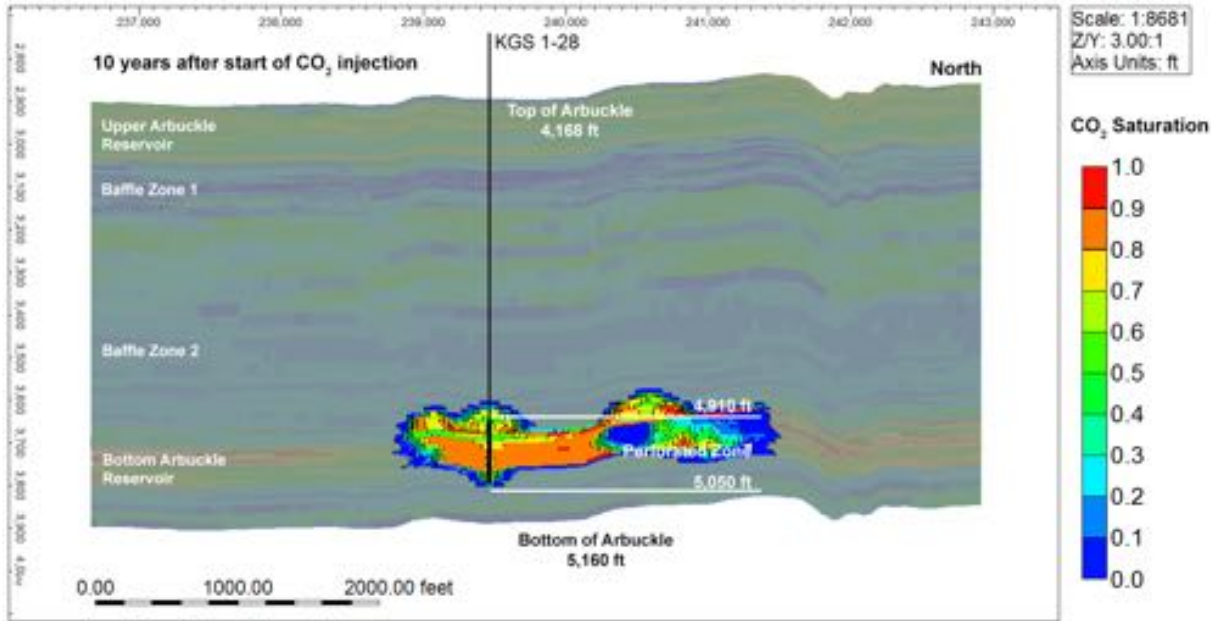
Figure A.9k. Dissolved CO$_2$ spatial distribution in aerial and cross-sectional view for the largest migration alternative model (k-1.25/phi-0.75) at 10 years from start of injection.

Figure A.9l. Dissolved CO_2 spatial distribution in aerial and cross-sectional view for the largest migration alternative model (k-1.25/phi-0.75) at 100 years from start of injection.

A2.3 Simulated Pressure Distribution

Figure A.10 presents the bottomhole pressure (at a reference depth of 5,050 ft) for the base case and the two cases that resulted in highest pressures and plume migration. The bottomhole pressures for all nine alternative cases are listed in table 7. For all three cases presented in fig. A.10, the pressure increases when CO_2 injection operations start and then drops to nearly pre-injection values when injection ceases. The pressure is influenced by

permeability and porosity, as these two parameters are independent (decoupled) variables in CMG. Therefore, as expected, the highest bottomhole pressure (BHP) of 2,361 psi at a depth of 5,050 ft is observed for the low permeability–low porosity case. This pressure represents an increase of 268 psi over pre-injection levels and results in a pressure gradient of 0.467 psi/ft, which is less than the maximum allowable pressure gradient of 0.675 psi/ft corresponding to 90% of the fracture gradient (0.75 psi/ft).
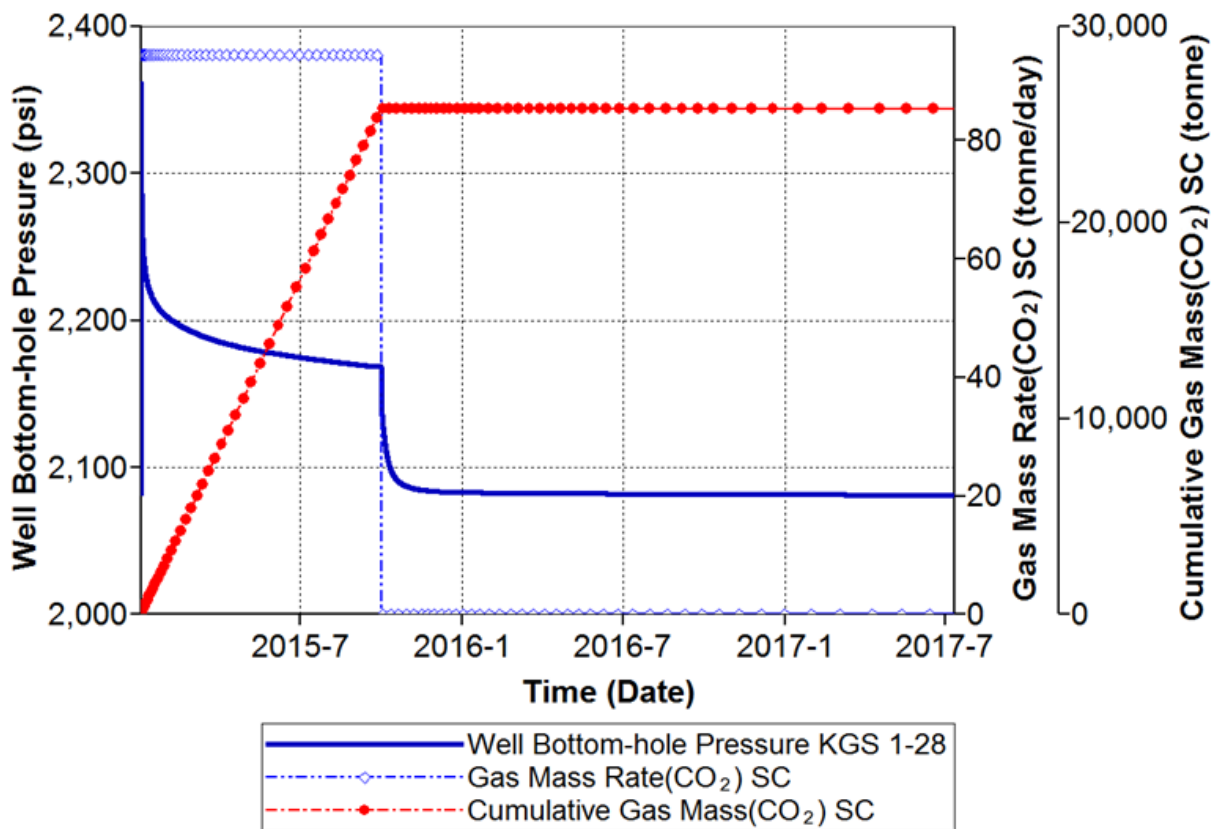
Figure A.10—Maximum well bottomhole pressure at a depth of 5,050 ft for minimum porosity and minimum permeability (k-0.75/phi-0.75) case.

Figure A.11 presents the change in pore pressure at the base of the confining zone (Simpson Group) for the case that resulted in the highest pressures and plume spread. The maximum pressure increase at the end of the injection period is fairly small and varies between 0.7 psi and 0.8 psi. As observed for pressures at the bottom of the well, the highest pressure is noted for the low permeability/low porosity case (k-0.75/phi-0.75).

Figure A.13a–e presents the lateral distribution of pressure in the Arbuckle injection

interval (at an elevation of 4,960 ft) for the k-0.75/phi-0.75 case, which resulted in the maximum induced pore pressures. The pressures increase from commencement of injection to nine months and then drop significantly by the end of the first year (three months after operations stop). The pressures also drop very rapidly at short distances from the injection well at the end of the nine-month injection period, as shown in fig. A.12. The pressures at the end of the nine-month injection period drop from about 96 psi a short distance from the injection well to less than 15 psi at the geologic characterization well, KGS 1-32, which is approximately 3,500 ft southwest of the injection well. The maximum induced pressure at the model boundary is only 7–12 psi.

Figure A.13a–e also shows the vertical pressure distribution for the maximum induced pressure case (k-0.75/phi-0.75). The confining effect of the mid-Arbuckle baffle zones is evident in the plots as the large pressure increases are mostly restricted to the injection interval. The pressures decline rapidly at a short distance from the injection well. The pressures throughout the model subside to nearly pre-injection levels soon after injection stops, as shown in the one-year pressure plot in fig. A.13e.
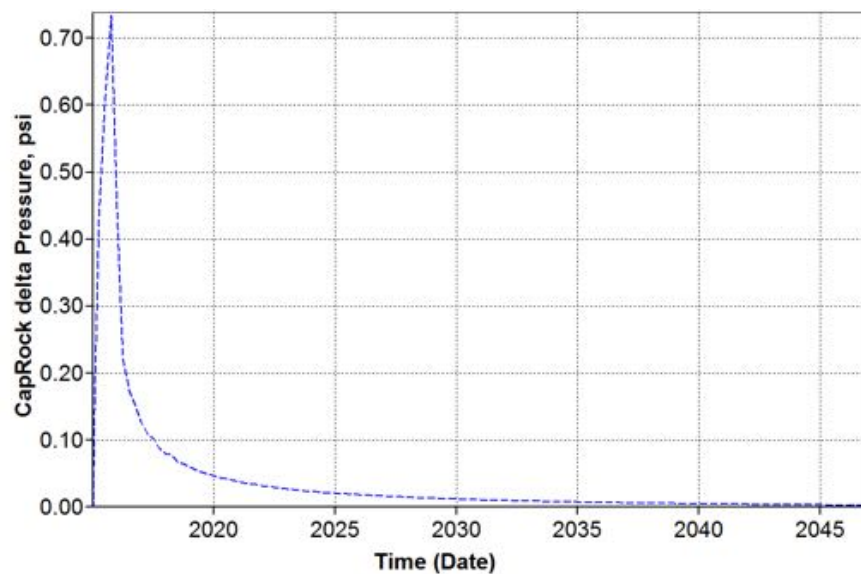
Figure A.11. Change in pore pressure at the base of the confining zone (i.e., base of Simpson Group) at the injection well site for the maximum induced pressure (k-0.75/phi-0.75).
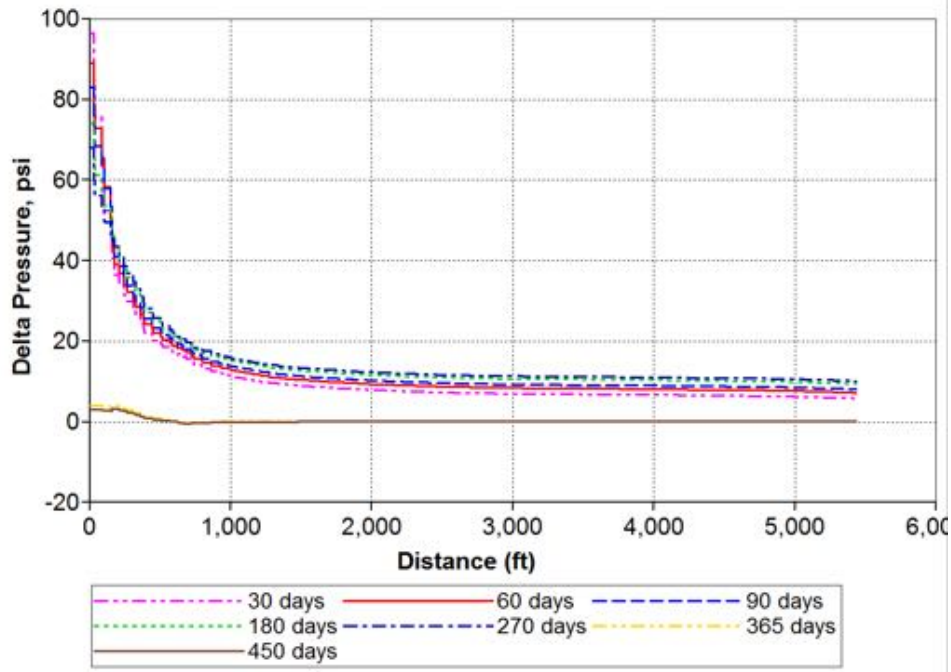
Figure A.12. Pore pressure as a function of lateral distance from the injection well (KGS 1-28) at seven time intervals for the highest induced pressure case (k-0.75/phi-0.75).
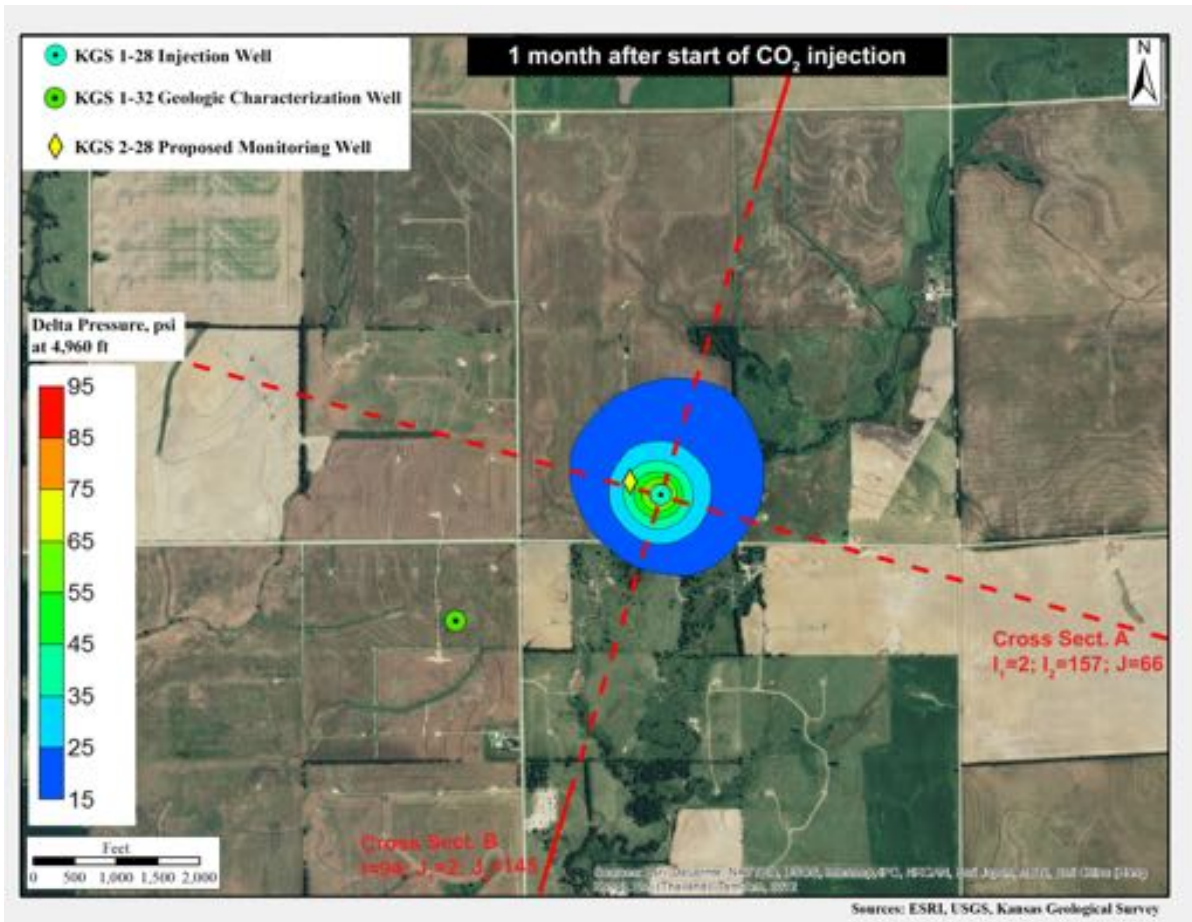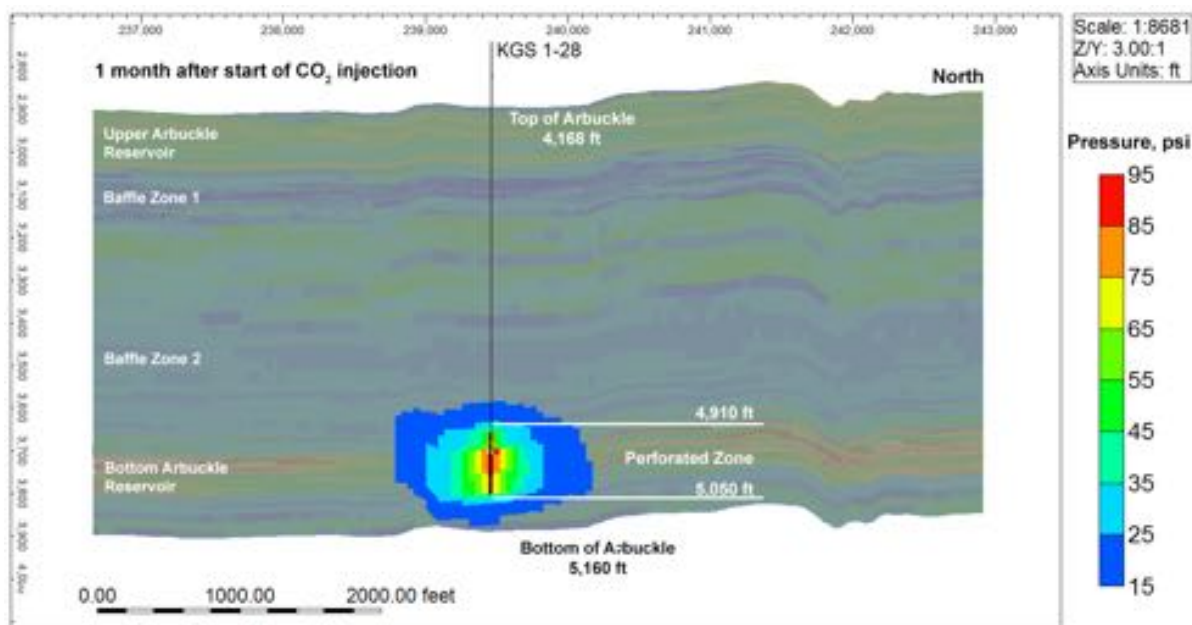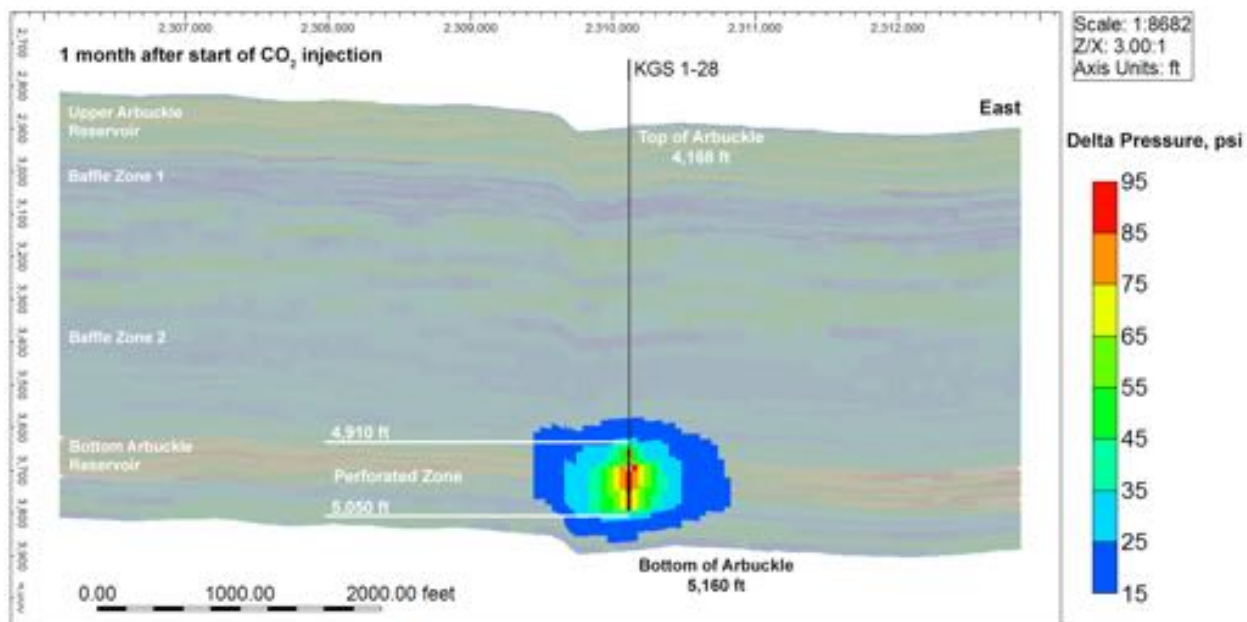
Figure A.13a. Simulated increase in pressure in aerial and cross-sectional views at one month from start of injection for the low permeability–low porosity (k-0.75/phi-0.75) alternative case, which resulted in the largest simulated pressures.

3 months after start of CO_2 injection

3 months after start of CO_2 injection
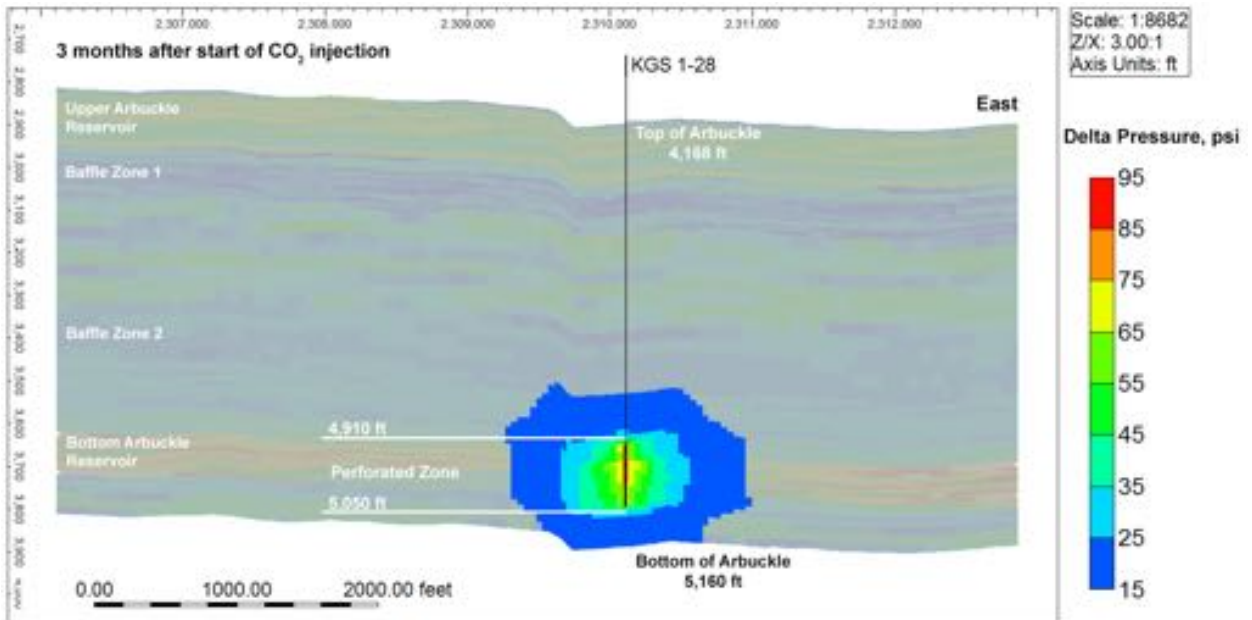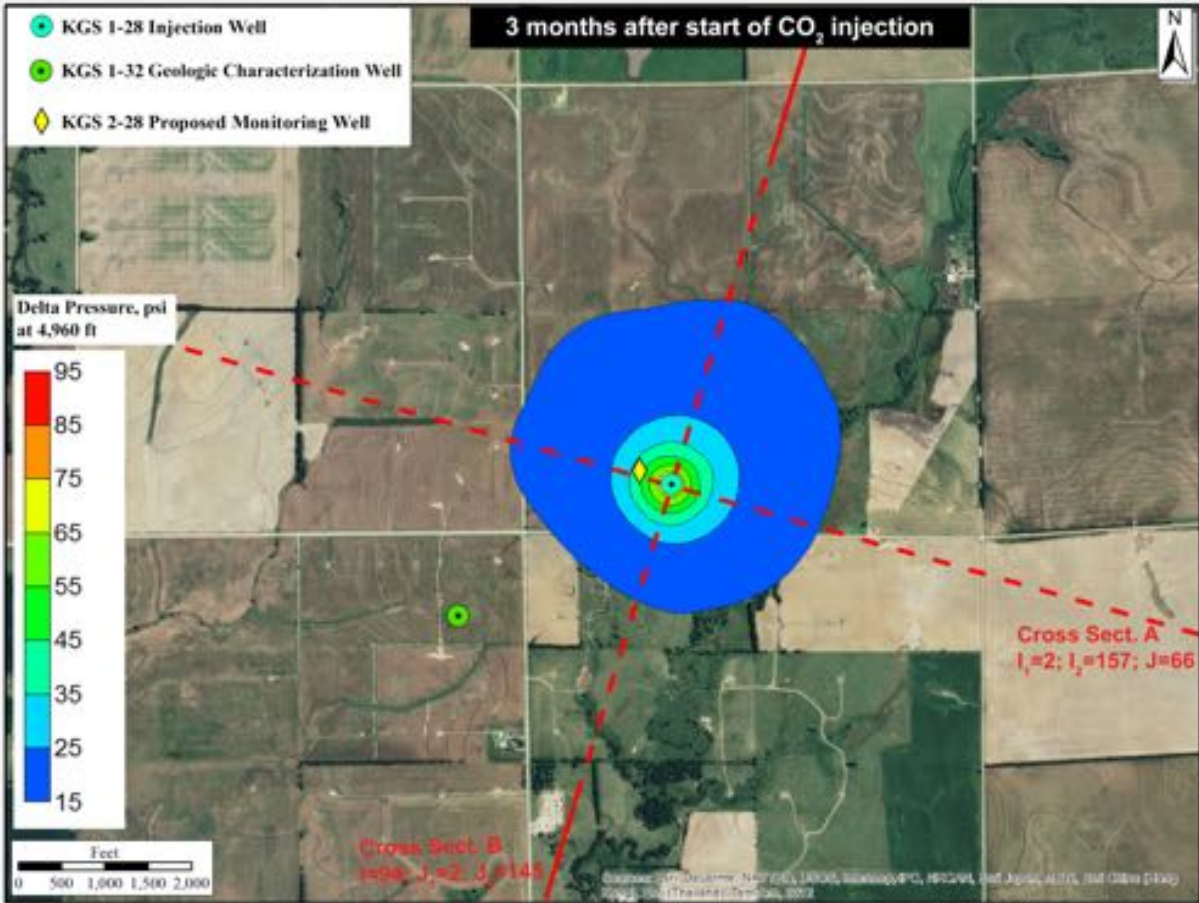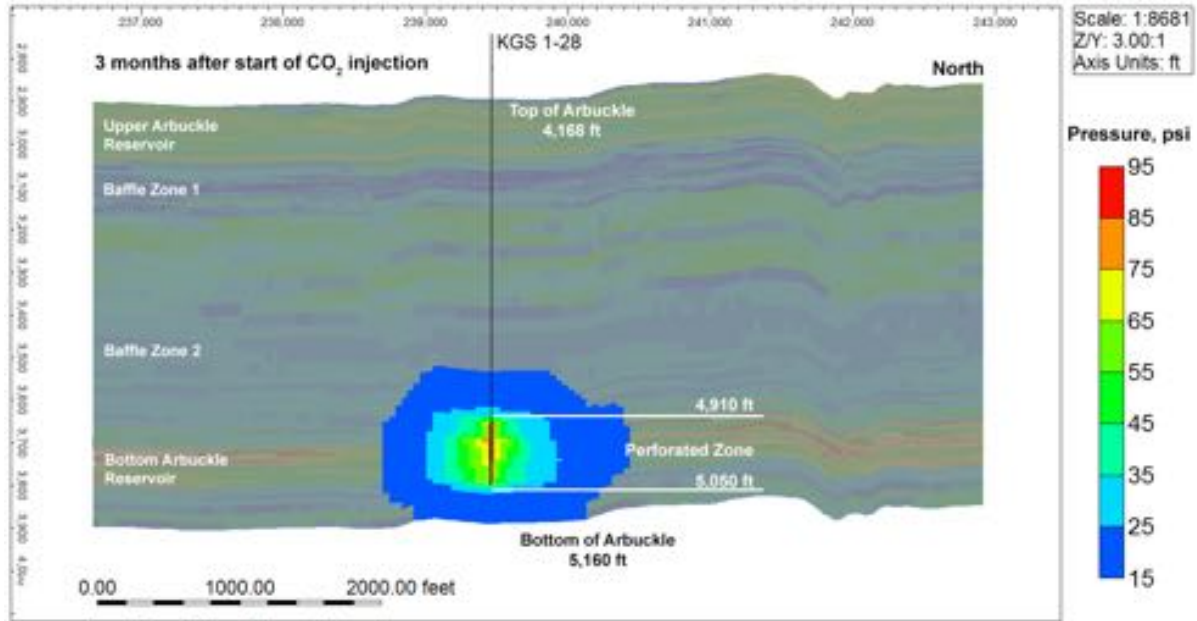
Figure A.13b. Simulated increase in pressure in aerial and cross-sectional views at three months from start of injection for the low permeability–low porosity (k-0.75/phi-0.75) alternative case, which resulted in the largest simulated pressures.
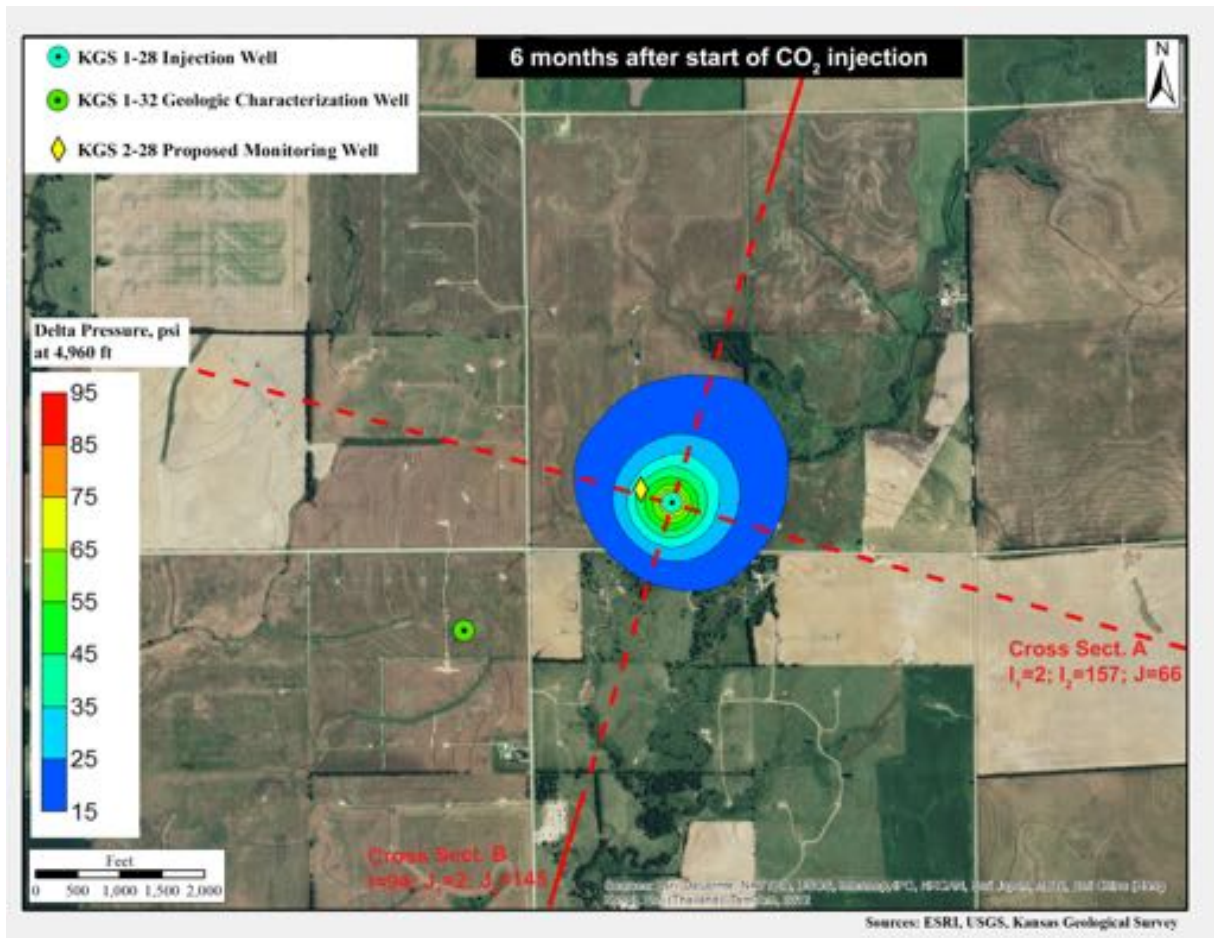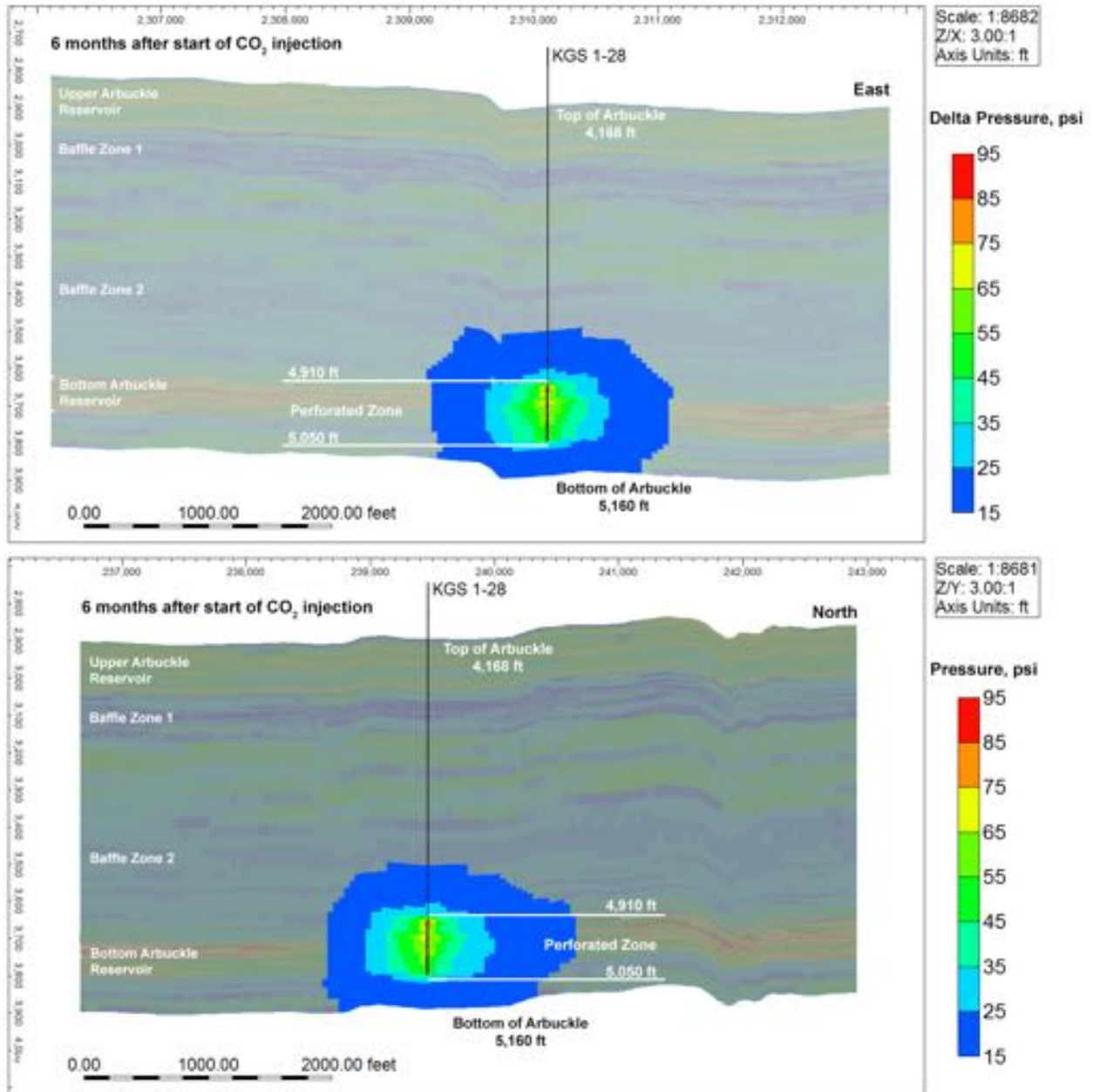
Figure A.13c. Simulated increase in pressure in aerial and cross-sectional views at six months from start of injection for the low permeability–low porosity (k-0.75/phi-0.75) alternative case, which resulted in the largest simulated pressures.

9 months after start of CO₂ injection
Injection stops
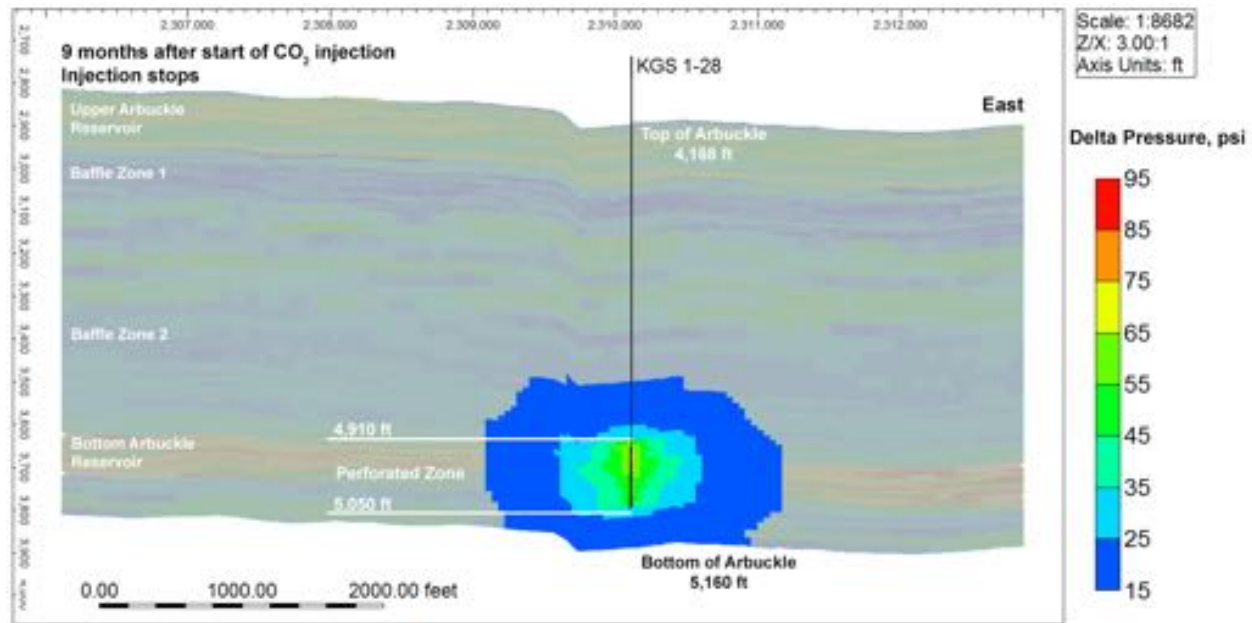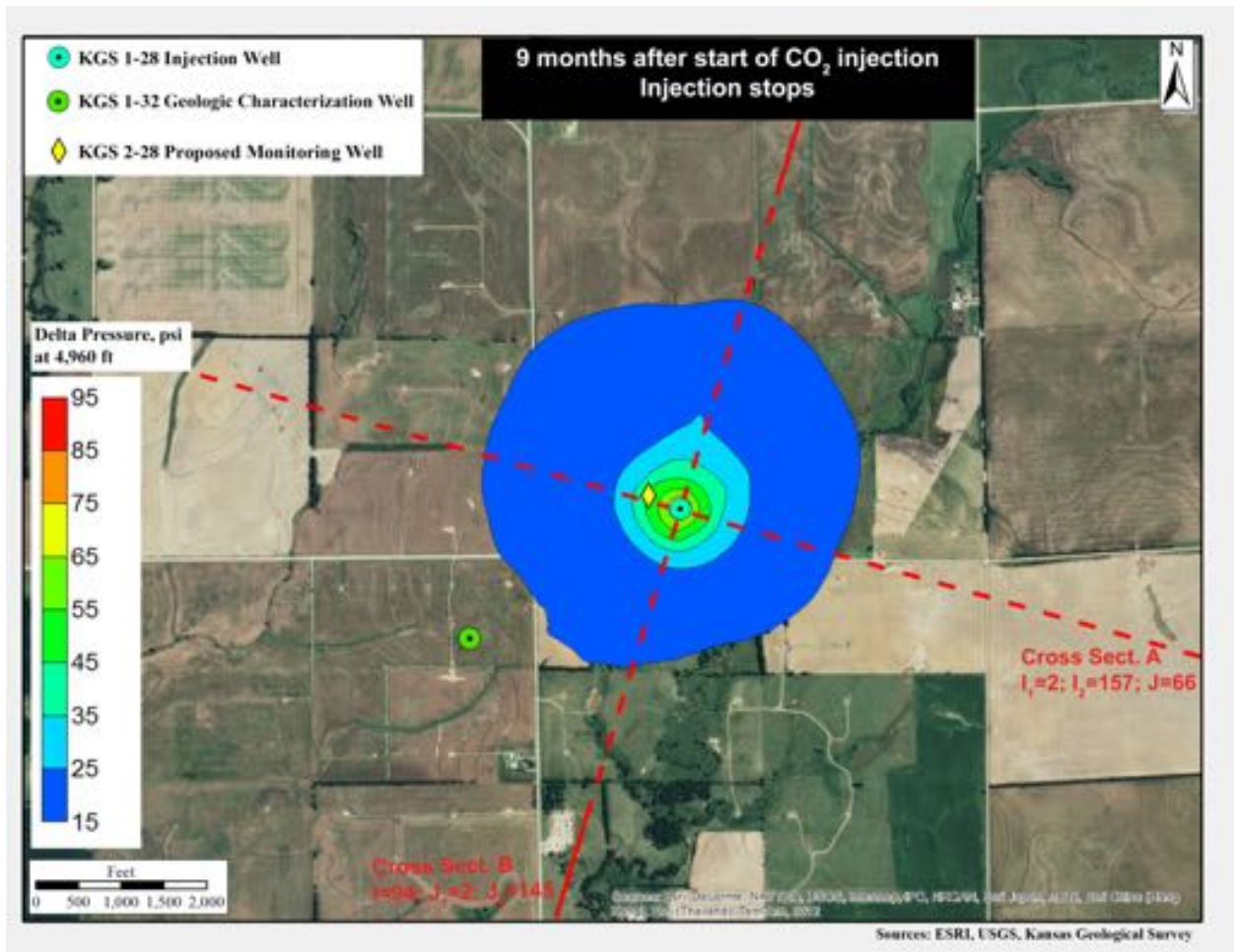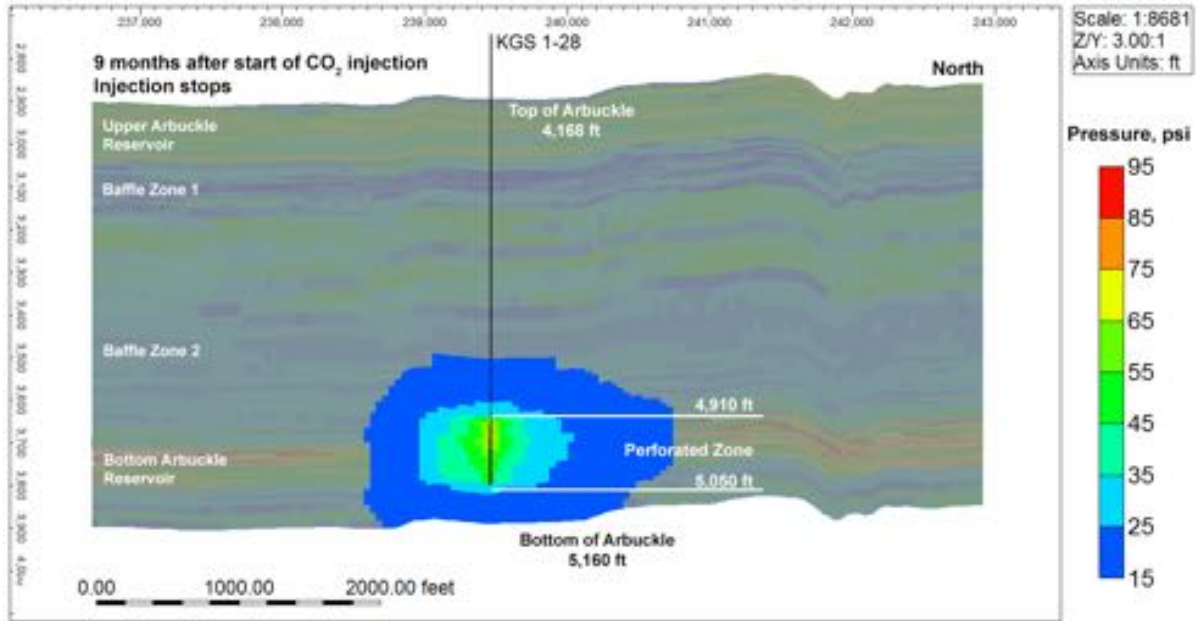
Figure A.13d. Simulated increase in pressure in aerial and cross-sectional views at nine months from start of injection for the low permeability–low porosity (k-0.75/phi-0.75) alternative case, which resulted in the largest simulated pressures.
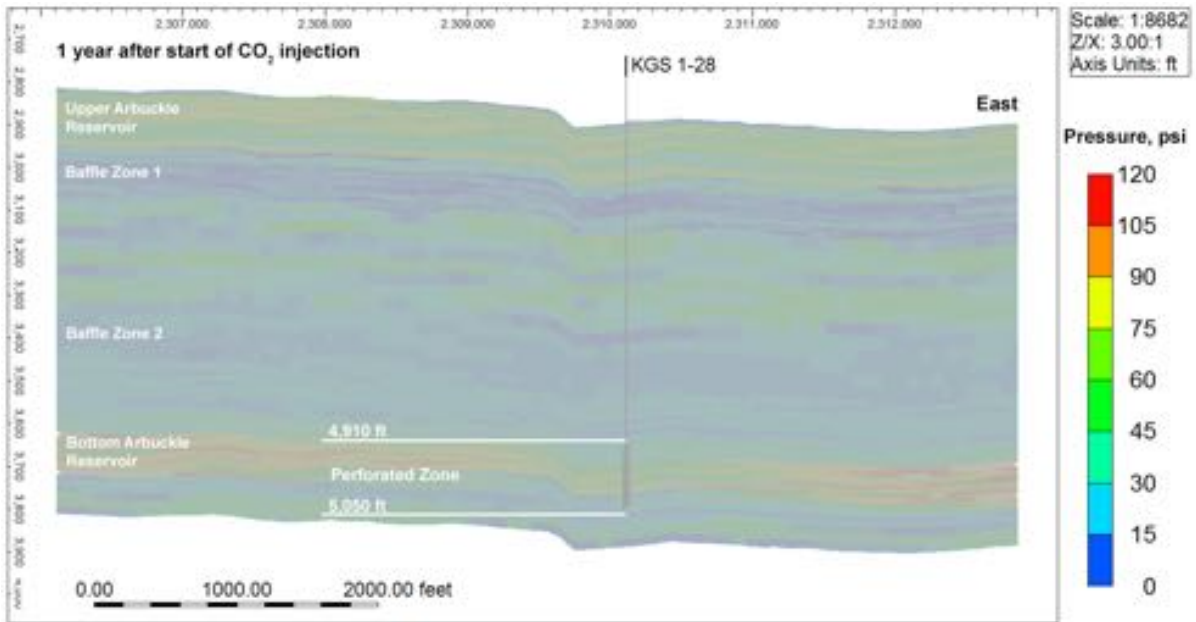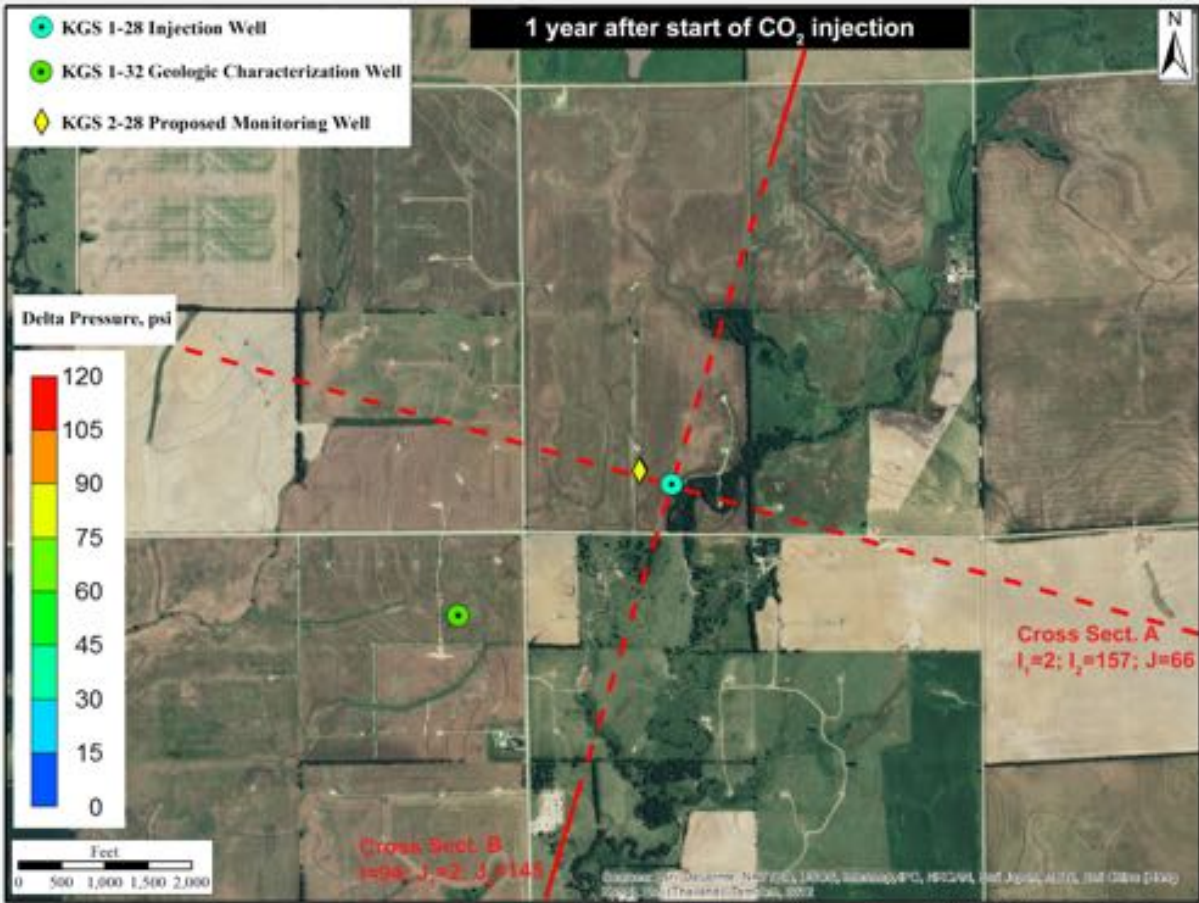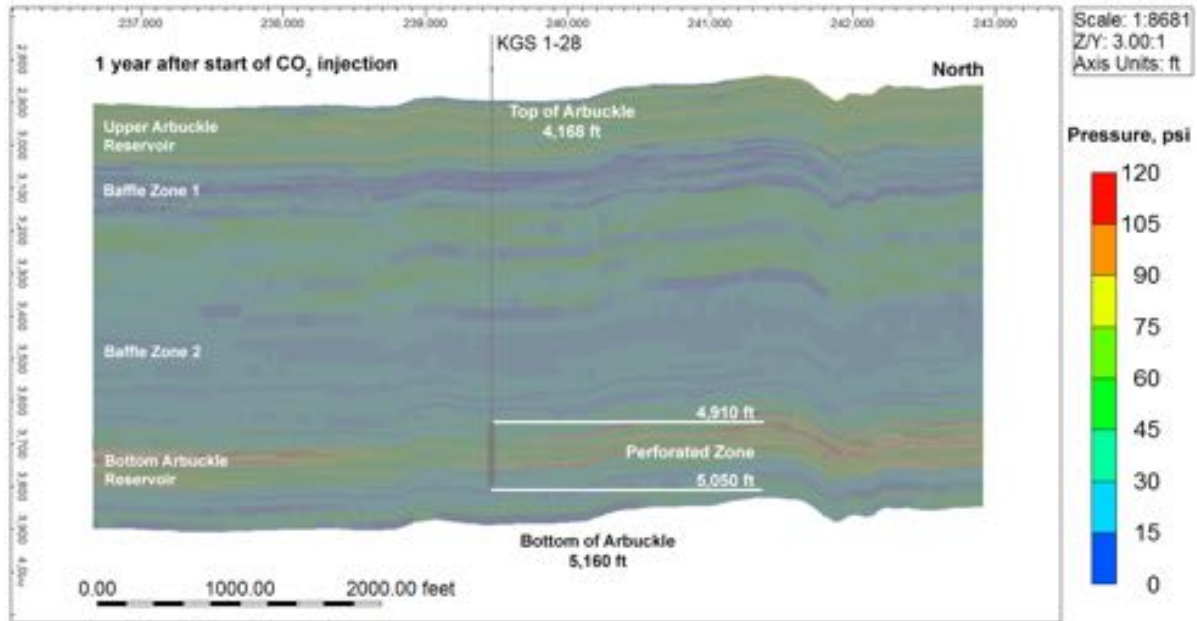
Figure A.13e. Simulated increase in pressure in aerial and cross-sectional views at one year from start of injection for the low permeability–low porosity (k-0.75/phi-0.75) alternative case, which resulted in the largest simulated pressures.

Appendix B. Capillary Pressure and Relative Permeability Drainage and Imbibition Tables for 9 Rock Types

Table B.1. RQI vs. rock type assignments.

RT	RQI from	RQI To	Ave RQI
1	40	10	25
2	10	2.5	6.25
3	2.5	1	1.75
4	1	0.5	0.75
5	0.5	0.4	0.45
6	0.4	0.3	0.35
7	0.3	0.2	0.25
8	0.2	0.1	0.15
9	0.1	0.01	0.055

Table B.2. Capillary pressure and relative permeability drainage and imbibition tables for rock type 1 (RQI=25).

RQI range from 40-10- Ave RQI =25					RQI range from 40-10- Ave RQI =25				
Pc	Sw	SCO2	Krw	krCO2	Pc	Sw	SCO2	Krw	krCO2
0	1	0	1	0	0	0.652	0.348	0.075032	0.0000
0.012	0.933	0.0666	0.8758	0.0000	0.005	0.4689	0.5311	0.027558	0.0184
0.015	0.765	0.2348	0.5973	0.0011	0.01	0.3693	0.6307	0.013298	0.0650
0.018	0.651	0.3494	0.4368	0.0065	0.02	0.2627	0.7373	0.004674	0.1645
0.02	0.593	0.4075	0.3646	0.0129	0.03	0.2060	0.7940	0.002204	0.2440
0.03	0.414	0.5862	0.1818	0.0664	0.04	0.1706	0.8294	0.001225	0.3045
0.04	0.321	0.6789	0.1110	0.1285	0.05	0.1463	0.8537	0.000756	0.3512
0.05	0.264	0.7360	0.0757	0.1848	0.06	0.1285	0.8715	0.000502	0.3882
0.06	0.225	0.7748	0.0553	0.2329	0.07	0.1150	0.8850	0.000352	0.4181
0.07	0.197	0.8031	0.0425	0.2736	0.08	0.1042	0.8958	0.000257	0.4428
0.08	0.175	0.8246	0.0338	0.3081	0.09	0.0955	0.9045	0.000194	0.4635
0.09	0.158	0.8415	0.0276	0.3377	0.1	0.0883	0.9117	0.00015	0.4812
0.1	0.145	0.8552	0.0230	0.3631	0.2	0.0525	0.9475	2.64E-05	0.5751
0.15	0.103	0.8974	0.0115	0.4509	0.3	0.0391	0.9609	9.21E-06	0.6135
0.2	0.081	0.9192	0.0070	0.5024	0.4	0.0319	0.9681	4.31E-06	0.6345
0.3	0.058	0.9418	0.0035	0.5605	0.5	0.0274	0.9726	2.38E-06	0.6479
0.4	0.046	0.9535	0.0021	0.5926	0.6	0.0243	0.9757	1.46E-06	0.6572
0.5	0.039	0.9608	0.0014	0.6131	0.7	0.0221	0.9779	9.6E-07	0.6641
0.6	0.034	0.9657	0.0010	0.6273	0.8	0.0204	0.9796	6.68E-07	0.6693
0.7	0.031	0.9693	0.0008	0.6379	0.9	0.0190	0.9810	4.84E-07	0.6735
0.8	0.028	0.9720	0.0006	0.6459	1	0.0179	0.9821	3.63E-07	0.6769
0.9	0.026	0.9741	0.0005	0.6524	2	0.0127	0.9873	5.25E-08	0.6931

1	0.024	0.9759	0.0004	0.6576		3	0.0109	0.9891	1.64E-08	0.6989
1.5	0.019	0.9812	0.0002	0.6740		4	0.0099	0.9901	6.99E-09	0.7019
2	0.016	0.9840	0.0001	0.6825		5	0.0093	0.9907	3.55E-09	0.7038
3	0.013	0.9868	0.0001	0.6915		6	0.0089	0.9911	2.01E-09	0.7051
4	0.012	0.9883	3.62E-05	0.6962		7	0.0086	0.9914	1.23E-09	0.7060
5	0.011	0.9892	2.40E-05	0.6991		8	0.0084	0.9916	7.91E-10	0.7067
6	0.010	0.9898	1.70E-05	0.7011		9	0.0082	0.9918	5.31E-10	0.7073
7	0.010	0.9903	1.27E-05	0.7025		10	0.0081	0.9919	3.68E-10	0.7077
8	0.009	0.9906	9.76E-06	0.7036		12	0.0079	0.9921	1.9E-10	0.7084
9	0.009	0.9909	7.73E-06	0.7045		14	0.0077	0.9923	1.05E-10	0.7089
10	0.009	0.9911	6.26E-06	0.7052		20	0.0074	0.9926	0	0.7112
12	0.009	0.9915	4.30E-06	0.7063		30	0.0072	0.9928	0	0.7112
14	0.008	0.9917	3.10E-06	0.7071		40	0.0071	0.9929	0	0.7112
18	0.008	0.9920	1.77E-06	0.7081		50	0.0070	0.9930	0	0.7112
20	0.008	0.9922	1.38E-06	0.7085		60	0.0069	0.9931	0	0.7112
25	0.008	0.9924	7.86E-07	0.7092		70	0.0069	0.9931	0	0.7112
30	0.007	0.9925	4.75E-07	0.7097		80	0.0069	0.9931	0	0.7112
40	0.007	0.9927	1.87E-07	0.7103		90	0.0069	0.9931	0	0.7112
50	0.007	0.00	0.00	0.7112		100	0.0068	0.9932	0	0.7112
60	0.007	0.00	0.00	0.7112		150	0.0068	0.9932	0	0.7112
70	0.007	0.00	0.00	0.7112		200	0.0068	0.9932	0	0.7112
80	0.007	0.00	0.00	0.7112		300	0.0067	0.9933	0	0.7112
90	0.007	0.00	0.00	0.7112						
100	0.007	0.00	0.00	0.7112						
150	0.007	0.00	0.00	0.7112						
200	0.007	0.00	0.00	0.7112						
300	0.007	0.00	0.00	0.7112						

Table B.3. Capillary pressure and relative permeability drainage and imbibition tables for rock type 2 (RQI=6.25).

PC	Sw	SCO2	Krw	krCO2	Pc	Sw	SCO2	Krw	krCO2
0	1.000	0	1	0	0	0.652	0.348	0.121501	0
0.06	0.954	0.046311	0.911705	1.19E-06	0.005	0.606	0.3943	0.0967	0.0005
0.07	0.833	0.167467	0.699192	0.000318	0.01	0.566	0.4341	0.0783	0.0026
0.08	0.740	0.259685	0.555519	0.002142	0.02	0.501	0.4987	0.0537	0.0125
0.09	0.668	0.33234	0.453456	0.006265	0.03	0.451	0.5492	0.0385	0.0281
0.1	0.609	0.391133	0.378118	0.012725	0.04	0.410	0.5897	0.0286	0.0469
0.15	0.428	0.571954	0.187715	0.066459	0.05	0.377	0.6229	0.0219	0.0673
0.2	0.334	0.665688	0.114064	0.128606	0.06	0.349	0.6508	0.0172	0.0881
0.3	0.237	0.762741	0.056377	0.232473	0.07	0.326	0.6744	0.0137	0.1088
0.4	0.187	0.813051	0.03411	0.306934	0.08	0.305	0.6948	0.0112	0.1289
0.5	0.156	0.844044	0.023058	0.361178	0.09	0.287	0.7125	0.0092	0.1482
0.6	0.135	0.865142	0.016719	0.402126	0.1	0.272	0.7281	0.0077	0.1666
0.7	0.120	0.880474	0.012724	0.434061	0.2	0.180	0.8196	0.0020	0.3047
0.8	0.108	0.892145	0.010033	0.459649	0.3	0.138	0.8615	0.0008	0.3868
0.9	0.099	0.901339	0.008128	0.480615	0.4	0.114	0.8859	0.0004	0.4403
1	0.091	0.90878	0.006727	0.498113	0.5	0.098	0.9018	0.0002	0.4778
1.5	0.068	0.931663	0.003218	0.555021	0.6	0.087	0.9131	0.0001	0.5056
2	0.056	0.943525	0.001885	0.586423	0.7	0.078	0.9215	0.0001	0.5270
3	0.044	0.955808	0.000866	0.620361	0.8	0.072	0.9281	0.0001	0.5441
4	0.038	0.962174	0.000487	0.638539	0.9	0.067	0.9334	0.0000	0.5580
5	0.034	0.966097	0.000305	0.649939	1	0.062	0.9377	0.0000	0.5696
6	0.031	0.968767	0.000204	0.657789	2	0.042	0.9584	0.0000	0.6275
7	0.029	0.970707	0.000144	0.663539	3	0.034	0.9660	0.0000	0.6496
8	0.028	0.972184	0.000104	0.667942	4	0.030	0.9700	0.0000	0.6614
9	0.027	0.973348	7.73E-05	0.671427	5	0.028	0.9725	0.0000	0.6688
10	0.026	0.974289	5.84E-05	0.674257	6	0.026	0.9742	0.0000	0.6739
12	0.024	0.975722	3.45E-05	0.678581	7	0.025	0.9754	0.0000	0.6776
14	0.023	0.976764	2.09E-05	0.681738	8	0.024	0.9763	0.0000	0.6804
18	0.022	0.978181	7.69E-06	0.686051	9	0.023	0.9771	0.0000	0.6827
20	0.021	0.978686	4.49E-06	0.687594	10	0.022	0.9777	0.0000	0.6845
25	0.020	0.979611	7.99E-07	0.690425	12	0.021	0.9786	0.0000	0.6873
30	0.020	0.980241	0	0.692357	14	0.021	0.9793	0.0000	0.6894
40	0.019	0.981	0	0.692357	20	0.020	0.981	0	0.6924
50	0.018	0.982	0	0.692357	30	0.0185	0.9815	0	0.6924
60	0.018	0.982	0	0.692357	40	0.0180	0.9820	0	0.6924
70	0.018	0.982	0	0.692357	50	0.0177	0.9823	0	0.6924
80	0.018	0.982	0	0.692357	60	0.0174	0.9826	0	0.6924
90	0.018	0.982	0	0.692357	70	0.0173	0.9827	0	0.6924
100	0.017	0.983	0	0.692357	80	0.0172	0.9828	0	0.6924

Table header: RQI range from 10-2.5-Ave RQI= 6.25

150	0.017	0.983	0	0.692357
200	0.017	0.983	0	0.692357
300	0.017	0.983	0	0.692357

90	0.0171	0.9829	0	0.6924
100	0.0170	0.9830	0	0.6924
150	0.0168	0.9832	0	0.6924
200	0.0166	0.9834	0	0.6924
300	0.0165	0.9835	0	0.6924

Table B.4. Capillary pressure and relative permeability drainage and imbibition tables for rock type 3 (RQI=1.75).

Pc	Sw	SCO2	Krw	krCO2		Pc	Sw	SCO2	Krw	krCO2
\multicolumn{5}{l}{**RQI range from 2.5-1 -Ave RQI=1.75**}		\multicolumn{5}{l}{**RQI range from 2.5-1 -Ave RQI=1.75**}

Pc	Sw	SCO2	Krw	krCO2	Pc	Sw	SCO2	Krw	krCO2
0	1.000	0	1	0	0	0.654	0.346	0.189511	0
0.3	0.868	0.131574	0.752199	0.000167	0.005	0.643	0.356679	0.179635	1.18E-05
0.4	0.679	0.320874	0.45511	0.007077	0.01	0.633	0.366974	0.170445	7.54E-05
0.5	0.563	0.437491	0.307641	0.026021	0.02	0.614	0.386496	0.153889	0.000452
0.6	0.483	0.516876	0.223065	0.052417	0.03	0.595	0.404715	0.139439	0.001237
0.7	0.425	0.574567	0.169764	0.081749	0.04	0.578	0.421759	0.126767	0.002468
0.8	0.382	0.618479	0.13386	0.111382	0.05	0.562	0.437739	0.115606	0.004143
0.9	0.347	0.653076	0.108447	0.13999	0.06	0.547	0.452754	0.105734	0.006245
1	0.319	0.681071	0.089755	0.166978	0.07	0.533	0.46689	0.09697	0.008742
1.5	0.233	0.767174	0.042942	0.275299	0.08	0.520	0.480224	0.08916	0.011601
2	0.188	0.811808	0.025156	0.349104	0.09	0.507	0.492822	0.082176	0.014787
3	0.142	0.858022	0.011556	0.440498	0.1	0.495	0.504746	0.075912	0.018263
4	0.118	0.881978	0.006492	0.494509	0.2	0.404	0.596381	0.038024	0.062589
5	0.103	0.896736	0.004068	0.530205	0.3	0.344	0.656344	0.021774	0.111804
6	0.093	0.906783	0.002728	0.555603	0.4	0.301	0.698778	0.013632	0.158065
7	0.086	0.914084	0.001915	0.574635	0.5	0.270	0.730464	0.009096	0.199413
8	0.080	0.919641	0.001388	0.589451	0.6	0.245	0.755069	0.006367	0.235796
9	0.076	0.924019	0.001031	0.601328	0.7	0.225	0.774756	0.004626	0.267721
10	0.072	0.927562	0.000779	0.611071	0.8	0.209	0.790883	0.003463	0.295801
12	0.067	0.932954	0.00046	0.62613	0.9	0.196	0.804346	0.002656	0.32061
14	0.063	0.936873	0.000279	0.63725	1	0.184	0.815765	0.002079	0.342646
18	0.058	0.942205	0.000103	0.652624	2	0.124	0.876117	0.000346	0.474936
20	0.056	0.944107	5.99E-05	0.658174	3	0.099	0.900586	0.000104	0.5365
25	0.052	0.947587	1.07E-05	0.668423	4	0.086	0.913988	4E-05	0.572243
30	0.050	0.949955	0	0.675469	5	0.078	0.922497	1.78E-05	0.595694
40	0.047	0.050045	0	0.675469	6	0.072	0.928401	8.61E-06	0.612315
50	0.045	0.949955	0	0.675469	7	0.067	0.932748	4.38E-06	0.62474
60	0.044	0.050045	0	0.675469	8	0.064	0.93609	2.29E-06	0.634396
70	0.043	0.949955	0	0.675469	9	0.061	0.938742	1.21E-06	0.642127
80	0.042	0.050045	0	0.675469	10	0.059	0.940901	6.39E-07	0.648464
90	0.042	0.949955	0	0.675469	12	0.056	0.944208	1.63E-07	0.658247
100	0.041	0.050045	0	0.675469	14	0.053	0.946628	3.17E-08	0.665464
150	0.040	0.949955	0	0.675469	20	0.0489	0.9511	0	0.675469
200	0.039	0.050045	0	0.675469	30	0.0452	0.9548	0	0.675469
300	0.038	0.949955	0	0.675469	40	0.0433	0.9567	0	0.675469
					50	0.0421	0.9579	0	0.675469
					60	0.0413	0.9587	0	0.675469
					70	0.0407	0.9593	0	0.675469
					80	0.0403	0.9597	0	0.675469

90	0.0399	0.9601	0	0.675469
100	0.0396	0.9604	0	0.675469
150	0.0387	0.9613	0	0.675469
200	0.0383	0.9617	0	0.675469
300	0.0378	0.9622	0	0.675469

Table B.5. Capillary pressure and relative permeability drainage and imbibition tables for rock type 4 (RQI=0.75).

RQI range from1-0.5-Ave RQI=0.75				
Pc	**Sw**	**SCO2**	**Krw**	**krCO2**
0	1.000	0	1	0
0.7	0.989	0.010684	0.977573	1.03E-08
0.8	0.885	0.115298	0.770825	0.000158
0.9	0.802	0.19772	0.624483	0.001403
1	0.736	0.264415	0.516846	0.004553
1.5	0.530	0.469544	0.247276	0.046594
2	0.424	0.575878	0.14486	0.106509
3	0.314	0.685977	0.066547	0.216321
4	0.257	0.74305	0.037386	0.298998
5	0.222	0.778209	0.023425	0.360567
6	0.198	0.802143	0.015709	0.40763
7	0.180	0.819537	0.011027	0.444629
8	0.167	0.832776	0.007996	0.474444
9	0.157	0.843207	0.005936	0.498975
10	0.148	0.851647	0.004484	0.519515
12	0.136	0.864493	0.002649	0.551989
14	0.126	0.873829	0.001606	0.576531
18	0.113	0.886533	0.000591	0.611239
20	0.109	0.891064	0.000345	0.623988
25	0.101	0.899354	6.14E-05	0.647835
30	0.095	0.904997	0	0.664456
40	0.088	0.912	0	0.664456
50	0.083	0.917	0	0.664456
60	0.080	0.920	0	0.664456
70	0.078	0.922	0	0.664456
80	0.076	0.924	0	0.664456
90	0.075	0.925	0	0.664456
100	0.074	0.926	0	0.664456
150	0.071	0.929	0	0.664456
200	0.069	0.931	0	0.664456
300	0.067	0.933	0	0.664456

RQI range from1-0.5-Ave RQI=0.75				
Pc	**Sw**	**SCO2**	**Krw**	**krCO2**
0	0.657	0.3426	0.254272	0
0.005	0.653	0.34683	0.248578	1.95E-06
0.01	0.649	0.350608	0.243564	1.04E-05
0.02	0.642	0.358013	0.233934	5.73E-05
0.03	0.635	0.365222	0.224805	0.000156
0.04	0.628	0.372245	0.216145	0.000315
0.05	0.621	0.379087	0.207923	0.00054
0.06	0.614	0.385757	0.200112	0.000837
0.07	0.608	0.39226	0.192687	0.001205
0.08	0.601	0.398603	0.185624	0.001648
0.09	0.595	0.404792	0.178902	0.002165
0.1	0.589	0.410832	0.172499	0.002755
0.2	0.536	0.464129	0.122488	0.012366
0.3	0.493	0.507166	0.090005	0.027205
0.4	0.457	0.542681	0.067988	0.045221
0.5	0.427	0.572511	0.05254	0.064908
0.6	0.402	0.597939	0.041384	0.085264
0.7	0.380	0.619885	0.033129	0.105653
0.8	0.361	0.639028	0.026894	0.125682
0.9	0.344	0.65588	0.022099	0.145117
1	0.329	0.670835	0.018353	0.163825
2	0.238	0.76151	0.004223	0.308916
3	0.195	0.804785	0.001439	0.398896
4	0.170	0.830335	0.000595	0.458797
5	0.153	0.847279	0.000275	0.501402
6	0.141	0.859378	0.000136	0.533259
7	0.132	0.86847	6.97E-05	0.557999
8	0.124	0.875564	3.64E-05	0.577784
9	0.119	0.881261	1.91E-05	0.593981
10	0.114	0.885942	9.89E-06	0.607495
12	0.107	0.893189	2.35E-06	0.628788
14	0.101	0.898549	3.83E-07	0.64483
20	0.091345	0.908655	0	0.664456
30	0.082976	0.917024	0	0.664456
40	0.078568	0.921432	0	0.664456
50	0.075829	0.924171	0	0.664456
60	0.073955	0.926045	0	0.664456
70	0.072588	0.927412	0	0.664456
80	0.071544	0.928456	0	0.664456

90	0.07072	0.92928	0	0.664456
100	0.070052	0.929948	0	0.664456
150	0.067993	0.932007	0	0.664456
200	0.066922	0.933078	0	0.664456
300	0.06581	0.93419	0	0.664456

Table B.6. Capillary pressure and relative permeability drainage and imbibition tables for rock type 5 (RQI=0.45).

RQI range from 0.5-0.4 -AveRQI=0.45				
Pc	Sw	SCO2	Krw	krCO2
0	1.000	0	1	0
1.5	0.869	0.13133	0.728436	0.000433
2	0.691	0.309055	0.426733	0.012203
3	0.507	0.493071	0.196037	0.075452
4	0.412	0.588461	0.110132	0.150391
5	0.353	0.647226	0.069006	0.217992
6	0.313	0.687229	0.046276	0.275433
7	0.284	0.7163	0.032485	0.323737
8	0.262	0.738428	0.023554	0.364521
9	0.244	0.755861	0.017485	0.399251
10	0.230	0.769968	0.013208	0.429108
12	0.209	0.791439	0.007804	0.477694
14	0.193	0.807042	0.004731	0.515487
18	0.172	0.828276	0.00174	0.570433
20	0.164	0.835848	0.001017	0.591042
25	0.150	0.849704	0.000181	0.630181
30	0.141	0.859136	0	0.657904
40	0.129	0.871	0	0.657904
50	0.121	0.879	0	0.657904
60	0.116	0.884	0	0.657904
70	0.113	0.887	0	0.657904
80	0.110	0.890	0	0.657904
90	0.108	0.892	0	0.657904
100	0.106	0.894	0	0.657904
150	0.100	0.900	0	0.657904
200	0.097	0.903	0	0.657904
300	0.095	0.905	0	0.657904

RQI range from 0.5-0.4 -AveRQI=0.45				
Pc	Sw	SCO2	Krw	krCO2
0	0.662	0.3376	0.303762	0
0.005	0.660	0.340035	0.299527	9.31E-07
0.01	0.658	0.342056	0.296043	4.32E-06
0.02	0.654	0.346051	0.289234	2.17E-05
0.03	0.650	0.349988	0.282627	5.66E-05
0.04	0.646	0.353867	0.276216	0.000112
0.05	0.642	0.35769	0.269993	0.00019
0.06	0.639	0.361458	0.263952	0.000293
0.07	0.635	0.365173	0.258086	0.000421
0.08	0.631	0.368835	0.252388	0.000575
0.09	0.628	0.372445	0.246854	0.000757
0.1	0.624	0.376005	0.241476	0.000965
0.2	0.591	0.409058	0.195229	0.004565
0.3	0.562	0.43808	0.159845	0.010708
0.4	0.536	0.463776	0.13233	0.018927
0.5	0.513	0.486696	0.110624	0.028732
0.6	0.493	0.507273	0.093283	0.039698
0.7	0.474	0.525854	0.079272	0.051479
0.8	0.457	0.542719	0.067836	0.063798
0.9	0.442	0.558101	0.058416	0.076443
1	0.428	0.572188	0.050593	0.089247
2	0.333	0.667435	0.015085	0.209236
3	0.280	0.719672	0.005809	0.302188
4	0.247	0.752861	0.00257	0.37216
5	0.224	0.775901	0.001235	0.425955
6	0.207	0.792873	0.000623	0.468401
7	0.194	0.805921	0.000323	0.50269
8	0.184	0.816279	0.000169	0.530952
9	0.175	0.824712	8.73E-05	0.554649
10	0.168	0.831717	4.41E-05	0.574807
12	0.157	0.842699	9.51E-06	0.607283
14	0.149	0.85093	1.18E-06	0.632329
20	0.133303	0.866697	0	0.657904
30	0.119999	0.880001	0	0.657904
40	0.112904	0.887096	0	0.657904
50	0.108465	0.891535	0	0.657904
60	0.105413	0.894587	0	0.657904
70	0.103181	0.896819	0	0.657904
80	0.101474	0.898526	0	0.657904
90	0.100123	0.899877	0	0.657904

100	0.099027	0.900973	0	0.657904
150	0.095639	0.904361	0	0.657904
200	0.093872	0.906128	0	0.657904
300	0.092035	0.907965	0	0.657904

Table B.7. Capillary pressure and relative permeability drainage and imbibition tables for rock type 6 (RQI=0.35).

Pc	Sw	SCO2	Krw	krCO2
0	1.000	0	1	0
2	0.877	0.123328	0.735111	0.000517
3	0.641	0.359319	0.337702	0.028507
4	0.518	0.481652	0.189719	0.085537
5	0.443	0.557015	0.118874	0.147538
6	0.392	0.608316	0.079717	0.205299
7	0.354	0.645598	0.05596	0.256603
8	0.326	0.673976	0.040575	0.301522
9	0.304	0.696334	0.030121	0.340775
10	0.286	0.714425	0.022753	0.375181
12	0.258	0.74196	0.013444	0.432345
14	0.238	0.761971	0.008151	0.477718
18	0.211	0.789202	0.002998	0.544952
20	0.201	0.798912	0.001751	0.570525
25	0.183	0.816682	0.000312	0.619585
30	0.171	0.828778	0	0.654704
40	0.156	0.844	0	0.654704
50	0.146	0.854	0	0.654704
60	0.140	0.860	0	0.654704
70	0.135	0.865	0	0.654704
80	0.131	0.869	0	0.654704
90	0.129	0.871	0	0.654704
100	0.126	0.874	0	0.654704
150	0.119	0.881	0	0.654704
200	0.116	0.884	0	0.654704
300	0.112	0.888	0	0.654704

RQI range from 0.4-0.3-AveRQI=0.35

Pc	Sw	SCO2	Krw	krCO2
0	0.666	0.3336	0.331434	0
0.005	0.665	0.335485	0.327663	1.02E-06
0.01	0.663	0.336962	0.324729	4.09E-06
0.02	0.660	0.339892	0.31896	1.84E-05
0.03	0.657	0.342789	0.313323	4.57E-05
0.04	0.654	0.345654	0.307814	8.77E-05
0.05	0.652	0.348489	0.302428	0.000146
0.06	0.649	0.351293	0.297162	0.00022
0.07	0.646	0.354066	0.292014	0.000313
0.08	0.643	0.35681	0.286979	0.000423
0.09	0.640	0.359525	0.282055	0.000551
0.1	0.638	0.362211	0.277239	0.000699
0.2	0.612	0.387591	0.234413	0.003207
0.3	0.589	0.410551	0.199686	0.007508
0.4	0.569	0.431428	0.171251	0.013357
0.5	0.550	0.450496	0.147761	0.02048
0.6	0.532	0.467985	0.1282	0.028619
0.7	0.516	0.484086	0.111791	0.037549
0.8	0.501	0.49896	0.097935	0.047081
0.9	0.487	0.512744	0.086162	0.057056
1	0.474	0.525556	0.076101	0.067344
2	0.383	0.617117	0.025884	0.171715
3	0.329	0.671216	0.010677	0.261114
4	0.293	0.70711	0.004916	0.332769
5	0.267	0.732746	0.002417	0.390243
6	0.248	0.752016	0.001235	0.436996
7	0.233	0.767054	0.000642	0.475643
8	0.221	0.779132	0.000334	0.508076
9	0.211	0.789057	0.000171	0.535663
10	0.203	0.797364	8.46E-05	0.55941
12	0.189	0.810502	1.67E-05	0.598202
14	0.180	0.82044	1.58E-06	0.628559
20	0.160303	0.839697	0	0.654704
30	0.143833	0.856167	0	0.654704
40	0.134967	0.865033	0	0.654704
50	0.129393	0.870607	0	0.654704
60	0.125548	0.874452	0	0.654704
70	0.122729	0.877271	0	0.654704
80	0.12057	0.87943	0	0.654704
90	0.118859	0.881141	0	0.654704

100	0.11747	0.88253	0	0.654704
150	0.113167	0.886833	0	0.654704
200	0.110919	0.889081	0	0.654704
300	0.108578	0.891422	0	0.654704

Table B.8. Capillary pressure and relative permeability drainage and imbibition tables for rock type 7 (RQI=0.25).

RQI range from 0.3-0.2 -AveRQI=0.25				
Pc	Sw	SCO2	Krw	krCO2
0	1.000	0	1	0
3	0.874	0.126025	0.713363	0.00093
4	0.704	0.295794	0.400764	0.020055
5	0.600	0.400378	0.251109	0.059641
6	0.528	0.471572	0.168394	0.107504
7	0.477	0.523311	0.11821	0.156382
8	0.437	0.562692	0.08571	0.203061
9	0.406	0.593719	0.063627	0.246344
10	0.381	0.618825	0.048063	0.285955
12	0.343	0.657037	0.028399	0.354793
14	0.315	0.684807	0.017217	0.41181
18	0.277	0.722597	0.006334	0.499664
20	0.264	0.736073	0.003699	0.534031
25	0.239	0.760732	0.000658	0.601293
30	0.222	0.777518	0	0.650445
40	0.201	0.799	0	0.650445
50	0.188	0.812	0	0.650445
60	0.179	0.821	0	0.650445
70	0.172	0.828	0	0.650445
80	0.167	0.833	0	0.650445
90	0.163	0.837	0	0.650445
100	0.160	0.840	0	0.650445
150	0.150	0.850	0	0.650445
200	0.145	0.855	0	0.650445
300	0.140	0.860	0	0.650445

RQI range from 0.3-0.2 -AveRQI=0.25				
Pc	Sw	SCO2	Krw	krCO2
0	0.675	0.325	0.373628	0
0.005	0.674	0.325972	0.371226	1.32E-07
0.01	0.673	0.32694	0.368843	1.34E-06
0.02	0.671	0.328866	0.364134	8.78E-06
0.03	0.669	0.330777	0.3595	2.42E-05
0.04	0.667	0.332674	0.354939	4.86E-05
0.05	0.665	0.334557	0.350451	8.25E-05
0.06	0.664	0.336427	0.346033	0.000127
0.07	0.662	0.338282	0.341684	0.000181
0.08	0.660	0.340124	0.337403	0.000246
0.09	0.658	0.341953	0.333189	0.000323
0.1	0.656	0.343769	0.32904	0.00041
0.2	0.639	0.361226	0.290889	0.001907
0.3	0.622	0.377506	0.258077	0.004516
0.4	0.607	0.392727	0.229724	0.008143
0.5	0.593	0.406991	0.205113	0.012669
0.6	0.580	0.420385	0.183663	0.017973
0.7	0.567	0.43299	0.164895	0.023938
0.8	0.555	0.444872	0.148415	0.030462
0.9	0.544	0.456095	0.133894	0.03745
1	0.533	0.466712	0.12106	0.04482
2	0.452	0.548164	0.048647	0.127684
3	0.399	0.601328	0.022053	0.208901
4	0.361	0.638888	0.010743	0.280171
5	0.333	0.666901	0.005458	0.341131
6	0.311	0.688635	0.002831	0.393146
7	0.294	0.706012	0.001474	0.437759
8	0.280	0.720239	0.000758	0.476313
9	0.268	0.732112	0.000377	0.509902
10	0.258	0.742177	0.000178	0.539395
12	0.242	0.758338	2.85E-05	0.588718
14	0.229	0.77076	1.24E-06	0.628299
20	0.20468	0.79532	0	0.650445
30	0.18316	0.81684	0	0.650445
40	0.171379	0.828621	0	0.650445
50	0.163902	0.836098	0	0.650445
60	0.158714	0.841286	0	0.650445
70	0.154895	0.845105	0	0.650445
80	0.15196	0.84804	0	0.650445
90	0.14963	0.85037	0	0.650445

100	0.147734	0.852266	0	0.650445
150	0.141841	0.858159	0	0.650445
200	0.13875	0.86125	0	0.650445
300	0.135525	0.864475	0	0.650445

Table B.9. Capillary pressure and relative permeability drainage and imbibition tables for rock type 8 (RQI=0.15).

RQI range from 0.1-0.01 -AveRQI=0.15				
Pc	Sw	SCO2	Krw	krCO2
0	1.000	0	1	0
5	0.941	0.059018	0.838383	0.000148
6	0.826	0.174245	0.56222	0.006198
7	0.742	0.257984	0.394669	0.024002
8	0.678	0.321723	0.286162	0.051411
9	0.628	0.37194	0.212433	0.084796
10	0.587	0.412576	0.160468	0.121264
12	0.526	0.474422	0.094815	0.196341
14	0.481	0.519367	0.057484	0.268306
18	0.419	0.580531	0.021146	0.393949
20	0.398	0.602342	0.012351	0.447404
25	0.358	0.642253	0.002198	0.55825
30	0.331	0.669422	0	0.64403
40	0.296	0.704	0	0.64403
50	0.274	0.726	0	0.64403
60	0.260	0.740	0	0.64403
70	0.249	0.751	0	0.64403
80	0.241	0.759	0	0.64403
90	0.235	0.765	0	0.64403
100	0.230	0.770	0	0.64403
150	0.214	0.786	0	0.64403
200	0.206	0.794	0	0.64403
300	0.197	0.803	0	0.64403

RQI range from 0.1-0.01 -AveRQI=0.15				
Pc	Sw	SCO2	Krw	krCO2
0	0.698	0.3025	0.445231	0
0.005	0.696	0.303506	0.441579	1.36E-06
0.01	0.696	0.304011	0.439754	3.44E-06
0.02	0.695	0.305017	0.43613	1.08E-05
0.03	0.694	0.30602	0.43254	2.28E-05
0.04	0.693	0.307018	0.428985	3.98E-05
0.05	0.692	0.308013	0.425464	6.18E-05
0.06	0.691	0.309003	0.421976	8.91E-05
0.07	0.690	0.309989	0.418521	0.000122
0.08	0.689	0.310971	0.4151	0.00016
0.09	0.688	0.31195	0.41171	0.000204
0.1	0.687	0.312924	0.408353	0.000253
0.2	0.678	0.322455	0.376468	0.00106
0.3	0.668	0.331617	0.347426	0.002437
0.4	0.660	0.340431	0.320934	0.004363
0.5	0.651	0.348917	0.296735	0.006805
0.6	0.643	0.357093	0.274601	0.009727
0.7	0.635	0.364976	0.254329	0.013089
0.8	0.627	0.372581	0.23574	0.016856
0.9	0.620	0.379925	0.218674	0.020989
1	0.613	0.387019	0.202989	0.025457
2	0.553	0.446681	0.099601	0.082468
3	0.509	0.491341	0.0509	0.149335
4	0.474	0.526085	0.026542	0.216548
5	0.446	0.553924	0.013886	0.280345
6	0.423	0.576754	0.007172	0.339428
7	0.404	0.595832	0.003592	0.393561
8	0.388	0.612026	0.001704	0.442954
9	0.374	0.625951	0.00074	0.487988
10	0.362	0.638059	0.000278	0.529089
12	0.342	0.658102	1.31E-05	0.601124
14	0.325968	0.674032	0	0.64403
20	0.293082	0.706918	0	0.64403
30	0.262675	0.737325	0	0.64403
40	0.245378	0.754622	0	0.64403
50	0.234156	0.765844	0	0.64403
60	0.226259	0.773741	0	0.64403
70	0.220385	0.779615	0	0.64403
80	0.215838	0.784162	0	0.64403
90	0.212208	0.787792	0	0.64403

100	0.20924	0.79076	0	0.64403
150	0.19994	0.80006	0	0.64403
200	0.195016	0.804984	0	0.64403
300	0.189845	0.810155	0	0.64403

Table B.10. Capillary pressure and relative permeability drainage and imbibition tables for rock type 9 (RQI=0.055).

RQI range from 2.5-1 -Ave RQI=0.055				
Pc	Sw	SCO2	Krw	krCO2
0	1.000	0	1	0
18	0.900	0.099708	0.471353	0.015556
20	0.850	0.150401	0.275312	0.060399
25	0.757	0.243167	0.048989	0.294839
30	0.694	0.306314	0	0.631616
40	0.613	0.387	0	0.631616
50	0.563	0.437	0	0.631616
60	0.529	0.471	0	0.631616
70	0.505	0.495	0	0.631616
80	0.486	0.514	0	0.631616
90	0.471	0.529	0	0.631616
100	0.459	0.541	0	0.631616
150	0.422	0.578	0	0.631616
200	0.403	0.597	0	0.631616
300	0.384	0.616	0	0.631616

RQI range from 2.5-1 -Ave RQI=0.055				
Pc	Sw	SCO2	Krw	krCO2
0	0.831	0.1688	0.631603	0
0.005	0.831	0.169147	0.626831	1.73E-06
0.01	0.831	0.169294	0.624815	3.93E-06
0.02	0.830	0.169588	0.620801	1.12E-05
0.03	0.830	0.169882	0.616809	2.24E-05
0.04	0.830	0.170175	0.61284	3.76E-05
0.05	0.830	0.170468	0.608892	5.7E-05
0.06	0.829	0.170761	0.604966	8.06E-05
0.07	0.829	0.171053	0.601063	0.000108
0.08	0.829	0.171345	0.59718	0.000141
0.09	0.828	0.171636	0.59332	0.000177
0.1	0.828	0.171928	0.589481	0.000218
0.2	0.825	0.174819	0.552249	0.000874
0.3	0.822	0.177674	0.517051	0.001983
0.4	0.820	0.180494	0.483787	0.003547
0.5	0.817	0.183279	0.452362	0.005563
0.6	0.814	0.186031	0.422686	0.008024
0.7	0.811	0.188749	0.394671	0.010921
0.8	0.809	0.191435	0.368237	0.014245
0.9	0.806	0.194089	0.343304	0.017986
1	0.803	0.196711	0.319798	0.022133
2	0.779	0.221319	0.149136	0.083595
3	0.757	0.243326	0.060698	0.174405
4	0.737	0.26313	0.019561	0.286135
5	0.719	0.28105	0.003917	0.41234
6	0.703	0.297347	0.000175	0.548192
7	0.687765	0.312235	0	0.631616
8	0.674108	0.325892	0	0.631616
9	0.661533	0.338467	0	0.631616
10	0.649915	0.350085	0	0.631616
12	0.629135	0.370865	0	0.631616
14	0.611084	0.388916	0	0.631616
20	0.568761	0.431239	0	0.631616
30	0.522277	0.477723	0	0.631616
40	0.491998	0.508002	0	0.631616
50	0.470635	0.529365	0	0.631616
60	0.454717	0.545283	0	0.631616
70	0.442376	0.557624	0	0.631616
80	0.432514	0.567486	0	0.631616
90	0.424443	0.575557	0	0.631616

100	0.41771	0.58229	0	0.631616
150	0.395809	0.604191	0	0.631616
200	0.383707	0.616293	0	0.631616
300	0.370611	0.629389	0	0.631616

References

Bennion, B., and Bachu, S., 2007, Relative permeability characteristics for supercritical CO_2 displacing water in a variety of potential sequestration zones: Society of Petroleum Engineers, SPE-95547-MS.

Bennion, B., and Bachu, S., 2010, Drainage and imbibition CO_2/brine relative permeability curves at reservoir conditions for high-permeability carbonate rocks: Society of Petroleum Engineers, SPE 134028-MS.

Benson, S., 2005, Overview of geologic storage of CO_2, in carbon dioxide capture for storage in deep geologic formations, Volume 2—Results from the CO_2 capture project: Elsevier Publishing, UK.

Burnside, N. M., and Naylor, M., 2014, Review and implications of relative permeability of CO_2/brine systems and residual trapping of CO_2: Int. J. Greenh. Gas Control, 23, p. 1–11

Bui, L. H., Tsau, J. S., and Willhite, G. P., 2010, Laboratory investigations of CO_2 near-miscible application in Arbuckle Reservoir: SPE Improved Oil Recovery Symposium, Tulsa, Oklahoma, 24–28 April 2010, SPE Publication 129710.

Carter, R. D., and Tracy, G. W., 1960, An improved method for calculating water influx: Petroleum Transactions, AIME, v. 219, p. 415–417.

Chang, K. W., Minkoff, S. E., and Bryant, S. L., 2009, Simplified model for CO_2 leakage and its attenuation due to geological structures: Energy Procedia, v. 1, p. 3,453–3460.

Dake, L. P., 1978, Fundamentals of Reservoir Engineering, Chapter 9, Elsevier Scientific Publishing Co., 1978.

Deutsch, C.V. 2002. Geostatistical reservoir modeling. Oxford University Press, Inc., New York, New York.

FutureGen Industrial Alliance, 2013, Underground injection control permit applications for FutureGen 2.0 Morgan County Class VI UIC Wells 1, 2, 3, and 4, Jacksonville, Illinois.

Kestin, J., Khalifa, H. E., and Correia, R. J., 1981, Tables of the dynamic and kinematic viscosity of aqueous NaCl solutions in the temperature range 20–150 °C and the pressure range 0.1–35 MPa: Journal of Physical and Chemical Reference Data, NIST, v. 10, p. 71–88.

Krevor, P., and Benson, S. M., 2012, Capillary pressure and heterogeneity for the CO_2/water system in sandstone rocks at reservoir conditions: Advances in Water Resources, v. 38, p. 48–59, ISSN: 0309-1708

Krevor, P., and Benson, S. M., 2015, Accurate determination of characteristic relative permeability curves: Advances in Water Resources, v. 83, p. 376–388

Li, Y. K., and Nghiem, L. X., 1986, Phase equilibrium of oil, gas and water/brine mixtures from a cubic equation of state and Henry's Law: Canadian Journal of Chemical Engineering, June, p. 486–496.

Loucks, R. G., 1999, Paleocave carbonate reservoirs: Origins, burial-depth modifications, spatial complexity, and reservoir implications: The American Association of Petroleum Geologists, Bulletin, v. 83, no. 11.

Lucia, F. J., 1999, Carbonate reservoir characterization: New York, Springer-Verlag, 226 p.

Pau, G. S. H., Bell, J. B., Pruess, K., Almgren, A. S., Lijewski, M. J., and Zhang, K., 2010, High resolution simulation and characterization of density-driven flow in CO_2 storage in saline aquifers: Advances in Water Resources, v. 33, no. 4, p. 443–455.

Søreide, I., and Whitson, C. H., 1992, Peng-Robinson predictions for hydrocarbons, CO_2, N_2, and H_2S with pure water and NaCI brine: Fluid Phase Equilibria, v. 77, p. 217–240.